High-resolution simulations of fluid flow in active hydrothermal systems: Applications to the Tjörnes Fracture Zone and Askja Volcanic Complex in Iceland

Matteo Lupi

Heriot-Watt University

Institute of Petroleum Engineering

A thesis submitted for the degree of

Doctor of Philosophy

30^{th} of June 2010

1. Reviewer: Prof. John W. Cosgrove

2. Reviewer: Dr. Helen Lewis

Day of the defense: 30^{th} of June 2010

Signature from head of PhD committee:

Abstract

This study provides new insights into the transient fluid flow dynamics that characterise high temperature hydrothermal systems. So far, these kind of studies have used process models that tend to over-simplify the geology and focus instead on the physical processes, hence not revealing the hidden behaviour that depends on the complex geological structures often encountered in hydrothermal systems. This study is one of the first examples where high resolution numerical simulations in two and three dimensions have been applied to hydrothermal systems in order to preserve geological detail in the models explicitly. Two prime examples in Iceland for seismicity-induced fluid flow and groundwater flow during volcanic eruptions, respectively, have been selected for this purpose. The first example is the Tjörnes Fracture Zone, a heavily faulted transform zone offshore in North Iceland where most of the Icelandic earthquakes occur. The work demonstrated that a moderate permeability contrast between the shallow sedimentary basins and deep crustal basement causes two distinct fluid flow regimes which are only connected during a seismic event. When such an event occurs, faults in the Tjörnes Fracture Zone inflate and connect the two fluid flow systems, causing hot fluids migrating from the basement into the basins at extreme flow rates. This explains key geochemical observations made in the Tjörnes Fracture Zone before and after a seismic event. The second study investigated the 1874 to 1875 volcano-tectonic episode at the Askja volcano, which is the third largest silicic eruption since settlement in Iceland. Here it was demonstrated how syn-eruptive groundwater flow inside the Askja caldera changed the eruptive style of the March 1875 eruption, causing a well-documented change from a wet to dry eruptive style. The results of this work provide some fundamental new insights into the transient dynamics of fluid flow in active high temperature hydrothermal systems and suggest that these kind of simulations may be used to complement studies assessing the risk and hazard of future volcanic eruptions and seismic events.

A babbo e mamma..

Acknowledgements

I am in a rush, as usual! I should have learnt something by now! These three years, almost four, will always stay with me. Here is where I understood what I want from life. When I arrived in Edinburgh it was pouring down, it was late and cold. Sebastian, you invited me in Stockbridge for dinner and everything started from there with a Gaggia and Paolo Conte.. Yes, because this is what I was and what it has been: an Italian in Scotland! I remember you on the stairs, holding Olivia, you closed the door of your house and opened the one of a new life! This is just an episode but it is also one of the many reasons why I do not want to thank you only for what you taught me, although it is a lot (!). Thanks for the thousands of "no problem" that you told me, thanks for the freedom that you gave me, thanks for the emails late at night to fix a mesh that did not want to work. Thanks for being supportive, enthusiastic and for covering my back "by default". I told you this several times already but I write it here, you have been great! You have been more than a supervisor, and it has been a pleasure to be part of your team! Colin, thank you for our scientific discussions and the enthusiasm that you have always transmitted to me. I still remember when we went to Iceland and had our first good chat. Thank you Lillemor, Alastair and Thor for having given to me this fantastic opportunity called Iceland. This magic country will always stay with me! Thank you Helen and John, you made me experience a great viva. I felt that my efforts during these years have been acknowledged with a very pleasant examination.

Thanks to the guys who shared their lives with me. Thank you Oscar for the time that we spent together either at lunch or in front of a beer. Thanks Susana for having being such a good friend, and for having given me a third chance after the plant that I tried to break and the eurovision party, I found

in you a really good friend (although ti puzzano i piedi!). Thanks Alejandro for having let me share with you heavy metal in the morning (and for the colombian dinner!), thank you Alessio for having lost our jackets together the first time, now I can say that it was rather cool. Thank you Karen for laughing with me and for having sent me emails at night saying: go home! Thanks Claudia, you gave me the excuse to invite Nicole out the first time (it was for one of your parties). Thanks Yan for your support, it really meant something to me when I have got the "Moscow news". Robert, we haven't had much time to spend together but I did enjoy the time we had in the office! Thanks Marta and Lukas for the nights in front of the bonfires and thanks Suzhanna for that hug. Thank you Celine for having guested me during my visits in Edinburgh. A special thanks goes to Adnan, Karen, Yan, Claudia, Robert and Christine for the post-viva surprise, it was unique and made my day even more special!

Grazie Nonna, noi due ci capiamo, a volte ci prendono in giro, ma dobbiamo ammetterlo, e' la verita'! Mi ricordo nonno come ti guardava, a volte mi sembra di vedere babbo quando guarda me! Nonni, un bacio a tutti voi, da "imbroglia popoli/lavativo" al nonno col cappello, passando per quello che mi fece scegliere Reno. Mamma anche noi due ci capiamo eh. Lo sai che questo dottorato e' anche buona parte tuo, con tutte le telefonate ed i discorsi sul bus! I "non ti preoccupare" ed i "bene eh"!!!! Babbo porto sempre con me nel moleskin le righe che mi scrivesti quando dovevo decidere per il lavoro. Mi hanno toccato il cuore. Lorenzo, te sei sempre zitto ma nei momenti piu' importanti mi fai sentire che ci sei. Grazie per quella telefonata!

Nicole, I would write pages here. Wherever I am, you are always with me, I can feel you! Somehow you are a bit like the sky but not because you are here, there and everywhere.. but simply because the sky is the home of the clouds!

Ad Majora!

Contents

List of Figures

List of Tables

1

Introduction

1.1 Large scale fluid flow in the Earth

The main forces driving fluid flow in the Earth's crust are solar radiation and the internal heat of the Earth. Fluids circulating in the crust are of both deep and shallow origins. Dehydratation of subduction plates, mantle degassing, and metamorphic process are sources of deep fluids. Sources of shallow fluids are meteoric waters that percolate in the shallow crust. Approximately 4.0×10^4 km^3 yr^{-1} of water percolates in the continental crust and mixes with continental brines (Cathles, 1990). Only a small volume, approximately 10% of the total amount of meteoric water that is recharged due to precipitation, surface run-off, and evapotranspiration, reaches a depth of more than one kilometer (Toth, 1963). At the regional scale, fluid flow can be driven by topography, differences in fluid density, compaction of terrains, thermohaline convection near evaporitic bodies and other phenomena (Raffensperger and Garven (1995a), see Figure 1.1).

Conductive heat flow measured at the surface ranges from 0 to 0.35 W m^{-2} (Chapman and Pollack, 1975), with a mean value of approximately 0.07 W m^{-2}. The most significant contribution to geothermal heat flow is provided by the decay of radioactive isotopes (i.e. uranium, thorium and potassium) and the sustained nuclear fission reaction in Earth's inner core. A small contribution is also due to the residual heat from the planetary accretion. The internal heat causes a geothermal gradient which describes the rate at which the temperature increases with depth. Assuming a typical thermal conductivity of 2 W (m K)$^{-1}$ for the continental crust, the average continental

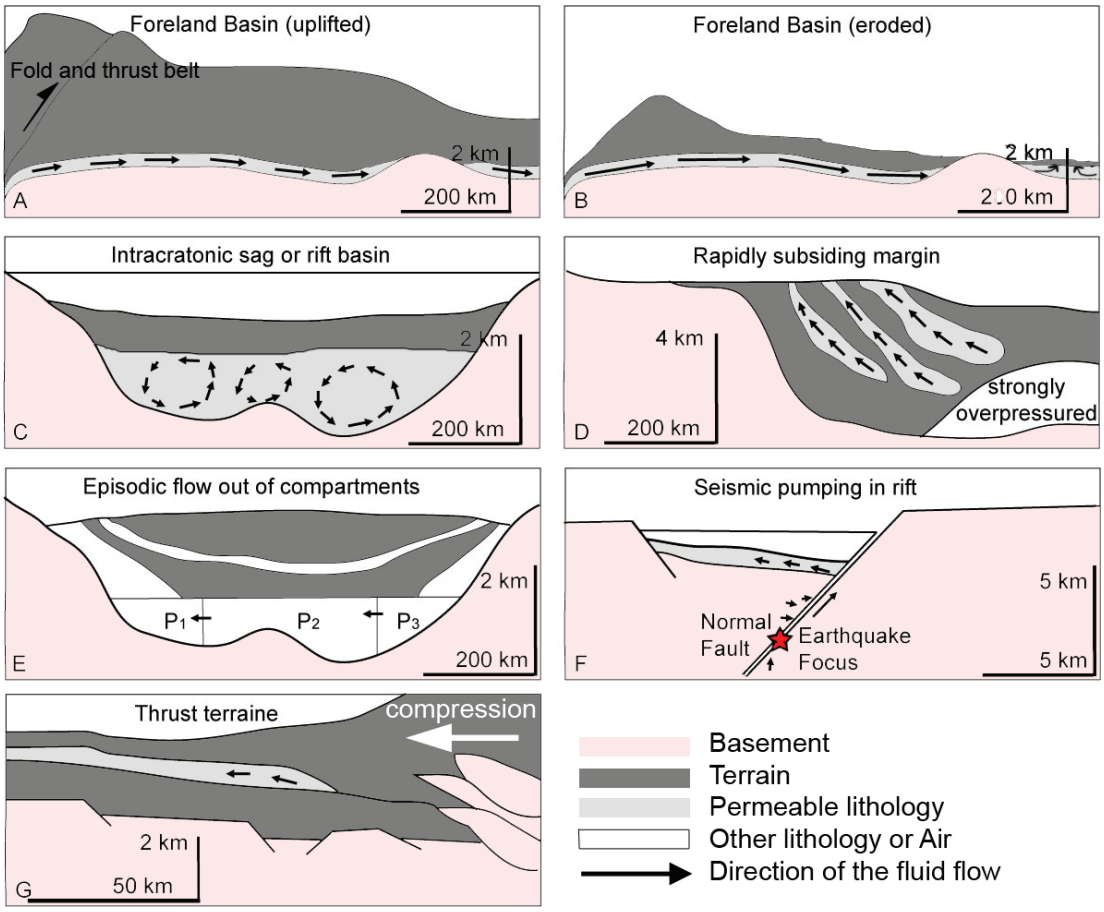

Figure 1.1: Regional driving forces for fluid flow in the upper Earth's crust. - In uplifted foreland basins (a) the maximum fluid flow rate varies from 1 to 10 m yr^{-1} and fluid flow is driven by differences in elevation head; in eroded foreland basins (b) the maximum flow rate varies from 1 to 100 m yr^{-1} and fluid flow is driven by differences in elevation head; in intracratonic sag or rift basins (c) the maximum flow rate varies from 0.1 to 1 m yr^{-}1 and fluid flow is driven by differences in fluid density; in rapidly subsiding margins (d) the maximum flow rate varies from 0.1 to 1 cm yr^{-1} and fluid flow is driven by differences in pore pressure P_f due to variations in porosity and permeability; in compartmented crust (e) characterised by different pore pressures P_f, episodic fluid flow out of these compartments can occur, fluid flow is driven by differences in pore pressure P_f; post-seismic states (f) can be characterised by large volumes of fluids (between 10^6 – 10^7 m^3) pumped upwards along the damaged area of the fault; in thrust terrains (g) the maximum flow rate varies from 0.1 to 1 m yr^{-}1 and fluid flow is driven by differences in pore pressure P_f due to porosity changes. Modified after Raffensperger and Garven (1995a,b).

geothermal gradient ranges between 20 and 35 °C km^{-1} (Ingebritsen et al., 2006).

The average heat flow values of the continental crust range from 0.04 W m^{-2} in old cratons areas to 0.07 W m^{-2} in Tertiary areas while for the oceanic crust the average heat flow ranges from 0.05 W m^{-2} in old oceanic crust ($\sim$ 200 Ma) to more than 0.3 W m^{-2} close to the mid ocean ridges (MOR) (Ingebritsen et al., 2006). Isothermal or even negative geothermal profiles can be found where groundwater recharge occurs from higher topographic levels characterised by low temperatures. This can lead to negative near-surface heat flow rates of $\leq$ 0 W m^{-2} (Ingebritsen et al., 2006). Approximately 20 % to 25 % of the heat loss is dispersed near MORs (Sclater et al., 1980; Stein and Stein, 1994; Williams and Von Herzen, 1974), which indicates the importance of the hydrothermal circulation in the Earth's thermal balance. Here significantly higher heat flow rates and geothermal gradients, up to 500 °C km^{-1}, are observed due to shallow magmatic bodies (Ingebritsen et al., 2006).

1.2 Sub-aerial and sub-sea fluid flow systems

Large-scale fluid flow can occur below the sea floor (sub-sea fluid flow) as well as on land (sub-aerial fluid flow). The main differences between sub-aerial and sub-sea fluid flow systems are their crustal structures and the properties of the fluids that characterise them (Figure 1.2). The continental crust consists mainly of granitic, sedimentary, and metamorphic rocks. It has an average density of approximately 2700 kg m^{-3} and its average thickness varies between 35 and 40 km. The standard oceanic crust is comprised of gabbros, basaltic dikes, pillow basalts and sedimentary layers, from deep to shallow, respectively. Its average thickness lies between 7 and 10 km and its average density is approximately 3000 kg m^{-3}. While fluids flowing in the upper continental crust are mostly brines diluted by meteoric waters, fluids flowing in sub-sea environments are H_2O-NaCl rich fluids with a salinity of approximately 3.2% NaCl, although higher and lower salinities have been observed close to MORs due to boiling and phase separation of H_2O-NaCl fluids (Von Damm, 1995). NaCl is the dominant chemical component in the brines of sub-aerial and sub-sea fluids. NaCl strongly affects the fluid properties and their phase state over a wide range of pressures, temperature, and compositions (cf. Driesner and Heinrich (2007); Driesner (2007), see Figure 1.3) and subsequently has a significant impact on the flow processes (Geiger et al., 2005). NaCl-H_2O fluids

can boil and separate into a high-density brine and low-density vapour at temperatures and pressures much above the critical point of pure water (374 °C and 22.064 MPa). This allows for two fluid phases, vapour and liquid brine to flow simultaneously under certain pressure, temperature, and salinity conditions.

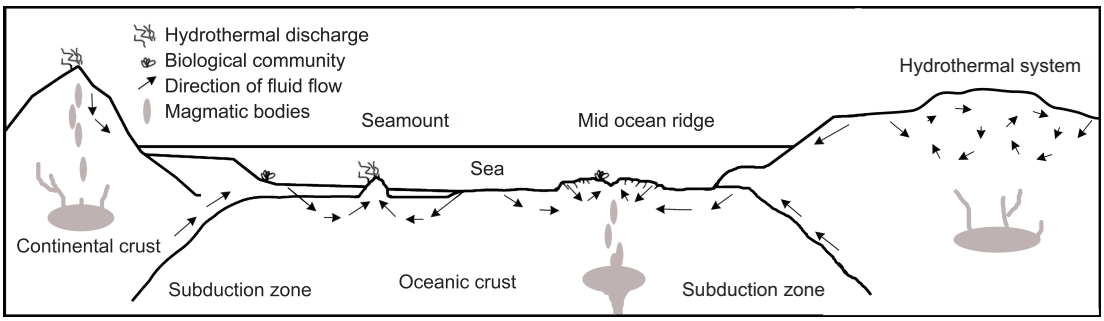

Figure 1.2: Idealised tectonic setting of sub-aerial and sub-sea systems - Fluid flow is shown from left to right for back-arc volcanic systems, accretionary prisms, seamounts, MORs and continental hydrothermal systems. Flow directions are schematically shown by black arrows. Magmatic bodies are shown in grey and the biological communities by closed curved lines. Modified after Ingebritsen et al. (2006).

The forces driving fluid flow (Figure 1.2) vary in sub-sea and sub-aerial systems. For instance, the elevation head which strongly influences fluid flow in sub-aerial systems is usually not the primary driving force in sub-sea systems. Geothermal gradients dominate sub-sea systems, most notably at MOR and their flanks. Fluid flow in continental environments mainly occurs from topographic highs towards topographic lows while in sub-sea environments it often occurs from topographic lows towards topographic highs (Figure 1.2).

In density- and topography-driven fluid flow systems the pore pressure usually increases with depth and lies within 10% of the hydrostatic pressure gradient (Zoback and Zoback, 1997). Near-hydrostatic pore pressures have been found up to 10 km depth in crystalline rocks (Rojstaczer et al., 2008). Regions with pore pressures above hydrostatic, so called "over-pressured regions", are often encountered in crustal areas characterised by an active geology (e.g. sediment compaction, metamorphic dehydratation, magmatic intrusion). Over-pressured regions can also be found due to the occurrence of heterogeneous permeabilities, chemical osmosis, or heterogeneous pore fluids (such as oil and gas) (Neuzil, 1995; Osborne and Swarbrick, 1997). In this work, the term over pressure is expressed by the adimensional pore fluid factor $\lambda = P_f/(\rho_r g z + \tau)$,

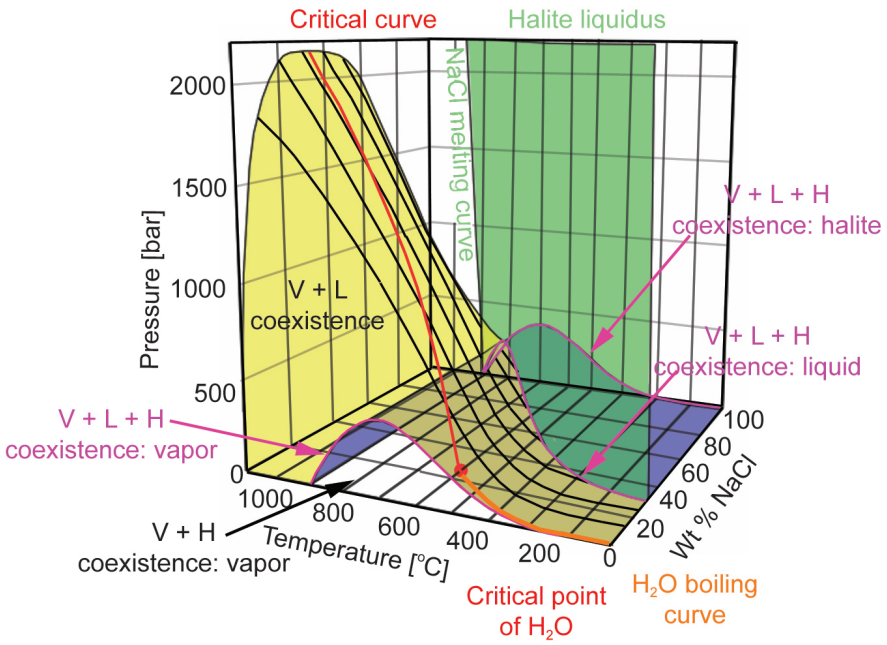

Figure 1.3: Phase diagram of H_2O-NaCl in temperature – pressure – composition coordinates. - The most relevant elements of the phase diagram are: i) the region underneath the yellow surface (vapour + liquid coexistence) bounding a large region where vapor + liquid coexist; ii) (vapour + liquid + halite coexistence) bounding the region where vapour + halite coexist; iii) the green surface (the halite liquidus) between the halite liquidus and the vapour + liquid + halite coexistence surface, halite coexists with a liquid brine. H = halite, L = liquid, V = vapour. Modified after Driesner and Heinrich (2007).

and indicates values of λ greater than 0.4. Here ρ_r is the rock density, g is the gravitational acceleration, z the depth, τ the tensile strength of the rock, and P_f the pore pressure. The pore fluid factor λ was introduced for the first time by Hubbert and Rubey (1959) for fault overthursts. Figure 1.4 shows a schematic representation of the depth dependence of λ.

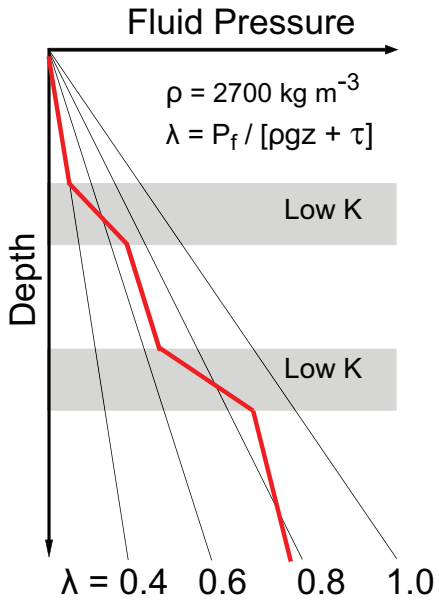

Figure 1.4: Schematic variation of pore pressure in the crust. - The pore fluid factor λ is defined as the ratio of pore pressure and the sum of lithostatic load $\sigma_v = \rho g z$ and tensile strength τ. The black lines show the depth variation for different λ values. The grey areas represent lithologies characterised by low permeability values (lower than 1.0×10^{-17} m^2) where higher pore pressures may be encountered (Manning and Ingebritsen, 1999; Neuzil, 1995). Pore fluid factors of λ=0.4 characterise near-surface fluid-saturated areas where pores and fractures are well connected. In areas characterised by lower permeabilities the pore fluid factor can increase. The red line shows a schematic variation of λ with depth. For values of λ close to the unity (or less, (Sibson, 1974, 1981)) failure can occur. Modified after Sibson and Rowland (2003).

1.3 High temperature hydrothermal systems

In this work, the terminology "hydrothermal systems" refers, if not otherwise specified, to the fluid flow dynamics that can occur in both volcanic and hydrothermal system. Hydrothermal systems develop in the upper crust when a fluid phase coexists with

a source of heat. The thermal energy necessary to the development of hydrothermal systems is usually provided by magmatic intrusions. Only a few examples of high temperature hydrothermal systems, i.e. with fluid temperatures above the critical point of pure water, occur in regions where little or no magmatic activity is present (Ingebritsen et al., 2006). These systems are often related to deep circulation of meteoric waters in highly permeable geological environments. Economically exploitable shallow hydrothermal systems are commonly associated with Quaternary magmatic bodies: Smith and Shaw (1975) estimated that pre-Quaternary intrusions, with volumes less than 10^3 km^3, have already cooled down to ambient temperature by conduction alone. Most high temperature continental hydrothermal systems are associated with silicic magmatic bodies (Hildreth, 1981). High temperature hydrothermal systems associated with mafic magmas are rare and can only be found in areas characterised by mantle plumes, such as Iceland and Hawaii (Ingebritsen et al., 2006).

The study of fossil hydrothermal systems has shown, by means of oxygen isotope data, that strong circulation of brines diluted with meteoric waters can occur close to the magmatic bodies intruded at mid-crustal depths (e.g. Taylor (1971) and Norton and Taylor Jr. (1979)). Pioneering quantitative studies in the late 1970ties have investigated the complex fluid circulation near magmatic bodies (Cathles, 1977; Norton and Knight, 1977). They showed how variations in host-rock permeability affect the extent and vigour of convection of meteoric waters and diluted brines above magmatic intrusions. Circulation of fluids in high temperature hydrothermal systems is facilitated by the cyclical transient permeability behaviour, which is function of the initial permeability distribution (before the intrusion), mineralization of the host rocks, changes in pressure and temperature and the rate at which fluids are released from the magma during its cooling (Ingebritsen et al., 2010). When the permeability of the host rock is low enough, over pressure builds up and hydraulic fracturing and rock failure can occur (Sibson, 1974, 1981). This is thought to be a key process for forming economic ore deposits in high temperature hydrothermal systems (Cox and Ruming, 2004). When new fractures are created, fluids start to circulate inside these fractures. With time, tectonic stress and precipitation of mineral phases reduce the overall permeability of the host rocks and a new cycle of over pressure build up can start.

In numerical simulations of high temperature hydrothermal systems, the upper boundary condition for sub-aerial hydrothermal systems is commonly the water table.

Its morphology mimics the surface topography and is affected by annual and secular climate variations (Hurwitz et al., 2003). The upper boundary for fluid circulation in sub-sea environments is the sea-floor. Here the temperature is approximately constant (i.e. few degrees Celsius) and the lateral variation of hydrostatic pressure, which depends upon the depth, varies minimally in space. For both sub-aerial and sub-sea systems, the lower boundary can be reasonably considered to be a no-flow, constant-heat boundary, if no degassing occurs from the lower part of the crust.

1.3.1 Economic and scientific importance of hydrothermal systems

1.3.1.1 Geothermal energy

Geothermal energy has been known to humans for a long time. Cataldi and Chellini (1995) show evidences of drawings that represent an erupting volcano in the Neolithic village of Catal Hüyük in the old Anatolia. Geothermal resources have been used by ancient societies in many ways. For instance in China, salt was extracted from geothermal fields since 2000 years BC (Wang, 1995) and in Japan thermal springs were used to cook food since 6000 years BC (Sekioka, 1995). Today geothermal resources only supply a relatively marginal amount of the world's total energy demand (less than 1%). However, they have the potential to significantly contribute to climate change mitigation because of their favourable carbon footprint and the opportunity to use carbon dioxide (CO_2) as a geothermal working fluid (Pruess, 2006; Pruess et al., 2003).

The geothermal systems are classified as low enthalpy, intermediate enthalpy, and high-enthalpy systems (Benderitter and Cormy, 1990; Hochstein, 1990; Muffler and Cataldi, 1978), the temperature of the extracted fluids increases from low to high. For instance, Hochstein (1990) suggests for low-, intermediate-, and high enthalpy systems temperatures of less than 125 °C, from 125 °C to 225 °C, and more than 225 °C, respectively. The latter are usually associated with magmatic hydrothermal systems.

The most common use of geothermal energy is for powering heat pumps, heating (in particular for greenhouses and swimming pools), and industrial purposes (Fridleifsson et al., 2008). There is potential to increase production from low-enthalpy geothermal systems by at least a factor 15 (Table 1.1).

In 2005, 97% of the electricity supply and 71% of the direct use of thermal energy was generated from geothermal resources in the ten countries that lead the world in

Region	Installed Capacity in 2005 [GW]	Potential [GW]
North America	3.52	30.0
Asia	3.29	42.0
Europe	1.12	15.8
Oceania	0.44	9.0
Central and South America, Caribbean	0.42	38.0
Africa	0.14	14.0
World Total	8.93	148.8

Table 1.1: Estimated potential (in Gigawatt) of enhanced geothermal systems word wide. Source: Glitnir Bank - *www.glitnirusa.com/energy*.

geothermal energy production (Glitnir bank report (2007), see Table 1.2).

The two main disadvantages of geothermal energy concern the location (it is restricted to areas with high crustal heat flow) and the investment to construct geothermal power plants. Another drawback is that geothermal energy cannot be easily transported.

1.3.1.2 Ore deposits

Another important aspect of hydrothermal systems is that economically viable ore deposits are often associated with hydrothermal systems. Evans (1993) divides the processes that lead to the occurrence of ore deposits into four groups: internal processes, metamorphic processes, surficial processes, and hydrothermal processes. Internal processes include magma dynamics such as fractional crystallization (e.g., accumulation of and Mg-Fe rich minerals) and liquid immiscibility between melts of differing compositions (usually sulfide segregation of nickel-copper-platinoid sulfides and silicates). Metamorphic processes can concentrate elements that can be transported in crustal fluids and lead to the formation of ore concentrations. Concentrations of quartz, sulfides, gold, carbonates, and oxides are often found in areas that featured dynamic metamorphism (Evans, 1993). Surficial processes are phenomena that accumulate mineral phases in the regolith. They consist of dissolution, transport, and precipitation of mineral phases in the first meters below the ground surface. High temperature hydrothermal fluids mobilise, circulate, concentrate mineral phases in the crust. Figure 1.5 shows how circulation of fluids can concentrate mineral phases above a cooling

Country	GWh electric	Country	GWh thermal
United States	17,917	China	12,605
Philippines	9,253	Sweden	10,001
Mexico	6,282	United States	8,678
Indonesia	6,085	Turkey	6,901
Italy	5,340	Iceland	6,806
Japan	3,467	Japan	2,862
New Zealand	2,774	Hungary	2,206
Iceland	1,483	Italy	2,099
Costa Rica	1,145	New Zealand	1,969
Kenya	1,088	Brazil	1,840
Sum of Top 10	54,834	Sum of Top 10	54,125
All Other	1,952	All Other	19,979
World Total	56,786	**World Total**	75,943

Table 1.2: Top 10 countries in geothermal energy usage in 2005 in Gigawatt Hours. Source: Glitnir Bank - *www.glitnirusa.com/energy.*

magmatic intrusion. The mineral precipitation of the ore phases occurs in regions of enhanced permeability. World-class Cu-Au-Mo deposits are usually associated with high temperature hydrothermal systems.

1.3.2 Near MORs hydrodynamics

Another scientifically relevant aspect of high temperature hydrothermal systems are MORs. In the mid 1960ties, the discovery of hydrothermal brines and metalliferous sediments in the Red Sea confirmed, for the first time, the occurrence of hydrothermal activity at MORs. Experimental studies carried by Bischoff and Dickson (1975) have shown that the reaction between seawater and basalts at the temperature of 200 °C produces large amounts of heavy metals and H_2S, in agreement with the occurrence of the large sulfide deposits found on the seafloor. Detailed studies of sub-sea hydrothermal systems opened new scenarios on the origin of life on Earth. Chemosyntetic bacteria populate the ecosystems associated with hydrothermal vents at MORs (Lutz and Kennish, 1993). Chemical energy rather than solar energy can lead to the formation of metal- and gas-tolerant ecosystems. Their independence from photosynthesis is one of the arguments suggesting that life originated in hydrothermal systems near MORs

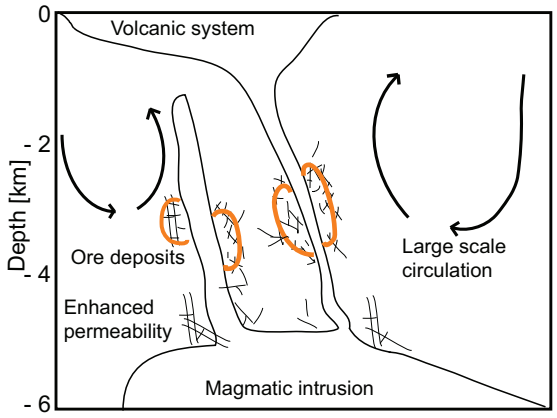

Figure 1.5: Schematic representation a porphyry ore deposit - Fluids liberated from the magma (cooled by large scale convection) circulate in areas of enhanced permeability and can cause mineral precipitation and formation of Cu-Au-Mo ore deposits. Modified after Geiger (2004)

(Brack et al., 2010; Knoll, 2004; Martin et al., 2008; Russell and Kanik, 2010; Wald, 1964).

The significance of MOR systems on the Earth's thermal budget was discussed previously. However, quantifying the flow processes that cause the rapid heat loss directly at the MOR is very complex because extreme gradients of temperature and density are coupled with an intense tectonic activity (Coumou et al., 2008). Hydrothermal systems off-axis of the MOR are characterised by convective hydrothermal flow driven by density gradients. Sampling of fluids through the sediments of the shallow oceanic crust in off-axis hydrothermal systems indicates upwelling and downwelling fluids with pore velocities of few millimeters per year (Langseth et al., 1988). Away from MORs where small density gradients drive "passive" convection, the hydrothermal circulation becomes less intensive due to the reduction of both heat flow and crustal permeability. Convection becomes completely restricted when the geothermal gradient returns to standard oceanic setting values far from the MORs.

Another important aspect of MOR systems is that they control the pH of the ocean. For instance, if the sources and sinks of solutes were absent from the MORs, the oceans would be more alkalin (pH 10, sodium bicarbonate dominated) than it is nowadays (pH 8, sodium chloride dominated) (Mackenzie and Garrels, 1966).

1.4 Seismicity and fluid flow in hydrothermal systems

Hydrothermal systems are often characterised by constant seismic tremor caused by deep movement of fluids (Hellweg, 2000; McClain et al., 1993) and hydrofracturing (Gudmundsson, 2001). Field evidences can be found around exhumed magmatic intrusions where fracture networks often occur. The fractures usually show a sub-horizontal and sub-vertical orientation (Figure 1.6) and form as consequence of elevated pore pressures (Gudmundsson, 1999; Sibson, 1974, 1981). Note that in this thesis the terminology "fracture" refers to the apertures (from meter to centimeter scale) that characterise the geological units. The only exception is the wording "Tjörnes Fracture Zone" where the word "Fracture" identifies a kilometer scale transform region. Hydrofracturing occurs when pore pressure exceeds the sum of the least principal stress and the tensile strength of the rocks (Sibson, 1981). Such conditions can already occur at near-hydrostatic pore pressures (Rojstaczer, 1988). In the upper crust, hydrofracturing is likely to occur if the pore pressure reaches 1.5 times the hydrostatic pressure or 0.5 times the lithostatic pressure (Rojstaczer, 1988). Elevated pore pressures not only lead to hydrofracturing but also play an important role in earthquake dynamics. Several international projects (i.e. San Andreas Fault Observatory at Depth or the Japanese drilling vessel Chikyu) are focusing on a better understanding of the fault dynamics at elevated pore pressures in transform and normal faults, respectively.

There is a poor understanding of the range of the pore pressures at seismogenic depths and only models or hypothesis can be formulated (Hickman et al., 1995). Elevated pore pressures at depth facilitate the dilatant slip of faults, possibly leading to high magnitude seismic events (Hickman et al., 1995; Hubbert and Rubey, 1959; Miller et al., 2004). Improvements in hypocenters location techniques have recently allowed to constrain the upward-trends of seismic swarms related to rapid upwards migration of fluids. Earthquake swarms can be driven by a pulse of elevated pore pressures rising from depth as shown by two examples which occurred in Italy and California, respectively. The first one consisted of a series of seismic events in 1997 (Miller et al., 2004). The sequence started with two 5.7 M_w and 6.0 M_w events caused by the breach of a reservoir characterised by elevated pressures of CO_2. The aftershock sequence has been explained by the migration of high-pressured fluids along the fault that was activated by the mainshock (Miller et al., 2004). A second example is provided by the 1998 seismic

sequence of the Mammoth Mountain, Long Valley, California. The seismic event, caused by a dike intrusion, was characterised by two seismic regions: the first one from 7 to 9 km depth, the second one from 2 to 3 kilometers above the dike. The shallowest seismicity was interpreted being due to the upwards migration of fluids leaving the dike along paths of enhanced permeability (Prejean et al., 2003). Both these examples support the concept of transient and cyclic permeability (e.g. Cathles and Adams (2005), Miller and Nur (2000), and Sibson (1990)). Such behaviour suggests the existence of a link between the deep (at near-lithostatic pressures) and the shallow (at near-hydrostatic pressures) parts of the crust (Rice, 1992).

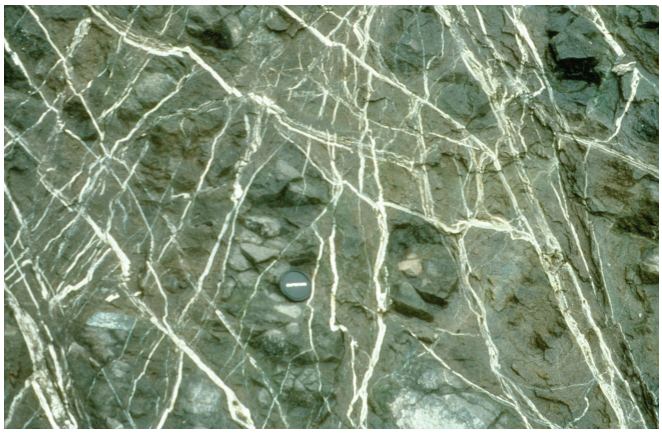

Figure 1.6: Network of fractures in the damaged zone of a transform fault - An intense fracturing characterises the damaged zone of the Húsavik Flatey Fault, the main transform fault of the Tjörnes Fracture Zone, Iceland. The formation of the veins is due to the occurrence of elevated pore pressures inside the fault. This part of the fault was located originally 1500 m depth (Gudmundsson, 2001). Photograph courtesy of Prof Agust Gudmundsson, Royal Holloway College, London.

The release of over pressure during a seismic event can cause abrupt changes in the groundwater flow patterns (Boullier et al., 2004; Bower et al., 1978; Ekstrom et al., 1992; Fleeger, 1999; Hill et al., 1993; Manga, 2001; Roeloffs, 1988, 1998; Rojstaczer et al., 1995; Rojstaczer and Wolf, 1992; Waller et al., 1965), particularly in hydrothermal and volcanic systems (c.f. Manga and Brodsky (2006)) where fluid flow is frequently convective and hence very sensitive to small variations in permeability (Geiger et al., 2005). This is well-documented by field data that display rapid, post-seismic changes such as temperature fluctuations in mid ocean ridges, discharge changes at black-smoker

vents (Johnson et al., 2000), water level changes in deep wells (Roeloffs et al., 2003), and changes in geyser periodicity (Husen et al., 2004). Systematic and statistically significant changes in geothermal fluid chemistry (Figure 1.7) have been measured at Húsavik in the Tjörnes Fracture Zone, North of Iceland, before and after a 5.8 M_w earthquake (Claesson et al., 2004, 2007). These changes have been interpreted as potential precursors to seismic activity. Claesson et al. (2004, 2007) suggested that the hydrogeochemical changes were due to the sudden mixing of two different and initially separated fluids. The first ones were fluids that have reacted with hot basalts at approximately 4 km depth, the second were dominantly meteoric waters located at 1200 m depth. The post-seismic decay of the hydrogeochemical concentrations has been related to fault sealing (Claesson et al., 2007). Testing and quantify the hypothesis of Claesson et al. (2004, 2007) by means of high resolution simulations, is one of the key aims of this study.

1.4.1 Groundwater flow during volcanic eruptions

Phreatic, phreatomagmatic, and phreatoplinian eruption occur where an external source of water is available and waters can be removed rapidly (Wohletz, 1986, 2003). Lakes, sea water, glaciers, and heavy rain, are possible source of water for these kind of events, (cf. Bertagnini and Landi (1996); Houghton et al. (2000)). This is not the case at the Askja volcano in Iceland where none of these sources was available. Nevertheless, the deposits of 28 – 29 March 1875 Askja eruption show evidences of interaction between the rising magma and water (Carey, 2008; Carey et al., 2008, 2009a,b). Another aim of this study is to explain how water could be involved in the 28 – 29 March Askja volcano eruption.

1.5 Overall scope of the study

The overall scope of this study is stated here while the specific focuses of each chapter are declared in sections 4.1.1, 5.1.1, and 6.1.1. In this study high resolution simulations have been used to investigate the fluid flow dynamics that characterise high temperature hydrothermal systems. So far, fluid flow in high temperature hydrothermal systems has usually been investigated using process models that tend to over-simplify the geology and focus on an accurate description of the physical processes instead (Ingebritsen et al.,

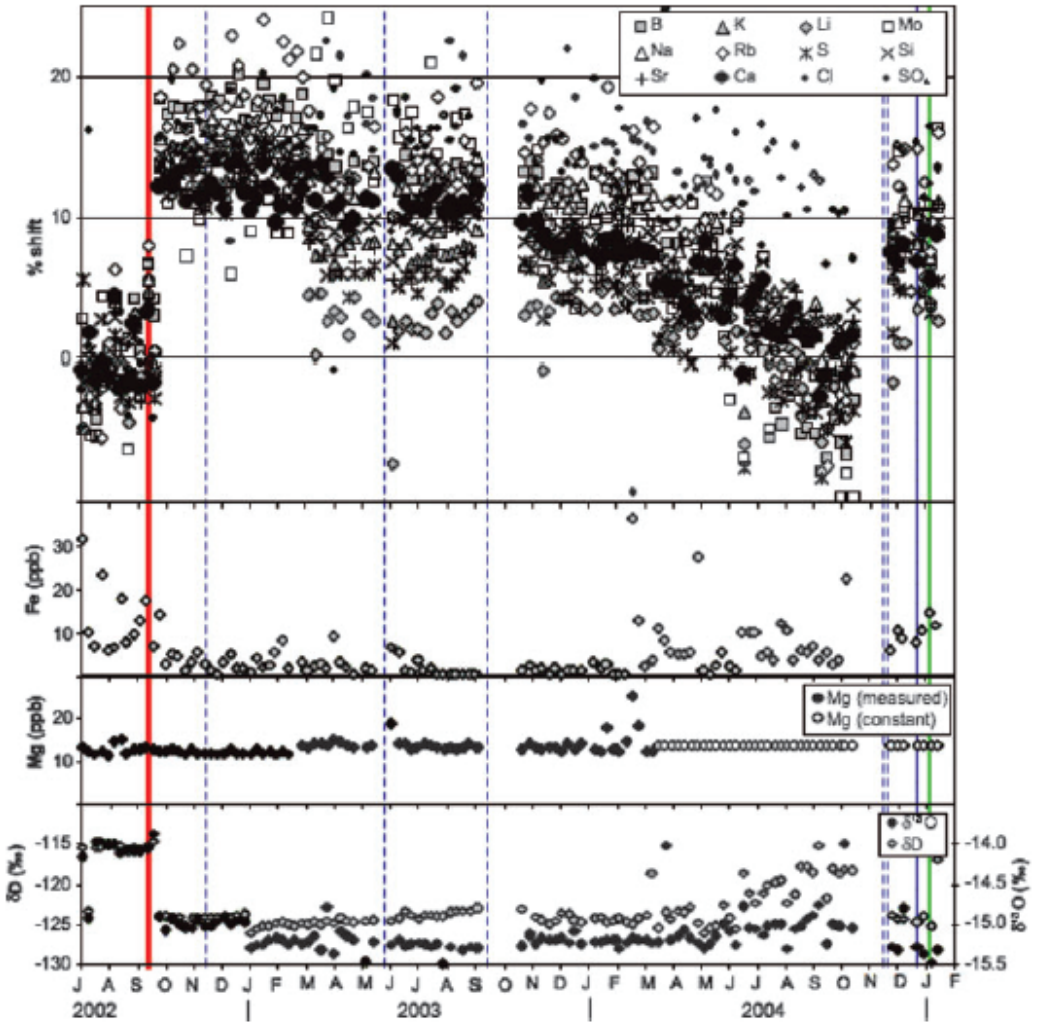

Figure 1.7: Hydrogeochemical variations over time from the borehole HU-01 in Húsavik, Iceland. - The hydrogeochemical analysis from Claesson et al. (2004, 2007) account for: first plot, B, K, Li, Mo, Na, Rb, S, Si, Sr, Ca, Cl and SO_4 concentrations; second plot, Fe concentrations; third plot, Mg concentrations; fourth plot, δD and δ^{18}O concentrations. Prior to the September 2002 5.8 M_w seismic event (red vertical line) an increase of the concentration of the geochemical elements occurred. During post-seismic times the hydrogeochemical concentrations decrease to pre-seismic values.

2010). These models can be too constrained in terms of geology to allow the system to evolve freely and reveal its emergent (hidden) behaviour. Given today computational resources and improvement in algorithms, at least 2D simulations of high temperature hydrothermal systems that account for a high level of geological realism are possible but surprisingly rare. Two prime examples have hence been selected to understand the dynamics of fluid flow in seismically and volcanically active regions: the Tjörnes Fracture Zone and the Askja volcano, Iceland. In the first case, the objective was to understand i) the fluid flow regimes that characterise the TFZ, ii) how the permeability of a hot and weak fluid-saturated crust can be altered, iii) the time-scale and magnitude of the permeability change, (iv) how results from i), ii) and iii) can be applied to explain the observed data by Claesson et al. (2004, 2007), see Figure 1.7. In the second case the objective was to describe the syn-eruptive groundwater dynamics caused by the 28 – 29 March 1875 Askja volcano eruption and explain their effect on the eruption.

1.6 Outline

This thesis is organized as follows. Chapter 2 provides an overview on the historical development of numerical simulations of high temperature hydrothermal systems, including a review of the most common assumptions and the most widely used simulators. Chapter 3 introduces the geology of Iceland focusing on hydrothermal and volcanic systems. Chapter 4[1] investigates the large scale fluid flow dynamics of the Tjörnes Fracture Zone and suggests a possible mechanism to explain the observations made by Claesson et al. (2004, 2007). Chapter 5[2] applies such a mechanism to the Tjörnes Fracture Zone to analyse fluid flow before, during, and after the fluid-induced seismic events in high temperature hydrothermal systems. Chapter 6[3] sheds light on fast fluid flow dynamics that occurred during the 28 – 29 March 1875 Askja eruption and explains how groundwater flow can affect the style of an eruption. Chapter 7 draws the general conclusion and suggests future areas of research.

[1] Published as Lupi et al., 2010. Journal of Geophysical Research. doi:10.1029/2009JB006640.
[2] In revision for the Journal of Geophysical Research.
[3] In review for the Journal of Volcanology and Geothermal Research.

2

Review of numerical simulations in hydrothermal systems

2.1 The need for numerical simulations

As discussed in the previous chapter, the study of fluid flow in hydrothermal systems is challenging for various reasons. These include, but are not limited to, the complexity of the geological structures, the longevity of hydrothermal fluid flow over tens of thousands of years, the extreme gradients of temperature and pressure, the complex thermodynamics of hydrothermal fluids, and the transient variations in permeability due to changes in the local stress field and mineral precipitation/dissolution. Field studies of fossil hydrothermal systems only yield a time-integrated picture of the flow processes. Laboratory experiments are conducted in idealised geometries and at much lower pressure-temperature conditions (Elder, 1967; Emmanuel and Berkowitz, 2006; Sondergeld and Turcotte, 1977). However, equations for groundwater motion, heat, and solute transport as well as mechanical deformation and chemical reactions can be formulated to describe the transient fluid flow processes in these environments. These will be discussed in more detail in chapters 4, 5, and 6. While these equations can only be solved analytically for simplified geometries and boundary conditions (Bergins et al., 2005; Pruess et al., 1987; Woods, 1999), numerical simulations can be used to integrate field observations, quantify the flow processes, identify the key drivers and sensitive parameters, and add insights into their hidden, i.e. emergent, behaviour. Numerical simulators disassemble the complexity of processes interacting in geological systems into

individual components (e.g. heat flow or permeability stress relations). This reduction allows for the expression of each individual component mathematically, and if the numerical solution is accurate, the simulation of their interactions can provide geologically representative and quantitative results. More generally numerical simulations are now referred to as "the third pillar of scientific discovery", complementing theory and experimentation. Although state-of-the-art numerical techniques cannot yet fully describe complex fluid flow dynamics of hydrothermal systems, particularly at MORs or near magmatic intrusions, great advancements in numerical methods have been achieved over the last decade (cf. Ingebritsen et al., 2010).

The first quantitative analyses of fluid flow in hydrothermal systems have been conducted by Wooding (1957) and Donaldson (1962), who investigated the thermal regime of the Wairakei area, New Zealand. Cathles (1977) and Norton and Knight (1977) were the first to undertake numerical simulation studies of fluid flow in high temperature hydrothermal systems. Their mathematical formulation was restrained by the computational power available at the time. The subsequent limitations consisted in neglecting all the driving forces for fluid flow with the exception of the lateral variation in fluid density, ignoring the boiling processes and considering quasi-state fluid flow over time. Despite these crude approximations, they provided important results that are still valid today. For instance, they showed the occurrence of convection cells above magmatic intrusions. A key finding was that advective heat transport in hydrothermal systems occurs at permeabilities greater than 10^{-16} m^2. Below this permeability threshold, diffusion prevails. They also demonstrated that a single intrusion takes tens of thousands of years to cool, with the controlling factors being the permeability of the host rock and size of the magmatic body. The total fluid mass needed to cool the intrusion is approximately equal to the mass of the intrusion itself. Generally, the hottest hydrothermal systems with the largest and most long-lived liquid-vapor zones evolve above magmatic intrusions if the permeability is 1.0×10^{-15} m^2. Higher and lower permeabilities lead to cooler hydrothermal systems because heat cannot be transferred fast enough from the intrusion to the rapidly circulating fluid, or the fluid circulates too slow to remove the heat from the intrusion fast enough (Driesner, 2010; Hayba and Ingebritsen, 1997). Such insight into the fundamental dynamics would not have been possible without the help of numerical simulations. The limitations of the pioneering studies conducted by Cathles (1977) and Norton and Knight (1977) were later addressed by Delaney (1982),

Dutrow and Norton (1995), Hanson (1992), and Sammel et al. (1988) who accounted for thermal pressurization, by Hanson (1995) who accounted for magmatic production of fluids, by Dutrow and Norton (1995), Gerdes et al. (1995), Norton and Knight (1977), and Parmentier (1981) who accounted for lateral and temporal variations of permeability and by Hanson (1996), and Sammel et al. (1988) who accounted for topography effects. Despite such major improvements, these studies did not completely include multi-phase – multi-components flow, a dynamic combination common to most magmatic hydrothermal systems (Ingebritsen et al., 2010). This issue was addressed in the last decade when the arrival of a new generation of simulators (Battistelli et al., 1997; Croucher and O' Sullivan, 2008; Geiger et al., 2006,a; Kissling, 2005a,b; Lewis and Lowell, 2004, 2009; Oldenburg and Pruess, 2000), coupled with more available computing power, allowed the dynamic study of the complex flow processes related to boiling and phase separation in hydrothermal systems. Studies were carried out on cooling plutons (Driesner and Geiger, 2007; Hayba and Ingebritsen, 1997), revisiting the original findings of Cathles (1977) and Norton and Knight (1977). Further applications included ignimbritic bodies (Hogeweg et al., 2005; Keating, 2005), stratovolcanoes (Fujimitsu et al., 2008; Hurwitz et al., 2003), and mid ocean ridge systems (Coumou et al., 2006, 2008, 2009). Other significant advances in the numerical simulation of hydrothermal systems include the modelling of precipitation and dissolution of mineral phases as well as fluid-rock interaction (Cline et al., 1992; Fontaine et al., 2001; Geiger et al., 2002; Giambalvo et al., 2002; Steefel and Lasaga, 1994; Xu and Pruess, 2001; Xu et al., 2004), mechanical deformation induced by fluid flow (Hurwitz et al., 2007; Hutnak et al., 2009; Todesco et al., 2004), and the possibility to include geological structures with more realism (Geiger et al., 2004, 2006,a; Paluszny et al., 2007; Zyvoloski et al., 1997).

2.2 Assumption in numerical modelling of hydrothermal systems

Any numerical simulations invoke key assumptions and simplifications to maintain a reasonable computational cost and running time. These will inevitably lead to some limitations which must be understood as they can bias the interpretation of the results. Therefore the key assumptions in numerical modelling of hydrothermal systems

are reviewed here. If not noted otherwise, all these assumptions are employed in the simulations presented in chapter 4, 5, and 6.

2.2.1 The Representative Elementary Volume - REV

Heat and mass transport in hydrothermal systems is usually modelled at large scales (from hundreds of meters to several kilometers) and not at local scales (micrometers to millimeters) where small features like pore geometries and fracture apertures can be resolved individually to analyse their impacts on fluid flow. This is simply because the computational power required to simulate large-scale flow processes with this kind of resolution is not yet available. To model hydrothermal fluid flow at the continuum, i.e. meter to kilometer scale, the domain is hence assumed to be made of solid and porous media. Rock properties like porosity, permeability, thermal conductivity, or dispersivity must be averaged to represent the properties of the fluid-saturated geological media at the continuum scale. This averaging is based on the fundamental assumption that the fluid and rock properties do not vary across a minimum distance, meaning that a rock property can be considered constant throughout a representative elementary volume (REV) (Bear, 1988), see Figure 2.1. In order to use this assumption, the REV has to be large compared to the fine scale heterogeneities (e.g, grain size in a granular porous media) but small in comparison to the size of the model. Theoretically the REV can be as large as the model for a homogeneous medium but in reality all geologic media have some large-scale heterogeneity (e.g. faults) where the rock properties begin to diverge. Ideally, these spatial changes in rock properties are captured in a numerical simulation but even this is often challenging because of the small-scale variations in geology will still require an extremely detailed numerical grid and too much computational resources. Hence further averaging techniques, so-called upscaling, are needed (Renard and De Marsily, 1997). An illustration of such an issue are fractured porous rocks with poorly connected fractures. These usually do not have a REV scale, respectively the REV scale is at the scale of the entire domain of interest (Berkowitz, 2002). This renders simulations of hydrothermal fluid flow in fractured rocks particularly challenging.

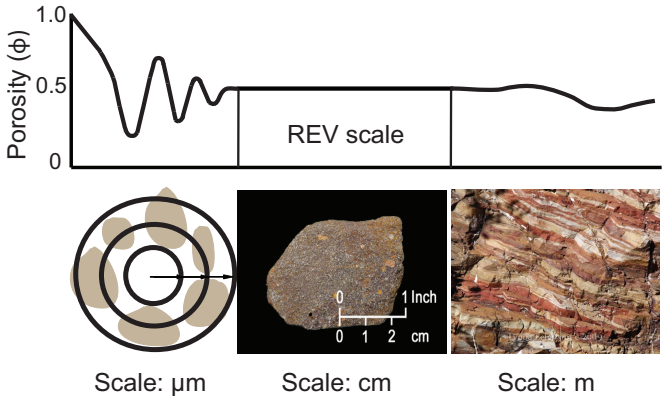

Figure 2.1: Representative Elementary Volume, REV - Some rock parameter can only be defined uniquely at a certain scale. For instance the porosity ϕ at the μ scale is either 1 (when grains are encountered) or 0 (when void spaces are encountered). By enlarging the averaging area, ϕ will increase and decrease as more grains and voids are encountered. Once the averaging area has become sufficiently homogeneous, ϕ can be considered essentially constant (cm scale). The area (or volume in 3D) range over which a property remains constant has been termed representative elementary volume (REV) (Bear, 1972). If the averaging area becomes too large, the large-scale heterogeneities of the porous media cause a deviation in the value from the REV scale.

2.2.2 Darcian flow

Darcy's law (equation 2.1) describes the rate at which a fluid flows through a porous media (Darcy, 1856)

$$\vec{q} = -\mathbf{K}\nabla h, \tag{2.1}$$

where $\vec{q}$ is the volume flux or Darcy velocity (a vector in 2D and 3D), $\mathbf{K}$ the hydraulic conductivity (a tensor in 2D and 3D), and h the hydraulic head. The one-dimensional form of the Darcy's law for a vertical flow can be expressed as

$$q_z = -K_z \frac{dh}{dz}, \tag{2.2}$$

The hydraulic conductivity is function of the fluid density ρ_f and fluid viscosity μ_f, respectively. If these parameters vary significantly, fluid flow can not be expressed by equation 2.2 (Ingebritsen et al., 2006). In this case $\mathbf{K}$ should be expanded as

$$\mathbf{K} = \frac{\mathbf{k}\rho_f g}{\mu_f}. \tag{2.3}$$

where g is the vector of gravitational acceleration. In equation 2.3, the intrinsic permeability $\mathbf{k}$ is the only property of the porous media. M. King Hubbert (Hubbert, 1940) decomposed the hydraulic head in Darcy's law into elevation head and pressure head, i.e. $\mathrm{h} = \mathrm{z} + \mathrm{P}_f/(\rho_f\ g)$, which provides a more convenient form of Darcy's law for variable density flow, as occurring in hydrothermal systems (Ingebritsen et al., 2006)

$$\vec{q} = -\frac{\mathbf{k}}{\mu_f}\left(\nabla P_f - \rho_f \mathbf{g}\right), \tag{2.4}$$

where P_f is the pore pressure and $\mathbf{g}$ is the vector of gravitational acceleration.

For two-phase fluid flow, e.g. during liquid and vapor flow, relative permeability values k_r must be introduced for each of the phases in Darcy's law (Ingebritsen et al., 2006). This is because the presence of one phase hinders the flow of the other phase. Relative permeabilities are functions of the volumetric saturation and vary between 0 and 1. Two basic relative permeability models are usually invoked in hydrothermal systems: the relative permeability function of Corey (1957) assumes $k_{rs} + k_{rw} < 1$ while Sorey et al. (1980) assume $k_{rs} + k_{rw} \sim 1$. k_{rs} and k_{rw} are the relative permeabilities of steam and water, respectively. Thus, the one-dimensional variable-density steam and liquid water flows can be described as follows

$$q_s = -\frac{k_{rs}k}{\mu_s}\left(\frac{\partial P_f}{\partial z} + \rho_s g\right), \tag{2.5}$$

and

$$q_w = -\frac{k_{rw}k}{\mu_w}\left(\frac{\partial P_f}{\partial z} + \rho_w g\right), \tag{2.6}$$

respectively. Note that capillary pressures are neglected here (see section 2.2.5). It is important to note that Darcy's law is, fundamentally, still an empirical law, especially in the case of two-phase flows. Another key assumption of Darcy's law is that flow is laminar. Flow rates that violate Darcian flow conditions are rare in nature but can occur in specific systems, i.e. geyser conduits, at MORs, in reservoir characterised by cavernous porosity, and during phreatic eruptions. This limit is given by the Reynolds number, $Re = (\rho_f q L)/\mu_f$ (Vennard, 1961). L is a characteristic length that can be related to the median grain size or to $\sqrt[2]{k}$ (Ward, 1964). Above certain Reynolds numbers, fluid flow becomes turbulent and the flow rate estimated from the above Darcy equations is over-predicted for a given permeability because the energy loss due to turbulence is not accounted for. Bear (1979) shows that for single phase flow in a granular porous media,

laminar flow becomes turbulent above Reynolds numbers of $\sim$ 1 to 10. In lithologies characterised by an intense fracturing, the transition from laminar to turbulent flow can occur for $Re \sim 1000$ (Ingebritsen et al., 2006).

2.2.3 Thermal equilibrium at the REV scale

Thermal equilibrium between fluid and rock is often assumed in numerical modelling of hydrothermal systems. This implies that although fluid(s) and rock have different specific enthalpies, the fluid and solid phases are assumed to have the same temperature at the REV scale (Ingebritsen et al., 2006). This is based on the fact that rocks generally have a high thermal conductivity compared to fluids and that sub-surface fluid flow occurs a slow rates (Ingebritsen et al., 2010). This assumption is usually appropriate at large scale but cannot be applied at the pore scale (Wu and Hwang, 1998), for non-equilibrium systems (Emmanuel and Berkowitz, 2006), or fractured porous rocks with poorly connected fractures (Geiger and Emmanuel, 2010).

2.2.4 Thermal conduction and radiative heat transfer

The thermal conductivity of fluids and rocks is usually expressed as a bulk conductivity where the individual conductivities of the rock and fluid phases are weighted by porosity (Bear, 1972; Raffensperger, 1997). While this is generally a reasonable assumption due to the low porosity of hydrothermal systems, Sass et al. (1992) and Vosteen and Schellschmidt (2003) also showed that the thermal conductivity of rocks decreases non-linearly with depth. Above 600 °C, radiative heat transfer component becomes also important and can be approximated by a radiative-thermal-conductivity component that increases with increasing temperature (Clauser, 1988). In numerical modelling of hydrothermal systems, temperature-dependence of the thermal conductivity and radiative heat transport are usually neglected.

2.2.5 Capillary pressure

As discussed previously, two basic relative permeability models are usually invoked to model the interference of vapour and liquid during two-phase flow in hydrothermal systems. Capillary pressure, the difference in pressures between fluid phases at their interface, is commonly neglected in hydrothermal systems simulations. This can be

justified by the fact that the surface tension of water vanishes at the critical point where the properties of steam and liquid merge (Ingebritsen et al., 2010) and, more practically, by the lack of empirical data on steam-liquid capillary behavior (Li and Horne, 2007).

2.2.6 Boussinesq approximation

Early studies of fluid flow in hydrothermal systems used the "Boussinesq approximation". The Boussinesq approximation assumes that the transient variations in fluid density are negligible over time, conserving fluid volume rather than fluid mass. It is mathematically expressed by

$$\nabla \cdot \vec{q} = 0. \tag{2.7}$$

The Boussinesq approximation can lead to erroneous results in transient, variable-density flow cases because it neglects the effects of fluid expansion and pressurisation due to in situ heating, it does not consider elevated compressibilities of hydrothermal fluids and cannot capture the hydrodynamics of two-phase flow and phase separation (Evans and Raffensperger, 1992; Furlong et al., 1991; Hanson, 1992; Jupp and Schultz, 2000). Yet, it is still used today in numerical simulations of hydrothermal fluid flow (Fontaine et al., 2007) but not in the work presented here.

2.2.7 Fluid properties and reactive transport simplifications

Hydrothermal systems are characterised by the presence of salts (primarily NaCl) and non-condensable gases (mainly CO_2). As mentioned previously, the thermodynamic complexity of H_2O-NaCl-(CO_2) mixtures affects fluid phases equilibria and hence an equation of state (EOS) describing the fluid properties and phase states as function of pressure, temperature, and composition for these three components is needed. Due to the lack of data and thermodynamic models, however, adequate EOS that cover a wide range of temperatures and pressures are still absent (Ingebritsen et al., 2010). An EOS for H_2O-NaCl(-CO_2) mixtures exists only for sub-critical temperatures (below 350 °C) and over a narrow range of compositions (Battistelli et al., 1997). Reliable EOS have been developed for binary H_2O-NaCl systems which are applicable over the

wide pressure-temperature-salinity conditions typically encountered in high temperature hydrothermal systems, i.e. up to 1000 °C, 500 MPa, and 100 % X_{NaCl} (Driesner and Heinrich, 2007; Driesner, 2007). Coumou et al. (2008, 2009), Geiger et al. (2005), and Driesner and Geiger (2007) have employed these EOS already to analyse fluid flow including phase separation in sub-aerial and sub-sea high temperature hydrothermal systems. This EOS is also used in this work (chapters 4 and 5)

Hydrothermal fluid flow is also strongly affected by reactive processes, which alter the rock and fluid properties (Ingebritsen et al., 2006). Most simulators neglect the reactive transport because the coupling of these processes with the solution of heat, mass, and momentum conservation equations is challenging. In addition, more detailed experiments and accurate thermodynamic descriptions are needed to model fluid-rock interactions at temperature and pressure conditions that are typically encountered in high temperature hydrothermal systems.

2.2.8 Permeability approximation

Permeability can vary over several orders of magnitude for the most common geological media (Ingebritsen et al., 2006), hence it strongly dictates fluid flow behaviour (Figure 2.2). For instance, in volcanic systems, the permeability of near-surface basalts and

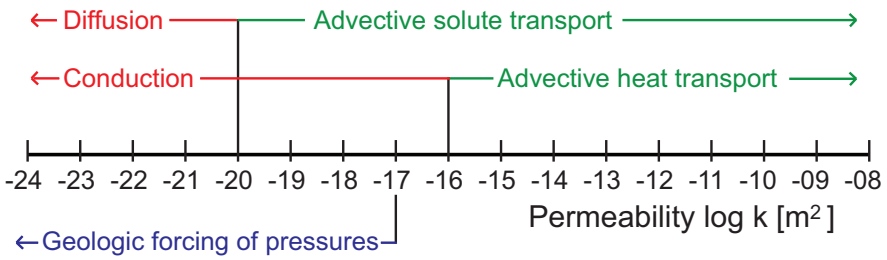

Figure 2.2: Range of permeabilities found in the most common geologic media. - For permeabilities lower than 1.0×10^{-20} m^2 solute transport occurs by diffusion. Conduction of heat dominates at permeabilities lower than 1.0×10^{-16} m^2. Above these thresholds advection of solutes and heat occur. Geological forcing, e.g. due to mineral dewatering or thermal expansion, can occur if permeabilities are lower than 1.0×10^{-17} m^2. Modified after Ingebritsen et al. (2006).

compositionally identical rocks at 1 to 2 km depth has shown variations of seven orders of magnitude (from 10^{-9} m^2 to 10^{-16} m^2) at Kilauea volcano (Ingebritsen and Scholl, 1993). Permeability is a scale-dependent property (Ingebritsen et al., 2006) and its

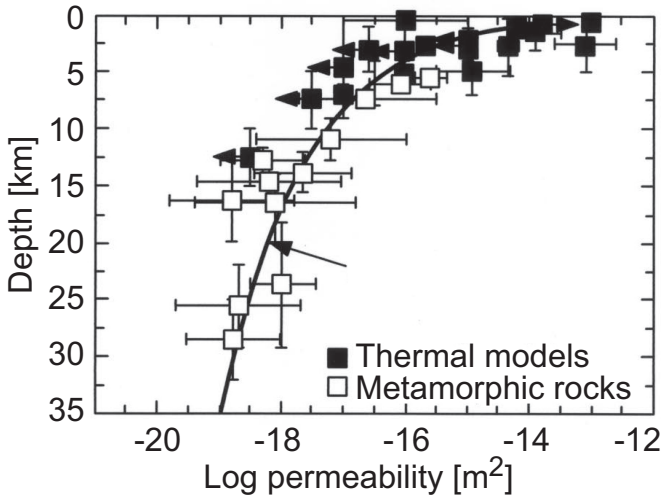

Figure 2.3: Idealised decay of permeability in the continental crust - Depth-dependence of permeability in the continental crust according to the relation $\log(k) = \log(k_0) - 3.2 \cdot z$, where $\log(k_0)$ is the permeability at 1 km depth ($1{\times}10^{-14}$ m^2) and z denotes the depth in kilometer. Solid squares indicate geothermal systems and open squares indicate metamorphic systems. Modified after Manning and Ingebritsen (1999).

value is usually determined (from small to regional scale) by laboratory experiments, *in situ* well tests, and numerical models. The scale-dependent character of the permeability is more prominent in fractured and crystalline rocks. Brace (1980) and Brace (1984) highlight that permeability in fractured crystalline rocks show approximately a 10^3-fold variation between core-scale and *in situ*-scale. Several studies attempted to constrain the systematic variations of permeability in the crust (Björbsson and Bodvarsson, 1990; Brace, 1980, 1984; Clauser, 1992; Fisher, 1998; Manning and Ingebritsen, 1999; Saar and Manga, 2004; Talwani et al., 2007). They all concluded that permeability is depth-dependent because of the increasing confining pressure, effective stress, temperature, and degree of metamorphism with depth. The most widely used relation was established by Manning and Ingebritsen (1999) who used thermal data to calibrate a depth-dependent permeability curve for the continental crust (Figure 2.3). Although permeability is commonly anisotropic due to layering (Figure 2.4), the above crustal-scale permeability-depth curves assume an isotropic permeability throughout. It should be noted that the permeability approximation by Manning and Ingebritsen (1999) does not hold if elevated fluid pressures prevail and recent work by the authors (Ingebritsen and Manning, 2010) and by Rojstaczer et al. (2008) show how crustal permeability

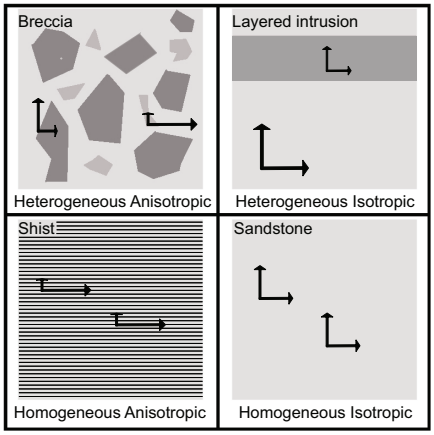

Figure 2.4: Heterogeneity and anisotropy in permeability - In a heterogeneous-anisotropic medium permeability varies with both space and orientation, for example in breccias, while in heterogeneous-isotropic medium it varies with position but not with direction, for example in layered intrusions. In a homogeneous-anisotropic medium permeability does not vary with position but varies with direction, for example in shists. In a homogeneous-isotropic medium permeability does not vary with position nor direction, which is the case in sandstones.

evolves transiently. As discussed in Chapter 1, this transient evolution of permeability due to deformation, hydraulic fracturing, mineral precipitation and dissolution, is paramount to hydrothermal systems and must be modeled adequately.

2.3 Simulators

The oil crisis of the 1970ties triggered concerted efforts to develop numerical simulators for the exploration of geothermal resources (Ramey, 1980). These efforts lead to three different simulators that are now well established and widely applied to hydrothermal systems. These are FEHM (Keating et al., 2002; Zyvoloski et al., 1988, 1997), HYDROTHERM (Hayba and Ingebritsen, 1994; Kipp et al., 2008), and the TOUGH family of codes, including the predecessors SHAFT and MULKOM (Pruess, 1988, 1991, 2004; Pruess et al., 1999). All simulators are capable of solving the governing equations for heat and mass transport under two-phase, i.e. vapour-liquid, conditions and account for boiling and condensation processes. However, differences in terms of numerical methods (e.g., finite element vs. finite differences), additional capabilities (e.g.,

reactive transport and deformation), and applicability (e.g., graphical user interface) exist. These are reviewed briefly below and summarised in Table 2.1.

2.3.1 FEHM

FEHM (Zyvoloski et al., 1997) has been developed at the Los Alamos National Laboratory to investigate coupled subsurfaces processes in complex geological environments. FEHM uses the Control Volume Finite Element (CVFE) method developed on the basis of finite element methods. A specialised grid generation software, LaGriT, exists for FEHM, which produces unstructured finite element grids in 2D and 3D based on tetrahedra, hexahedra, quadrilaterals, and triangles. This type of unstructured finite element meshing allows for a relatively flexible representation of geological structures. FEHM solves for groundwater fluid flow in confined and unconfined aquifers including deformation. It also handles non-isothermal processes (Kwicklis et al., 2006), water-CO_2 (Pawar, 2007), methane hydrate dissociation (Pawar et al., 2004), and reactive transport (Robinson et al., 2000). The range of validity of FEHM is up to temperatures of 1500 °C, and up to pressures of 110 MPa. FEHM is free and available online at http://fehm.lanl.gov/.

2.3.2 HYDROTHERM

HYDROTHERM (Hayba and Ingebritsen, 1994; Kipp et al., 2008) simulates 2D and 3D single- and two-phase heat and mass flow of pure water in hydrothermal and groundwater systems. Its range of validity is up to temperatures of 1200°C and fluid pressures up to 1000 MPa. HYDROTHERM allows for the simulation of confined and unconfined groundwater systems. Permeabilities can also vary as a function of temperature to model the cooling and crystallisation of magmatic intrusions. HYDROTHERM uses a structured grid (finite differences) to discretize the governing equations. This greatly restricts the geometric flexibility in terms of representing geological structures (Geiger et al., 2006,a). A great advantage of HYDROTHERM is its graphical user interface, which allows to setup and configure simulations in an intuitive way. HYDROTHERM is available for free at http://wwwbrr.cr.usgs.gov/projects/GWSolute/hydrotherm/.

2.3.3 TOUGH2

The TOUGH family of codes covers a wide range of fluid flow problems in different geological environments. TOUGH2 (Pruess et al., 1999) is the most commonly used simulator. It simulates multi-phase and multi-component fluid flow in 2D and 3D and comprises a variety of EOS (e.g., pure water, water-tracer, water-CO_2, water-air). It has been applied to a wide range of problems including nuclear waste isolation, geothermal reservoir engineering, and CO_2 storage. Specialised versions of TOUGH are TOUGHREACT (includes chemical reactions), NaCl-TOUGH2 (includes an EOS for H_2O-NaCl fluid flow), TOUGH2-BIOT and TOUGH-FLAC (both include deformation). All TOUGH codes use the integral finite difference (Edwards and Trump, 1972; Narasimhan and Witherspoon, 1976), which is equivalent to conventional upwind-weighted finite difference methods. It hence has limitations in representing complex geological structures or requires non-standard grid generation procedures (Geiger et al., 2006,a). The range of validity of TOUGH2 is up to temperatures of 350 °C and up to pressures of 100 MPa. TOUGH2 is a proprietary software and can be found at http://esd.lbl.gov/TOUGH2/.

2.4 Complex Systems Modelling Platform CSMP++

The Complex Systems Modelling Platform CSMP++ has been created by S. K. Matthäi in 1995 and improved with the help of several co-developers from ETH Zurich, Imperial College London, Montan University of Leoben, and Heriot-Watt University. It is an adaptable and flexible simulator that has been applied to a wide range of problems including, but not limited to, the formation of ore deposits (Driesner and Geiger, 2007; Geiger et al., 2002), heat transport at mid ocean ridges (Coumou et al., 2006, 2008, 2009), the recovery of oil and gas from fractured hydrocarbon reservoirs (Belayneh et al., 2006; Geiger et al., 2009; Matthai et al., 2007), or heat and mass transport in fractured reservoirs (Geiger and Emmanuel, 2010; Matthai and Belayneh, 2004). This section briefly reviews the key features and advantages of CSMP++ (Matthai et al., 2004, 2005, 2007) and describes the most important steps of the model building and mesh generation process. CSMP++ is an application programmer interface for PC, Macintosh, or Linux hardware environments, that is the CSMP++ user needs to write a script for a specific application. This provides maximum flexibility to simulate a wide

range of geological processes and include additional constitutive relations, for example stress-dependent variations in permeability. In this work, the prototype of a 2D and 3D hydrothermal fluid flow simulator that was written by S. Geiger at Heriot-Watt University based on CSMP++ was used for all numerical simulations. CSMP++ is written in C++ and uses finite element and finite volume methods to discretize complex geological structures in 2D and 3D (Figure 2.5). It uses algebraic multigrid methods to invert the resulting system of algebraic equations (Stüben, 2001) and is available in parallel (Coumou et al., 2008c). Both have the advantage that high-resolution meshes, which resolve complex geological structures at great detail, can be run at reasonable computational cost. CSMP++ is available for free for academic users and can be found at: http://csmp.ese.imperial.ac.uk/wiki/Home.

2.4.1 Simulating hydrothermal systems with CSMP++

The process of dividing any given geometry (e.g. a geological interpretation of a seismic profile) into discrete counterparts (e.g., finite elements) is referred to as discretization (Figure 2.5). The discretization of a geometry is challenging procedure despite the advancement of computer design tools. Erroneous geological interpretations and inaccurate model constructions can cause misleading approximations and simplifications that bias the results and/or their interpretations.

Porous media consist of large and fine scale complex heterogeneities. High aspect ratio structures, that is for 2D structures the ratio of the longest and shortest dimension of the geological unit like faults and thin geological layers, are very challenging to reconstruct geometrically. These units are key features of the geological heterogeneity of the crust and should be retained during the discretization process and in the numerical models. High-aspect ratio structures are notoriously difficult to represent with structured (e.g., finite difference) grids (Figure 2.6). In CSMP++, unstructured finite element meshes are created with the software ANSYS ICEM^{TM}based on CAD models created with Rhinoceros 4.0^{TM}(Paluszny et al., 2007). They allow to represent complicated structures like faults, folded layers and unconformities accurately. Another key feature of CSMP++ is the finite volume grid that is constructed on the finite element mesh (Figure 2.7). This provides great numerical stability for advection dominated flows, while retaining the geometric flexibility of finite element methods (Geiger et al., 2004; Matthai et al., 2007; Paluszny et al., 2007)

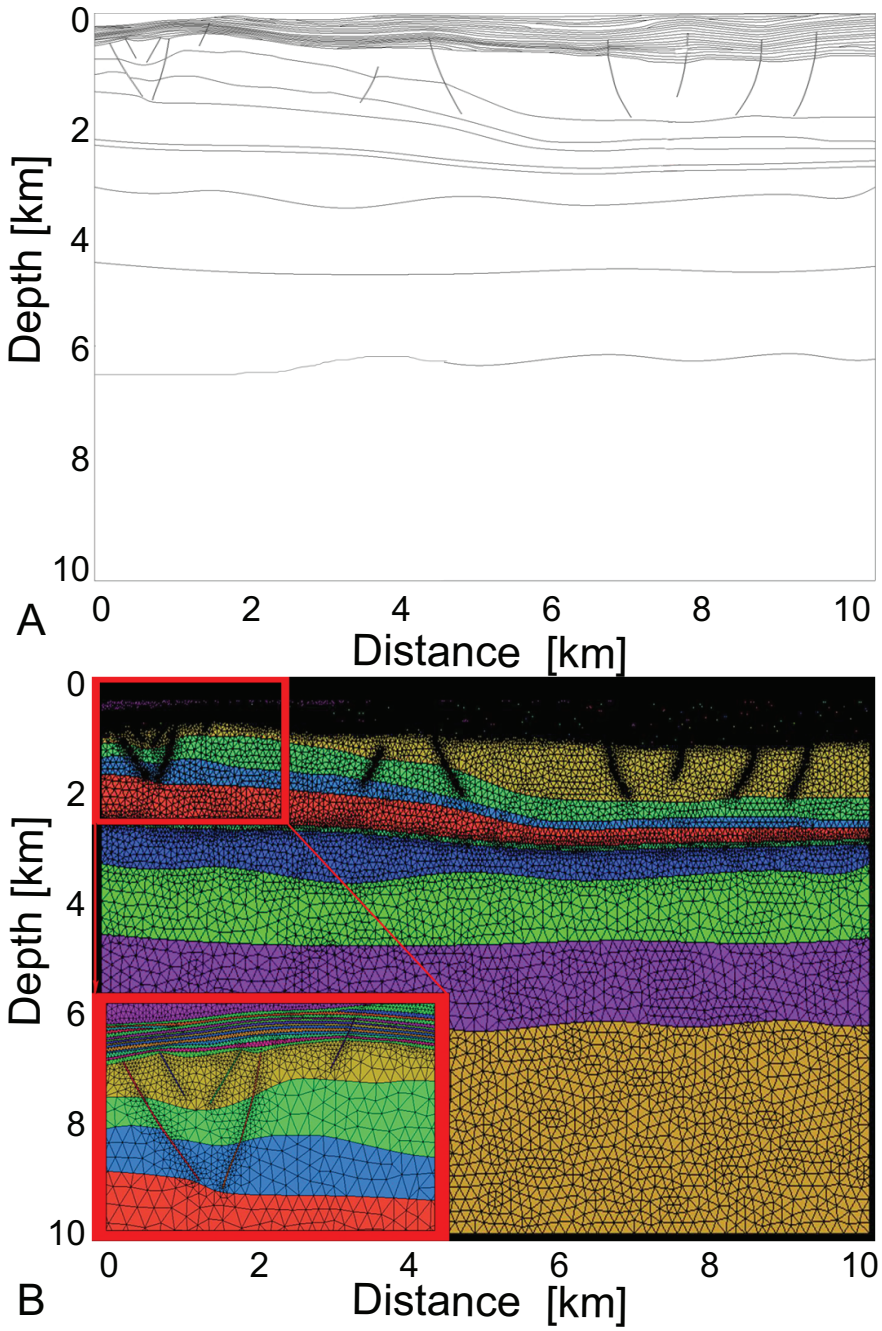

Figure 2.5: Geometry and mesh of a 10 km deep illustrative cross section for a CSMP++ simulation - The model geometry constructed with Rhinoceros 4.0^{TM}has been meshed into adaptively refined finite elements using ANSYS ICEM^{TM}. The red inset shows how the detail of the sedimentary layers in the cross section above is preserved.

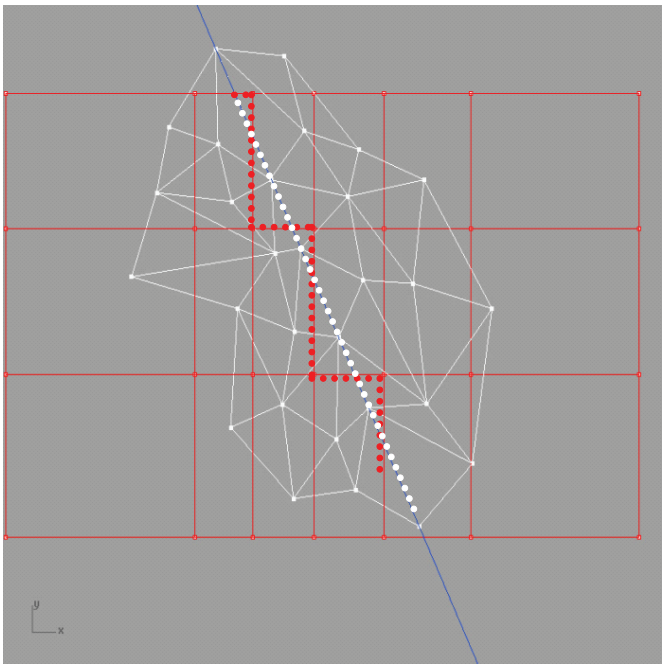

Figure 2.6: Finite difference and fine element meshes - The blue line shows a schematic representation of a fault that is approximated by finite difference (red) and finite elements (white).

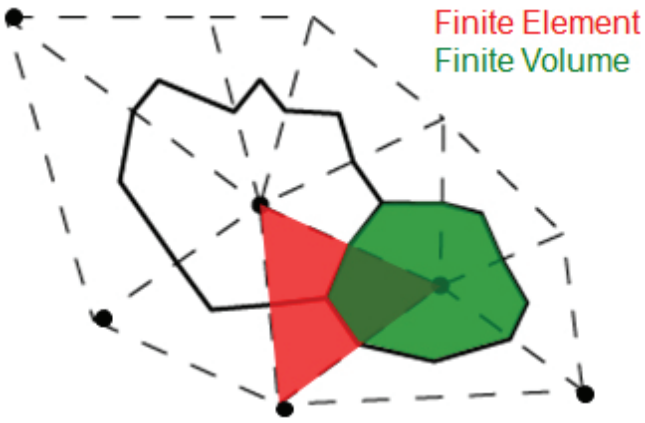

Figure 2.7: Finite element and finite volume mesh - Finite volumes (in red) are centered around each corner node of a finite element (green). Modified after Geiger et al. (2004)

One of key features of CSMP++ is the concept of "groups". A group is a user-defined region of finite elements. The inset of Figure 2.5 shows different geological units (represented with different colours), each of which corresponds to a single group where physical processes and rock properties can vary spatially and temporally. For instance, faults are joined into one single group and each sub-horizontal sedimentary layer constitutes an individual group. Moreover, groups allow to restrict the computation of physical processes to selected areas of the model domain. For instance, it is possible to allow for the calculation of permeability as a function of effective fault-normal stress in a certain region/group only (i.e., in the faults).

Simulator	T_{max}	P_{max}	DM	RT	D	CO_2	X_{NaCl}
	$°C$	MPa	/	/	/	/	/
FEHM	1500	110	Finite Elements	√	√	√	X
TOUGH2	350	100	Integrated Finite Difference	√	√	√	√
HYDROTHERM	1200	1000	Finite Difference	X	X	X	X
CSMP++	1000	500	Finite Element Finite Volume	√	√	X	√

Table 2.1: Capabilities of the simulators described in section 2.3 modified after Ingebritsen et al. (2010). The abbreviations DM stands for "discretization method" , RT for "reactive transport", D for "deformation", and the √ symbol indicates the capability of the simulator to model the process reported at the top of each column. Note that TOUGH2 includes the entire family of TOUGH codes, i.e. TOUGHREACT, TOUGH2-BIOT, TOUGH-FLAC, and NaCl-TOUGH.

3

Hydrothermal and volcanic activity in Iceland

3.1 Background

Iceland has been created by the interaction of the mid Atlantic ridge and the hot spot mantle plume and it is the region where the largest portion of the mid ocean ridge crops out on land. Iceland is often referred to as "a natural laboratory" because tectonic, magmatic, hydrothermal, and seismic events occur frequently and are strongly associated and coupled. The easy accessibility of Iceland and its active geology improved the knowledge on long standing geological questions. For instance, paleomagnetic surveys and mapping of magnetic anomalies shed light on sea floor spreading (Breivik and Faleide, 2006; McDougall et al., 1976, 1977). Structural, geochemical and petrological studies highlighted the fundamental interactions between a mid ocean ridge and a hot spot mantle plume (Breddam, 2002; Elliott et al., 1991; Herzberg and Gazel, 2009; Kitagawa et al., 2008; Oskarsson et al., 1982; Saemundsson, 1974; Sigvaldason, 1974; Sonnette et al., 2010; Verzhbitsky et al., 2009). Iceland's geographical location, at the boundary between air and water masses of tropical and Arctic origin, not only allowed for important advancements in geological studies but it constitutes an important laboratory for the investigation of atmospheric and oceanic processes (Bianchi and McCave, 1999; Broecker et al., 1985; Koe et al., 1993; Rahmstorf, 1995; Serreze et al., 1997) as well as glacier dynamics (Ehlers and Gibbard, 2004; Einarsson and Albertsson, 1988; Geirsdottir, 2004). For instance, the geology of the Tjörnes region, in the North of

Iceland, holds evidences of the shift from Miocene greenhouse conditions to Quaternary icehouse conditions and records of more than 20 glaciations that occurred over the last 2.5 Ma (Ehlers and Gibbard, 2004; Einarsson and Albertsson, 1988; Geirsdottir, 2004). For all these reasons, Iceland offers a perfect environment to improve our fundamen-

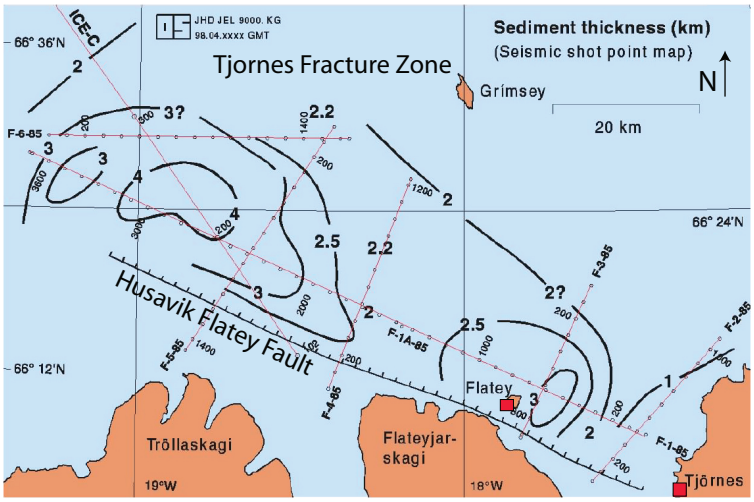

Figure 3.1: Thickness of sedimentary basins and directions of seismic profiles in the Tjörnes Fracture Zone - The seismic profile that is the basis of the study in chapters 4 and 5 (F-1-85) runs parallel the Húsavik Flatey Fault and cuts the sedimentary basins of the Tjörnes Fracture Zone originated by a normal regime. The red squares indicate the location of two boreholes, one on the Flatey island (600 m deep) and one on the Tjörnes peninsula, called Húsavik-Hola nr. 1 (1500 m deep). The latter is the borehole monitored by Claesson et al. (2004, 2007) to reveal the hydrogeochemical variations. This borehole has been used to correlate, where possible, the sedimentary layers. The log of this borehole is shown in Figure 3.2. The Flatey borehole, approximately 15 km distant, correlates with the upper sedimentary lithologies of the Húsavik-Hola nr. 1. Image modified after Richter (2006).

tal understanding of fluid flow in active hydrothermal and volcanic systems by using high-resolution simulation. In this regard, the Icelandic regions of the Tjörnes Fracture Zone and Askja volcano are two prime examples that have been selected to achieve this objective. The Tjörnes Fracture Zone (TFZ) (Figure 3.1), the first subject of study, is a heavily faulted and fractured transform area in northern Iceland where clear evidence for a link between fluid flow and seismicity exists (Claesson et al., 2004, 2007). The second subject of study is the Askja volcano, Iceland's only active volcano not covered by an ice-cap, where the only direct observation of a phreatoplinian eruption was done

in 1875 (Anonymous, 1875).

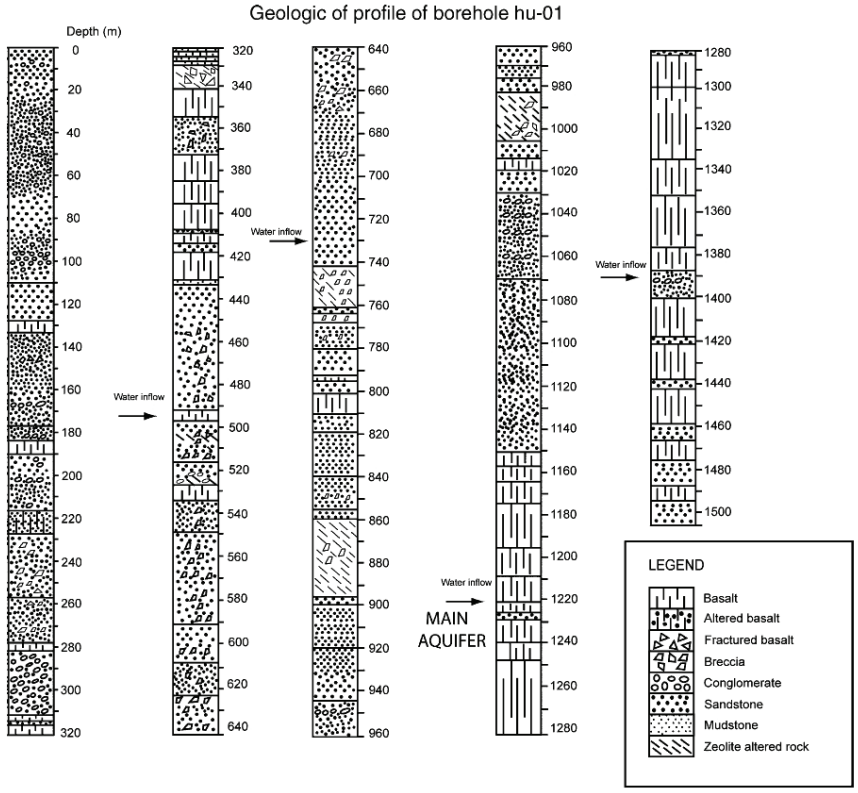

Figure 3.2: Vertical profile of the borehole Húsavik-Hola nr. 1 - The main aquifer occurs at 1220 m depth. Modified after Tomasson et al. (1969)

3.2 Key features of the Icelandic crust

Iceland is located above one of the largest hot spot plumes of the Earth (Wilson, 1963) and is cut by the mid Atlantic ridge (Figure 3.4). The Icelandic hot spot, approximately 56 – 61 Ma old, varied its location over time (Larsen et al., 1992; Saunders et al., 1997). Its trace is recognisable along the Iceland-Faroe ridge where the base of such a plume has been identified around 450 km depth (Bjarnason et al., 1996; Foulger et al., 2000). Recent surveys established that the average crustal thickness in SW-, N-, and NE-Iceland, is approximately 20 km (Allen, 2001; Bjarnason et al., 1993; Brandisdottir et al., 1997; Darbyshire et al., 1998; Menke et al., 1996, 1998; Staples et al., 1997). In older areas, such as the Eastern Fjords, the Icelandic crust is significantly thicker,

Figure 3.3: Öskjuvatn caldera formed as consequence of the 28 – 29 March 1875 Askja volcano eruption - Along the rim of the Öskjuvatn caldera crop out fractured basaltic lava flows. The caldera is bounded by steep hyaloclastic mountains.

reaching a maximum of approximately 35 km (Staples et al., 1997). Despite its thickness (approximately four times thicker than a "normal" oceanic crust, Allen (2001); Bjarnason et al. (1993); Brandisdottir et al. (1997); Darbyshire et al. (1998); Menke et al. (1996, 1998); Staples et al. (1997)), the Icelandic crust is characterised by a typical oceanic sequence (i.e. peridotite, gabbro, sheeted dikes, pillow basalts, and sediments, from deep to shallow depths, respectively). The Icelandic crust often contains 1 to 2 km thick magma chambers at approximately 3 km depth (Brandisdottir et al., 1997).

3.3 Heat flow in Iceland

The total thermal energy released from the Icelandic lithosphere is thought to be in the range of 30 GW, which is five times greater than the world average heat flux per unit area. 50% of this amount is provided by heat conduction, 20% from rising magmas, and the remaining 30% from fluid flow in geothermal areas (Arnórsson et al., 2008). The thermal energy that is thought to be stored within the first 10 km of the Icelandic crust is approximately 1.2 EJ, approximately 9% of which are contained in the uppermost

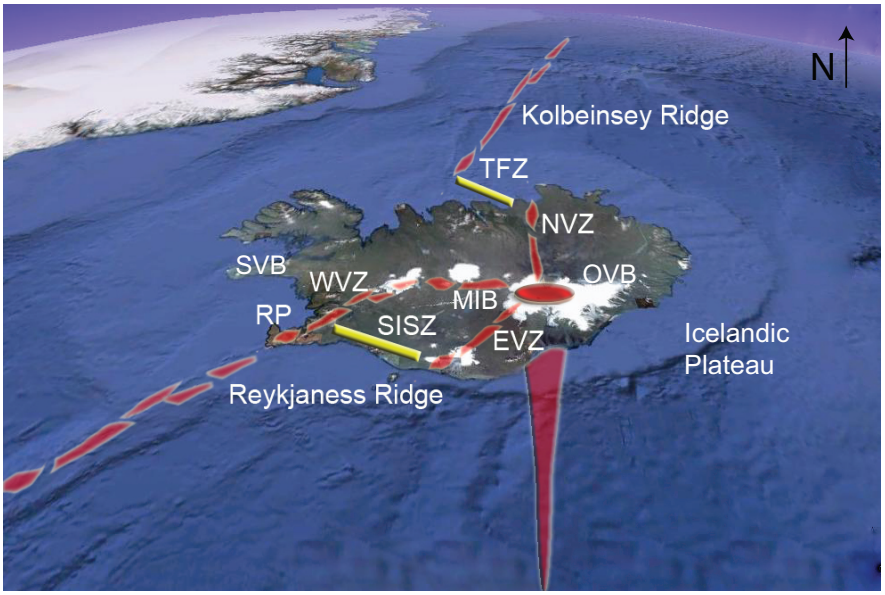

Figure 3.4: Aerial view of Iceland. - The Icelandic plateau rises more than 3000 m above the surrounding seafloor and is the only currently active part of the North Atlantic Igneous Province (Gudmundsson, 2000; Saunders et al., 1997). The mid Atlantic ridge and the Icelandic hot spot are shown in red. The mid Atlantic ridge divides Iceland into three main regions: one between the Mid-Iceland Belt and the South Iceland Seismic Zone, one between the eastern coast and the Northern and Eastern Volcanic Zones, and one bounded by the western Fjords, the Western Volcanic Zone, the Mid-Iceland Belt, and the Northern Volcanic Zone. The Icelandic hot spot is located underneath the Vatnajökull glacier which is the eastern white region on the map. The neovolcanic belts are areas were Holocenic volcanism occurs. They are abbreviated as follows: SVB, Snaefellsnes Volcanic Belt; RP, Reykjaness Peninsula; WVZ, Western Volcanic Zone; MIB, Mid-Iceland Belt; EVZ Eastern Volcanic Zone; ÖVB, Oraefi Volcanic Belt; NVZ, Northern Volcanic Zone. Thirty volcanic systems occur in the neovolcanic zones: three in the Reykjaness Peninsula, six in the Western Volcanic Zone, two in the Mid-Iceland belt, five in the North volcanic zone, eight in the Eastern Volcanic Zone, and nine occurring in intraplate volcanic belts (Thordarson, 2008). The transform regions that offset segments of the mid Atlantic ridge are indicated with yellow bars and are the South Iceland Seismic Zone (SISZ) and the Tjörnes Fracture Zone (TFZ).

3 km. Iceland is characterised by low- and high-temperature hydrothermal systems. Low-temperature hydrothermal systems occur in Quaternary and Miocene geological formations. They are characteristic of highly faulted areas where sub-recent faulting provides fluid flow paths that connect shallow and deep crustal levels. The heat source is provided by hot rocks at depth and the maximum temperature reached at 1 km depth is approximately 150 °C (Fridleifsson, 1979). Although density-driven fluid flow can occur in low-temperature hydrothermal systems, topographic-driven flow is also common. High-temperature hydrothermal systems are located in volcanic belts and close to rifting areas. They are characterised by density driven fluid flow (Arnórsson and Andrésdóttir, 1995). In high-temperature hydrothermal areas, temperatures above 200 °C can be reached at approximately 1 km depth (Fridleifsson, 1979). The geothermal fluids of the Icelandic hydrothermal systems consist of sea and meteoric waters. In the shallow crust these fluids are usually ice-age waters (Arnórsson et al., 2008).

Because Iceland is lacking hydrocarbon resources but high heat flow rates are common, the exploitation of subsurface geothermal energy is well developed. In 2005, Iceland produced approximately 1,400 GWh electricity and 6,800 GWh thermal energy from geothermal resources, ranking it among the top 10 countries world-wide in the use of geothermal power (Table 1.1). Hence continuous efforts are made on the exploitation of the Icelandic hydrothermal systems. The newly established Iceland Deep Drilling Project has the aim to drill until depths greater than 4 km in order to reach fluids at temperatures greater than 400°C and produce geothermal energy economically more efficiently (Elders et al., 2008). Although the potential of most of the Icelandic hydrothermal systems is well known and they are well studied (Armannsson et al., 1987; Bodvarsson et al., 1984a,b,c; Foulger, 1995; Foulger et al., 1995; Gunnarsson et al., 1992; Pruess et al., 1984; Schiffman and Fridleifsson, 2007), the relevant fluid dynamics are usually only investigated for exploitation and reservoir engineering purposes. They are hence not available publicly or aim to answer specific scientific questions such as the link between large-scale fluid flow and seismicity.

3.4 Seismicity in Iceland

Seismicity in Iceland is very intense. More than 2.5×10^5 seismic events were recorded between 1994 to 2007 and approximately 1.0×10^4 of them had a magnitude larger than

2 M_w (Jakobsdóttir, 2008). The South Iceland Lowland (SIL) system is the automatic network that is used as the national seismic network since 1993 (Jakobsdóttir, 2008). Initially installed in South Iceland only, the SIL network has been expanded and it now counts more than 50 stations across Iceland. The average depth of the focal mechanism of the Icelandic earthquakes ranges from 8 to 12 km depth, suggesting that the brittle – ductile boundary occurs approximately at these depths. Below the brittle – ductile boundary, ductile behavior may or reduce (at least at the local scale) stress accumulation (Rögnvaldasson et al., 1998).

The largest events are of tectonic nature (Garcia et al., 2002) and occur in the SISZ and in the TFZ (Figure 3.4) where magnitudes greater than 7 M_w have been recorded (Stefansson and Halldorsson, 1988). Two 6.6 M_w seismic events were recorded in the SISZ in 2000 and a 5.2 M_w event was recorded in 2003. The TFZ recorded 5.5 M_w and 5.8 M_w seismic events in 1994 and 2002, respectively. Low magnitude seismic events, other than tectonic origin (ridge-driven), can also be of magmatic and hydrothermal origins (Garcia et al., 2002; Hensch et al., 2007; Stefansson et al., 2008). While in the SISZ earthquake-fault planes strike approximately North – South, the tectonic environment of the TFZ is more complex because of the interaction of three tectonic regimes (Einarsson, 1991; Garcia et al., 2002; Rögnvaldasson et al., 1998; Saemundsson, 1974).

The seismic activity does not only occur in the SISZ and in the TFZ. Close to the Western, Eastern, and Northern Volcanic Zone (Figure 3.4) seismic events range from 3 M_w to 4 M_w. The only exception is the occurrence of a 5 M_w event occurred before the eruption of the Gjàlp volcano, whose epicenter was located under the Vatnajökull glacier (eastern white-coloured area in Figure 3.4). Most of these volcanoes are covered by ice caps, rendering their survey more complicated. The only Icelandic volcano that is seismically active and not covered by an ice cap is the Askja volcano which will be discussed in detail later.

3.5 Geological structure of the Tjörnes Fracture Zone

Chapters 4 and 5 focus on the fluid flow dynamics that characterise the Tjörnes Fracture Zone. This region is a 80 km wide fracture zone (Garcia et al., 2002) that offsets the mid Atlantic ridge in northern Iceland. Bounded by the Kolbeinsey Ridge, the Grimsey Lineament and the Dalvik Lineament (Figure 3.5), the Tjörnes Fracture Zone is the

geological expression of the rifting processes. Overall it is a transtensional fracture zone where 500 to 4000 m deep sedimentary basins are filled with marine and glacial-related sediments (see sections 4.2 and 5.2 for more detail on these lithologies) (Gunnarsson, 1998; Richter, 2006).

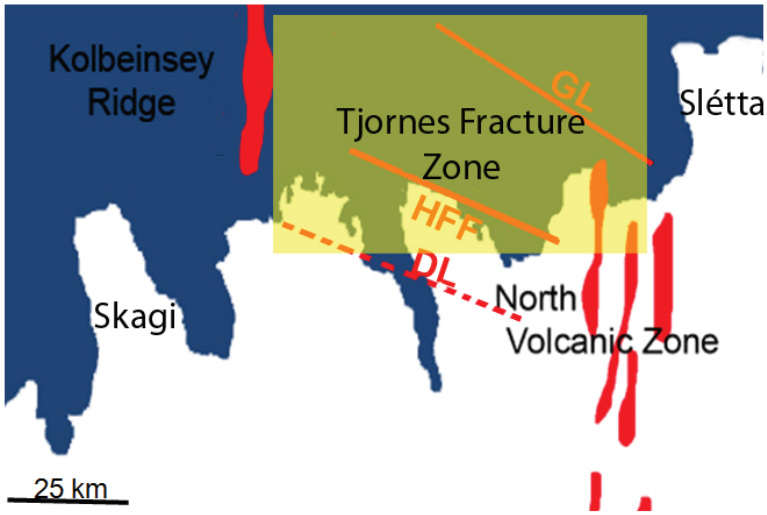

Figure 3.5: Tjörnes Fracture Zone. - The yellowish rectangle highlights the Tjörnes Fracture Zone that is the fracture region that separates the North Volcanic Zone and the Kolbeinsey Ridge. The main geological structures of the TFZ are the Grimsey Lineament (GL), the Húsavik Flatey Fault (HFF), and the Dalvik Lineament (DL).

The regional geodynamic setting shown in Figure 3.5 (Bergerat et al., 2000; Saemundsson, 1974) is characterised by three tectonic regimes: dextral ENE – WSW trending transtension, NE – SW Húsavik Flatey Fault-perpendicular extension and a NW – SE Húsavik Flatey Fault-parallel extension (Garcia et al., 2002). Garcia et al. (2002) suggest that the two minor extensional regimes may correspond to a slip partitioning of the main transtensional regime into two minor regimes, similarly to what Garfunkel (1981) suggests for the Dead Sea transform region. Although the overall tectonic regime of the TFZ can be defined as transtensional, flower structures also occur locally. A large roll-over structure, with amplitude and wavelength of approximately 1 km and 10 km, respectively, appears in the TFZ close to the Kolbeinsey ridge (Richter, 2006). Several synthetic and antithetic listric faults, associated with a crustal-scale listric fault dipping towards South-West, are present in the TFZ (Richter, 2006).

The main tectonic structures of the TFZ – the Grimsey lineament, the Húsavik

Flatey Fault and the Dalvik lineament – trend parallel to the whole transform zone that strikes approximately 60° to the axes of the Kolbeinsey Ridge (Gudmundsson, 1992). The on-land expression of the Grimsey lineament is hardly visible but offshore it is clearly identifiable by seismicity. The micro-earthquake epicenters define a lineament trending about N52°W with right-lateral transform faulting (Stefansson et al., 2008). The Grimsey lineament has been seismically active at least since 1967. It is strongly connected to the North Volcanic Zone as shown by the occurrence of a seismic swarm which preceded the volcano-tectonic episode at Krafla in 1975 (Gudmundsson et al., 1993).

The Húsavik Flatey Fault is also a right-lateral transform fault and a key tectonic feature of the TFZ. Close to the town of Húsavik it has a right-lateral displacement between 5 and 10 km. The fault mainly runs off-shore and its displacement may reach a maximum of 60 km close to Eyafjorður (Saemundsson, 1974). On land it joins the North trending normal faults of the Theistareykir fissure swarm (Gudmundsson et al., 1993). From borehole data it has been estimated that the maximum vertical displacement is approximately 1.4 km (Tryggvason, 1973). The Húsavik Flatey Fault crops out on the Flateyjarskagi Peninsula at the western end of the TFZ (see Figure 4.1b). Here a 3 to 5 km wide damaged zone, characterised by small scale transform faults, transform-parallel trending fault cores of completely crushed rocks and extensive mineral vein patterns, is visible (Gudmundsson, 2007). Offshore the fault flanks the Flateyjarskagi peninsula (parallel to a 3 to 4 km deep graben) and almost reaches the Kolbeinsey Ridge at the eastern end of the TFZ. Most of the seismic activity is concentrated close to the Kolbeinsey ridge and between the mouth of the Eyafjordur and the Flatey shelf (Hensch et al., 2007).

The Dalvik lineament lies sub-parallel to the Húsavik Flatey Fault and runs close to the town of Dalvik, as shown by the consistent seismic activity which begins almost 30 km south of Húsavik. Usually the seismicity is localised offshore in the western part, although a strong earthquake swarm occurred in 1934 close to the town of Dalvik. It has been proposed that these seismic events were related to a transform fault with a right-lateral slip movement (Einarsson, 1976; Sykes, 1967).

3.6 Fluid flow and seismicity in the Tjörnes Fracture Zone

Chapter 4 investigates the regional fluid flow dynamics in the TFZ, which is characterised by steep geothermal gradients, hydrothermal activity, and strong seismicity. Fluid flow is simulated within the TFZ using a high resolution model that was based on the available geological and geophysical data and that represents the complex geological structures and the thermodynamical processes that drive the regional fluid flow in a physically realistic way. The results show that convective heat flow and mixing of cold and saline seawater with deep hydrothermal fluids control the large-scale fluid flow. The distribution of faults has a strong influence on the local hydrodynamics by focusing flow around clusters of faults. This explains the nature of isolated upflow zones of hot hydrothermal fluids which are observed in the TFZ. An important emergent characteristic of the regional fluid flow in the TFZ is the occurrence of two different fluid flow systems. Although they are not physically separated and fluids can flow from one system to the other, they are dominated by different dynamics. The one in the sedimentary basins is advection dominated and comprises more vigorous convection, while the one in the crystalline basement is dominated by very slow advection and heat conduction. These two flow systems yield fundamental insights into the connection between regional hydrothermal fluid flow and seismicity. The fluid flow dynamics and the interplay of these systems are studied in chapter 4 as they form the basis of a toggle switch mechanism that is thought to have caused the hydrogeochemical anomalies recorded at Húsavik before and after the 5.8 M_w earthquake in September 2002 (Claesson et al., 2004, 2007).

Since fluid flow in the TFZ occurs in two different systems that can only be effectively linked during a seismic event, further high-resolution simulations to analyse the pre-, co- and post-seismic fluid flow and fault behaviour in the seismically active region of the TFZ were carried out. These are discussed in chapter 5 along with a fault-inflating mechanism that is suggested to explain part of the low-magnitude seismic events that occur in the TFZ. This approach showed that the TFZ is characterised by four distinct areas where elevated pore pressures, i.e. pore pressures above hydrostatic pressure, occur. This is consistent with geophysical observations. At depth, critical pore pressures, i.e. pore pressures close to lithostatic pressures, are reached while low hydrostatic pore pressures prevail between 7 km depth and the top of the basement. The faults of the

TFZ are often characterised by critical pore pressures that reduce the effective stress acting on them. When this happens, faults can release elevated pore pressures in less than five minutes, which is accompanied by a sudden increase in permeability of over seven orders of magnitude. At this time, short-lived but extreme fluid fluxes of more than 0.01 m s^{-1} occur. In post-seismic times, fault permeabilities decay back to their pre-failure values in 2 to 3 years as the pore pressure dissipates and the effective fault normal stress increases. These results have two important implications. First, they demonstrate how the fault-controlled permeability of seismically active hydrothermal systems is constantly regenerated due to a toggle switch mechanism. This provides a consistent explanation for the distinct geochemical changes observed by Claesson et al. (2004, 2007) in the TFZ before and after a magnitude 5.8 M_w earthquake, which is a prime example for seismicity induced fluid flow in seismically and hydrothermally active oceanic crust. Secondly, they provide another line of evidence in the growing number of observations that crustal permeabilities are constantly evolving due to internal and external forcing and many geological processes are dominated by short-lived catastrophic flow events during prolonged geological time-scales.

3.7 Sub-aerial volcanism in Iceland

Iceland is not only seismically very active, it is also subject to intense volcanic eruptions that make it one of the most active sub-aerial volcanic regions on Earth (Thordarson, 2008). In terms of erupted magmatic volumes, Iceland is the most productive of the currently active hot spot systems, although not the most volcanically active. Approximately 5.0 km^3 of magma are erupted in Iceland every century, which is approximately 1.4 times more than the volume of magma erupting in Hawaii over the same period of time (Thordarson, 2008). Icelandic magmatism is dominated by mafic magmas (91%), followed by intermediate (6%) and silicic magmas (3%) (Thordarson, 2008). The sub-aerial volcanic activity is concentrated along the neovolcanic zones (Figure 3.4). These are 15 to 50 km wide parallel belts where active faulting and volcanism occur (Thordarson, 2008). Each neovolcanic zone consists of several volcanic systems that are usually lined parallel to the main direction of the neovolcanic zone. These systems show an average lifetime of 1.0 $\pm$ 0.5 Ma and consist of dike swarms, central volcanos, or a

combination of both (e.g. Gudmundsson (1995, 2000); Jakobsson (1978, 1979); Saemundsson (1978, 1979)). The eruptive nature of Icelandic volcanic systems can be explosive, effusive, and a combination of both. The Eastern volcanic zone (Figure 3.4) is the most active volcanic belt: more than 80% of all Holocene eruptions occurred here. Almost all known volcano types are present in Iceland (Rossi, 1996) and their activity covers almost all known eruptive styles (Larsen and Eiriksson, 2007; Rossi, 1996; Thordarson and Larsen, 2007). Record suggest that sub-glacial explosive mafic events are the most common eruptions in Iceland (Thordarson, 2008). The water is provided by the occurrence of ice-caps on top of the most active Icelandic volcanoes, with the exception of the Askja volcano (Figure 3.3).

Icelandic phreatic eruptions are usually associated with major volcano-tectonic episodes and appear to be confined to high-temperature geothermal systems often located below ice-caps (Thordarson, 2008). Such eruptions are caused by the sudden heating of geothermal fluids by shallow magmatic bodies (Saemundsson, 1991). This leads to the over-heating and over-pressurisation of the fluids and results in a phreatic eruption. Sub-glacial phreatomagmatic eruptions are commonly driven by the interaction between water and melt and occur when limited amounts of water are available. Phreatoplinian eruptions in Iceland represent 1.6% of the total post-glacial eruption tally (Thordarson, 2008). They can occur in ice-free or ice-capped central volcanos as well as in large mafic fissure eruptions (Sparks et al., 1981; Thordarson, 2008). Phreatoplinian eruptions involve the interaction of highly vesiculated magmas with external water. This interaction enhances the power of the explosive activity making phreatoplinian eruptions significantly more vigorous than Plinian eruptions.

The 28 – 29 March 1875 Askja volcano rhyodacite eruption, the third largest silicic explosive event since the settlement in Iceland, provides the only example of silicic phreatoplinian volcanism on Earth directly observed by mankind. It was part of a larger volcano-tectonic episode that took place in the North Volcanic Zone from 1874 to 1876. The eruption began on the 28^{th} of March at 9 pm with a subplinian event (phase B) which lasted for approximately 1 hour. In the early morning of the 29^{th} of March, after a pause of approximately 6.5 hours, the eruption resumed with a phreatoplinian phase (phase C1) for around one hour. This phase was followed by approximately 2 hours of explosive activity which was characterized by the emplacement of dilute density

currents (phase C2) that became dryer with time. The Plinian phase D commenced at 7 am and lasted for 5 to 6 hours.

Although field and laboratory data confirm the wet nature of this eruption, the source of external water that drove the phreatoplinian activity is uncertain. In chapter 6, a new three-dimensional groundwater flow model was hence developed to integrate geological data, numerical discrete fracture techniques, and eyewitness records. This helps to explain the explosive activity that occurred in March 1875 at Askja. The results show that the water necessary to maintain the phreatoplinian phase was stored within the lava pile and that the rapid groundwater flow through the fractured lavas provided enough water to drive the hour-long phreatoplinian eruption. The decline of the groundwater table during the eruption then causes the progressive dry-out of the phreatoplinian phase and the shift towards Plinian activity.

4

Fluid flow in the Tjörnes Fracture Zone.

4.1 Introduction

Iceland is a geologically young and volcanically active region. Its formation is connected to the seafloor spreading processes which separate the North-American and European plates. The mid Atlantic ridge cuts through Iceland, creating a unique geologic scenario (Figure 4.1a). Rock ages range from late Tertiary (in the western, eastern and northern fjords) to recent times. The latter can be found in the central active volcanic belts, where the mid Atlantic ridge crops out (Jóhannesson and Sæmundsson, 1998). Iceland's young crust is still warm and volcanic activity, intense seismicity and large hydrothermal fields are abundant (Arnórsson, 1995a,b; Palmason and Saemundsson, 1974; Saemundsson, 1979). The study of fluid flow in hydrothermal systems has a long history in Iceland because geothermal energy is plentiful (Flóvenz, 2008). Consequently, major research efforts focus on understanding heat transfer and phase distribution in geothermal fields that are currently used for providing Iceland with energy (e.g., (Bodvarsson et al., 1984a,b,c)). However, there is also long-standing, more scientific interest in investigating the interaction between fluid flow and magmatic intrusions (c.f., Driesner and Geiger (2007); Ingebritsen et al. (2010); Lowell (1991)) for which Iceland provides an excellent natural laboratory. Recently it was demonstrated that there is a strong coupling between regional fluid flow dynamics and seismic events in magmatic-hydrothermal systems (Manga and Brodsky, 2006). This is documented by rapid post-seismic changes in

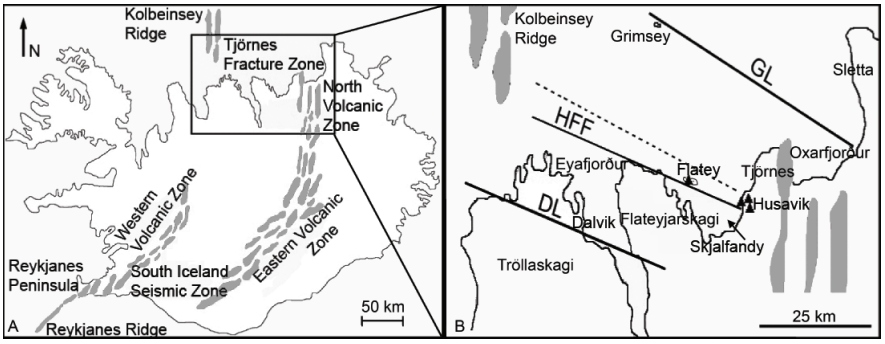

Figure 4.1: Maps of Iceland and of the Tjörnes Fracture Zone. - (a) The mid Atlantic ridge and the most important volcanically and tectonically active regions are shown in dark. (b) Close up of the Tjörnes Fracture Zone. The black bold lines represent the Grimsey Lineament (GL), the Húsavik Flatey Fault (HFF), and the Dalvik Lineament (DL). The dotted line represents the trace of the seismic line from which the two-dimensional geological model for the numerical simulations has been reconstructed. The black triangles are the locations of the boreholes and include the borehole "Húsavik-Hola nr. 1", where hydrogeochemical variations before and after a 5.8 M_w earthquake were observed (Claesson et al., 2004, 2007).

black-smoker vent temperatures (Johnson et al., 2000), variations in geyser periodicity (Husen et al., 2004) and water-level changes in deep wells (Hill et al., 1993; Roeloffs et al., 2003).

In northern Iceland, variations in the hydrogeochemistry of ice-age waters were detected at Húsavik before and after a 5.8 M_w earthquake (Claesson et al., 2004, 2007). The town of Húsavik is located in the Tjörnes Fracture Zone (TFZ) (Figure 4.1b), which is the highly tectonised transform area that connects the rift segments of the mid Atlantic ridge. Several faults, grabens and sedimentary layers characterise this seismically active region (Gudmundsson, 2007; Gunnarsson, 1998; Gudmundsson et al., 1993; Rögnvaldasson et al., 1998; Saemundsson, 1974). In addition to tectonically induced earthquakes, two further types of seismic events occur in this area: dike-induced and hydrothermally-induced earthquakes (Hensch et al., 2007). Claesson et al. (2004, 2007) suggested that the chemical variations observed at Húsavik are caused by a "toggle switch" mechanism in permeability (Miller and Nur, 2000): the permeability of some fault region can instantaneously increase during a seismic event and decreases slowly during the post-seismic period when minerals precipitate and the effective normal stress on the fault decreases. During a seismic event at Húsavik, the permeability increase of

certain fault regions are thought to connect two different fluid reservoirs one in the sedimentary basins and one in the basement. They are characterised by different geothermal gradients, fluid flow regimes and contain fluids of different chemical signatures. Fluids from one reservoir are then transported upwards from great depth along the fault into the second reservoir, causing the instantaneous change in hydrogeochemistry observed at Húsavik. When the fault permeability decays, the communication between the two reservoirs decreases, causing the gradual change in hydrogeochemistry observed at Húsavik. Although chemical, seismic, and geophysical data indicate a strong connection between hydrothermal fluid flow and seismicity in the TFZ (Claesson et al., 2004, 2007; Hensch et al., 2007; Stefansson et al., 2008), a regional fluid flow model that explains how these processes in the TFZ are fundamentally interlinked does not exist yet.

Traditionally, new insights into the hydrodynamics of hydrothermal systems were gained by "process models" which tend to idealise the geological structures and instead focus on a more detailed description of the physical processes (e.g., (Cathles, 1977; Coumou et al., 2008; Fisher et al., 2003; Fontaine et al., 2007; Garven et al., 2001; Hanson, 1995; Hayba and Ingebritsen, 1997; Hurwitz et al., 2003; Join et al., 2005; Lowell et al., 2007; Wilcock, 1998)). However, given today's computational power and progress in numerical algorithms for modelling hydrothermal systems (Ingebritsen et al., 2010), a dynamic fluid flow model that accounts for both physical complexity and geological detail has been developed. This approach is still little used but offers a tremendous upside because it allows to reveal the hidden, i.e. emergent, properties of a hydrothermal system while specifically considering a geological model that incorporates the key structures observed in nature (Matthai et al., 2004). It has hence be constructed a detailed two-dimensional geological model along a seismic cross-section using the available geological, geophysical and borehole data for the TFZ. This model accounts for the faults, the unconformities and the lateral discontinuities which characterise the geology of the TFZ. The code "Complex System Modelling Platform – CSMP++" (Matthai et al., 2007), a state-of-the-art simulator for modelling fluid flow in structurally complex reservoirs, has been used to simulate the transient evolution of fluid flow in this geological model using representative boundary conditions for the TFZ. In addition, a more realistic thermodynamic description for binary hydrothermal fluids containing NaCl and H_2O (Driesner and Heinrich, 2007; Driesner, 2007) has been used. Salt (NaCl) is the most abundant chemical component in hydrothermal fluids and has profound effects on

the thermodynamics and hydrodynamics (Coumou et al., 2009; Geiger et al., 2005). The most important thermodynamic effect is that NaCl-H_2O fluids can boil and separate into a high-density brine and low-density vapour at temperatures and pressures much above the critical point of pure water and two fluid phases can flow simultaneously under certain pressure, temperature, and salinity conditions. These processes are not common in the Tjörnes Fracture Zone or at least in the simulations. Complex hydrodynamic systems can also evolve because salt and heat diffuse and advect at different rates, providing competing effects that try to stabilise or trigger hydrothermal convection. These thermodynamic and hydrodynamic effects cannot be captured if the fluid is assumed to be pure water.

4.1.1 Scope and structure of the chapter

The scope of the study presented in this chapter is to develop a dynamic fluid flow model for the TFZ that is based on high-resolution simulations. These simulations account for the geological complexity of the TFZ and the physical complexity of hydrothermal fluids. This fluid flow model aims to answer the following five question: (1) What is the link between large-scale hydrothermal fluid flow and seismicity in the TFZ? (2) Is the proposed toggle switch mechanism for the TFZ possible and where could it occur? (3) How do the abundant faults in the TFZ influence fluid flow and what is their role in linking hydrothermal fluid flow and seismicity? (4) Can the key parameters that control the large-scale flow behaviour be identified? (5) What is the nature and the origin of the low-temperature hydrothermal fluids in the TFZ?

The following sections of this chapter are organised as follows: in section 4.2 the geological model of the TFZ is presented. This is followed by a description of the model setup, including its hydraulic properties, boundary, and initial conditions. Then the mathematical model and the numerical methods are discussed. Finally the results and the explanation of how they relate to available geological data are discussed. From this a regional flow model for the Tjörnes Fracture Zone is developed. It describes the "inter-seismic" state, i.e. the hydrodynamic state between earthquakes. Section 4.5 discusses how this state may be altered by earthquakes in a toggle switch process.

4.2 Geological Setting

The Tjörnes Fracture Zone is the region located between the Slétta peninsula and the Kolbeinsey Ridge (Figure 4.1). The strong seismicity which occurs in this region is continuously monitored by the Icelandic Meteorological Office. The seismic events are induced by tectonic activity, hydrothermal fluid circulation, and dike intrusions (Hensch et al., 2007). The Grimsey lineament, the Húsavik Flatey Fault and the Dalvik lineament (Figure 4.1b) are highlighted by abundant micro-seismicity (Stefansson et al., 2008). Although the most abundant earthquakes are associated with these three geological structures, it is important to note that large earthquakes with a magnitude above four can also occur away from them, that is in the centre of the TFZ (Stefansson et al., 2008).

The thickness of the highly tectonised crust of the TFZ decreases from East to West: close to the North Volcanic Zone it is $\sim$ 26 km thick, in the vicinity of Grimsey Island it decreases to 16 km and reaches a minimum of 7 km close to the Kolbeinsey Ridge (Riedel et al., 2005). At least three well-defined sedimentary basins overlaying the oceanic crust can be identified in the TFZ (Gunnarsson, 1998) (Figure 4.1b): the Öxarfjordur Graben, the Skjálfandi Graben and the Eyjafjarðaráll Graben. Their formation has been related to the extensional tectonic regime which started in the late Miocene and is still active today (Gudmundsson, 2007). The origin of the basin infill is linked to the high erosion rate of the Icelandic glaciers during the Pleistocene. They probably have produced sediments that are coarser than typical marine sediments (Gunnarsson, 1998). Data from the borehole Húsavik-Hola nr. 1, near the town of Húsavik, show sandstones intercalated with gravels and inter-layered with lavas at a depth of 1.4 km (Tomasson et al., 1969). This provides a partial reference for the lithology of the seismic cross section used to construct the geological model (see section 5.2 for more insights). The sedimentary basins reach a maximum depth of $\sim$ 4 km. Below, picritic rocks occur up to 5 km depth. Gabbros, which characterise the lower oceanic crust, occur from 5 km depth to approximately 10 – 20 km depth (Riedel et al., 2005). This is highlighted by the seismic velocity structure of the TFZ Riedel et al. (2005). They have shown that the shallow crust of the TFZ is highly heterogenous and characterised by a sedimentary coverage intercalated with basaltic layers. Here the v_p seismic velocities range between 4 km s^{-1} and 5 km s^{-1}. At 4 km depth, the v_p seismic velocities increase below the top

of the crystalline basement (Riedel et al., 2005). This might be a consequence of the closing of cracks which reduces the percolation of water and subsequently causes less hydrothermal alteration of the rocks (Riedel et al., 2005). Below the gabbroic bodies a MgO rich mantle is present (Riedel et al., 2005).

4.3 Numerical simulations

We used multichannel seismic reflection data that were recorded in the Tjörnes Fracture Zone by the Icelandic National Energy Authority (Gunnarsson, 1998) as the basis for the two-dimensional geological model. The NW-SE trending seismic profile is shown in Figure 4.1. It runs parallel to the Húsavik Flatey Fault and terminates close to the town of Húsavik. It cuts the main sedimentary basins and the NE-SW trending faults of the TFZ but not the Grimsey lineament, the Húsavik Flatey Fault, or the Dalvik lineament. Therefore, this cross section only considers the second-order geological structures of the TFZ and does not account for the main geological features caused by the main transtensional regime that characterises this region. Being characterised by large damaged zones, the Húsavik Flatey Fault and the Grimsey Lineament may play a key role influencing the fluid flow dynamics of the TFZ. This is not captured with such a 2D cross section that runs parallel to these structures. Nevertheless, there are two main reasons for selecting this particular seismic line as the basis for the geological model. First, the main scope was to simulate fluid flow in the center of the TFZ where large-magnitude earthquakes can occur. This seismic line is located comparatively central in the TFZ. Secondly, of the different seismic lines recorded by the Icelandic National Energy Authority (Gunnarsson, 1998) and other seismic profiles of the TFZ (Riedel et al., 2005), this line has the best quality and also resolves a large number of faults and shallower sedimentary layers. Furthermore, it is located in the vicinity of bore-holes (Figure 4.1) which provide temperature measurements at depth and some indication as to how the shallow sedimentary layers could correlate to the stratigraphy of the TFZ.

4.3.1 Initial and boundary conditions

All simulations were run for ~ 1 Ma. This provides enough time for the flow system to evolve but is well below the age of the TFZ, which is 6 to 7 Ma (Gunnarsson, 1998),

such that we it is possible to assume that many of the geological structures along the two-dimensional cross section are already in place.

4.3.1.1 Initial conditions

The initial geothermal gradient and hydrostatic pressure, as well as the initial distribution of fluid properties (i.e., viscosity, density, heat capacity), have been computed iteratively using the boundary conditions for pressure and temperature discussed below. For this, equations 4.5 and 4.4 are solved at steady-state, i.e. with $\partial T/\partial t = \partial p/\partial t = 0$, and updated the fluid properties during each iteration using an equation of state for NaCl-H_2O(Driesner and Heinrich, 2007; Driesner, 2007). Note that an undisturbed initial hydrostatic pressure (see below) is assumed. Hence the fluid velocities in Equation 4.5 have been set to zero during the calculation of the initial geothermal gradient. These calculations imply that if the heat flow rate at the basal boundary is changed, the initial geothermal gradient will be different and with that the initial hydrostatic pressure because the fluid density is a function of temperature. The initial salinity was always set to zero in the crust.

4.3.1.2 Top, left and right boundary

The hydrostatic pressure in the sea above the TFZ varies along the seafloor according to the water depth given by the seafloor morphology. The hydrostatic pressure at the seafloor has been used as the boundary condition for the pore pressure and it has been assumed that the temperature of the seawater at the seafloor is 5°C and used a uniform seawater salinity of 3.2 Wt.% NaCl. These values have been applied as uniform boundary conditions for temperature and salinity, respectively, at the seafloor. The boundary conditions for pressure, temperature, and salinity have been kept constant during the simulation. The left, right, and basal boundaries are no-flow boundaries.

4.3.1.3 Heat flow at the basal boundary

A constant heat flow rate at the base of the model has been applied to the model. Data from Flovenz and Saemundsson (1993) indicate a heat flow rate of 0.15 W m^{-2} close to the city of Húsavik and lower rate of 0.10 W m^{-2} in the Tjörnes Fracture Zone. Flóvenz et al. (1985) and Flóvenz (2008) propose geothermal gradients of 50 to 60°C

km^{-1} for the sedimentary basins of the TFZ. Picritic rocks at shallow depths suggest a very hot upper mantle (Riedel et al., 2005) and Stefansson et al. (2008) infer partially molten basalts at 10 to 15 km depth in the TFZ. This could imply higher heat flow rates than originally suggested by Flovenz and Saemundsson (1993). Most of the simulations presented here used a heat flow rate of 0.18 W m^{-2}. Since the heat flow rate applied to the basal boundary will have a major impact on the geothermal gradient and on the flow dynamics, additional simulations (discussed further) have been ran to test the effects caused Fby lower heat flow rates of 0.15 W m^{-2} and 0.10 W m^{-2}.

4.4 Geometric and numerical modelling

4.4.1 Geometric modelling

Translating a geometrically complex environment like the TFZ into a computational grid that can be used for numerical simulations is challenging. First the geometry of the geological structures identified in the two-dimensional seismic cross-section (Gunnarsson, 1998) have been reconstructed using the CAD software Rhinoceros 4.0^{TM} (Paluszny et al., 2007). Then the resulting CAD geometry has been discretised into approximately 50,000 adaptively refined triangular finite elements using the commercial software ANSYS ICEM^{TM}.

The resulting numerical model includes 86 faults, classified as shallow and deep (Figures 4.3 and 4.4). They link the upper and the lower structural levels of the system. The shallow faults reach a maximum depth of 1 km while the deep faults start at 1 km and reach depths of 9 km. Each fault has been discretised by triangular finite elements such that the area of the finite elements is approximately equal to half the width of the fault squared. The finite element grid is hence significantly refined around the faults. Although field data suggest that the faults are structurally complex and consist of a high-permeability damaged zone and low-permeability fault core (Evans et al., 1997; Gudmundsson, 2001, 2007), only the damaged zone has been reproduced in the model and the faults are represented as discrete structures ranging from 120 m to 20 m in width. The influence of a low-permeability fault core on hydrothermal flow patterns has also been tested. Fluid flow in the TFZ, however, is predominantly parallel to the sub-vertical faults due to large-scale convection. Hence it is not influenced much by the low-permeability fault core, which would only be of importance if flow were

predominantly horizontal (i.e., across the faults). The temperature distribution for simulations accounting for faults characterised by low permeability fault-cores is shown in Figure 4.2[1]. By not discretising the fault cores of the individual faults, it was

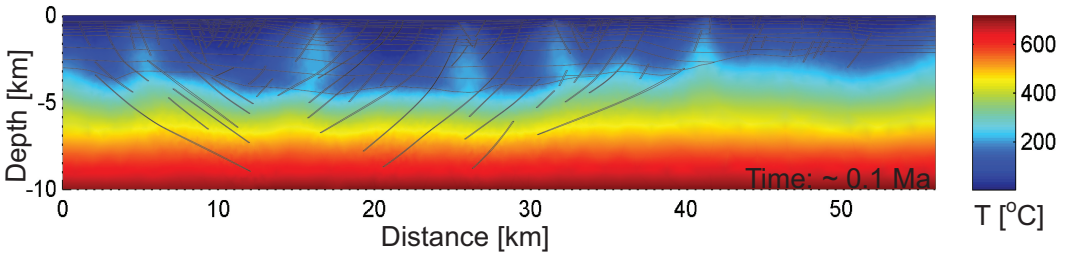

Figure 4.2: Temperature distribution for the TFZ after 0.1 Ma, assuming fault-cores inside the faults. - The temperature distribution has been obtained for a model configured according to Table 4.1. The faults are characterised by an impermeable core. This set of simulations was ran up a runtime of $\sim$ 0.1 Ma. The elevated number of small finite elements necessary to reconstruct the narrow fault-core areas (up to 10 m wide) increased the computational runtime. Note that the temperature distribution is approximately equal to the one of Figure 4.5a.

possible to speed up the simulations by a factor of 10 to 100. The discretisation of the very narrow fault core would require a very large number of excessively small finite elements. These small elements would require a significant reduction in the size of the time-step, which is directly proportional to the ratio between the area of a finite element and the flow velocity in it. We divided the crystalline basement into three parts (top, shallow and deep basement) to reproduce the geology shown by other seismic profiles of the TFZ (Riedel et al., 2005). The top basement, $\sim$ 100 m thick, is assumed to be strongly hydrothermally altered and characterised by frequent occurrence of joints and fractures. The shallow basement (between $\sim$ 100 and $\sim$ 600 m below the sediments) is characterised by permeabilities which guarantee the percolation of fluids at these depths (Riedel et al., 2005). The deeper parts of the basement are probably of gabbroic origin (Riedel et al., 2005) and assumed to have low permeability.

[1] This figure is not part of the published material

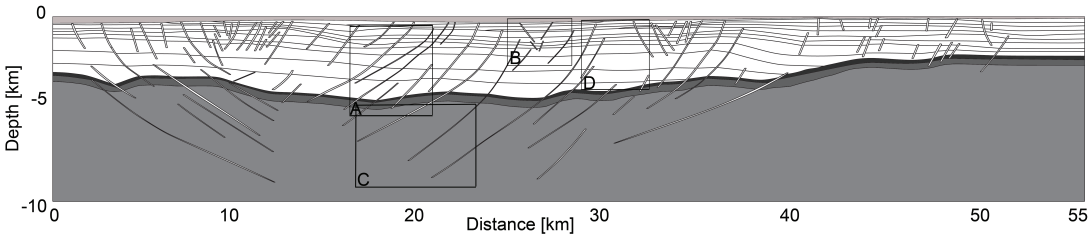

Figure 4.3: Geometry of the TFZ model. - The hydrostratigraphic units of the two-dimensional model used in the numerical simulations consist of faults, sedimentary layers, and crystalline basement. The hydraulic and petrophysical properties of the units are listed in Table 4.1. The light grey region at the top represents the sea that allows to see the irregular seafloor topography (note that the sea is not visualised in the following output results). The dark grey region in the centre of the figure is the top of the crystalline basement, the medium grey region is the shallow basement, and the light grey region the deep basement. Insets A to C show the locations of the flow fields depicted in Figure 4.8. Inset D shows the location of the sedimentary layers depicted in Figure 4.4.

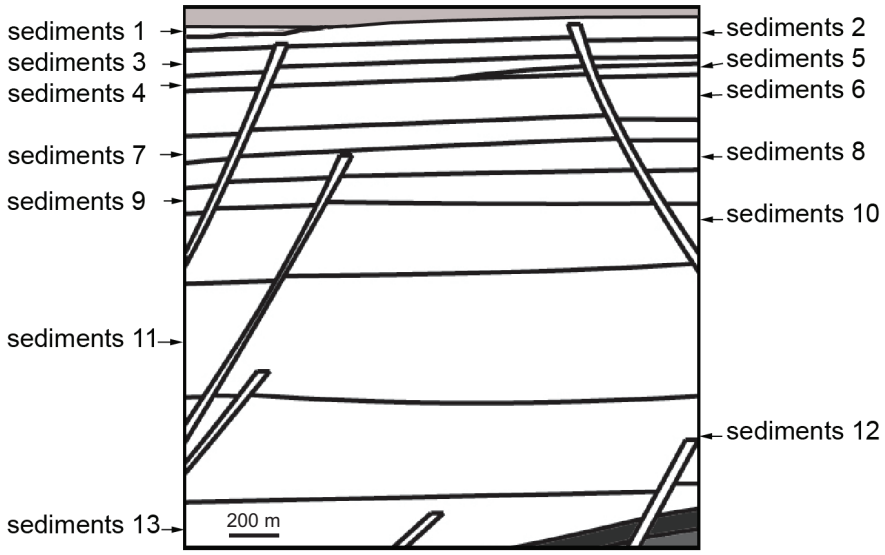

Figure 4.4: Close-up of the complex geometry of the TFZ two-dimensional model. - Close-up of Figure 4.3, inset D, showing the sedimentary layers, which have been correlated from the seismic cross-section and form the hydrostratigraphic units of the sedimentary basin. The hydraulic properties of the layers are listed in Table 4.1.

Group	$\log(k)$ [m^2]	ϕ [–]	c_{pr} [J/(kg m)]	ρ_r [kg/m^3]
Sediments 1	-13	0.25	1000	2700
Sediments 2	-13	0.25	1000	2700
Sediments 3	-14	0.20	1000	2700
Sediments 4	-14	0.20	1000	2700
Sediments 5	-15	0.15	1000	2700
Sediments 6	-15	0.15	1000	2700
Sediments 7	-15	0.15	1000	2700
Sediments 8	-16	0.15	900	2600
Sediments 9	-16	0.10	1200	2900
Sediments 10	-15	0.10	1000	2600
Sediments 11	-15	0.10	1000	2700
Sediments 12	-15	0.10	1000	2600
Sediments 13	-15	0.15	1100	2600
Shallow faults	-13.5	0.22	1100	2800
Group	$\log(k_0)$ [m^2]	ϕ [–]	c_{pr} [J/(kg m)]	ρ_r [kg/m^3]
Deep faults	-13.70	0.02	1200	2800
Top basement	-13.75	0.02	1200	3000
Shallow basement	-13.90	0.02	1200	3200
Deep basement	-14.00	0.02	1200	3200

Table 4.1: Values of the permeability k, porosity ϕ, heat capacity c_{pr}, and density ρ_r for all hydrostratigraphic units which comprise the hydrostatigraphy of the TFZ (see Figures 4.3 and 4.4 for their locations). The thermal conductivity and compressibility of all units is constant at 2.5 W m^{-1} $°C^{-1}$ and 10^{-12} Pa^{-1}, respectively. The dispersion tensor is isotropic and 10^{-6} m^2 s^{-1} in the sedimentary basins and 10^{-9} m^2 s^{-1} in the crystalline basement. $\log(k_0)$ denotes that the permeability of this unit varies as a function of depth according to Equation (4.1) and is the permeability at 1 km depth.

4.4.2 Geological characterisation of the model and petrophysical parameters

Our geological model of the TFZ contains 18 lithological units, which comprise the hydrostratigraphy (Figures 4.3 and 4.4). Each hydrostratigraphic unit is equipped with a unique set of hydraulic and petrophysical parameters, i.e. permeability k, porosity ϕ, density ρ_r, thermal conductivity K, heat capacity c_{pr}, and compressibility β_r. The subscript r denotes the rock. Each unit is listed in Table 4.1 along with its porosity, permeability, density, and heat capacity. The thermal conductivity of all units is held constant at 2.5 W m^{-1} $°C^{-1}$. However, the thermal diffusivity of the different rock types κ, defined as $\kappa = K/(\rho_r c_{pr})$, can still vary due to the local variations in density and heat capacity. The compressibility of all units is also held constant at 10^{-12} Pa^{-1}. However, the bulk compressibility of the fluid-saturated rock is dominated by the fluid compressibility, which varies with temperature and pressure. Dispersion of salt is described by an isotropic dispersion tensor, which is 10^{-6} m^2 s^{-1} in the sedimentary basins and 10^{-9} m^2 s^{-1} in the crystalline basement.

All hydraulic and petrophysical properties are constant in each unit over space and time with the exception of the permeability of the deep faults and crystalline basement. Here the permeability varies as a function of depth according to the relationship provided by Manning and Ingebritsen (1999)

$$\log(k) = \log(k_0) - 3.2 \cdot \log(z), \tag{4.1}$$

where $\log(k_0)$ is the permeability that the layer would have at 1 km depth and z denotes the depth in kilometres. Manning and Ingebritsen (1999) used $\log(k_0) = -14$ m^2.

A close-up of the sedimentary basins and the layering of the shallow crust is shown in Figure 4.4. The sedimentary units of the first 1.5 km are assumed to be coarse grained sandstones as the main sedimentary lithologies that characterise the Húsavik-Hola nr. 1 (Figure 3.2). Geological information on the geology of the deeper crust are only provided by the seismic reflection data. For depths greater than 1.5 km deep Riedel et al., 2005 show that in the sedimentary basins the v_p seismic velocities slowly increase with depth (up to 4.5 km depth). For this reason it is assumed that the lithologies occurring between 1.5 km depth and the top of the basement (occurring approximately at 4 – 4.5 km depth) are progressively finer sandstones. The sedimentary units are classified according to depth (Table 4.1): "Sediments 1" are closest to the seafloor while

"Sediments 13" are situated just above the crystalline basement. The porosity and permeability (denoted as ϕ and k in Table 4.1, respectively) of the sedimentary units are assigned such that they generally decrease from top to bottom of the basins, mimicking the increased compaction of the oldest and deepest sediments. The porosity of the deep faults is assumed to be low due to the precipitation of mineral phases into the pore space. The basement and deep faults (i.e., below 1 km depth) have depth-dependent permeabilities. The corresponding values for $\log(k_0)$ (Eq. 4.1) are listed in Table 4.1. The shallow faults (between 0 to 1 km depth) have constant permeabilities.

4.4.3 Key Assumptions

Several assumptions and simplifications with respect to the numerical simulation have been made. These were practical decisions driven by the necessity to keep the computational cost reasonable.

The mathematical formulation used in this study does not account for two-phase flow and the dynamic formation of a brine and vapour phase. However, in the numerical implementation it has been checked for each time step if pressure, temperature, and salinity conditions could lead to the formation of brine and vapour. In this case the simulation is terminated automatically because the mathematical model is inadequate for this physical processes. Over the many simulations ran in this study this situation was rarely encountered. This is because the downwelling of cold, saline seawater continuously cools the hydrothermal system, depressing the geothermal gradient and avoiding boiling, particularly at shallower depths. Super-critical transition from brine-like to vapour-like fluids, as it can occur at great depth in the TFZ, is still modelled correctly by the equations.

It has been assumed that all hydraulic and petrophysical properties are constant with time. The decrease (or the enhancement) of properties like permeability and porosity due to external factors (e.g., changes in regional stress, creation of new faults during the extension of the TFZ, mineral precipitation or dissolution) are not accounted for. Including the transient evolution of permeability and porosity into the numerical simulations will add another level of complexity and uncertainty because models to describe these processes are not well-constrained.

This study also assumes that the boundary conditions are constant through time. This neglects, for example, any changes in heat flow due to changes in magmatic activity or changes in seafloor topography due to sediment deposition.

The simulations account only for two-dimensional geometries. This implies that convection in the fault plane, which is likely to occur during hydrothermally driven fluid flow and may be affected by regional groundwater flow (Bächler et al., 2003), is neglected. A three-dimensional flow model of the TFZ would require a significant simplification of the geological structures to keep computational costs reasonable. It would also add another level of uncertainty. Due to the scarcity of three-dimensional seismic data and lack of constraints on regional groundwater flow in the TFZ, it is unknown how far the faults extend in the third dimension and how regional groundwater flow, particularly in the faults, could affect hydrothermal flow patterns locally. Given the geological complexity of the TFZ, the insights from a detailed two-dimensional model are still significant.

4.4.4 Mathematical formulation

The mathematical model for NaCl-H_2O fluid flow developed by Geiger et al. (2006) and modified by Coumou et al. (2009) has been used. Salt (NaCl) is the most abundant chemical component in hydrothermal fluids and has profound effects on their thermodynamics (Driesner and Heinrich, 2007; Driesner, 2007) and hydrodynamics (Coumou et al., 2009; Geiger et al., 2005). Mass conservation of a NaCl-rich fluid is given by

$$\phi \frac{\partial \rho_f}{\partial t} = -\nabla \cdot (\mathbf{v_f} \rho_f), \tag{4.2}$$

where ϕ is the porosity, ρ_f the fluid density and $\mathbf{v_f}$ the Darcy velocity. Note that here and in the following, source/sink terms are neglected for simplicity.

Momentum conservation is given by Darcy's law

$$\mathbf{v_f} = -\frac{k}{\mu_f}[\nabla P_f - \rho_f \mathbf{g}], \tag{4.3}$$

where k is the permeability (here assumed to be a scalar), μ_f the fluid viscosity, P_f the pore pressure and $\mathbf{g}$ the vector of gravitational acceleration. Darcy's law and the mass conservation equation can be combined to formulate a pressure diffusion equation

$$\rho_f \beta_t \frac{\partial P_f}{\partial t} = \nabla \cdot \left[\left(\frac{k}{\mu_f} \rho_f \right) \nabla P_f \right] - \nabla \cdot \left[\frac{k}{\mu_f} \rho_f^2 \mathbf{g} \right] + \rho_f \phi \left[\gamma_f \frac{\partial X}{\partial t} - \alpha_f \frac{\partial T}{\partial t} \right]. \tag{4.4}$$

α_f and γ_f are the thermal expansivity and the chemical expansivity, respectively. β_t is the total compressibility of the fluid and rock, given by $\beta_t = (1-\phi)\beta_r + \phi\beta_f$. The subscripts r and f denote the rock and the fluid, respectively.

Conservation of energy can be approximated as

$$\left[(1-\phi)\,\rho_r c_{pr} + \phi\,(\rho_f c_{pf})\right]\frac{\partial T}{\partial t} = -\nabla\cdot(\mathbf{v_f} c_{pf}\rho_f T) + \nabla\cdot(K\nabla T)\,, \tag{4.5}$$

where c_{pf} is the isobaric heat capacity and K is the thermal bulk conductivity of fluid and rock.

Mass conservation of NaCl is given by

$$\phi\frac{\partial(\rho_f X_f)}{\partial t} = -\nabla\cdot(\mathbf{v_f}\rho_f X_f) + \nabla\cdot(\mathbf{D}\nabla\rho_f X_f)\,, \tag{4.6}$$

where $\mathbf{D}$ is the dispersion tensor, which is assumed to be isotropic and symmetric. X_f is the mass fraction NaCl.

4.4.5 Numerical Solution

The numerical model was implemented in the "Complex System Modelling Platform – CSMP++" (Matthai et al., 2007). The governing equations have been solved by a combination of finite element and finite volume methods (Geiger et al., 2006,a). The finite element method approximates the diffusive parts of the governing equations while the finite volume method approximates the advective parts. The advective parts were solved explicitly using a higher-order flux approximation (Geiger et al., 2004). The diffusive parts were solved implicitly, using an algebraic multigrid solver to invert the resulting system of linear equations (Stüben, 2001).

The governing equations were linearised by decoupling the pressure equation (Eq. 5.3) from the energy and solute conservation equations (Eq. 4.5 and 4.6) (Geiger et al., 2006,a). They can then be solved sequentially for each time-step in five steps. First the diffusion of temperature and salinity is calculated with the finite element method and implicit time-stepping. Next, the advection of temperature and salinity is computed by using the finite volume method and explicit time-stepping. Afterwards the fluid properties are updated and the diffusion of the pore pressure is computed by the finite element method and implicit time-stepping. Finally the velocity field is updated. The size of the time-increment was computed during each time-step. It is directly proportional to the smallest ratio of the area of a finite element and the flow rate in the finite element.

Hence the time-step is adapted automatically as the flow rates in the model increase or decrease. This allows to resolve changes in the transport processes at the rate at which they occur.

During each time-step the fluid properties μ_f, ρ_f, and c_{pf}, and their derivatives β_f, α_f and γ_f, needed for the solution of Equations 4.2 to 4.6, were directly computed from an equation of state for NaCl-H_2O for the given temperature, pressure, and salinity field. The equation of state is valid from 0 °C to 1000 °C, 1 bar to 5000 bar, and 0 to 100 Wt.% NaCl (Driesner and Heinrich, 2007; Driesner, 2007).

4.5 Results

4.5.1 General flow patterns

Figures 4.5 and 4.6 show the evolution of the temperature field and fluid flow rates over a time window of 1 Ma. Figure 4.7 shows the temperature field after 0.9 Ma with its horizontal average removed (see caption of Figure 4.7). The heat flow rate was set to 0.18 W m^{-2} in this simulation. Figure 4.8 depicts the fluid flow field in selected regions of the geological model (see Figure 4.3 for their locations). The simulations show the occurrence of two separate fluid flow systems in the Tjörnes Fracture Zone. The first is located in the sedimentary basins and it is characterised by comparatively vigorous convection. The second occurs in the crystalline basement where fluids convect at much lower rates. These two fluid flow systems are also expressed by a distinct change in the geothermal gradient. In the shallow sedimentary basins the average geothermal gradient is ~ 40°C km^{-1} while it is between 90 °C km^{-1} and 100 °C km^{-1} in the basement. Fluid communication between the two fluid flow systems is limited. The downwelling of fluids from the sedimentary basins into the crystalline basement is limited and occurs mostly along faults. Migration of fluids from the basement to higher structural levels occurs only in regions where zones of hot upwelling fluids are located across both systems.

Zones of hot upwelling fluids develop in the sedimentary basins and rise from the top of the basement and reach shallow depths (less than 800 m deep) during the early stages of the system's evolution (Figure 4.5a). Downwelling and upwelling areas are clearly separated and recognisable through the entire vertical profile of the TFZ. The upflow zones comprise temperatures that are up to 170 °C hotter than the average horizontal temperatures while temperature of the downflow areas are approximately 60 °C colder

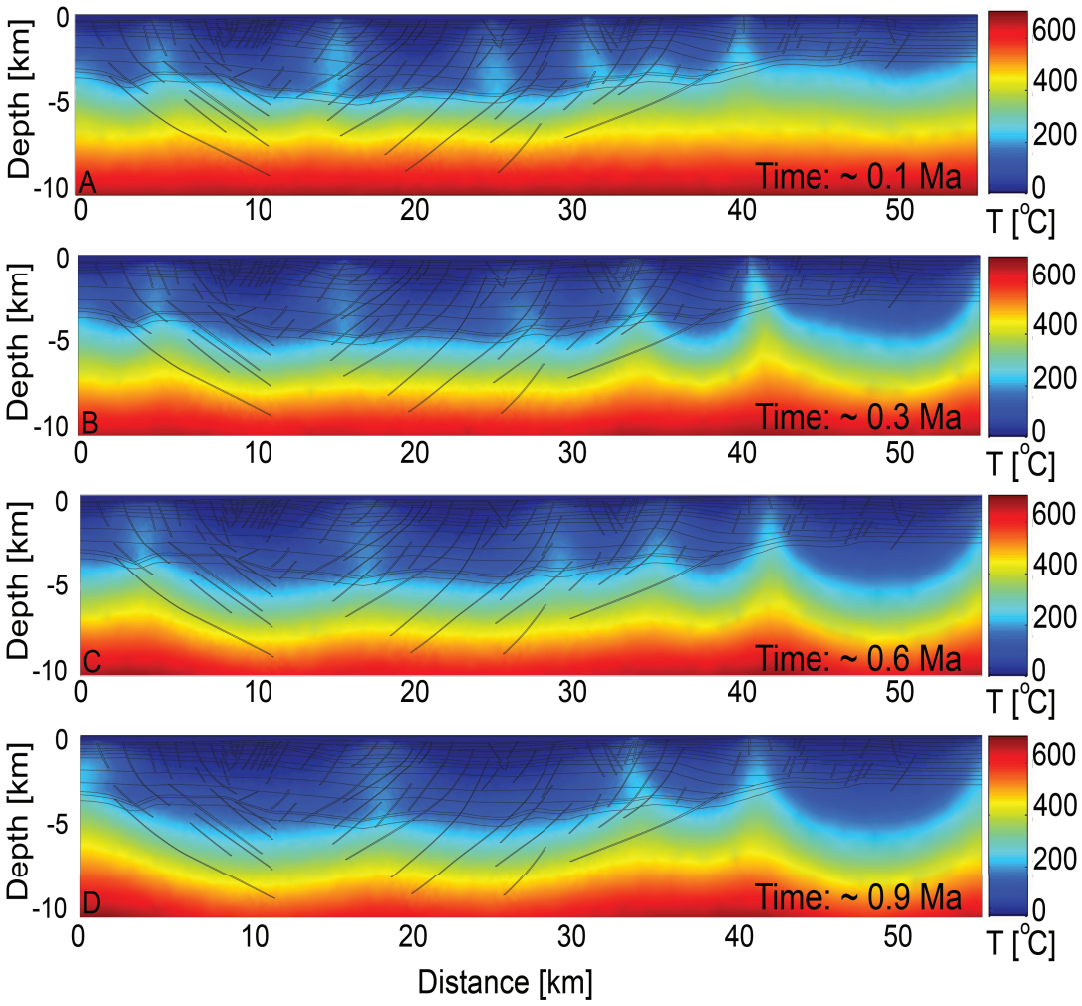

Figure 4.5: Evolution of the fluid temperatures over 1 Ma. - Fluid temperatures evolution in the TFZ at ∼ 0.1 Ma (a), ∼ 0.3 Ma (b), ∼ 0.6 Ma,(c) and ∼ 0.9 Ma (d). The lines show the outlines of the faults, the crystalline basement, and the sedimentary layers. The basal heat flow is 0.18 W m^{-2}.

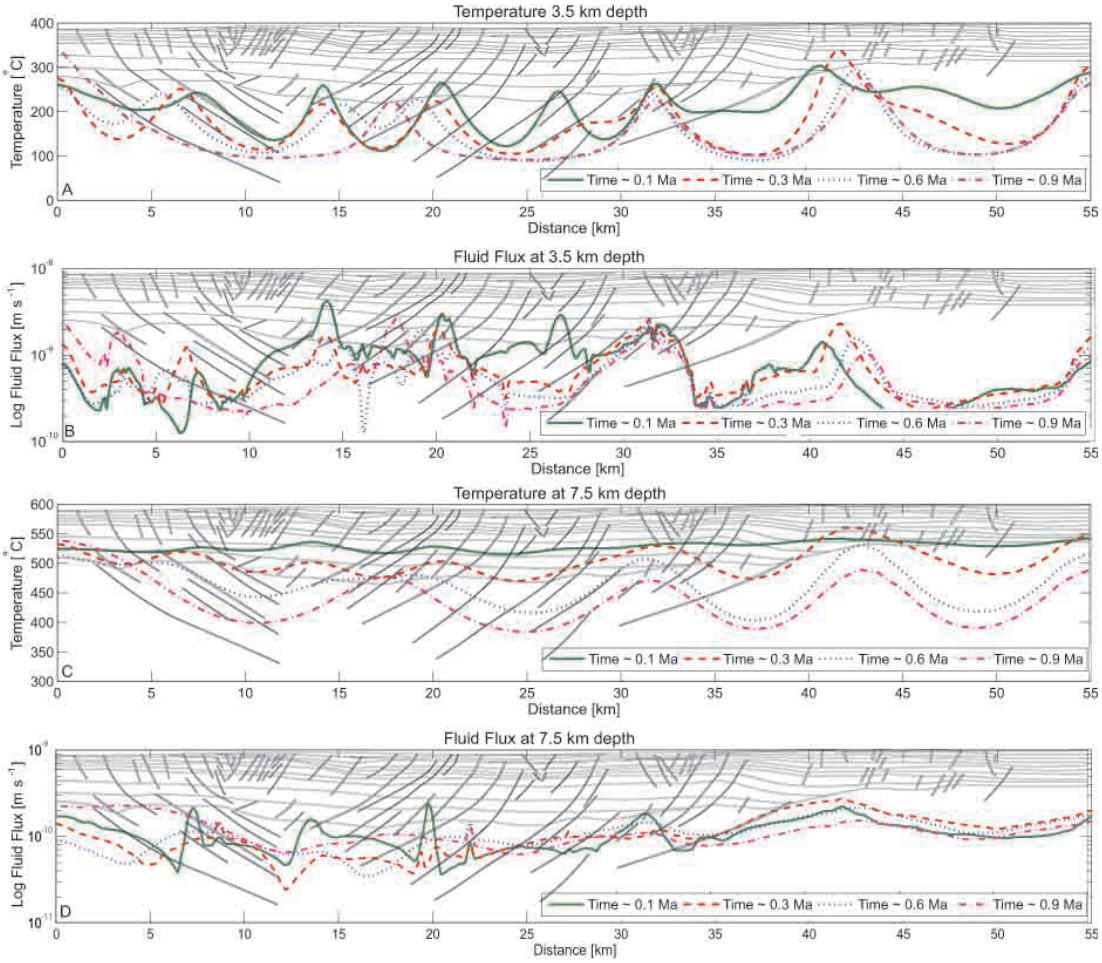

Figure 4.6: Horizontal temperature and velocity profiles in the TFZ. - Horizontal profiles of temperatures (a and b) and flow rates (b and d) at 3.5 km and 7.5 km depth and different times. The basal heat flow rate is 0.18 W m^{-2}. The fault-hosted upflow zones in the basement and sedimentary basin are characterised by elevated temperatures and flow rates.

than the average horizontal temperature (Figure 4.7). After $\sim$ 0.1 Ma, at least six upflow zones have formed, most of which are up to 4 to 5 km wide. Their locations are not constant. Some plumes merge such that the number of upflow zones decreases with time. For example the central plume of Figure 4.5a (located between 20 and 30 km) continuously moves from west to east, by approximately 5 km in 0.9 Ma (i.e., less than 1cm/yr). This lateral migration is also visible in the horizontal temperature and velocity profiles (Figure 4.6). The lateral migration seems to be mainly controlled by the irregular contact between the more permeable sedimentary lithology and the top of the crystalline basement as well as the clusters of faults (Figure 4.8). After 0.8 Ma, the upflow zones are still migrating slowly in the crust and the system does not reach a steady state despite the presence of permeable faults which can act as main flow conduits and stabilise fluid flow. Since changes in permeability or the formation of new faults during extension of the TFZ are not accounted, it can be speculated that the flow system will never reach a true steady state. If longer runtimes would be considered, the simulations may reach a steady state. Nevertheless, this state might not be representative of the fluid flow in the TFZ because the simulations do not account for the spreading rate that characterise this region. The consequent permeability variation of the crust would strongly affect the fluid flow paths of the convective system in the TFZ (Geiger et al., 2004). High salinity fluids, originally located at higher structural levels, reach the deepest parts of the crystalline basement after 0.35 Ma. At this time the salinity of the system is relatively uniform (3.2 Wt %) for the entire crust. Fluids percolate downwards slightly faster in the faults, reaching 9 km depth in the early stages of the simulations ($\sim$ 0.15 Ma). The hydrothermal upflow zones concentrate around clusters of faults (Figures 4.5 and 4.8a). They are characterised by flow rates that can be more than one order of magnitude higher compared to the background flow rates in the basement and sedimentary basin (Figure 4.6). The elevated flow rates in the vicinity of the faults transport hot fluids upwards and consequently the temperatures in the upflow zones are elevated too. They are up to 200 °C higher in the sedimentary basin and up to 100 °C higher in the basement compared to the surrounding rocks (Figure 4.6). The difference between the temperature in the upflow zones and the horizontal temperature average decreases with increasing depth (Figure 4.7). Over time, the temperature difference between the hot upflow zones and surrounding rocks of the basement tends to increase while the difference in fluid flow rates decreases. The

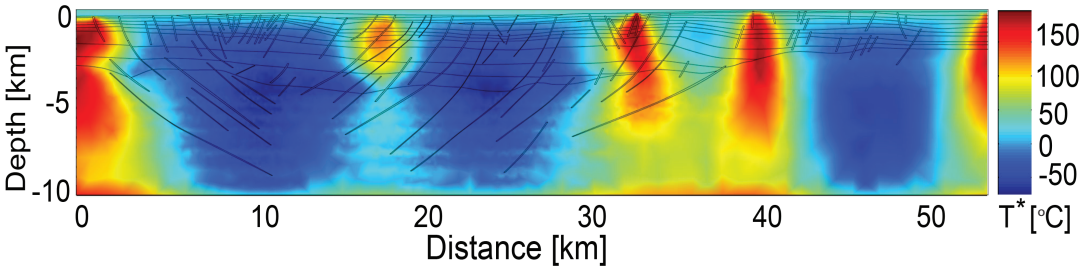

Figure 4.7: Temperature field after 0.9 Ma with its lateral average removed. - The reduced temperature shown in Figure 4.5d, $T^{\star}$, is computed as $T^{\star}(x,z,t) = T(x,z,t) - \hat{T}$, where $\hat{T}$ is the horizontal temperature average given by $\hat{T}(z,t) = \frac{1}{x_{\max}} \int_0^{x_{\max}} T(x,z,t)dx$. Note that the horizontal stripes are an artefact, arising from calculating $\hat{T}$ on an unstructured finite element mesh with greatly varying element sizes.

difference in temperature and flow rates between the upflow zones and surrounding rocks of the sedimentary basin, on the other hand, remains relatively constant but here the upflow zones migrate laterally over time. The fluid flow rates in the basement are at least one order of magnitude lower compared to the sedimentary basins, which emphasises the two different fluid flow regimes. Fluid flow occurs mainly in a single fault in the fault clusters. However, flow can leave one fault and move to another, thereby bridging the less permeable host-rocks (Figure 4.8a). This creates hydrothermal upflow zones that are wider than the individual faults. These flow patterns in the vicinity of fault clusters also suggest that “master faults”, which here are defined as major through-going faults that connect the deep basement with the sedimentary basin and focus large volumes of fluids, may not be present in the TFZ. This behaviour is probably due to two factors: first, the high degree of geological realism that is considered in this study. Such behaviours cannot be simulated with process models that oversimplify the geological heterogeneity of the crust. Second, the Husavik Flatey Fault is not considered in this cross section. This may have a strong impact on the fluid flow close to the fault because the large damaged region of the Husavik Flatey Fault can drive and focus flow acting as a "preferential channel" for fluids.

The occurrence of the two separate flow systems is caused by the geological structure of the TFZ. Fluid flow in the sedimentary basins is dominated by advective transport because the high permeability sediments allow for convection to occur. However in the crystalline basement, heat transport is dominated by conduction since the permeability

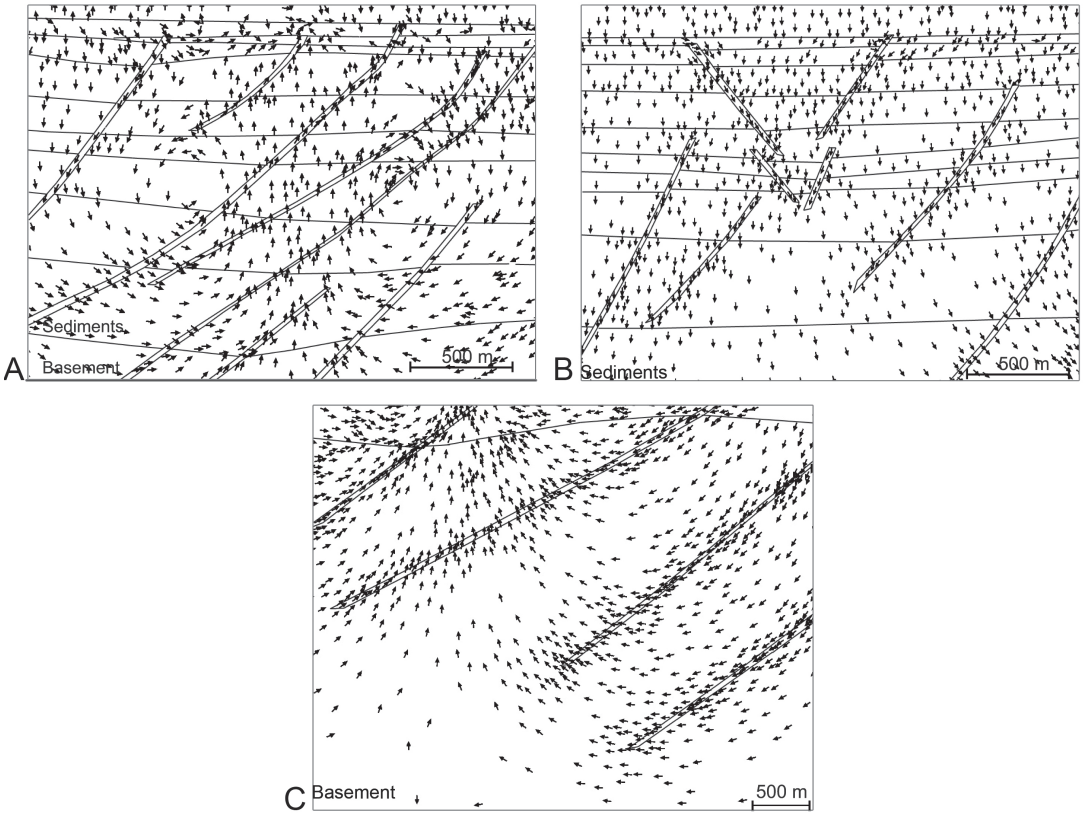

Figure 4.8: Close-ups of the flow fields. - The locations of figures a, b, and c are shown in Figure 4.3. (a) shows the convection patterns at the contact between sedimentary basin and crystalline basement in the vicinity of a cluster of faults (inset A in Figure 4.3). (b) shows the downward motion of fluids in the faults and sedimentary basin (inset B in Figure 4.3). (c) shows the migration of fluids from one fault to another in the crystalline basement (inset C in Figure 4.3). Note that the velocity vectors are not proportional to the flow rates and only a fraction of the actual velocity vectors is shown. They only indicate the fluid flow directions.

is less than 10^{-16} m^2 (Manning and Ingebritsen, 1999). Solute transport is driven by diffusion and advection in the sedimentary basins and in the crystalline basement. This is because the lowest permeability that is imposed at depth reaches 10^{-19} m^2, which is still higher than the lowest permeability above which solute advection can occur (Manning and Ingebritsen, 1999).

4.5.2 Sedimentary basins

The temperature distribution in the sedimentary layers is not homogeneous due to the occurrence of narrow upflow zones which separate large areas of cold fluids which percolate downwards from the seafloor. They cool large parts of the basins by kilometer-scale convective circulation before mixing with the hot fluids rising from the top of the crystalline basement. Such strong convection was also inferred from seismic data by Riedel et al. (2005). The upflow and downflow regions show different geothermal gradients and different Darcy velocities (Figure 4.5 and 4.6). In the sedimentary basins, the downwelling zones are characterised by temperatures ranging from 5 °C to $\sim$ 200 °C. Hence large regions of the TFZ have an average geothermal gradient of $\sim$ 40 °C km^{-1}, which is low if a heat flow rate at depth of 0.18 W m^{-2} is considered but explains the low heat flow rates inferred by Flovenz and Saemundsson (1993).

Parts of the Húsavik Flatey Fault are exhumed on the Flateyjarskagi peninsula where the rocks have been uplifted by $\sim$ 1.5 km (Gudmundsson, 1999). Veins from these exhumed parts of the Húsavik Flatey Fault were probably not created by deep hydrothermal fluids but from relatively local and cold fluids that were driven downwards and towards the faults by gravity (Gudmundsson, 1999). Such flow patterns are also recognisable in the numerical simulations (Figure 4.8b). The downwards motion proposed by Gudmundsson (1999) occurs in more than 90% of the area of the model. The remaining 10% are characterised by upflow zones where plumes of hot fluids migrate from the lower crust upwards through the sedimentary layers (Figure 4.5).

The temperatures at the base of the upwelling plumes range between 300 °C and 350 °C. These are the highest fluid temperatures in the sedimentary basins. The temperatures of the uppermost parts of the upflow areas are in good agreement with the geological observations in the Húsavik region. The borehole Húsavik-Hola nr. 1 (Tomasson et al., 1969), located at the east end of the geological model and approximately 1500 m away from the Húsavik Flatey Fault, shows temperatures of 105 °C at depths of

1.2 km. The simulations show that the temperature at the top part of the plumes is approximately 105 °C at ∼ 1.4 km depth, comparable to the borehole temperatures. Further evidence of shallow and isolated geothermal activity is the occurrence of a hot spring 100 m south of the Laugardalur fault (Tomasson et al., 1969). The Laugardalur fault runs on-land, parallel to the Húsavik Flatey Fault, and is located 1.5 km North of Húsavik. Moreover, a few warm springs in the Húsavik harbour indicate a geothermal anomaly near the town of Húsavik which is also observed in the numerical simulations.

At the contact between the deepest sedimentary unit (sediment 13) and the top of the crystalline basement, strong lateral fluid flow occurs (Figure 4.8). This is due to the low permeability of the crystalline rocks which allows the percolation of only small volumes of fluids. Therefore the downwelling fluids are forced to flow laterally along the sediments-basement contact and they become part of the fluid pressure system necessary for the the upwelling zones to form.

4.5.3 Basement

In contrast to the relatively cold sedimentary basins, the temperatures of the crystalline basement range from ∼ 200 °C in the shallower parts to ∼ 750 °C in the deeper parts (Figure 4.5). The basement cools as the convective system in the overlaying sedimentary basin evolves (Figure 4.6). Although convection in the basement is less vigorous compared to the sedimentary basins and the difference in flow rates between upflow zones and surrounding rocks decreases with time, temperatures are elevated around the fault clusters that host the upflow zones and depressed below the large areas where fluids percolate downwards in the sedimentary basin (Figure 4.5, 4.6, and 4.7). The downwards fluid motion in the basement is influenced by plumes of rising, hot fluids in the sedimentary layers (Figure 4.8c). Below these areas, in the shallower parts of the crystalline basement, the upflow motion affects fluid advection over large distances. The effects are on a kilometre scale and depend on the structural features of the crust. Figure 4.8 shows how fluids leave the fault to flow upwards through the basement and contribute to the hot shallow plume.

4.6 Discussion

4.6.1 Relation to geological observations

There is a considerable amount of geological data for the TFZ that gives insight into local flow phenomena. The simulations help to put these observations into a coherent context. One key observation in the numerical results is the presence of isolated upflow regions in the TFZ which are surrounded by relatively large regions where cold fluids percolate downwards. Isolated systems of upwelling hydrothermal fluids have been observed in the TFZ (Riedel et al., 2001; Tomasson et al., 1969) and even include hot hydrocarbon bearing fluids rising from deep sources (Geptner et al., 2006). The juxtaposition of warm upwelling fluids and large areas of cold downwelling fluids causes strong lateral variations in geothermal gradients. This may explain at least partly the variations in heat flow measurements reported for the TFZ (Flóvenz, 2008; Flovenz and Saemundsson, 1993; Flóvenz et al., 1985; Fridleifsson, 1994; Palmason, 1974) and confirms the cold fluids which are thought to have formed the vein patterns around the Húsavik Flatey Fault (Gudmundsson, 1999).

A key limitation is that this model is based on a two-dimensional geometry because a three-dimensional model with the same level of geological detail would have been computationally too intensive. Hence, it is not possible to account for the effects of regional groundwater flow on convection or for convection of fluids in the fault plane itself, which often occurs in hydrothermal systems (Bächler et al., 2003). It is therefore likely that the hot upwelling areas are not aligned with the cross section but are more widespread in the TFZ. However, this still agrees well with the isolated occurrence of hot upwelling fluids discovered in the TFZ and the two-dimensional model still provides a physically realistic explanation for their occurrence.

4.6.2 Influence of the faults

The faults play a crucial role in controlling the large-scale and small-scale fluid flow in the TFZ. Most notably, the upflow regions are located in areas where clusters of faults occur and seem not to be associated with “master faults” which connect the upper sedimentary basins with the basement and could hence link the two distinct flow systems. It is important to reiterate that the location and extent of the faults has been interpreted from the seismic line. The concept of upflow zones centering around fault

clusters may hence partly be due to the interpretation of the seismic section; wider faults (or additional large faults) may change this picture but would also require a re-interpretation of the seismic cross section and a revision of the geological model which was not attempted.

Additional simulations have been ran to analyse the influence of the fault permeability on fluid flow using two different scenarios, "low-permeability" and "open conduit" faults. In the first case, the shallow part of the faults have a constant permeability of 10^{-16} m^2, while the deep parts have a depth dependent permeability and are less permeable than the crystalline basement by 2 orders of magnitude. In the second case, both the shallow and the deep parts of the faults have a constant permeability of 10^{-14} m^2.

Figure 4.9 shows the comparison between the temperature distributions obtained applying the low-permeability and open conduit settings. There are distinct differences in the resulting temperature patterns but also variations from the temperature distributions obtained for the fault permeabilities listed in Table 4.1 (Figure 4.9). The "v-shaped" upflow pattern induced by the graben located in the western part of the model is wider in the open conduit case and the easternmost upflow area does not occur in the same location. In the open conduit case, the crystalline basement is characterised by lower temperatures at depth; between $\sim$ 100 and 150 °C at 6 km. The shape of the upflow zones is different for the low-permeability and the open conduit scenarios (Figure 4.11). While both settings show that hot upflow zones still originate at the top of the basement, their shape and location depend on the permeability of the faults (Figure 4.11). The upflow zones in the low-permeability case are characterised by a narrow base just above the basement. Here the fluids have temperatures of $\sim$ 200 °C and the width of the upflow zones increases towards its central part where fluid temperatures are between 125 °C and 175 °C. Fluid flow is not focused into the faults and instead the faults act as barriers to flow. Fluids flow in between these barriers through the sedimentary basin. With this setting it is possible to observe upflow zones up to 6 km wide. Yet, the overall pattern is not affected by the presence of low-permeability faults and the two different flow systems still occur. Most of the faults of the TFZ are thought to be still active (Bjarni Richter, personal communication). Although not necessarily, this may imply that low-permeability faults throughout the TFZ are less probable. Hence the case where the faults are characterised by low permeabilities is less likely. If the

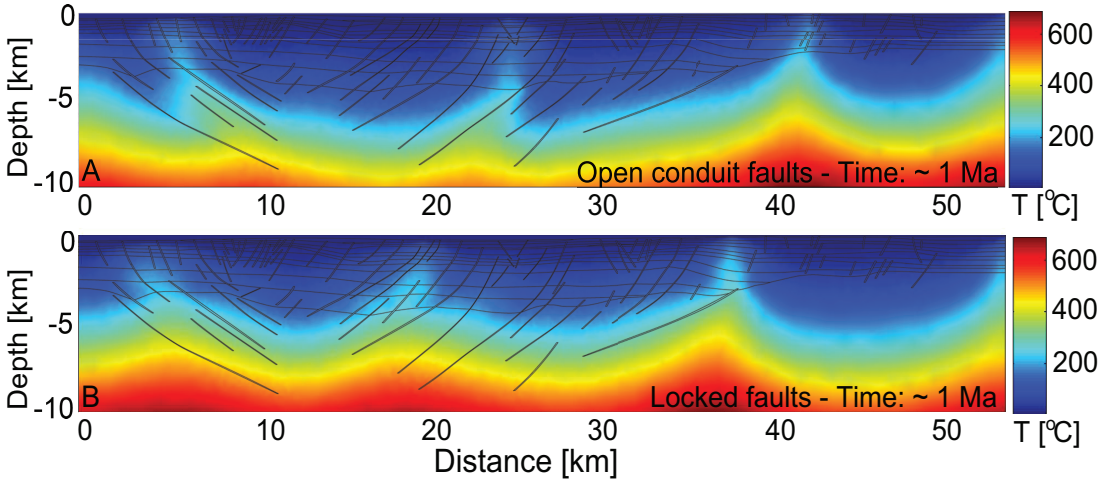

Figure 4.9: Temperature fields after 1 Ma for two different configuration settings. - The temperature distributions after 1 Ma obtained applying the "low-permeability" and the "open conduit" setting are shown in a and b respectively. In the low-permeability case the basement shows higher temperature and the "v-shaped" upflow pattern induced by the graben in the eastern part of the model is narrower. In the open conduit case the geothermal gradient in the basement is lower. Cold fluids of $\sim$ 100 to 150 °C can reach depths of up to 6 km.

fault permeability in the open conduit case is increased even further to 10^{-13} m^2, the rising hydrothermal fluids reach 300 °C and separate into a brine and vapour phase at shallow depths (less than 300 m depth). The basement cools down strongly in the vicinity of the deep faults and can locally reach temperatures of 300 °C at 8 km depth (Figure 4.10[1]). These permeabilities lead to the occurrence of high flow rates and to the dynamic formation of a brine and vapour phase. The width of the upflow zones in this case is narrower, up to 2 km wide, as observed in other hydrothermal systems where faults are thought to have a similarly high permeability (Heft et al., 2008). The maximum Darcy velocities of $\sim$ 1 m s^{-1} for this setting have the same magnitude as the velocities predicted by for another off-axis seafloor hydrothermal system, the Lau Basin in Australia (Schardt et al., 2006). In this case the flow rates are significantly higher than the fluid flow rates typically predicted for a mid ocean ridge system (Coumou et al., 2008). However, geological data of the TFZ do not show mid ocean ridge like behaviour, with high fluid temperatures and boiling at shallow depths. Also, it is probably

[1] This figure is not part of the published material

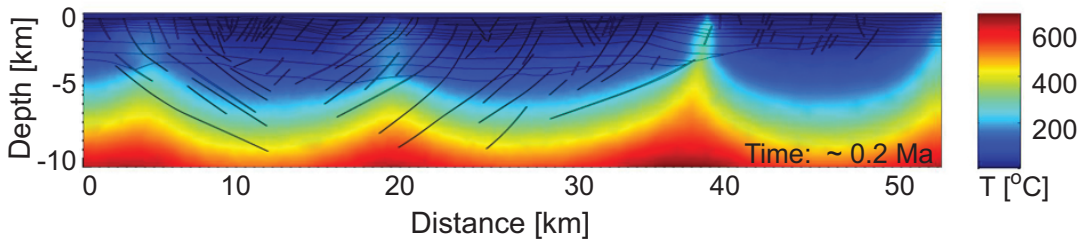

Figure 4.10: Temperature distribution in the TFZ by assuming high permeability faults. - For fault permeabilities of 1.0×10^{-13} m^2 the basement at 8 km depth can reach low temperatures of approximately 300°C. Similar temperatures can be recorded at very shallow depths inside the faults.

unlikely that faults at 10 km depth have such high permeabilities, at least for extended periods. Hence a model where the permeability contrast in the crystalline basement between crust and faults is not large, perhaps a factor 2 to 5, and where at least some of the shallow faults in the sedimentary basin are 10 to 50 times more permeable than the sedimentary rocks is favored.

4.6.3 Influence of the heat flow

We ran additional simulations with a basal heat flow of 0.10 W m^{-2} and 0.15 W m^{-2} to analyse the influence of different heat flow rates on fluid flow. The temperature distribution obtained are shown in Figure 4.12[1]. A heat flow of 0.1 W m^{-2} results in a relatively homogeneous geothermal gradient of $\sim$ 55 °C km^{-1}. Although such a geothermal gradient agrees well with the data from Flóvenz et al. (1985), large convection cells or isolated upflow zones are far less pronounced in the sedimentary basins and essentially absent in the basement (Figure 4.13). In contrast to the strong lateral variations in temperature observed along an horizontal profile for the high heat flow rates (Figure 4.6), the same profile for a heat flow rate of 0.1 W m^{-2} show only small lateral changes in temperature (Figure 4.13). The elevated temperatures are not clearly correlated to elevated flow rates, although the flow rates vary laterally over two orders of magnitude in the sedimentary basin and one order of magnitude in the basement (Figure 4.13). Due to the absence of a large-scale convection system, the separation

[1] This figure is not part of the published material

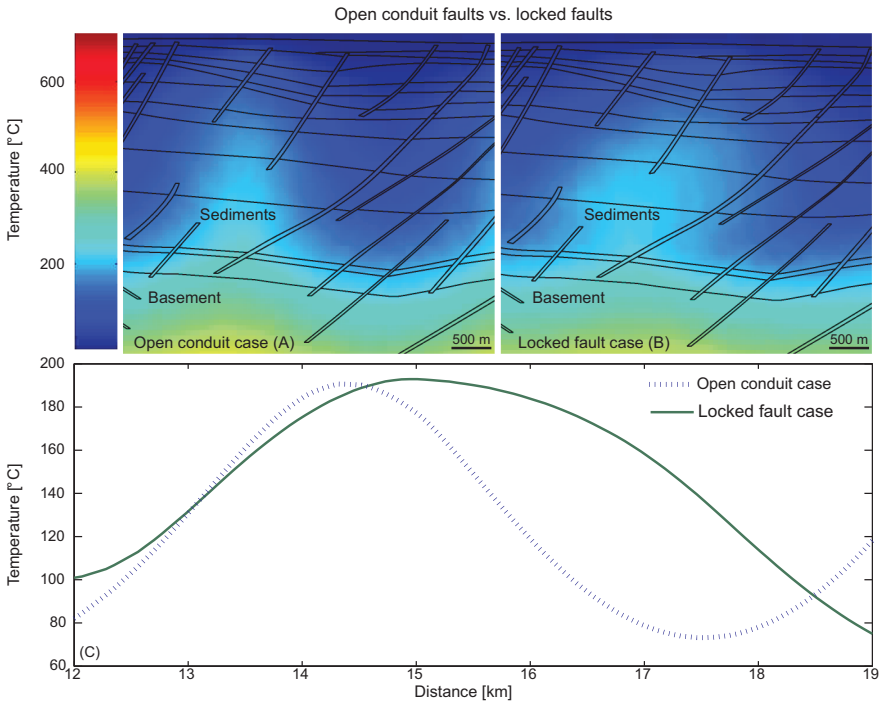

Figure 4.11: Comparison between the shape of the upflow zones in the "low-permeability" (a) and "open conduit" (b) case. - The plumes in the "low-permeability" case show a colder base just above the basement and are wider in the central part, as is visible in the temperature profile taken horizontally across the structure (c). The lines show the outlines of the faults and sedimentary layers.

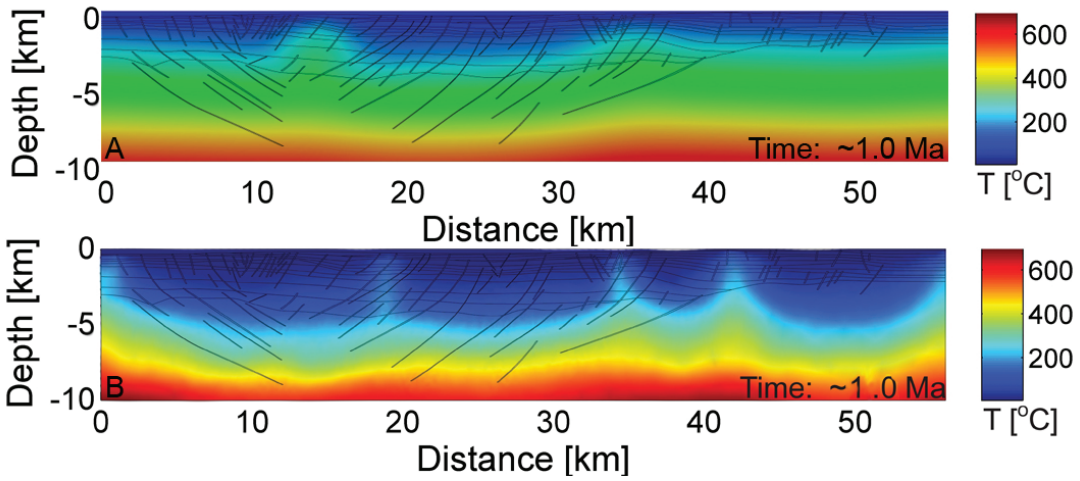

Figure 4.12: Temperature distribution for the TFZ after $\sim$ 1 Ma. - The temperature distribution has been obtained for models configured according to Table 4.1 and assuming an heat flow rate of a) 0.10 W m^{-2} and b) 0.15 W m^{-2}. The temperature distribution of b) does not strongly differ from Figure 4.5d. Compared to Figure 4.5d the isotherms are slightly more depressed and the convection less vigorous.

into two fluid flow systems is also missing. At a heat flow rate of 0.15 W m^{-2}, convection occurs in the sedimentary basins and in the crystalline basement but the presence of two different fluid flow systems is still less pronounced (Figure 4.12). Since there is geological evidence for large-scale convection in the TFZ (Riedel et al., 2005), a high heat flow rate of 0.18 W m^{-2} is favoured.

4.6.4 Possible relation between large scale fluid flow and the seismic events

A key aim of this study was to provide insight into the proposed link between hydrodynamics and seismicity in the TFZ. The most pertinent feature that emerges in the simulations is the formation of two different flow systems: one in the sedimentary basins, comprising more vigorous convection, and one in the crystalline basement, dominated by conduction. Fluid exchange between the two systems is limited due to a moderate permeability contrast at the basin-basement interface and a restricted number of upflow zones that connect basement and sedimentary basins. Based on seismic data, such a flow system was also proposed for the TFZ by Riedel et al. (2005) and by Geoffroy and Dorbath (2008) for the Reykjanes Peninsula in the south of Iceland. Geoffroy and

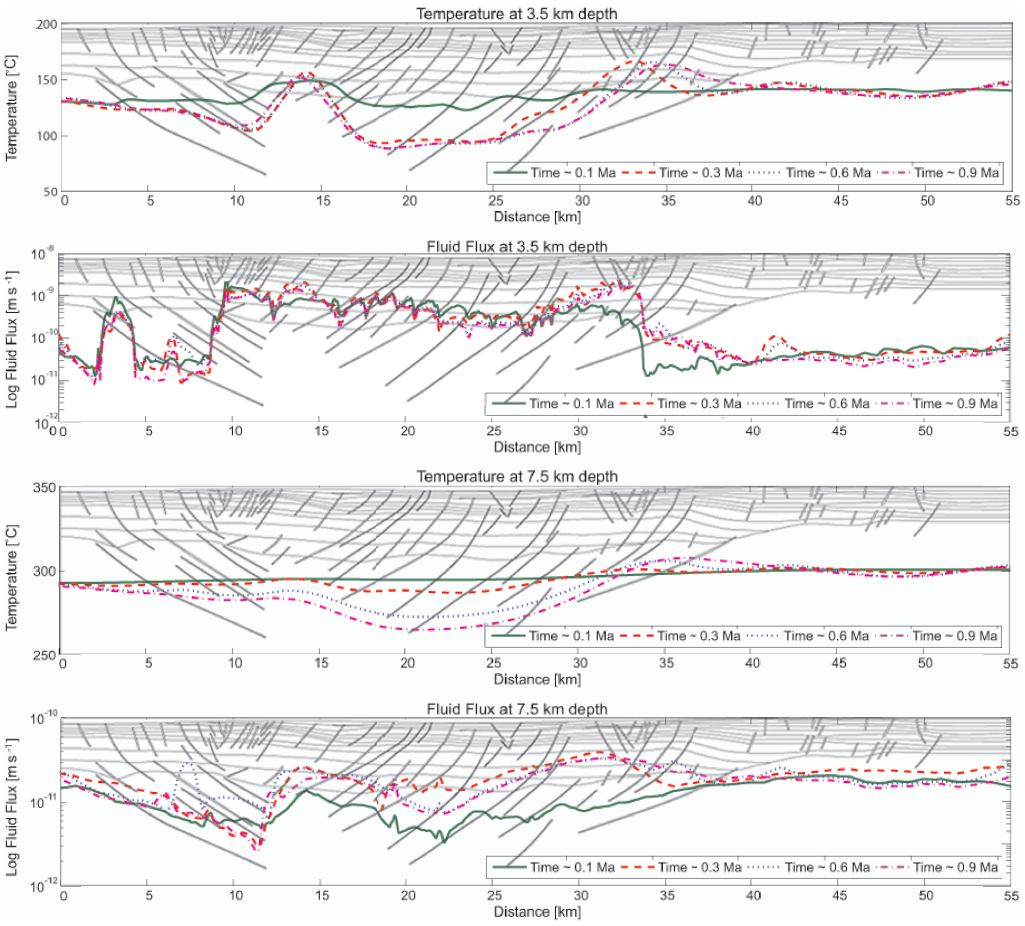

Figure 4.13: Horizontal temperature and velocity profiles in the TFZ for a het flow rate of 0.1 W m^{-2} - Horizontal profile of temperatures (A, C) and flow rates (B, D) at 3.5 km and 7.5 km depth and different times. Compared to a setting that consider a heat flow rate of 0.18 W m^{-2} (Figure 4.6), the fault-hosted upflow zones in the sedimentary basin are less pronounced and essentially absent in the basement.

Dorbath (2008) speculated that two flow systems are separated at approximately 2 to 3 km depth by an impermeable barrier. They can communicate when the impermeable barrier is breached during a large-magnitude earthquake. The simulations show that the formation of two distinct flow domains is in fact very likely and a direct consequence of a relatively small permeability contrast between basement and sedimentary basin. At least for the TFZ a continuous impermeable layer is not necessary to create these two domains, which may be relatively common in hydrothermal systems. If the flow system is disturbed during a seismic event such that the two fluid reservoirs begin to communicate, mixing of shallow and deep fluids is probable. This was proposed for the TFZ by Claesson et al. (2004, 2007) who provided hydrogeochemical evidence of deep fluids rising to 1 km depth near the town of Húsavik immediately after a 5.8 M_w earthquake which occurred in September 2002 in the TFZ.

Recent research has demonstrated that fluids driven by overpressure can migrate along faults at great speed (up to 1 km day^{-1}) due to the sudden enhancement of permeability caused by the dynamic changes in effective stress during seismic events (Miller et al., 2004; Sibson, 2007). Data for the TFZ suggest that the pore pressure in the crystalline basement can be above hydrostatic, possibly close to lithostatic (Crampin et al., 2002; Stefansson et al., 2008). Such excess pore pressure can be readily explained by accounting for a relatively small mantle degassing rate of 1.5×10^{-9}m s^{-1} for Iceland (Fridriksson et al., 2006) which causes an increase in pore pressures in the basement (Figure 4.14). The dehydration of altered (hydrate) mafic basement during burial could also cause such elevated pore pressure in the crystalline basement. It is hence suggested that the simulations represent the initially stable "inter-seismic" state in the TFZ (Figure 4.15a). Co-seismic permeability changes away from the earthquake epicentre have recently been demonstrated (Elkhoury et al., 2006) and here is suggested that such a mechanism enhances the permeability of a fault (Figure 4.15b). The areas of permeability enhancement and decay, that is the location where a toggle switch mechanism occurs, are probably in the vicinity of the fault-hosted upflow zones, or below them in case of large-magnitude earthquakes which occur at greater depth. The faults in the upflow zones are already partially open and probably mechanically weak. Pulses of over-pressured fluids from the crystalline basement can move upwards along these faults during co-seismic permeability enhancement, temporarily changing the fluid temperature and chemistry in the sedimentary basins as observed by Claesson et al. (2004,

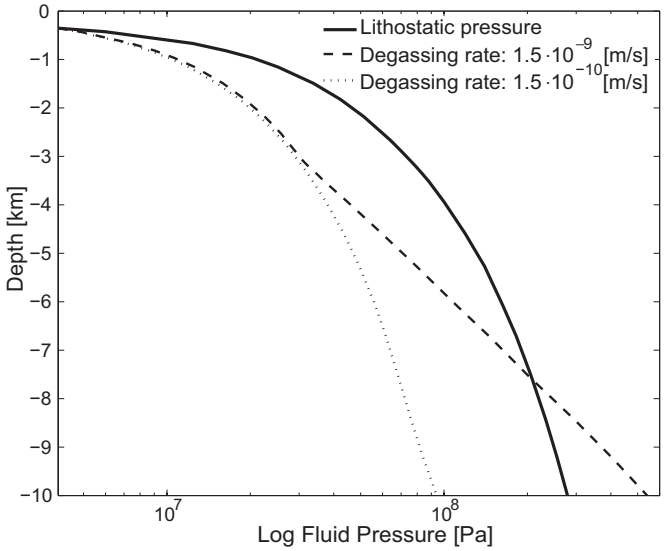

Figure 4.14: Fluid and lithostatic pressure as a function of depth and mantle degassing rates. - Pore pressures above hydrostatic can occur due to moderate mantle degassing rates. Since no degassing rates are available for the TFZ, it is assumed a value of 1.5×10^{-9} m s^{-1}, similar to the average degassing rate proposed by Fridriksson et al. (2006) for South Iceland.

2007). Notably, the numerical simulations as well as geological observations suggest an upflow zone of hot hydrothermal fluids in the vicinity of Húsavik. Fluid flow rates of up to 1 m s^{-1} have been observed for high permeability faults ($k = 10^{-13}$ m^2) even in the absence of an over-pressured basement. This implies that basement fluids can readily be transported over kilometer distances in a few hours. As the pressure dissipates, the fault permeability begins to decrease and the pore pressure in the basement begins to build up, completing the toggle switch cycle (Miller and Nur, 2000). An important prerequisite for this toggle switch mechanism in the TFZ is that the permeability of the deep faults is sufficiently low to not release the build-up of excess pressure in the basement. A second important prerequisite is the occurrence of two different fluid flow rates between the sedimentary basin and crystalline basement. At the same time the fault permeability must also be higher than the average permeability of the basement to allow the formation of fault-hosted upflow zones. The simulations suggest that fault permeabilities 2 to 5 times higher than the basement permeability create the right conditions for the toggle switch mechanism to occur. These values specifically refer to the TFZ but may be valid for similar environments characterised by the different fluid flow

regimes (i.e. diffusion and advection dominated) where elevated pore pressures occur.

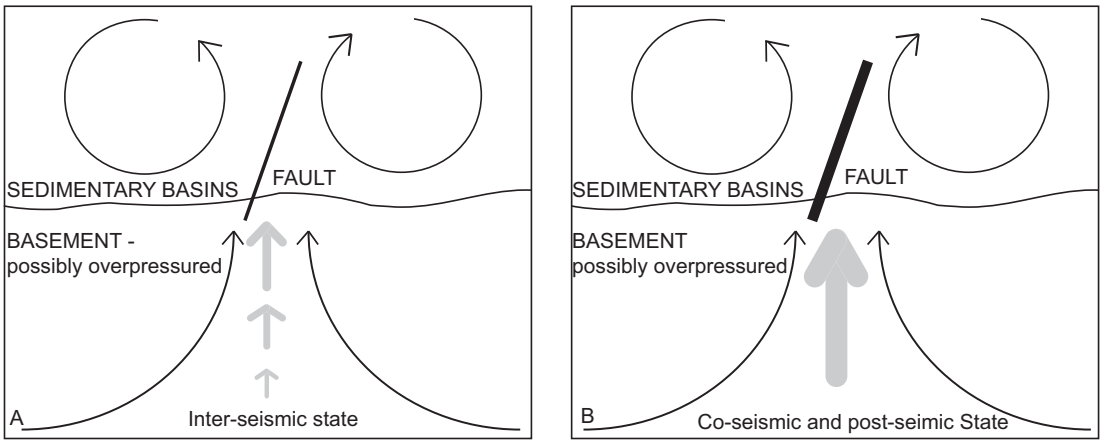

Figure 4.15: Schematic representation of part of the "toggle switch mechanism" in the TFZ. - This idealised sketch shows the "inter-seismic" (a) and co- and immediate post-seismic states (b) of the crust. The curved arrows depict the two flow systems in the sedimentary basins and in the crystalline basement, respectively. The black line represents an idealised fault. Its thickness is proportional to its permeability. The vertical arrows show the fluids upwelling from the basement. Co-seismic permeability increase, and a possibly overpressured basement, lead to rapid and short-lived fluid escape from the basement in the already existing upflow zones.

While the model can explain the co- and immediate post-seismic changes in hydrogeochemistry and switching of fluid sources observed by Claesson et al. (2004, 2007), it does not offer a direct explanation as to why statistically significant changes in hydrogeochemistry at Húsavik have also been observed before the 5.8 M_w earthquake. Claesson et al. (2004, 2007) attribute these pre-seismic variations to stress-induced local changes in permeability and subsequent leakage of deeper fluids, which were in equilibrium with hot basalt, into shallower crustal sections. This hypothesis is still inline with the model because the build-up of excess pressure in the basement may well lead to a local enhancement of permeability shortly before the seismic event, probably in the vicinity of the fault-hosted upflow zones where fluid flow is being focused and the crust is already weakened. A detailed modelling effort would be required to study the effects of pre-seismic variations in fault permeability as the stress field changes.

5

Fluid-induced seismicity in Tjörnes Fracture Zone

5.1 Introduction

Iceland has formed by the interaction of the mid Atlantic ridge and the Icelandic hot spot plume (Allen et al., 2002; Bjarnason, 2008; Darbyshire et al., 1998). The resulting scenario is a geodynamically active and geologically young system. The oldest rocks, of Tertiary age, crop out in NW and E Iceland while the central areas that bound the Mid Atlantic Ridge are characterised by Quaternary to recent lithologies. Since 1960, Iceland has been one of the most studied natural laboratories due to its strong volcanism, active tectonics, and intense seismicity. The mid Atlantic ridge runs across Iceland and is clearly recognisable in the geology of the central region, which consists of elongated ridge fissures and faulted areas. In the South and North of Iceland, the Mid Atlantic Ridge is offset by two transform areas: the South Iceland Seismic Zone (SISZ) and the Tjörnes Fracture Zone (TFZ). These regions are affected by intense seismicity (Stefansson et al., 2008; Stefánsson et al., 2003), which is continuously monitored by the South Iceland Lowland automatic network (Bodvarsson et al., 1996; Jakobsdóttir, 2008).

The TFZ (Figure 5.1) in northern Iceland is an offshore rift-ridge transform zone (Gudmundsson, 2007) consisting of faulted sedimentary basins and crystalline basement (Riedel et al., 2005). Two types of seismic events occur in the TFZ: high-magnitude (larger than 4 M_w) earthquakes due to regional tectonic stresses and plate movement (Garcia et al.,

2002; Stefansson et al., 2008) and low-magnitude seismic swarms (less than 3 M_w) that occur locally due to dike intrusions or hydrothermal activity (Hensch et al., 2007). Elevated pore pressures are thought to prevail throughout the TFZ (Stefansson et al., 2008). Claesson et al. (2004) and Claesson et al. (2007) observed distinct geochemical changes in thermal waters near the town of Húsavik at the eastern end of the TFZ before and after a 5.8 M_w earthquake in September 2002. Cu, Zn, Mn, and Cr levels showed statistically significant anomalies up to 10 weeks before the earthquake while other elements such as Na, Ca, K, δ^{18}O and δD showed significant changes between 2 to 9 days after the earthquakes. The chemical anomalies dissipated after two years and element concentrations and isotopes ratios returned to their original pre-earthquake values. They speculated that variations in the stress field caused two aquifers to mix, with additional fluids leaking upwards from a deeper and hotter basaltic aquifer. Using high-resolution fluid flow simulations, Lupi et al. (2010) demonstrated that the natural large-scale flow system in the TFZ probably comprises two distinct regimes: a deep system with slow convective flow in the basement and a shallow system with faster convection in the sedimentary basins. Limited fluid exchange between the two different regimes occurs along a few faults, most notably at the eastern end of the TFZ where the geochemical anomalies were measured and hot waters are observed in the harbour of Húsavik. These two flow systems are only likely to mix due to a major external perturbation, i.e. if local stress changes around a fault, for example during seismic pumping (Sibson, 1985). This would allow fluids from the deeper flow regime to leak into the shallower one thereby creating the distinct hydrogeochemical changes observed in Húsavik.

The concept that seismicity affects not only hydrogeochemistry but also, more generally, fluid flow, is well established. Examples of post-seismic changes in regional groundwater flow include variations in flow patterns within volcano-hydrothermal systems (Manga and Brodsky, 2006), temperature fluctuations in mid ocean ridge black-smoker vents (Johnson et al., 2000), water-level changes in deep wells (Roeloffs et al., 2003), over-pressure and earthquake-induced sediment failure at continental slopes (Stigall and Dugan, 2010), and variations in geyser periodicity (Husen et al., 2004). Such geological responses do not necessarily need to occur only in the vicinity of an epicenter. Seismic waves can travel great distances and affect groundwater flow in far-field regions, as observed in induced micro-seismicity and pore pressure changes recorded in

hot continental crust up to 1250 km away from the epicenter of a major earthquake in the western USA (Hill et al., 2002). On the other hand, the notion that elevated pore pressures, that is pore pressures above hydrostatic pressure, can weaken porous media and ultimately induce seismicity was recognised in the early work of Terzaghi (Terzaghi, 1925, 1923). Pore pressures can reduce the effective normal stress acting on the faults and cause the fault to inflate, or in the case of a seismic event, to slip which both can lead to a sudden increase of permeability (Rice, 1992; Rubey and Hubbert, 1965; Sibson, 1990). In these circumstances faults act as valves and allow fluids to migrate upwards in the crust at high rates (Cox, 1995; David et al., 1994; Evans et al., 1997; Rice, 1992; Sibson, 1990, 2007; Stanislavsky and Garven, 2003; Wiprut and Zoback, 2000). Examples of induced seismicity include, but are not limited to, seasonal seismicity in volcanic areas (Christiansen et al., 2005), production-induced seismicity due to high fluid injection rates (Zoback and Zinke, 2002), or the occurrence of pore pressure driven aftershock sequences (Miller et al., 2004).

Crustal permeabilities are generally assumed to decay exponentially as a function of depth, with bulk permeabilities of 10^{-16} to 10^{-17} m^2 between 4 and 10 km depth (Jiang et al., 2010; Manning and Ingebritsen, 1999; Saar and Manga, 2004). In intra-plate regions, hydraulically conductive and critically stressed faults probably maintain these bulk permeabilities, which keeps pore pressures at hydrostatic levels (Townend and Zoback, 2000). Recent theoretical studies (Ingebritsen et al., 2010; Rojstaczer et al., 2008) lend further support and demonstrate that crustal permeabilities are constantly evolving due to internal and external forcing to maintain sub-critical pore pressures. On the other hand, the close coupling between seismicity and fluid flow due to critically high pore pressures, that is pore pressures close to lithostatic pressure, in seismogenic zones continually weakens the rock by regenerating fracture-controlled permeability that decreases and increases over orders of magnitude locally and transiently (Sibson, 1992). Recent field evidence also points to extreme fluid fluxes that may accompany such short-lived permeability increase (Cox and Ruming, 2004; Okamoto and Tsuchiya, 2009). An elegant conceptual model behind this process is the toggle switch mechanism (Miller and Nur, 2000) that simplifies the real geomechanic behaviour of the faults and highlights how fluid-controlled seismic events can occur along fault planes. The toggle switch mechanism occurs in four states: 1) fault zone compaction, 2) fluid pressure increase, 3) dilatant slip and/or fault inflation and/or slip 4) fault sealing (Figure 5.2).

When dilation occurs in a certain fault region, this is often associated with compaction of others fault regions. This is not accounted in the simulations where either fault dilation or compaction for the whole fault is only considered.

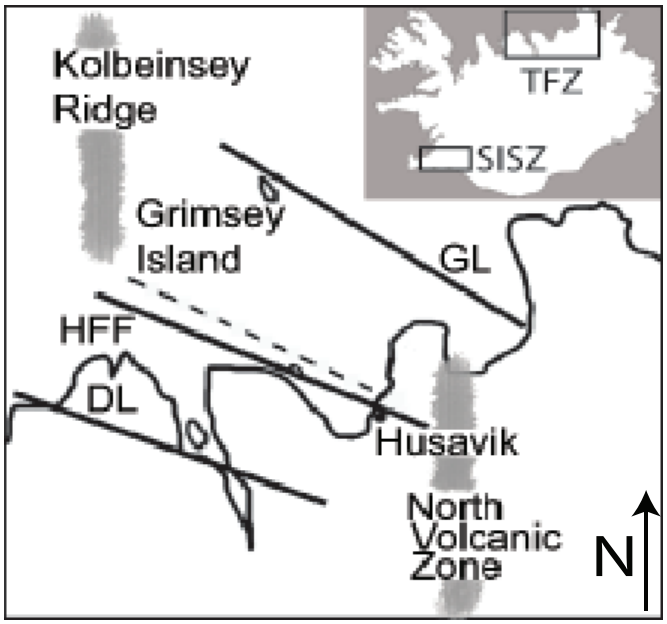

Figure 5.1: Map of the Tjörnes Fracture Zone and surrounding regions. - The inset shows the locations of the South Iceland Seismic Zone (SISZ) and the Tjörnes Fracture Zone (TFZ). The mid Atlantic ridge is represented on-land (North Volcanic Zone) and offshore (Kolbeinsey Ridge) by the wide grey shaded areas. The main geological structures in the TFZ are the Grimsey Lineament (GL), the Húsavik Flatey Fault (HFF) and the Dalvik Lineament (DL). The Tjörnes Peninsula is located between the Húsavik Flatey Fault and the Grimsey Lineament. The dashed line shows the direction of the seismic profile used in the simulations.

For this study the pressure diffusion equation coupled with a spatially and temporally varying permeability that evolves as a function of the effective fault normal stress (Rice, 1992) has been solved to describe fluid flow in hydrothermal systems (Geiger et al., 2006) This allows to model how faults inflate due to local changes in pore pressure. A high-resolution geological model based on a seismic profile of the TFZ (Gunnarsson, 1998) was developed for the simulations (Figure 5.4). The conceptual model is shown in Figure 5.2 and the workflow is summarised in Table 5.1 where the computational procedure is described. The simulations started with the inter-seismic state where fluid flow in the TFZ is characterised by two separated convective sys-

tems, one in the sedimentary basins and one in the basement. The pre-seismic state is characterised by an increase of the fluid production rates at the bottom boundary, for example due to volatiles rising from the ductile-brittle boundary or a dike intrusion at depth (Hensch et al., 2007; Stefansson et al., 2008). This causes a steep increase in pore pressures in the TFZ. A seismic event then causes a fault to unlock (Miller and Nur, 2000; Miller et al., 2004). As consequence, faults which originally comprise low permeabilities, begin to inflate. This enhances their permeabilities and cause the faults to "unzip" themselves from bottom to top, accelerating fluid flow in the faults. This permeability increase then allows pore pressures to dissipate. During the post-seismic state, the permeability of the faults decays to its original values.

5.1.1 Scope and structure of the chapter

The scope of the study presented in this chapter is to apply the concept of the toggle switch mechanism in a series of high-resolution simulations and use the TFZ as a case study to model the pre-, co- and post-seismic fluid flow behaviour. The simulations account for fault inflation and the sudden permeability enhancement accompanying it. This helped to answer the following questions: 1) Can the hydrochemical variations observed before and after the September 2002 earthquake in the TFZ be explained by a toggle switch mechanism? 2) How can critical pore pressures be generated and maintained in the TFZ and how are they distributed? 3) What are the time-scales of the complete toggle switch cycle? 4) What is the nature of co- and post-seismic fluid flow in the vicinity of a fluid-induced seismic event?

This chapter is organised as follows. First the geology of the Tjörnes Fracture Zone is presented and then the geological and mathematical model are described, including the key assumptions. Next will be presented the results and discussed how they relate to time-scales of fluid flow in active hydrothermal systems.

5.2 Geological setting of the Icelandic seismic regions

Seismic events in Iceland are frequent and mostly distributed along the mid Atlantic ridge (Einarsson, 1991; Sigmundsson, 2006). The Tjörnes Fracture Zone (TFZ) and the South Iceland Seismic Zone (SISZ), generally described as transform zones (Bergerat and Angelier, 2007; Bergerat et al., 2000; Saemundsson, 1974), are the seismically

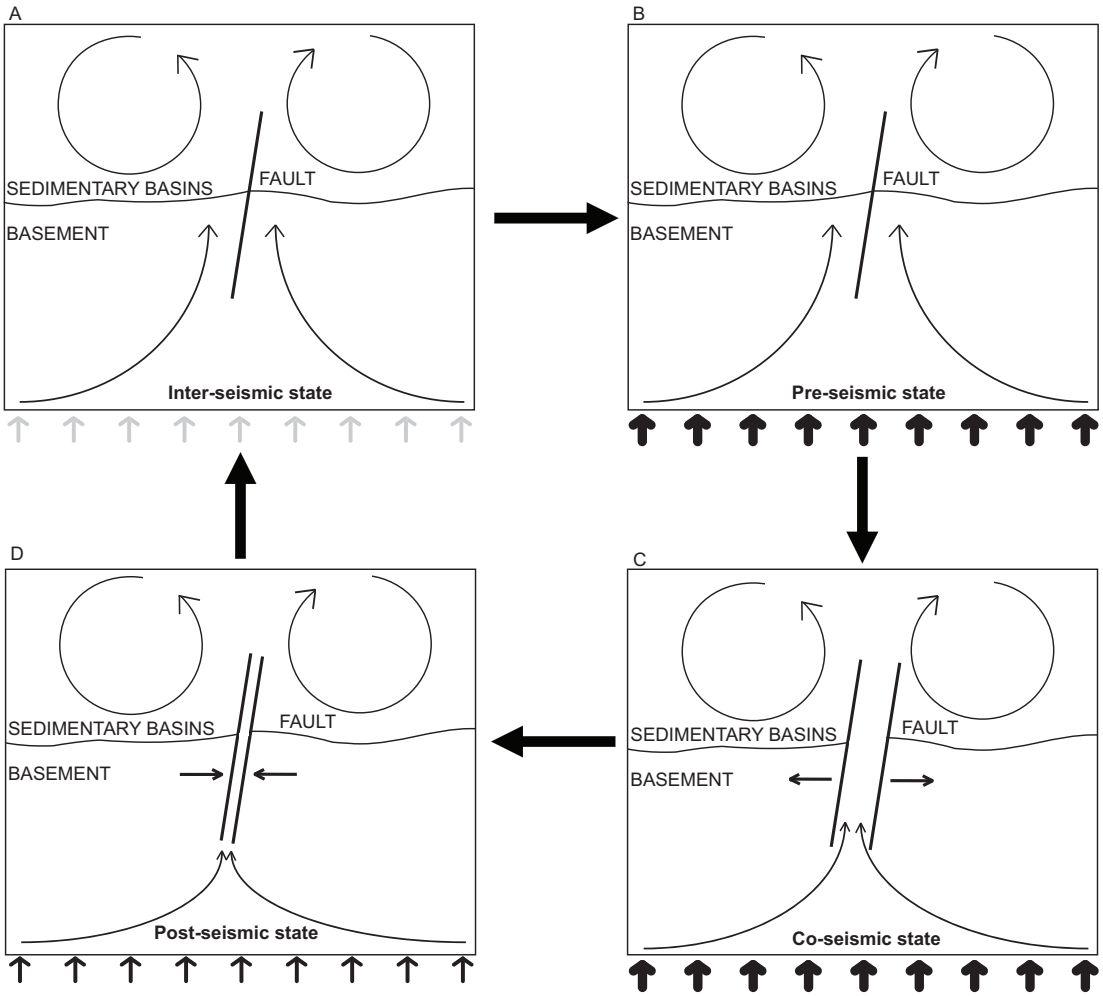

Figure 5.2: Conceptual picture of the toggle switch mechanism (Miller and Nur, 2000) as modelled in the simulations for the Tjörnes Fracture Zone. - The inter-seismic state a) shows two separated fluid flow systems, one in the sedimentary basins, characterised by intense convection and one in the basement, characterised by much slower convection (Lupi et al., 2010). An increase in the rate at which volatiles migrate upwards (possibly caused by a dike intrusion or a more intense mantle degassing) leads to the pre-seismic state b) and causes elevated pore pressures in the fault and in the basement. The fault inflates during the co-seismic phase c) which is accompanied by a sudden increase in fault permeability and mixing of deep and shallow fluids due rapid upwards migration of fluids. During the post-seismic state d), the fluid pressure dissipates and the faults close due to a decrease of the pore pressure and mantle degassing rate.

most active areas in Iceland. They offset segments of the mid Atlantic ridge and are characterised by both low- and high-magnitude seismic events. The TFZ is located between the Kolbeinsey Ridge and the North Volcanic Zone (Figure 5.1) and comprises sedimentary and magmatic lithologies (Riedel et al., 2005). The tectonic and geologic setting of the TFZ is described in sections 3.5 and 4.2, respectively. The shallower parts of the basins that characterise the Tjörnes crop out on the Tjörnes peninsula (Figure 5.1). They consist, from base to top, of Tertiary lava flows overlain by a sequence of sedimentary layers up to 500 m thick (Richter, 2006). Above these units a Pliocene lava succession alternating with marine sedimentary lithologies occurs. On top of these Pliocene lava flows, tills, and other glacial-origin sediments occur (Richter, 2006). The upper part of this succession has also been found on the Flatey Island (Figure 5.1) approximately 15 km offshore of Húsavik in a 600 m deep borehole. This implies a lateral continuity, at least for the shallow sediments. Below the sedimentary basins, picritic rocks occur in the basement up to 5 km depth while gabbroic rocks characterise the deep oceanic crust (Riedel et al., 2005). Below the gabbroic bodies a MgO rich mantle is present (Riedel et al., 2005).

As previously described in section 4.2, the main geological structures of the TFZ – the Húsavik Flatey Fault, the Grimsey Lineament, and the Dalvik Lineament – are highlighted by an abundant seismic activity (Stefansson et al., 2008). Microseismicity is intense and occurs mainly between 2 and 10 km depth but never below 16 km (Rögnvaldasson et al., 1998). Stefansson et al. (2008) suggest that this may be caused by elevated pore pressures that migrate upwards from the ductile crust across the brittle-ductile transition towards shallow depths. Low-magnitude events are caused by variations of the local stress fields (Garcia et al., 2002; Rögnvaldasson et al., 1998). These variations are due to dike intrusions, hydrothermal fluid flow, and deep fluid migration across the brittle-ductile transition (Hensch et al., 2007; Stefansson et al., 2008). High-magnitude earthquakes (up to 7.0 M_w), caused by the regional tectonic forces (Garcia et al., 2002), have been recorded in the area over the last century (Stefansson et al., 2008).

Table 5.1: Summary of the two simulation steps. The co- and post-seismic state simulations start from the physical conditions that characterise the pre-seismic state. When the mantle degassing rate of 5.4×10^{-9} m s $^{-1}$ is applied at the bottom boundary, for each time-step, CSMP++ recomputes the variation of fluid pressure across the model. Next, equations 5.4, 5.5, and 5.6 are computed and equation 5.3 is solved. The same cycle is applied for the next time-step.

Pre-seismic state
Type of simulation: Transient pressure-diffusion *Aim*: To evaluate the time required to reach a steady state pore pressure distribution in the TFZ *Method*: Different mantle degassing rates are applied at the bottom boundary. They range from 2.0×10^{-10} m s $^{-1}$ to 5.4×10^{-9} m s $^{-1}$
Co- and post-seismic state
Type of simulation: Transient pressure-diffusion *Aim*: To evaluate the fluid flow behaviour and the fault inflation during the co- and post-seismic state *Method*: A high mantle degassing rate of 5.4×10^{-9} m s $^{-1}$ is applied to the bottom boundary, which leads to fault inflation. The permeability is allowed to vary as a function of σ'_n.

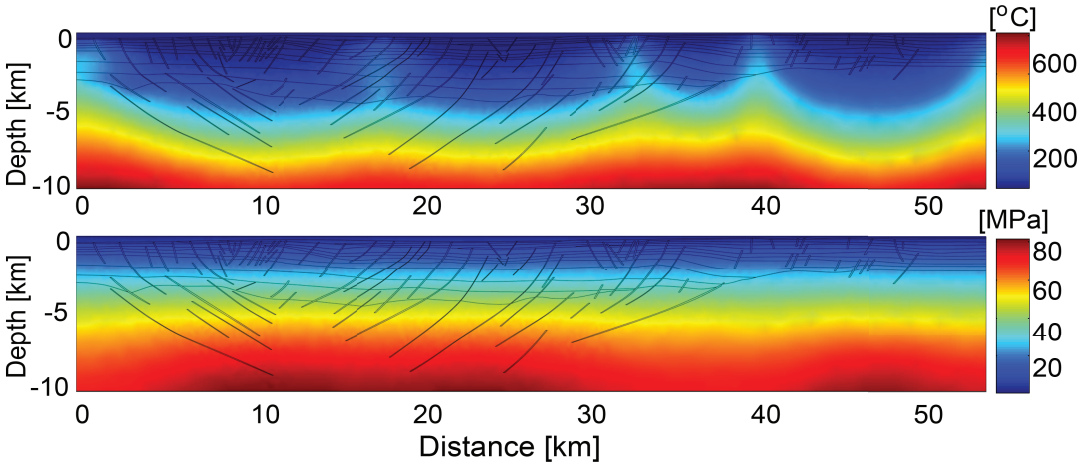

Figure 5.3: Initial temperature and pore pressure distribution in the TFZ after $\sim$ 0.9 Ma. - In oder to reproduce the elevated pore pressures that occur in the TFZ different fluid fluxes (from 2.0×10^{-10} m s^{-1} to 5.4×10^{-9} m s^{-1}) have been applied at the bottom boundary.

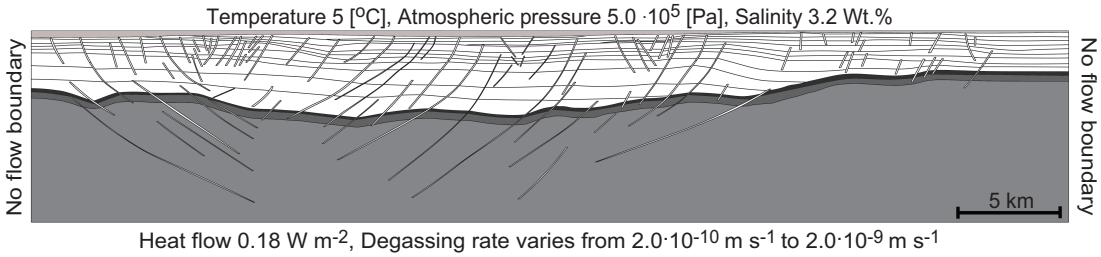

Figure 5.4: Model geometry, based on the interpretation of the seismic cross section by Gunnarsson (1998), and corresponding boundary conditions. - The model consists of the sea (light grey area), 13 sedimentary layers (white area) and the top-, middle-, and deep-basement (dark, middle and light grey areas, respectively). A total of 86 faults that have been identified in the seismic profile Rögnvaldasson et al. (1998) are divided into shallow- and deep-faults which range in width from 120 m (shallow structural levels) to 20 m at depth. The left and right boundary are no flow boundaries. The top boundary is characterised by constant values of temperature, pressure and salinity as shown. The bottom boundary accounts for a constant heat flow of 0.18 W m $^{-2}$ and a variable mantle degassing rate which ranges from 2.0×10^{-10} m s $^{-1}$ to 5.4×10^{-9} m s $^{-1}$.

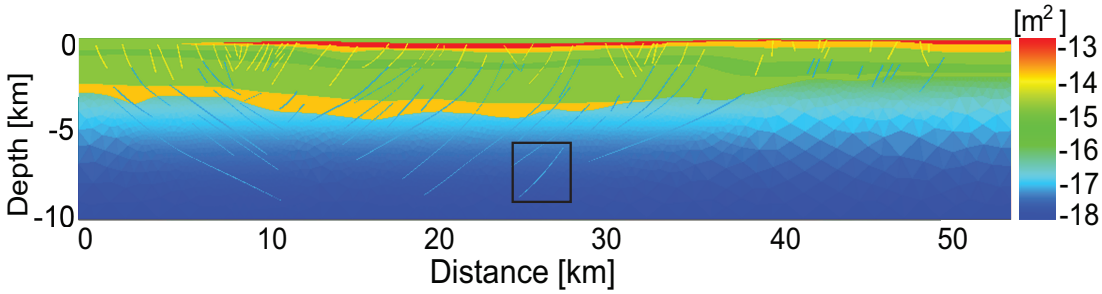

Figure 5.5: Permeability distribution of the Tjörnes Fracture Zone during the inter- and pre-seismic state. - The permeability of the deep faults and basement varies with depth according to the relation $\log(k) = \log(k_0) - 3.2 \cdot z$ (Manning and Ingebritsen, 1999). $\log(k_0)$ is the permeability at 1 km depth and z denotes the depth in kilometer (see Table 6.1 for values of $\log k_0$). The inset shows the location of the fault presented in Figure 5.12.

5.3 Model description

5.3.1 Geometrical modelling

Our geological model is based on the interpretation of a seismic profile of the TFZ (Gunnarsson, 1998) (Figure 5.4). It has been extended up to 10 km depth in order to include the likely position of the brittle-ductile transition. The model reproduces 13 sedimentary layers, 86 faults (shallow and deep) and the basement (separated into top, middle and deep) (Lupi et al., 2010). The faults are reproduced as high aspect ratio structures with widths varying from 20 m to 120 m and up to 500 m for large damaged areas. Geological unconformities, lens-shape sedimentary layers and layering off-set due to faulting are also reproduced. A CAD geometry was built (Paluszny et al., 2007) and discretised into approximately 50,000 adaptively refined triangular finite elements using the commercial software ANSYS ICEM^{TM}.

5.3.2 Conceptual model

The toggle switch mechanism (Miller and Nur, 2000) has been applied to the TFZ. The simulations involve two steps which are summarised in Table 5.1. The first simulation step models the pre-seismic state and starts with a representative pore pressure, temperature and salinity distribution (hereafter referred to as P-T-X-distribution) for the TFZ (Lupi et al., 2010). The P-T-X-distribution was obtained by simulating the regional fluid flow in the TFZ for a time window of $\sim$ 1 Ma. Seismic data show the occurrence of elevated pore pressures at depth caused by volatiles leaving the brittle-ductile boundary and migrating upwards (Stefansson et al., 2008). To reproduce this process, different fluid fluxes at the bottom boundary have been applied (ranging from 2.0×10^{-10} m s^{-1} to 5.4×10^{-9} m s^{-1}) to cause an enhancement of the upward fluid flow through the basement. Fluids migrate upwards in the crust and through the faults. This causes an increase in pore pressures inside the faults and in the deep parts of the crust. The results of this first step, the pre-seismic state, provide the initial pore pressure distribution in the TFZ and form the basis for the second simulation step that models the co- and post-seismic state. In this second step it is considered only a basal fluid flux rate of 5.4×10^{-9} m s^{-1}, as discussed further below. It is now assumed that a seismic event such the 5.8 M_w event in 2002 (Claesson et al., 2004, 2007) unlocks a fault (Miller et al., 2004). As consequence, the permeability of the faults is allowed to vary as

function of the evolving stress. This models the inflation of faults, which "unzips" them from bottom to top to release the elevated pore presure but not the dilatant slip of the fault itself. High permeability values are retained as long as the pore pressures remain elevated inside the faults. With time, when the fluid flux is reduced, the effective fault normal stress changes locally and the permeability of the faults returns to their original values as the faults deflate.

5.3.3 Mathematical Formulation

By combining the mass conservation equation for compressible fluids

$$\phi \frac{\partial \rho_f}{\partial t} = -\nabla \cdot (\mathbf{v_f} \rho_f) + Q \tag{5.1}$$

with the momentum conservation equation given by Darcy's law

$$\mathbf{v_f} = -\frac{k}{\mu_f}[\nabla P_f - \rho_f \mathbf{g}] \tag{5.2}$$

it is possible to derive the pressure diffusion equation for hydrothermal fluids (Geiger et al., 2006)

$$\rho_f \beta_t \frac{\partial P_f}{\partial t} = \nabla \cdot \left[\left(\frac{k}{\mu_f} \rho_f \right) \nabla P_f \right] - \nabla \cdot \left[\frac{k}{\mu_f} \rho_f^2 \mathbf{g} \right] + \rho_f \phi \left[\gamma_f \frac{\partial X}{\partial t} - \alpha_f \frac{\partial T}{\partial t} \right] + Q, \tag{5.3}$$

which is solved using an implicit finite element method. Here ϕ is the porosity (assumed to be constant), ρ_f the fluid density, $\mathbf{v_f}$ the Darcy velocity, k the permeability (assumed to be a scalar), μ_f the fluid viscosity, P_f the pore pressure and $\mathbf{g}$ the vector of gravitational acceleration. The source term Q in equation 5.1 and 5.3 represents the fluid flux rate at the basal boundary, X is the salinity and T the temperature of the hydrothermal fluids. β_f, α_f and γ_f are the compressibility, the thermal expansivity and the chemical expansivity, respectively. The system is treated as isothermal and isochemical and is considered $\frac{\partial T}{\partial t}$ and $\frac{\partial X}{\partial t}$ to be zero. ρ_f, μ_f as well as α, β and γ are computed from an equation of state for H_2O–NaCl fluids (Driesner and Heinrich, 2007; Driesner, 2007) during each time step.

5.3.4 Time scales and boundary conditions

The time window for each simulation step varies. The first set of simulations for the pre-seismic state are run for ~ 4.5 kyrs to ensure that the system reaches a steady-state pore

pressure distribution. In order to capture the fluid pressure build up adequately, time steps (Δt) of 1 yr are applied. The second simulation step considers much shorter time scales of tens of hours to a few years. This was necessary to resolve processes that act at very short time-scales, i.e. co-seismic fluid flow and post-seismic permeability decay. Simulations lasting for less than 24 hours are based on fixed time steps of minutes. Simulations lasting for more than 24 hours but less than two years use fixed time steps of hours, otherwise time steps of months are used. For each simulation the time step in multiple trial runs is reduced until a stable numerical result was obtained. This time step was then used in the subsequent simulations.

The model geometry and boundary conditions are shown in Figure 5.4. The right and the left model boundaries are no-flow boundaries while the top boundary is at sea-level. A fixed temperature of 5°C, a fixed pressure of 5.0×10^5 Pa and a fixed salinity of 3.2 Wt.% are assigned to the top boundary. The hydrostatic pressure acting on the sea-floor varies according to the depth of the sea which is given by the sea-floor topography.

5.3.4.1 Heat flow and fluid flux at the bottom boundary

A uniform basal heat flow of 0.18 W m^{-2} is used in both simulation steps. While the heat flow in the TFZ is relatively well constrained (Flóvenz, 2008; Flovenz and Saemundsson, 1993; Lupi et al., 2010), no direct measurements of the rates at which volatiles exsolve from the mantle (commonly referred to as "mantle degassing") and travel upwards across the brittle-ductile transition are available for the TFZ to the best of the knowledge. Because of the lack of knowledge of the exact mantle degassing rate, i.e. the volumetric flux of mantle-derived volatiles traveling upwards through the basement of the TFZ, basal fluid fluxes ranging between 2.0×10^{-10} m s^{-1} and 5.4×10^{-9} m s^{-1} are applied to analyse the effect of different mantle degassing rates. The upper value is slightly higher than the average surface degassing rate of 2.0×10^{-9} m s^{-1} measured in the South Iceland Seismic Zone (Fridriksson et al., 2006). The possible presence of partially molten basalts between 10 and 15 km depth around the Tjörnes peninsula (Stefansson et al., 2008), of volatiles in the hot spot material (Stefansson et al., 2008), and of shallow dikes (Hensch et al., 2007) may cause, at least locally, higher fluid fluxes, as they contribute additional volatiles.

5.3.5 Permeability modelling

5.3.5.1 Pre-seismic state

Geological Unit	$\log(k)$ [m^2]	$\log(k_0)$ [m^2]	$\log(\hat{k}_0)$ [m^2]	ϕ [-]	$\sigma^\star$ [MPa]	ρ_r [kg m^{-3}]
Shallow faults	-13.5	–	-10	0.22	10	2800
Deep faults	–	-13.7	-10	0.02	10	2800
Sedimentary basins	-13 to -16	–	-12.5	0.25 to 0.10	15	2600 to 2800
Basement	–	-14	-13.5	0.02	50	3000 to 3200

Table 5.2: $\log(k)$, $\log(k_0)$, ϕ, and ρ_r after Lupi et al. (2010), $\sigma^\star$ after Miller et al. (2004) (faults) and David et al. (1994) (basement and sediments). The tensile strength is 2 MPa, 10 MPa, and 90 MPa for sedimentary lithologies, faults, and basement, respectively.

For the pre-seismic state, the permeability values of Lupi et al. (2010) are used to characterise the hydrostratigraphy of the TFZ and the permeability distribution is shown in Figure 5.5. In general, sedimentary layers, shallow faults and the upper basement have constant permeabilities. The permeability of the sedimentary units decreases with depth, mimicking older and more compacted rocks. The damaged zone of the shallow faults is characterised by a permeability of 5.0×10^{-14} m^2. The time-averaged permeability of the deeper basement and of the deep faults is modelled by the relation $\log(k) = \log(k_0) - 3.2 \cdot z$ (Manning and Ingebritsen, 1999) where $\log(k_0)$ is the permeability at 1 km depth and z denotes the depth in kilometers. Manning and Ingebritsen (1999) used $\log(k_0) = -14$ m^2 for the continental crust. k_0 is varied depending on the lithology (Table 5.2).

5.3.5.2 Co- and post-seismic state

When the pore pressure inside the faults increase, the effective fault normal stress decreases locally and the fault inflates, i.e. its permeability increases. This effect has been modelled in the second simulation step by allowing the permeability of the faults to vary as a function of the effective fault normal stress σ'_n which is a function of the pore pressure P_f (Rice, 1992)

$$k = \hat{k_0} \exp \frac{-\sigma'_n(P_f)}{\sigma^\star}, \tag{5.4}$$

where $\hat{k_0}$ is the permeability at zero effective fault normal stress. Note that this model does not account strictly speaking for dilatant slip or hydraulic fracturing which occurs when the pore pressure exceeds the lithostatic load (Sibson, 1974, 1981) The characteristic stress $\sigma^\star$ (David et al., 1994; Rice, 1992) is a constant that expresses the degree of fracturing of a geological structure. $\sigma^\star$ is equal to the reciprocal of the pressure sensitivity coefficient and can be measured in laboratory experiments (David et al., 1994) or by fitting field data (Henry, 2000). Lower values of $\sigma^\star$ correspond to highly fractured rocks (Miller et al., 2004; Rice, 1992). The data of David et al. (1994) with $\sigma^\star = 50$ MPa have been used for the unfractured (picritic) basement and $\sigma^\star = 15$ MPa for the (unfractured) sediments. For the faults the same values as Miller et al. (2004), that is $\sigma^\star = 10$ MPa, have been used. The conceptual model of the permeability – pore pressure function expressed in equation 5.4 is shown in Figure 5.6 and the permeability – pore pressure functions used for the faults, basement, and sedimentary basin are shown in Figure 5.7. The effective fault normal stress is given by Ingebritsen et al. (2006)

$$\sigma_n' = \frac{\sigma_1 + \sigma_3 - 2P_f}{2} + \frac{\sigma_1 - \sigma_3}{2}\cos 2\theta, \tag{5.5}$$

where σ_1 and σ_3 are the largest and least principal stresses acting on the fault, respectively, and θ is the dip angle of the fault. The effect of the pore pressure is described in Figure 5.6. The complex tectonic state of the Tjörnes Fracture Zone is characterised by the interplay of transtensional and extensional stress regimes (Garcia et al., 2002; Gudmundsson, 1993; Saemundsson, 1974). The simulations consider an extensional regime where σ_1 is vertical, i.e. equal to the lithostatic load $\sigma_v = \rho_r g z$, where ρ_r is the rock density, g is the gravitational constant. The data presented account for an idealised extensional regime where $\sigma_3 = 0.7 \times \sigma_1$ (Jaeger et al., 2007) and $\theta = 40°$ (Jaeger et al., 2007; Zoback et al., 2003). σ_3 is oriented in the plane of Figure 5.4, i.e. the faults strike perpendicular to σ_n. Tests have been run also for a transform tectonic setting with σ_2 being vertical, $\sigma_1 = 1.1 \times \sigma_v$, $\sigma_3 = 0.625 \times \sigma_1$, and $\theta = 55°$ but no major impact on the results has been observed.

The pore fluid factor λ relates the pore pressure P_f to σ_v and the tensile strength τ (Sibson, 1974) as

$$\lambda = \frac{P_f}{\rho_r g z + \tau}, \tag{5.6}$$

which provides a simple measure as to how close the pore pressure is to lithostatic pressures. Rocks fracture hydraulically the latest if $\lambda \geq 1$ but probably, as in the

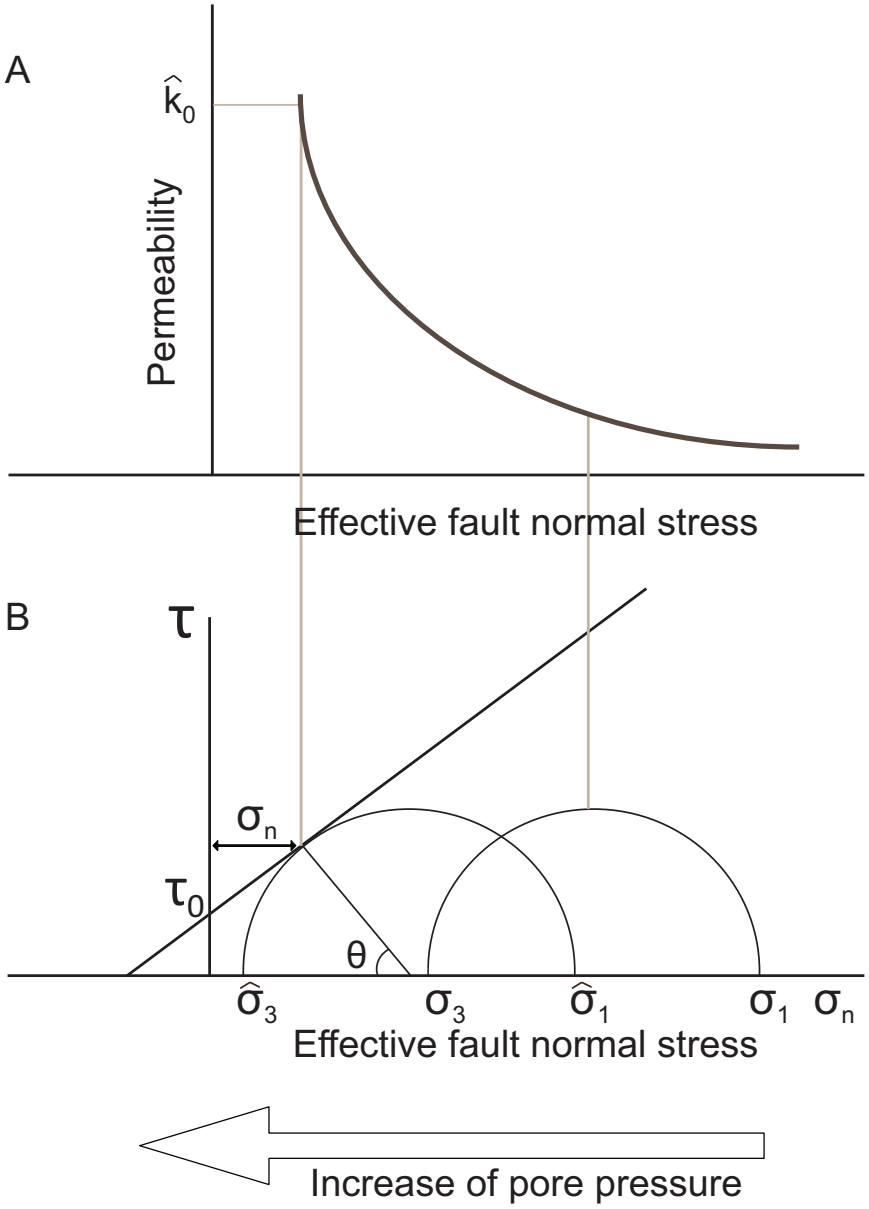

Figure 5.6: Conceptual cartoon of the Mohr circle. - a) Conceptual sketch showing the relation between permeability k and the effective fault normal stress σ'_n, which is a function of the pore pressure P_f, see Equations 5.4 and 5.5. θ is the dip angle and τ_0 is the shear stress when σ'_n is equal to zero. b) The Mohr circle shows how an increase in pore pressure reduces σ_1 and σ_3 to $\hat{\sigma_1}$ and $\hat{\sigma_3}$, respectively. This causes a decrease in effective fault normal stress and an exponential increase in permeability up to the maximum value $\hat{k_0}$ when the fracturing threshold is reached. Figure 5.7 shows the actual $k - \sigma'_n$ relation used in the simulations and models the fault inflation due to local changes in pore pressure.

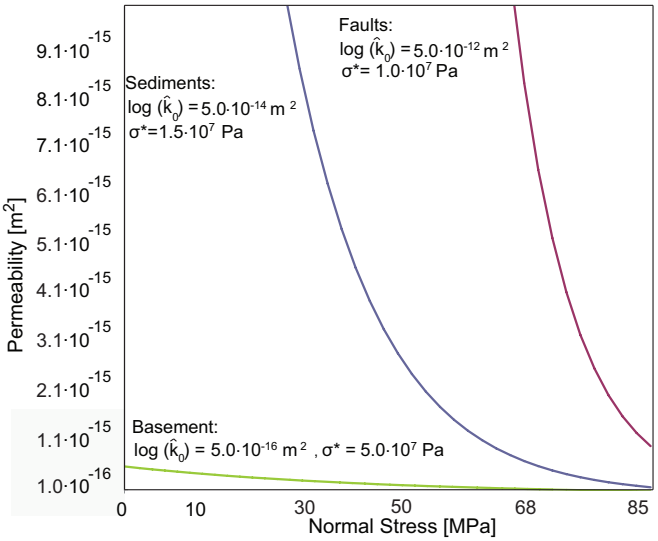

Figure 5.7: Permeability decay after (Rice, 1992). - The permeability decays as a function of increasing effective fault normal stress σ'_n for faults, sedimentary layers, and basement (Equation 5.4). The pore pressure ranges between hydrostatic and lithostatic at 8 km depth.

extensional regime considered here, at values of $\lambda < 1$. For example, Rojstaczer et al. (2008) propose that failure can occur if the ratio of pore pressure to hydrostatic pressure, that is $\lambda^\star = P_f/(\rho_f g z)$, is about 1.5. Since the exact value for $\lambda^\star$ where hydraulic fracturing can occur is difficult to establish, it is used $\lambda \geq 1$ as it represents the upper limit when this must occur. The resulting flow dynamics will not be affected by the choice of λ or $\lambda^\star$, which only serve to "label" the area where excess pressure occurs. The exact values for $\tau, \rho_f, \sigma^\star$ and $\hat{k_0}$ that have been used in the simulations are given in Table 5.2.

5.3.6 Key assumptions

Several assumptions and simplifications have been made to run the simulations at reasonable computational costs. It is assumed that all rock parameters (i.e. $k, k_0, \phi, \tau, \rho_r, \sigma^\star$ and $\hat{k_0}$) are constant in time during the pre-seismic state. Only the permeability is allowed to vary as a function of σ'_n, i.e. spatially and temporarily, during the co- and post-seismic states. This is incorrect for the porosity ϕ, which will also vary as rocks deform. However, this is still a reasonable assumption since, according to the cubic law (Snow, 1968), a change in fracture aperture, driven by the change in σ'_n, affects

the fluid fluxes cubically but porosity only linearly. Hence it is the orders of magnitude change in permeability k as a function of σ'_n, not the relatively moderate change in porosity ϕ, that will dominate the flow behaviour. This is also reflected in the exponential growth of permeability as a function of effective fault normal stress (Equation 5.4).

It has been assumed that the system is isothermal and isochemical over the short time period modelled because the pressure front travels much faster than the temperature front, which is retarded due to heat exchange between fluid and rock, while a change in salinity causes only a relatively small change in volumetric expansion, i.e. γ in Equation 5.3 is comparatively small (Geiger et al., 2005). In addition, earlier work demonstrated that salinity and temperature gradients in the vicinity of faults in the TFZ are probably small (Lupi et al., 2010) and hence will not cause major volume changes, which could affect the pore pressure, as fluids travel upwards during a seismic event.

The boundary conditions are assumed to be uniform and constant in time and space. In the simulations it is also consider the variation of heat flow and sea-floor morphology with time as negligible considering the short time window used in the simulations. The lack of lateral variations of heat flow and mantle degassing rate across the lower boundary are rather notable simplifications. Changes in the mantle degassing rate, or more generally vertical fluid flux, are likely to occur locally for example due to the intrusion of a dike at depth (Hensch et al., 2007). In addition the simulations do not account for fault/fracture sealing due to precipitation of mineral phases which may increase the rate at which the permeability decays (e.g. Claesson et al. (2007)). An important simplification comes from the use of a 2D cross section. By doing this, the complex three-dimensional stress acting on the faults has been oversimplified. It probably varies locally between compressional, extensional, transpressional, and transtensional regime, particularly in a complex tectonic setting like the TFZ which underwent changes in tectonic regimes over time (Garcia et al., 2002; Saemundsson, 1974). Hence the model only simulates the extensional regime and has been tested for a transform regime obtaining no significant differences. It is also not possible to simulate multiple seismic events occurring in the fault planes (e.g. seismic swarms) in the 2D simulations.

5.4 Results

5.4.1 Pre-seismic state

Figure 5.8 shows the pore pressure build up at 10 km depth where the permeability of the basement is $\sim 2.0 \times 10^{-17}$ m^2. While the maximum values of the pore pressure are a function of the mantle degassing rate and permeability, the time required to obtain a steady state pore pressure distribution does not vary. Maximum pore pressures are reached after approximately 700 yrs and results in values for λ of 0.55 for a mantle degassing rate of 2.0×10^{-9} m s^{-1} to λ 1 for a mantle degassing rate of 5.4×10^{-9} m s^{-1}. Figure 5.9 shows the increase of pore pressure along two different horizontal

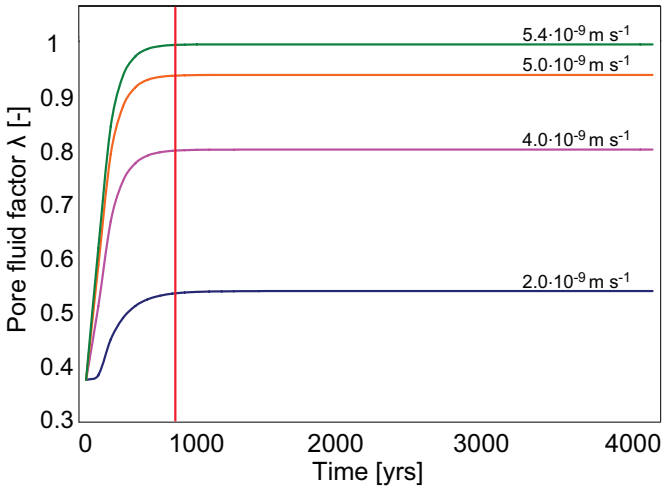

Figure 5.8: Build-up of the pore fluid factor. - Build-up of pore fluid factor $\lambda = P_f/(\sigma_v + \tau)$ at 9.9 km depth for different mantle degassing rates. The vertical line represents the time after which the pore pressure does not change any longer.

profiles at 8.8 km and 9.9 km depth, respectively, depth as a function of time. The build-up is characterised by a fast increase during the first 300 years, followed by a slower increase lasting for another 400 years, after which the maximum pore pressure is reached. Figure 5.9a shows that the pore pressure at 8.8 km exhibits three prominent peaks. These peaks represent the pore pressure inside faults and indicate that λ is close to 1. Additional simulations where the tensile strength of the faults has been varied from 2 MPa to 10 MPa yield similar results. This indicates that the permeability contrast between faults and host rocks, not tensile strength, controls the increase of pore pressure and its local distribution. Figure 5.9b shows that pore pressure variations

at 9.9 km depth are only minor. These smooth horizontal variations are related to the original pore pressure distribution. Due to the convective nature of the regional fluid flow in the TFZ, zones with higher hydrostatic pressures occur in areas where cold and dense fluids sink downwards (Figure 5.3). This causes the local and less prominent variations in pore pressure at larger depths.

The pore pressure distribution in the TFZ immediately before the co-seismic state, i.e. before the faults begin to inflate, is shown in Figure 5.10. Once the pore pressure reaches a steady state, it is possible to distinguish at least four main regions where elevated pore pressures occur. The deep crust shows high pore pressures ($\lambda \sim 0.85$), which gradually decrease towards the upper structural levels of the basement. At depth, the fluids are focused into the faults, causing values of λ close to 1 (i.e. critically high pore pressures) in the deeper parts of the faults (Figure 5.9a). Lower pore pressure values, with λ between 0.5 and 0.15, are present between 7.5 km depth and the top of the basement. The sedimentary basins are characterised by low pore pressures and λ between 0.3 and 0.5. The shallow crust, less than 1 km below the seafloor, has values of $\lambda \sim 0.15$. These values are well below the lithostatic pressure but they can reach up to 1.2 times the hydrostatic pressure. Hydraulic fracturing at shallow depths may occur if the pore pressure increases above 1.5 times the hydrostatic pressure (Rojstaczer et al., 2008). The results suggest that this is probably not the case for the shallow regions of the TFZ (Figure 5.11).

5.4.2 Co- and post-seismic state

Starting from the steady-state pore pressure distribution (Figure 5.10), the model now allows for the permeability to vary as a function of the effective fault normal stress (Equation 5.4) and simulate fault inflation during the toggle switch mechanism (Figure 5.2c). The resulting pore velocities, pore pressures and co- and post-seismic fault permeability evolution are presented here.

Figure 5.12 shows the pore pressure evolution along a 3.5 km long fault whose location is indicated by the inset black square in Figure 5.5. Horizontal profiles across the fault are presented for pore pressure (Figures 5.13 and 5.16), pore velocity (Figure 5.14) and permeability (Figure 5.15). The location of the profiles is indicated by the black line in Figure 5.12a (for Figures 5.14 and 5.15) and Figure 5.12f (for Figures 5.13

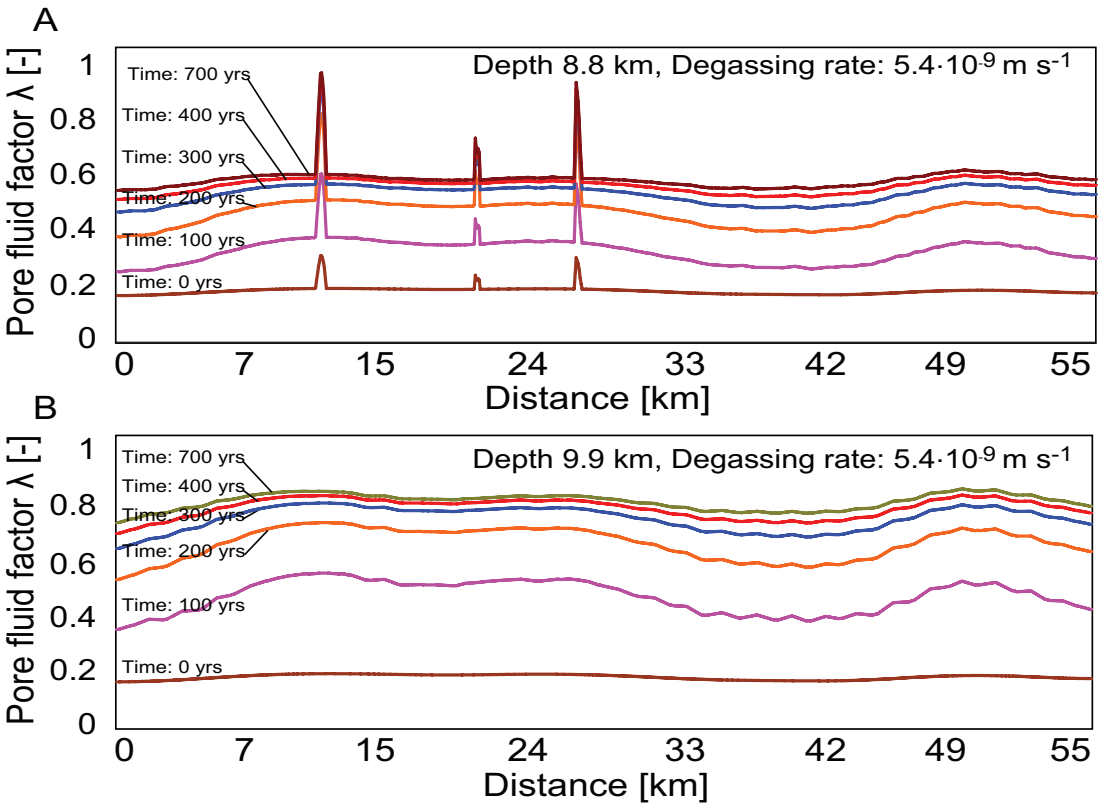

Figure 5.9: Pore fluid factor λ distribution along a horizontal profile at 8.8 km depth a) and 9.9 km depth b) at different times. - A large pore pressure increase occurs within the first 300 years. Afterwards the build-up is slower. The peaks in a) represent three faults which reach 8.8 km depth. The faults have pore pressures close to lithostatic conditions, resulting in λ approximately 1. The variations in b) are caused by lateral variations in hydrostatic fluid pressure (Figure 5.3b).

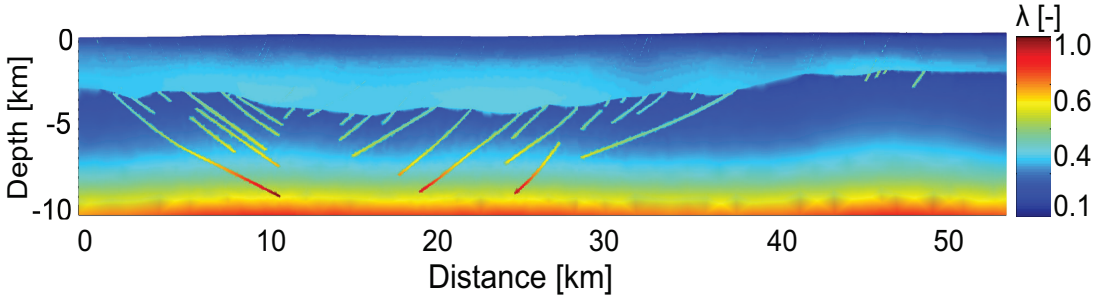

Figure 5.10: Pore fluid factor λ distribution before fault sudden faults permeability enhancements. - The permeability of the basement varies as $\log(k) = \log(k_0) - 3.2 \cdot z$, with $\log(k_0) = -14$ m^2 (Manning and Ingebritsen, 1999) and a basal fluid flux of $\sim 5.4{\times}10^{-9}$ m s^{-1}. The faults show higher pore pressures than the surrounding rocks, resulting in locally higher λ values.

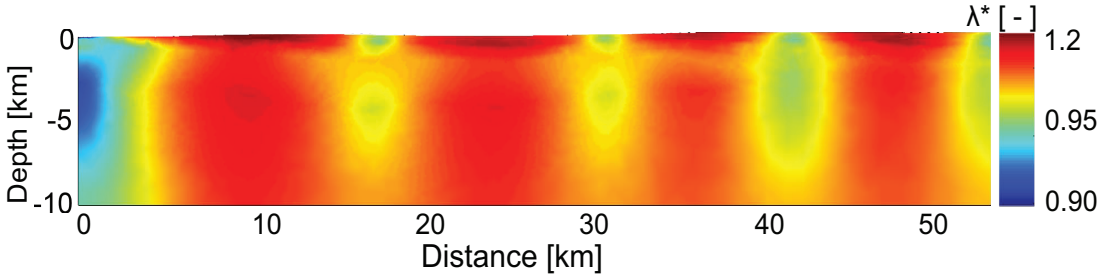

Figure 5.11: Distribution of the ratio of fluid pressure to hydrostatic pressure $\lambda^\star$, with $\lambda^\star = P_f/\rho_f g z$. - If $\lambda^\star$ is greater than 1.5 hydrofracturing may already be possible (Rojstaczer et al., 2008). The basal fluid flux and permeability model is identical to Figure 5.10.

and 5.16), respectively. These lines are not to scale and only indicate the location across the fault. However their correct length is shown in the corresponding figures.

Figure 5.12 shows how a fault inflates and unzip itself to release excess pore pressure. This occurs in the deeper part of the fault where λ is approximately 1 (Figure 5.12a). Pore pressure dissipates and λ falls below 0.85 after one minute (Figure 5.12b). The pore pressures continues to decrease (Figures 5.12c, d) in the deeper parts of the fault but also begin to build up in the upper parts of the fault (Figure 5.12e) because excess fluid travels upwards in the fault and cannot be released quickly enough into the basement. After 6 hours, values of λ close to 1 are reached at the top of the fault (Figure 5.12f). The pore pressure build-up in this region is shown in Figure 5.13. It increases rapidly during the first hour, followed by a slower build-up until values of λ close to 1 are reached. The fault permeability is enhanced but elevated pore pressures are maintained because the fault is confined within the low permeability basement. This prevents the pore pressure from diffusing fast enough from the fault into the basement. It is assumed that the basement is mechanically stronger and hence maintains a low permeability for longer time. However, pressure diffusion between fault and basement is clearly visible in Figures 5.12e and 5.12f by the expansion of a green halo, which represent values of $\lambda \sim 0.5$, away from the fault. Co-seismic pore velocities (i.e. $\mathbf{v_f}/\phi$) are shown in Figure 5.14. The highest velocities (up to ~ 0.03 m s^{-1}) are observed within the first minute after fault inflation occurs and maintained for five minutes. Afterwards they rapidly decrease, reaching minimum values of ~ 0.004 m s^{-1} after one hour. The high pore velocities are associated with the sudden co-seismic change in fault permeability. Figure 5.15 shows how the initially low permeability of the fault and basement increases suddenly during the first minute of the co-seismic state. The pre-seismic permeability contrast between basement and fault is one order of magnitude. After the fault starts to inflate, the permeability increase up to almost seven orders of magnitude, from $\sim 3.0\times10^{-16}$ to $\sim 8.0\times10^{-10}$ m^2. During the post-seismic state, the permeability decreases with time towards pre-seismic values as the elevated pore pressures dissipates and the fault normal stress σ'_n increases. The rate of permeability decay is a function of $\sigma^\star$ and $\hat{k}_0$ (Figure 5.7) and hence the permeability of the fault decreases more rapidly than the permeability of the basement. After four months, the two geological units have permeabilities of approximately 1.1×10^{-14} m^2 (Figure 5.15). After approximately

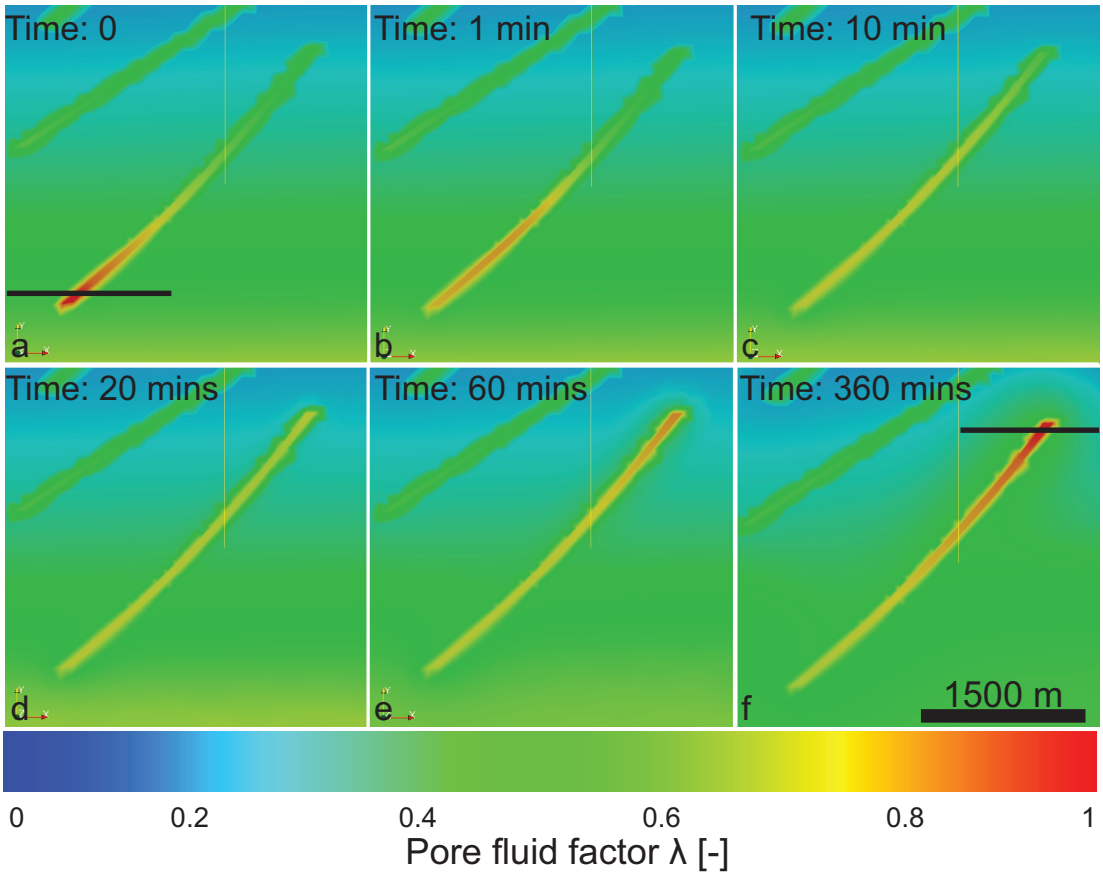

Figure 5.12: Co-seismic pore fluid factor evolution in the fault shown by the inset in Figure 5.5. - After permeability enhancement, the pore pressure within the fault decreases and move upwards where they accumulate at the top of the fault, resulting in the upwards migration of the maximum λ values. The horizontal line in Figure 5.12a shows the locations of Figures 5.14 and 5.15 while the line in Figure 5.12f shows the locations of Figures 5.13 and 5.16.

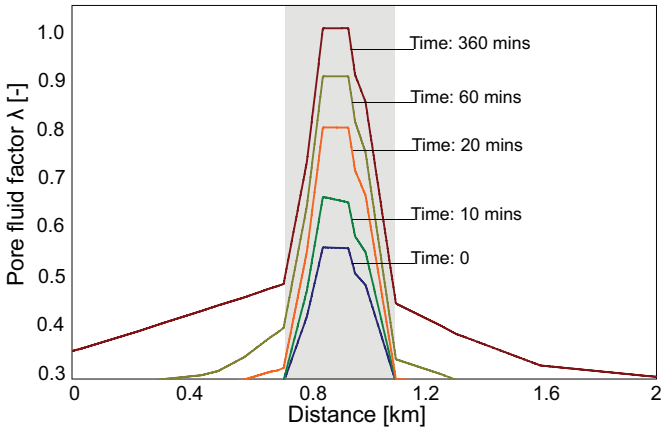

Figure 5.13: Build up of the pore fluid factor λ in the fault depicted in Figure 5.12f at 6.1 km depth. - The jagged lines are artifacts due to interpolating across the unstructured finite element grid. The gray-shaded area shows the variation of λ within the fault zone.

three years, the permeability of the fault is 2.0×10^{-15} m^2, which is close to the pre-seismic values. The difference between the pre- and post-seismic fault permeabilities can be attributed to external factors that will be discussed in the next section. If the basal fluid flux decreases and permeability enhancement does not occur, the TFZ can preserve elevated pore pressures for approximately less than four months (Figure 5.16). The reduction of the basal fluid flux can be due to several factors, for example a decrease in the volume of fluids rising from the brittle-ductile transition. Figure 5.16 shows the decay of the pore pressures as a function of time in the fault and basement when the high basal fluid flux is reduced.

During the first four months the decrease in pore pressure is much faster than during the following years and returns to background values after 10 years. Note the vastly different scales of $\sim$ 700 years for the pore pressure build up and $\sim$ 10 years for the pore pressure decay.

5.5 Discussions

Our simulations present new insights into the pre-, co- and post-seismic fluid flow dynamics in the TFZ connected to low-magnitude seismic events. Although the nature of the source for the high basal fluid flux, i.e. mantle-derived volatiles rising in the crust

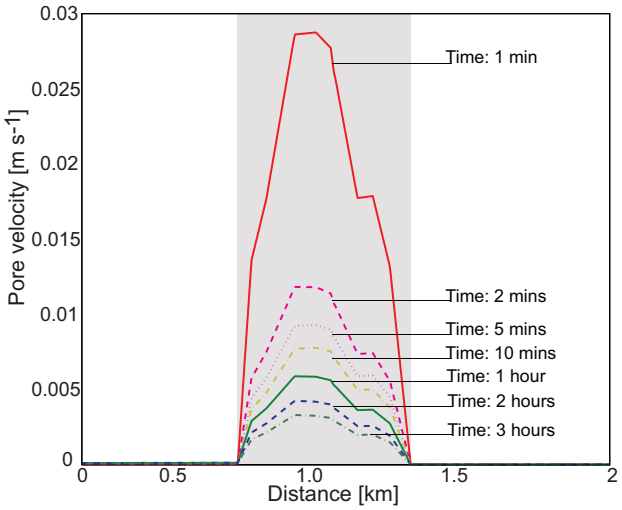

Figure 5.14: Co- and post-seismic velocity decrease in the fault depicted in Figure 5.12a at 9 km depth. - The jagged lines are artifacts due to interpolating across the unstructured finite element grid. The gray-shaded area shows the velocity variation within the fault zone.

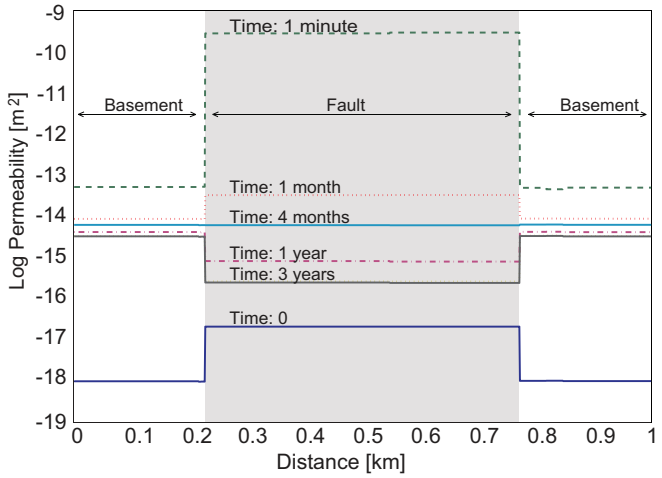

Figure 5.15: Permeability evolution in the fault and basement depicted in Figure 5.12a at 9 km depth. - The straight lines are due to a limited number of finite elements across the fault. The gray-shaded area shows the permeability variation within the fault zone.

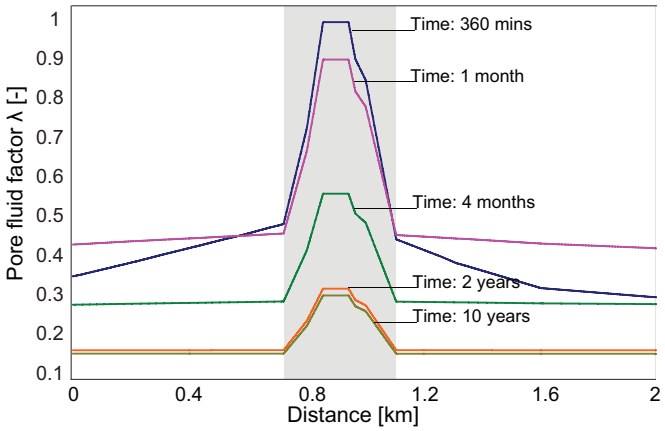

Figure 5.16: Post-seismic reduction in pore fluid factor λ in the basement and fault depicted in Figure 5.12f at 6.1 km depth. - The jagged lines are artifacts due to interpolating across the unstructured finite element grid. The permeability of the faults decreases more rapidly than the permeability of the basement due to different $\hat{k}_0$ and $\sigma^\star$ values. The gray-shaded area shows the variation of λ within the fault zone.

(Stefansson et al., 2008) or dike intrusions at depth (Hensch et al., 2007), is subject to speculation, the simulations indicate that the TFZ is characterised by a critically pressured deep crust where the faults have pore pressures close to lithostatic pressure. This lends support to the observations made by Crampin et al. (2002), who proposed elevated pore pressures in the Húsavik Flatey Fault.

Since the exact permeability distribution and basal fluid fluxes, including mantle degassing rates, for the TFZ are unknown, a large number of permeability-fluid flux combinations could cause similar pore pressure distributions in the TFZ. While a detailed parametric study is beyond the scope of this study and only scape was to analyse the principal mechanisms occurring during seismicity-induced fluid flow using a geologically reasonable model and parameter distribution, some further insight can be gained by rewriting the pressure diffusion equation (Equation 5.3) as

$$\frac{\partial P_f^\star}{\partial t} = \eta \nabla^2 P_f^\star + \Gamma, \tag{5.7}$$

where η is the hydraulic diffusivity defined as $\eta = k/\mu_f \beta_f$ and Γ is the source term. Note that $P_f^\star$ indicates that is only considered a reduced driving pressure, i.e. the hydrostatic fluid pressure component it has been excluded such that the equation expresses only the rate at which the driving fluid pressure propagates through the crust. Since μ_f and β_f

depend only weakly on pressure and the model assumes that temperature and salinity do not change with time, the permeability k and the mantle degassing rate Γ (or q in Equation 5.3) have the biggest impact on the rate at which fluid pressure increases and its subsequent distribution. Assuming a constant permeability, which is the case in the first part of the simulations, the characteristic distance of the pressure front is proportional to $2\sqrt{\eta t}$. Hence the time at which a steady state pore pressure is reached is the same for different basal fluid flux and constant permeabilities, i.e. constant η (Figure 5.8). However, for constant fluid flux and varying η, lower permeabilities would lead to a fast and probably more local increase in pore pressure while higher permeabilities would have the opposite effect. Hence certain combinations of low permeability and low fluid flux or high permeabilities and high fluid flux should provide pore pressure distributions similar to the ones presented here (Figure 5.10) but at different time scales. For example, using $\log(k_0) = -16$ m^2 in the depth dependent permeability model for the basement and a fluid flux of 2.0×10^{-10} m s^{-1} also causes a basement with elevated pore pressures and faults with pore pressures similar to what it has been modelled before (Figure 5.17) but it takes 5.5 kyrs for the pore pressures to build up. While the pore pressure distribution at 9.5 km depth is similar in Figure 5.10 and 5.17, the pore pressure distribution in the shallow regions differs strongly. The four regions characterised by elevated pore pressures described above are no longer present and the crust is characterised by elevated pore pressures only at depth. Low pore pressures occur in the TFZ where λ varies from 0.15 to 0.3 between 7.5 km depth and the sea-floor.

Since the permeability distribution in the TFZ is not well constrained and there are no direct surface degassing measurements for the TFZ, both pore pressure distributions are equally possible. However, geophysical observations in the TFZ help to judge which scenario is more likely. In the TFZ most of the shallow and deep fluid-induced seismic events are separated by an aseismic region at intermediate depth. The vertical extent of this area is at least 3 km but could be as large as 10 km (Hensch et al., 2007). Figure 5.10, but not Figure 5.17, shows the presence of a low over-pressured region that occurs between 4 and 8 km depth, i.e. between the top of the basement and 7.5 km depth. It is hence preferred a model with a slightly higher basal fluid flux of 5.4×10^{-9} m s^{-1}, representing the mantle degassing rate, and a permeability decay of $\log(k) = -14 - 3.2 \cdot z$ in the deeper basement because this specific distribution of pore pressures can explain the presence of the aseismic region discovered by Hensch et al.

(2007). There is some uncertainty in the results as the extensional regime in the TFZ

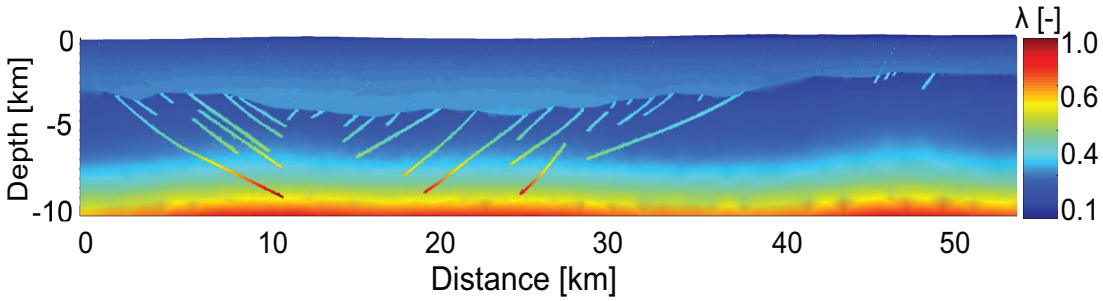

Figure 5.17: Pore fluid factor distribution for a low permeability basement. - The basement characterised by a permeability that vary as $\log(k) = \log(k_0) - 3.2 \cdot z$, with $\log(k_0) = -16$ m^2 and a low basal fluid flux of $\sim 2.0{\times}10^{-10}$ m s^{-1}. Note that the four distinct regions where elevated pore pressured prevail (see Figure 5.10) are no longer present.

has changed partly to a transtentional regime and vice versa during geological history (Garcia et al., 2002; Saemundsson, 1974). The 2D simulations also do not account for the complex stress field in 3D faults. Hence additional simulations have been carried out for a transform setting but a significant difference has not been observed (Figure 5.18[1]) This is probably because the difference in permeability at a given pore pressure

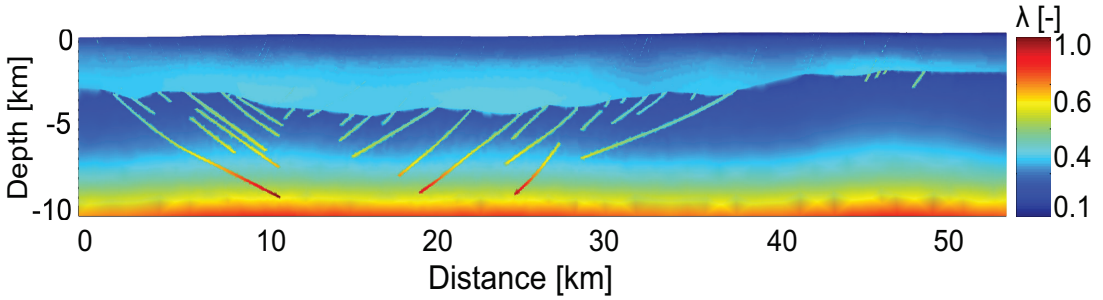

Figure 5.18: Pore fluid factor λ distribution before fault inflation for a transform regime. - The pore fluid factor λ distribution is similar to the one obtained for an extensional regime.

(Equations 5.4 and 5.5) does not vary greatly, that is usually less than 20 %, as σ'_n approaches zero in an extensional and transform regime. For this it is suggested that a change in permeability of at least an order-of-magnitude is required as σ'_n approaches

[1] This figure is not part of the submitted material

zero to observe a significant change in the flow system.

A pertinent feature emerging from the simulations is that deeper faults have comparatively high pore pressures causing λ to vary between 0.6 and 1 because they focus fluid flow at depth (Stefansson et al., 2008). Upwards fluid migration in the faults of the TFZ can lead to intense microseismicity (Riedel et al., 2001; Stefansson et al., 2008). The simulations offer a consistent explanation for this phenomenon (Figure 5.12): when faults inflate, pulses of over-pressured fluids move upwards in the fault enhancing its permeability. While the model does not reproduce the continuous microseismicity that occurs in the Grimsey Lineament and in the Húsavik Flatey Fault due to the orientation of the seismic profile, it still demonstrates how faults can focus pore pressure (Figure 5.10) and how pore pressures can diffuse from the faults into the basement, thereby creating small seismic events (Figure 5.12e – f). An important prerequisite for this mechanism to occur is a relatively constant rate at which volatiles are exsolved from the mantle as well as relatively low permeabilities in the basement and faults. If such a mantle degassing process were to stop at all in the TFZ, the pore pressures would dissipate in less than 10 years and it may take hundreds of years to build-up sufficient pore pressures again. Yet, earthquakes and seismic-induced fluid flow occur on much shorter time-scales in the TFZ (Claesson et al., 2007). It is hence suggested that regional and moderate mantle degassing rates of $\sim 3.0\times10^{-9}$ m s^{-1}, consistent with observed surface degassing rates in South Iceland (Fridriksson et al., 2006), maintain elevated pore pressures throughout the TFZ and keep the crust weak. Local changes in mantle degassing rate, for example due to dike intrusions (Hensch et al., 2007) or pockets of high-pressure fluids which move from one fault to another across low-permeability basement, a process also observed in the geological record of the TFZ (Gudmundsson, 1999), can cause the pore pressure to increase locally, leading to fault inflation or dilatant slip. An important point is that the permeability increase and decay occurs over very short time-scales, that is between minutes and a few years. This demonstrates how rapidly fault-controlled permeability of seismically active hydrothermal tectonic setting, like the TFZ, is regenerated due to the presence of fluid flow (Cox, 2010).

Mineral precipitation may play an important role to seal faults and reduce permeability. Claesson et al. (2007) have suggested that faults may seal within two years based on monitoring of variations in geothermal fluid geochemistry at Húsavik through a seismic cycle. The simulations show that the cycle of permeability increase and decay

can be completed in approximately this time frame and a decrease in effective fault normal stress, due to a dissipation of pore pressures, is sufficient to reduce the fault permeability close to original (low) values. However, as long as an increased mantle degassing rate is present, fault permeabilities will remain elevated to accommodate the extra flow and prevent significant pore pressure build-up. Hence mineral precipitation is probably critical to seal faults, at least in the TFZ, to complete the toggle switch mechanism cycle and allow for enough pore pressure to be generated such that pore pressure build-up can occur again in a few years. The permeability enhancement of faults is also thought to play an important role during the post-seismic mixing of shallow and deep fluids (Claesson et al., 2004). While the model explains the observed post-seismic mixing which leads to distinct changes in hydrogeochemistry (Claesson et al., 2004) by rapid upward migration of fluids within faults and possibly from fault to fault at rates of up to 0.03 m s^{-1}, it cannot readily explain the observed hydrogeochemical variations immediately before a seismic event. However, faults are characterised in the pre-seismic state by higher pore pressures than the surrounding rocks (Figure 5.10). In this situation, hydrofracture dilatancy can re-open and align fractures in the damaged areas of the faults (Sibson, 1981). This can allow shallow and deep fluids to mix during the pre-seismic state although at significantly slower rates compared to immediate co-seismic mixing. The post-seismic rates at which fluids migrate upwards in the faults, i.e the pore velocities, reach up to 0.03 m s^{-1}.

For the assumed basement and fault porosities of 2 %, the simulated pore velocities explain the co-seismic velocities observed by Hensch et al. (2007) for the TFZ well. Similar fluid velocities have also been modelled by Miller et al. (2004) for the 1997 seismic sequence in Italy, which was caused by the escape of deep fluids from an over-pressured reservoir but occurred in a different tectonic setting. Geological evidence (Okamoto and Tsuchiya, 2009) further suggests that such short-lived extreme velocity events may be the rule rather than the exception in hydrothermal systems. This includes continental hydrothermal systems as well. For example, Cathles and Shannon (2007) have shown that large hydrothermal ore deposits may be formed in tens to hundred of years due to short-lived extreme flow events and local permeability enhancement due to elevated pore pressures may be the key for economically viable deposits (Cox and Ruming, 2004).

6

Syn-eruptive groundwater flow model of the 1875 Askja volcano eruption

6.1 Introduction

The 28^{th} - 29^{th} of March 1875 rhyodacite eruption of the Askja volcano is unique. Firstly because it is the only phreatoplinian eruption documented with eye-witness accounts, and secondly because this eruption comprises three distinct shifts in eruptive activity. The former, together with detailed volcanological macro- and microscopic observations by Carey et al. (2008, 2009b), resolved the timing and nature of the shifts of eruptive style. This event is marked by a shift of the eruptive style which evolved from subplinian (dry) to phreatoplinian (wet), followed by the emplacement of pyroclastic density currents (drying out) and finally into Plinian (dry) activity (Carey et al., 2009a; Sparks and Sigurdsson, 1987). The dry-wet-dry shift makes the Askja 1875 eruption one of the very few events that showed both phreatoplinian and Plinian eruptive styles (Carey et al., 2009a,b; Smith and Houghton, 1995). The source of the water involved in the phreatomagmatic activity is not apparent. Eyewitness records state that except from a small pond, no standing water was present within the caldera prior to this event (Anonymous, 1875).

Geological and climatic factors affect the position of a groundwater aquifer whose location can dramatically vary among different geological environments. Several stud-

ies investigated and constrained the size and the position of water tables in volcanic systems (Di Napoli et al., 2009; Hurwitz et al., 2003; Ingebritsen and Scholl, 1993; Join et al., 2005; Violette et al., 1997). These studies reinforced the concept that localised groundwater systems, decoupled from the regional groundwater systems, exists within the top part of the volcanic edifices. This is the case of many volcanoes (i.e. Irazu, El Chichon, and Chiginagak volcano) that are characterised by summit crater lakes. In other instances, such as Kilauea on the island of Hawaii (Hurwitz et al., 2002; Keller, 1979), the aquifer occurs at greater depths and it is part of the regional groundwater system. At the Askja volcano the groundwater table is very shallow and the 28–29 March 1875 Askja eruption is an example of the interaction between the magma and a shallow groundwater aquifer.

The 28-29 March 1875 Askja eruption is also one of the few instances of a shift from wet to dry activity (e.g. Houghton et al. (2000)). For example, Smith and Houghton (1995) demonstrated how vent migration led to the change of the eruptive style during the eruption of the Taupo volcano, New Zealand $\sim$ 1800 B.P. (New Zealand). Two ash deposits of the same eruption show evidences of continuous interaction between water and magma (Walker, 1981). Phreatomagmatism is also a feature of the activity at Stromboli volcano, Italy, where explosive seawater-magma interaction took place after a lateral collapse of the volcanic edifice (Bertagnini and Landi, 1996; Giordano et al., 2008). Groundwater and hydrothermal systems are linked to magmatic dynamics as shown by oscillations in hydrothermal systems during unrest at caldera volcanoes (Gottsmann et al., 2007; Todesco, 2008). This underlines that coupled studies of magma migration, edifice deformation, and groundwater flow are important for hazard and risk assessments (Join et al., 2005; Sparks, 2003).

In this study CSMP++ (Matthai et al., 2007), a finite-elements finite-volumes simulator, is used to examine the syn-eruptive groundwater flow dynamics within the Askja caldera during the 28–29 March 1875 eruption. A high-resolution 3D model of the groundwater flow within the Askja caldera has been developed for this study. It is underpinned by information obtained from contemporary accounts, field measurements and their subsequent upscaling to obtain the effective permeabilities for a three-dimensional representation of lava cooling joint patterns. This information is used to calibrate the Askja groundwater flow model and add constraints to the timing of the simulations.

One challenge in modelling groundwater flow in volcanic environments is that permeability-porosity studies are focused on granular lithologies such as sandstones and only few concern porosity and permeability relations in volcanic rocks (Ingebritsen and Scholl, 1993; Saar and Manga, 1999; Sruoga et al., 2004; Stearns, 1942). Average permeabilities of unfractured lava flows are in the range of 1.0×10^{-14} m^2 and 1.0×10^{-11} m^2, and porosities range from 0.05% to 50% (Saar and Manga, 1999). These data are not directly applicable to the lava flows that fill the Askja caldera because they are not a good representation of the bulk permeability and porosity of a fractured lava pile. The permeability of the lava pile is greatly enhanced by open cooling-induced fractures (i.e. joints) and flow unit boundaries, which can be fracture-like or comprise highly porous rubble horizons in case of aa lavas. Using the fracture patterns mapped in the field, numerical discrete fracture and matrix techniques (Matthai et al., 2004) have been applied to estimate the effective permeability of the lava pile to populate the Askja caldera groundwater flow model with representative values.

6.1.1 Scope and structure of the chapter

The scope of this chapter is to examine whether the external water involved in the phreatoplinian C-phase of the 28 – 29 March eruption was supplied by the permeable lava pile within the Askja caldera. In particular it is investigated i) the groundwater dynamics around the C-phase vent and its possible temporal influence on the intra-caldera groundwater system and ii) the mechanisms that led to the drying out of the phreatomagmatic phase.

This work is structured according to the workflow followed during the development of the model: firstly the geological description of the Askja caldera and the specific features of the 28-29 March 1875 Askja eruption are presented. They are followed by a description of the methodologies used to estimate the lava flow permeabilities. Next, it is discussed the Askja caldera groundwater flow model and possible fluid flow scenarios are described. Finally it is shown how the syn-eruptive groundwater dynamics had significant effects on the eruptive style of the 28–29 March 1875 Askja eruption.

6.2 Geological context

The geology of Iceland is dominated by the interplay of the Icelandic hot spot and the mid Atlantic ridge (Allen et al., 2002; Bjarnason, 2008; Darbyshire et al., 1998). The regional plate tectonics control the geologic and geographic position of the Icelandic volcanic zones. The Askja volcano is located in the Northern Volcanic Zone and it is the central volcano of a larger complex referred to as the Askja volcanic system (Sigvaldason, 2002). The summit of the volcano rises approximately 800 m above the surrounding areas (Figure 6.1).

The Askja volcano has been visited irregularly by geologists since 1876, and these short visits have gradually increased the fragmentary knowledge of the volcano (Johnstrup, 1877; Jonsson, 1941; Spethmann, 1913; Thoroddsen, 1884, 1925; Van Bemmelen and Rutten, 1955). More recently, insights have been gained on the lithologies and eruptive dynamics that occurred in the area (Einarsson, 1962; Rymer and Tryggvason, 1993; Sigvaldason, 1979; Sparks et al., 1981; Sparks and Sigurdsson, 1987; Thorarinsson and Sigvaldason, 1962): these will be discussed in the following.

The Askja volcanic edifice was largely constructed from sub-glacial activity and produced a succession comprised of a range of hyaloclastic lithologies and inter dispersed pillow lavas that today circumscribes the Holocene Askja caldera (Sigvaldason, 2002). This subglacial succession is characterized by very low bulk permeabilities (Figure 6.1). Two out of the three nested calderas featured by the Askja volcano can be clearly identified in Figure 6.1. The Askja caldera (approximately 45 km^2) is filled with Holocene lava flows. The lava flows that formed in the last 1100 years are exposed on the current floor of the Askja caldera and along the rim of Öskjuvatn caldera. The majority of the historical lavas that predate the 1874–1930 volcano-tectonic period were produced by vents located on the Western side of the caldera. Therefore it is reasonable to assume that the shallow part of the lava pile (i.e. the first 100 m) consist of by pristine lavas (Brown et al., 1991; Rymer and Tryggvason, 1993). These shallow lava flows crop out along the margins of the Öskjuvatn caldera which nowadays contains a lake (Figure 6.1 and 6.3). The Öskjuvatn caldera formed as a consequence of the 1875 Askja activity.

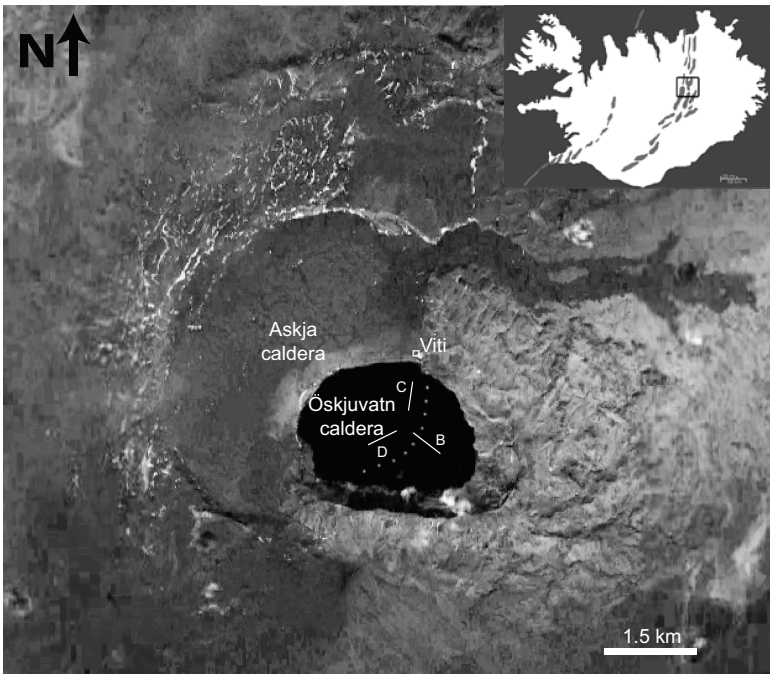

Figure 6.1: Aerial view of the Askja volcanic complex. - The main circular area is the Askja caldera. The dotted line which cuts the Öskjuvatn caldera represents the pre-eruptive margin of the Askja caldera. The white lines show the location of the fissural vents of the eruptive phases B, C and D (Carey et al., 2009a). The map of Iceland in the inset shows the mid Atlantic ridge (in grey) and the location of the Askja volcanic complex (black square). A closer view of the Öskjuvatn caldera is shown in Figure 6.3.

6.2.1 Holocenic eruptive history

During the Holocene, at least three violent main eruptions occurred at the Askja volcanic system: the March 1875 eruption, an earlier silicic event which is not well constrained temporally and volumetrically (Carey, 2008; Carey et al., 2009a), and a silicic explosive eruption around 2000 years BP (Larsen and Eiríksson, 2008). The 1875 eruption is part of the 1874 to 1876 volcano-tectonic rifting events which were associated with earthquakes and fissure eruptions up to 40 km away from the Askja volcanic system (Brandsdottir, 1992; Sigurdsson and Sparks, 1978; Sigvaldason, 2002). Precursor activity prior to the 1875 eruption featured phreatic eruptions, small silicic and basaltic phreatomagmatic eruptions, felsic effusive eruptions and possibly mafic effusive eruptions (Carey et al., 2008; Sigvaldason, 2002; Sparks et al., 1981). The first attempt to constrain the magma discharge rates and the tephra volumes produced during the 1875 eruption was carried out by Thorarinsson and Sigvaldason (1962). Further studies (MacDonald et al., 1987; Sigurdsson and Sparks, 1978a; Sigvaldason, 1979, 1982) concentrated on the petrology of the eruptive products. Other eruptive events include the Askja Fires (1874 – 1875), which are considered an example of rifting episode with dike injections from a shallow magma chamber (Sigurdsson and Sparks, 1978a). Further eruptions were recorded in 1921-22, 1929, 1931 (Sigvaldason, 1979; Sparks et al., 1981) and in 1961, which was the last record of the production of both aa and pahoehoe lava flows, covering an area of 11 km^2 (Thorarinsson and Sigvaldason, 1962).

6.2.1.1 The 1875 Askja eruption

The explosive products of the main activity are divided into three units B, C and D and are schematically shown in Figure 6.2. Carey (2008) divided units B, C and D, into further sub-units. Unit B, is a well sorted poumiceous subplinian fall, represents the first phase of the main eruption which began on the 28^{th} of March 1875 at 9:00 pm and lasted for 1 hour (Carey et al., 2009a). The next eruptive phase (unit C) produced the deposits divided in the sub-units C1 and C2 (Carey et al., 2009a). The onset of the phreatoplinian activity (phase C1), according to the historical records, occurred approximately at 5:30 am on the 29^{th} of March and lasted for more than 1 hour. It produced a widespread, poorly sorted, and very fine ash fall deposit that reached Scandinavia (Carey et al., 2009a; Sparks et al., 1981). This eruptive phase was followed by the emplacement of

dilute density currents originated in the weak parts of the phreatoplinian plume (phase C2). Nevertheless, before the onset of the new explosive activity, dilute to dry density currents were emplaced inside the Askja caldera (Carey, 2008). Carey et al. (2009a) further distinguished three sub-units inside the C2 deposits (lower, middle and, upper C2). The deposits of the first density currents (lower C2) are ash-rich, characterised by lapilli-lenses, and poorly sorted. They lack the well-sorted fine to coarse pumice lenses which characterise the middle C2 deposits. The top C2 deposits show well defined bed-sets, high abundance of well-sorted pumice lenses, and contain rounded coarse lapilli. Around 7:00 am, the Plinian phase of the eruption commenced (phase D) and lasted for approximately 5 to 6 hours. The associated deposits consist in a widespread Plinian fall which has been divided into five sub-units (Carey et al., 2008). It is composed of welded and non-welded deposits, possibly produced by fountaining activity from vents that were active simultaneously with the main Plinian eruption (Carey et al., 2008). The eruption continued throughout the afternoon of the 29^{th} of March with diminishing intensity until 6:00 pm. The eruptive activity at the Askja caldera did not stop with the March 1875 main event: phreatic and basaltic activity continued until the end of 1876 (Sigvaldason, 1979; Sparks et al., 1981).

Deposit	CH	MDR	VDR	DRE	Volume	Time	Total mass
	km	kg s^{-1}	m^3 s^{-1}	km^3	km^3	hours	kg
Unit B	8*	2.6×10^6	3.9×10^3	0.004	0.014	1	9.4×10^9
Unit C	22.8$^\bullet$	6.8×10^7	1.2×10^5	0.104	0.45	1	4.8×10^{11}
Unit D	26	2.5×10^7	6.9×10^4	0.213	1.37	6	5.0×10^{11}
peak:		3.5×10^7	9.5×10^4			4	

Table 6.1: The abbreviations stand for: CH, column hight; MDR, mass discharge rate; VDR, volume discharge rate; DRE, density rock equivalent. * Carey and Sparks (1986). $^\bullet$ Pyle (1989).

6.3 Geology of the Askja caldera

The Askja caldera is bounded by steep, yellowish, fine-sand grained hyaloclastic rocks. These lithologies also crop out at the base of the Víti crater, an explosion crater on the North-East rim of the Öskjuvatn caldera (Figure 6.1). The caldera is filled with histor-

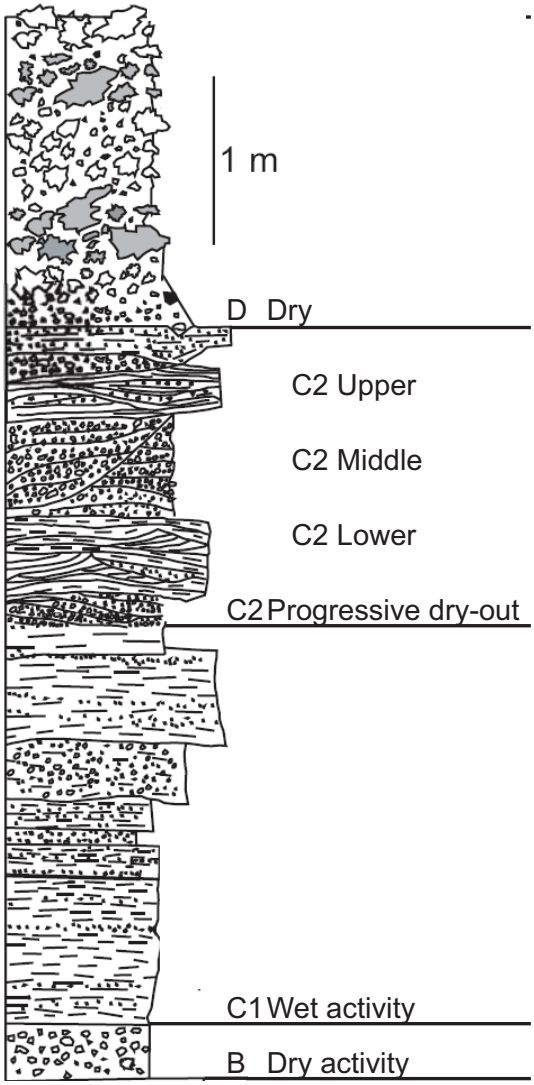

Figure 6.2: 1874-1876 explosive products observed within Askja caldera. Depositional sequence modified after Carey (2008) and Carey et al. (2009a) - Unit B is a widespread and well sorted poumiceous subplinian fall. Unit C1 is a widespread, poorly sorted, and very fine ash fall deposit produced by phreatoplinian activity. Unit C2 represents the products of dilute density currents they have bed-forms and grain size characteristics which are interpreted as a decreased role for the interaction of magma/water compared to the phreatoplinian phase. Unit D is a widespread Plinian fall made of both welded and non-welded deposits (Carey et al., 2008). Modified after Carey et al. (2009a).

ical and upper Holocene lava flows that are covered, in the areas close to the Öskjuvatn caldera, by the 1875 explosive deposits. Underneath the 1875 eruptive products, large cavities still containing the snow deposited prior to the 1875 eruption are also frequently encountered.

We surveyed more than 20 lava flows inside the Askja caldera and along the rim of the Öskjuvatn caldera (Figure 6.3). However, due to the steepness of the rims of the Öskuvatn caldera and the thickness of the lava flows (up to 12 m) the measurements are mostly confined to lavas in the lower part of the cliff face. Nevertheless, it is possible to distinguish two chemically different lava flows inside the Askja caldera: basaltic (Figure 6.4) and felsic (Figure 6.5) lava flows. The basaltic lava flows have a large aerial coverage, approximately 99% of the area, felsic lava flows cover the remaining 1%. The lavas crop out in well exposed vertical sections on the northern and western steep margins of the Öskjuvatn caldera. They appear as a stack of flows (Figure 6.6) where coherent lava-horizons are alternated with rubbly-clinkery horizons. Coherent lavas make up approximately 85% of the lava pile while fragmental horizons represent approximately 15% of the lava pile. Among the basaltic lava flows it has been

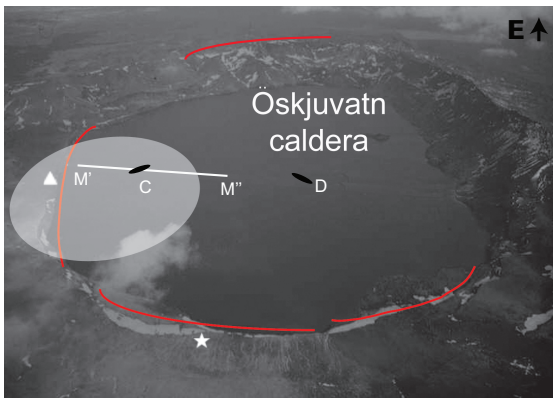

Figure 6.3: Aerial view of the Öskjuvatn caldera. - The triangle and the star indicate the location of the felsic lava flow and the representative basaltic lava flows, respectively. The red curves show the areas that have been surveyed in order to populate the Askja groundwater model with representative permeabilities. The white ellipsoidal surface indicates the estimated extension of the felsic lava flow. The profile M'–M" indicates the direction of the cross sections shown in Figure 6.11. Letters C and D indicate the position of the eruptive vents. See Figure 6.1 for scale.

possible to distinguish three morphotypes: pahoehoe, rubbly pahoehoe, and aa with

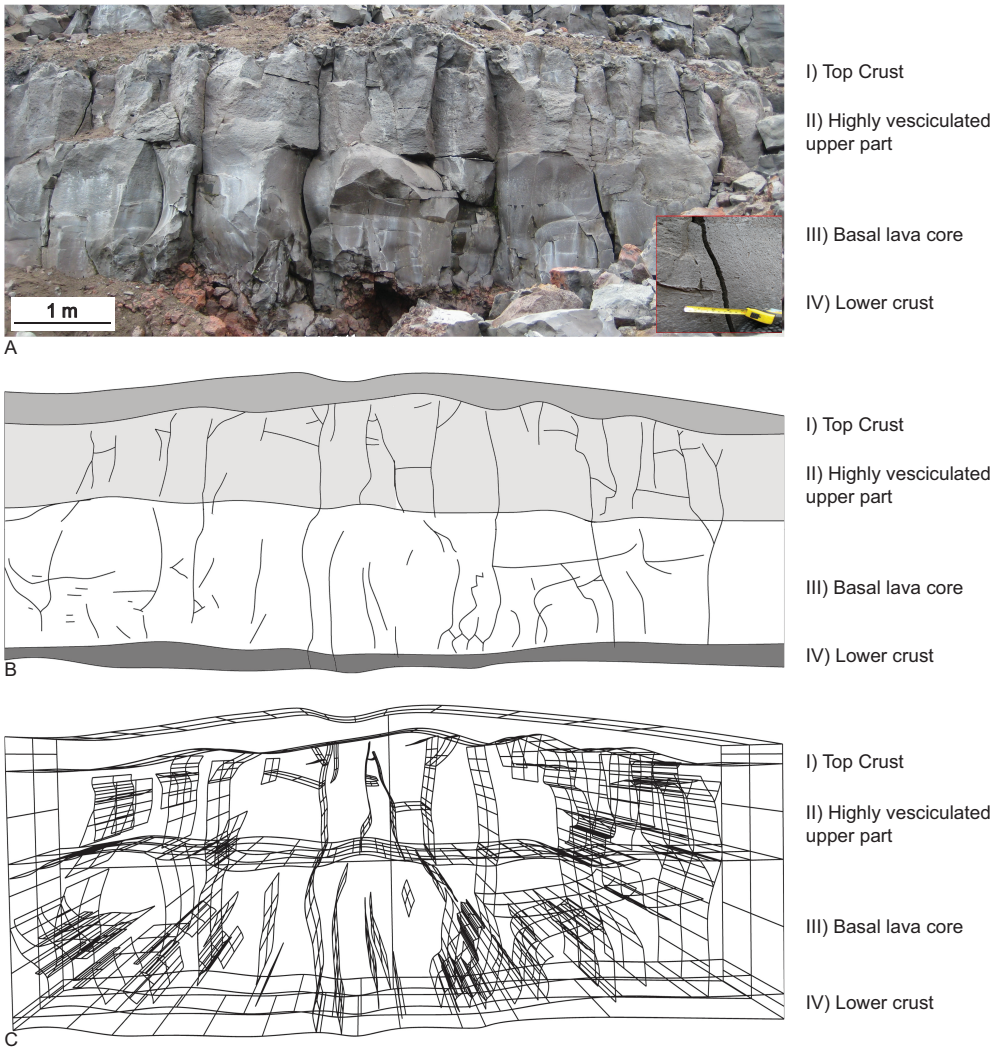

Figure 6.4: Rubbly pahoehoe lava flow used as a representative outcrop in order to compute the effective permeability of the basaltic morphotypes. - a) In the selected rubbly lava flow it is possible to clearly distinguish: I, loose material at the top of the lava flow in grey; II, highly vesiculated portion under the loose material in light grey; III, low vesiculated portion of the lava flow in white; IV, lower crust in dark grey. b) Reconstruction of the lava flow with the CAD software Rhinoceros 4.0 ^{TM}. c) 3D extrusion of the lava flow geometry perpendicular to the outcrop surface.

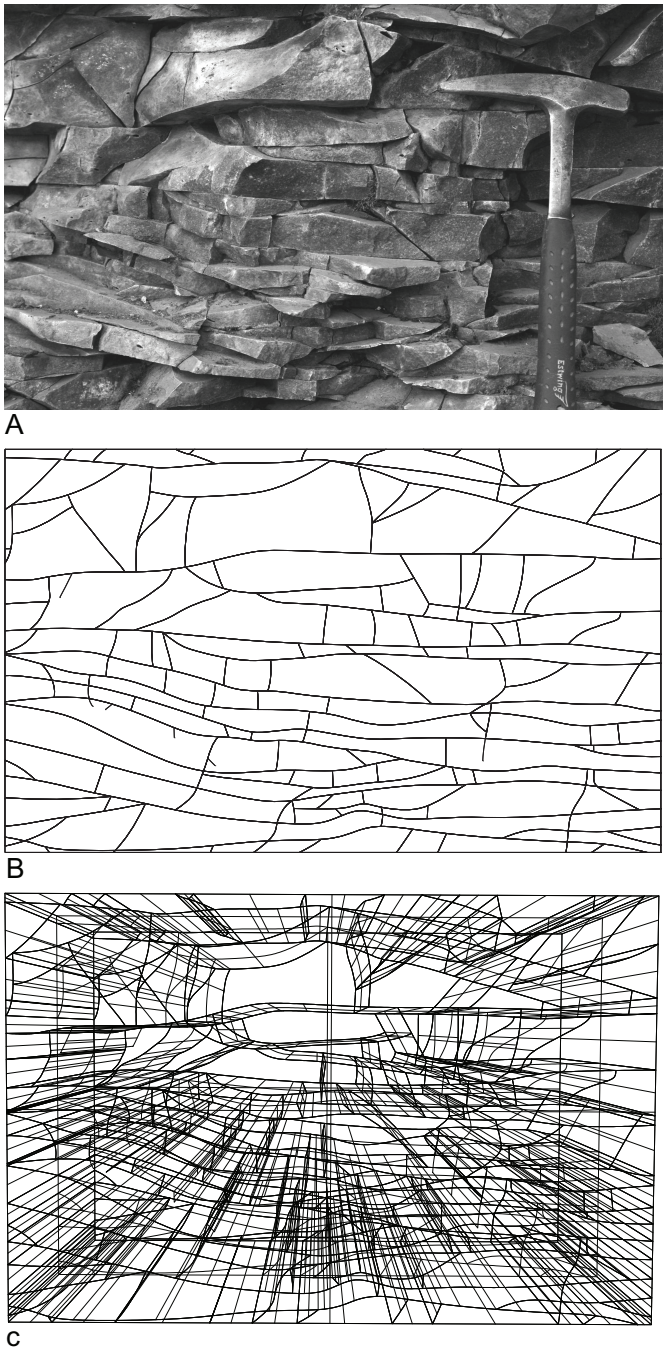

Figure 6.5: Fractured part of the felsic lava flow used to compute the effective permeability of the most fractured part of the outcrop. - a) Due to the morphology of the outcrop it has been possible to calculate only the effective permeability of the highly fractured part which most likely represents the area of the lava flow with the highest permeability. Close up of the area selected. b) Reconstruction of the selected area with the CAD software Rhinoceros 4.0 ^{TM}. c) 3D extrusion of the fracture geometry perpendicular to the outcrop surface.

relative distributions of approximately 20%, 70%, and 10%, respectively. Pahoehoe lava flows crop out on the northern-northwestern rim of the Öskjuvatn caldera. They appear as laterally continuous lobes with thicknesses varying between 2 m and 4 m. A specific range of lateral extensions cannot be provided due to the uneven and steep morphology of the Öskjuvatn caldera flanks. The pahoehoe lava flows commonly show a four fold vertical division which consists of a lower crust (quenched contact between the lava flow and the ground), a basal lava core, a highly vesiculated upper part, and a top crust. The thickness varies from 0.1 m to 0.3 m for the lower crust, 0.5 m to 2 m for the basal lava core, from 1 m to 2.5 m for the highly vesiculated upper part, and from 0.1 m to 0.3 m for the top crust. All the pahoehoe lava flows inside the Askja caldera exhibit intense fracturing. Rubbly pahoehoe lava flows make up the majority of the flows that crop out along the Öskjuvatn caldera. Like for pahoehoe lava flows, their lateral extension is difficult to estimate. Variations in the maximum thickness of these lava flows were observed across the caldera. On the northern rim they reach a maximum of 7 m to 9 m in thickness whilst on the western side the maximum thickness observed is 5 m. They exhibit a four fold division, similar to the one of pahoehoe lava flows. Whilst the basal lava core can range from 2 m to 4 m, the highly vesiculated upper part ranges from 4 m to 6 m. The top crust of rubbly pahoehoe lava flows differs from the one observed for the pahoehoe lava flows because of the presence of a horizon (from 0.2 m to 1 m thick) dominated by fresh rubbly fragments (from 0.05 m to 0.3 m in diameter). Aa lava flows are much less abundant and crop out only along the western rim of the Öskjuvatn caldera. They are laterally continuous for at least 30 m and their thickness varies between 3 m and 5 m. They appear as a coherent lava core enveloped by relatively thin and scoriaceous horizons of aa-clinckers. The maximum width of the internal vesicles, present in the central part of the coherent lava core, is approximately 4 cm. Irregular cooling joints characterise these aa lava flows.

Due to the necessity to compute the effective permeability of the pre-1875 fractured lava flows, and considering the difficulties in surveying the entire perimeter of Öskjuvatn caldera, a representative lava flow has been selected for the basaltic morphotypes, referred from hereafter as representative balsaltic lava flow (Figure 6.4a). It represents and incorporates the common features observed along the Öskjuvatn rim. This approach was used because a statistical study was beyond the scope of this work. This lava flow is a rubbly pahoehoe morphotype, laterally continuous for at least 200 m and

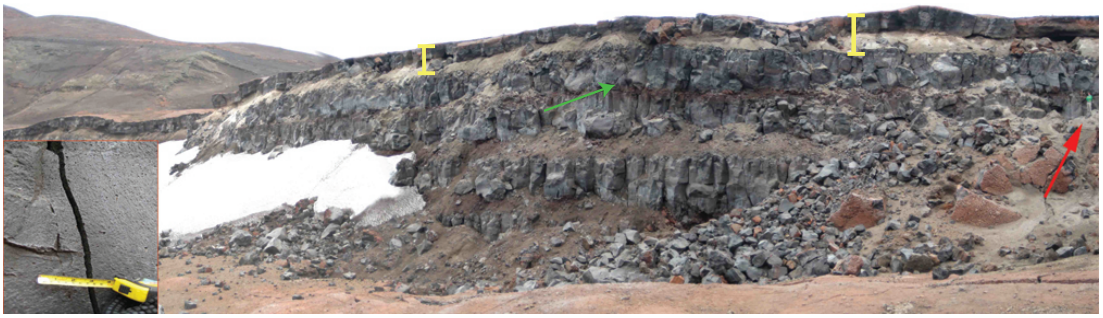

Figure 6.6: Basaltic lava flows on the Western margin of the Öskjuvatn caldera. - On this side of the caldera, the average thickness of the lava flows is $\sim$ 4 m. The basaltic lava flows that crop out on the northern rim of the Öskjuvatn caldera have an average thickness of 8 m. The yellow bars at the top of the outcrop show the 1875 eruptive products: the white pyroclastic fall and the reddish reomorphic 1875 lava, Carey et al. (2008). The inset shows one of the centimeter size fractures that characterises the basaltic lava flows. The green and the red arrows point to the rubbly layers that separate the coherent lavas and the scale on the outcrop, respectively.

approximately 5 m high, situated on the western rim of the Öskjuvatn caldera (Figure 6.3). The decision to use a rubbly pahoehoe morphotype as the representative lava flow was dictated by the fact that this morphotype is the most frequent among the basaltic morphotypes. In addition, rubbly pahoehoe and pahoehoe lava flows feature similar vesicular distributions (Thordarson and Self, 1998). The size of the vesicles varies gradually from 0.1 cm close to the basal lava core to a maximum of 8 cm below the top crust of the lava flow. Lens-shape vesicles with a horizontal main axis parallel to the outcrop surface and a maximum width of 3 cm occur in the lower part of the lava flows (i.e. between the upper part of the vesicular lower curst and the lower part of the central lava core). Pipe-shape vesicles are common in the middle- and upper-parts and their length reaches a maximum of 5 cm and their width 1 cm. The maximum diameter of the vesicles in the upper part of the lava flow reaches up to 5 cm. On the outcrop surface (48 m^2) approximately 100 main fractures (inset of Figure 6.6) have been measured which can be divided into two main sets of fractures: sub-vertical (most abundant) and sub-horizontal. Their length varies between 5 cm and 4 m and their aperture between 0.1 cm and 3 cm.

The only felsic lava flow found inside the Askja caldera (Figure 6.7), is exposed in a 12 m-high and 50 m-wide outcrop on the northern rim of the Öskjuvatn caldera. It

is characterised by a 4 m to 6 m thick base, a 4 m to 6 m central part, and a top part consisting of by fresh fragmental material (from 0.05 m to 0.4 m in diameter). In the lower part of the lava flow macroscopic vesicles were not encountered. However the middle part is characterised by macroscopic vesicles which are often lens-shaped with a maximum diameter of 10 cm observed below the top part of the lava flow. The intensive fracturing occurring at the base of the lava flow (Figures 6.7 and 6.5) is the main characteristic of this outcrop. This tight network is composed of both sub-horizontal and sub-vertical fractures. The intensive fracturing divides the base of the lava flow into prism-shape blocks (Figure 6.5). The centimeters-size matrix blocks are characterised by the lack of macroscopic vesicularly. The extended outcrop surface, the thickness of the lava flow, and the steepness of the caldera rim did not allow to measure the full length and aperture of all the fractures. In order to represent the highly fractured and most permeable part of the outcrop a region at the base of the felsic lava flow characterised by an intense fracturing (0.3 m high and 0.4 m wide, Figure 6.5a) has been selected. On this area it has been possible to measure approximately 140 fractures of lengths varying from 2 cm to the maximum length of the area of interest. Their aperture varies between 0.05 cm to 0.7 cm. The central part of the felsic lava flow is characterised by sub-circular regions (up to 3 - 4 m in diameter) bounded by bands of highly fractured rocks. The upper part of the lava flow is characterised by meter-long and centimeter-wide fractures. The intense fracturing featured at the base of the lava flow is probably caused by the shear movement of the viscous lava flow (Griffiths, 2000) while the middle and upper fracturing is due to cooling of the lava flow and caldera subsidence.

Overall, there is a significant contrast between the hyaloclastic succession making up the caldera flanks and the lava pile filling the Askja caldera. While the flanks have a low permeability, the caldera consists of fresh and highly fractured lava flows where secondary mineralisation filling the fractures and vesicles does not occur. Most lava flows are fully saturated with water. This is obvious by the frequent presence of water dripping out of the fractures (Figure 6.8). Despite the wide range of vesicularity observed for the different lava flows (from 10% to 60%), a common feature to all is the lack of interconnectivity of these vesicles.

Figure 6.7: Felsic lava flow cropping out on the Northern rim of the Öskjuvatn caldera. - The squared area on the right side is shown in the inset and depicts the intensive fracturing that characterises the felsic lava flow in more detail. The base of the flow (that continues below the ground surface) is highly fractured. The hammer, indicated by the red arrow in the inset, is used as a scale.

Figure 6.8: Water dripping from a fracture (less than 0.5 cm wide). - The image represents a part of the representative basaltic lava flow.

6.4 Numerical computation of effective permeabilities

As already mentioned in the introduction, permeability and porosity analysis of unfractured lava flows (Ingebritsen and Scholl, 1993; Saar and Manga, 1999; Sruoga et al., 2004; Stearns, 1942) cannot be used to characterise the intensively fractured lava flows that fill the Askja caldera. In order to compute numerically the effective permeabilities of the fractured basaltic and felsic lava flows with finite elements techniques first the 2D and 3D geometry of the two lava flows, i.e. the felsic lava flow and the representative basaltic lava flow, have been reconstructed by using the CAD software Rhinoceros 4.0 ^{TM}. Figures 6.4 and 6.5 show the workflow that has been followed. The frontal view of each lava flow (Figures 6.4a and 6.5a) has been imported in Rhinoceros 4.0 ^{TM} where the main geological features of the outcrops have been traced (Figures 6.4b and 6.5b). Next the planar geometries perpendicular to the outcrop surface have been extruded in order to recreate the models of the representative basaltic lava flow and felsic lava flow outcrops (Figures 6.4c and 6.5c). Based on field data, it has been assumed that the strike of the fractures is perpendicular to the outcrop surface. This allowed to consider the fractures, represented with their correct aspect ratio, embedded in a basaltic and felsic matrix, respectively, as smooth-walled planar surfaces.

The aperture value previously measured in the field has been assigned to each fracture. Then the representative basaltic lava flow has been divided into four parts: top crust, highly vesiculated upper part, basal lava core, and lower curst, respectively (Figure 6.4b) and varied the permeability of each part. The model has been tested for permeabilities ranging from 1.0×10^{-15} m^2 to 1.0×10^{-12} m^2 for the top crust, from 1.0×10^{-17} m^2 to 1.0×10^{-14} m^2 for the highly vesiculated upper part, from 1.0×10^{-18} m^2 to 1.0×10^{-14} m^2 basal lava core, and from 1.0×10^{-18} m^2 to 1.0×10^{-13} m^2 for the lower curst. The typical fracture aperture a characterising this outcrop was found to vary between 0.1 cm and 0.3 cm.

For the felsic lava flow it has been followed the same approach used for the representative basaltic lava flow. The numerical computation of the permeability has been focused on the base of the outcrop (up to 4 m high) where intense fracturing was observed. After having characterised each fracture with its field measured aperture, how different matrix permeabilities affect fluid flow has been tested. The matrix permeability values range from 1.0×10^{-12} m^2 to 1.0×10^{-20} m^2.

6.4.1 Mathematical modelling

The effective permeability of the fractured basaltic and felsic lava flows has been calculated using the method of Matthai et al. (2004). The mathematical model considers laminar and steady fluid flow through the complex fracture-matrix structure of both lava flows. The parallel plate law (Snow, 1968) was applied to calculate the effective permeability of a single fracture, k_f, as $k_f = a^2/12$, assuming smooth and planar fracture surface. For the resulting fracture permeability and testing for varying matrix permeabilities (see above) the pressure field for fixed pressure (Dirichlet) boundaries was computed by solving

$$0 = \frac{\partial}{\partial i} \cdot \left[\frac{k_i}{\mu} \frac{\partial P_f}{\partial i} \right] \quad i \in x, y, z \tag{6.1}$$

where k_i is the spatially varying fracture or matrix permeability in the i-direction, μ is the fluid viscosity, and P_f is the fluid pressure. The effective permeability $\hat{k_i}$ in i-direction is then calculated by inverting Darcy's law

$$q_i = -\frac{\hat{k_i} A_i}{\mu} \frac{\Delta P_i}{L_i} \quad i \in x, y, z, \tag{6.2}$$

where q_i is the total volumetric flux in i-direction through area A_i oriented perpendicular to the i-direction and $\hat{k_i}$ is the average (or effective) permeability of the fractured matrix flow in the i-direction. Mathematically, this is expressed as

$$\hat{k_i} = \frac{q_i \mu}{A_i} \frac{L_i}{\Delta P_i} \quad i \in x, y, z \tag{6.3}$$

where L_i is the length of the outcrop in the i-direction, and ΔP_i is the drop in fluid pressure over distance L_i in i-direction. This calculation is carried out for each i-direction, that is for the x, y, and z coordinate, yielding a vector of effective permeabilities with an entry for each spatial coordinate. However, this vector appears to be nearly isotropic, i.e. the effective permeabilities do not vary greatly in x, y, and z directions. Hence only the permeability in the x-direction is considered (the permeability is treated as a scalar) and it is used the main direction where fluid flow occurs towards the conduit.

6.4.2 Effective permeabilities of the fractured lava flows

Figure 6.9a shows the resulting horizontal effective permeability, perpendicular to the outcrop surface, across the basaltic lava flow as a function of matrix permeability. The

effective permeability is approximately 1.3×10^{-09} m^2 and the fraction of fracture volume to total model volume is 3.27×10^{-05}. The well connected fractures dominate the total permeability which is insensitive to the matrix permeability. Flow in the matrix is essentially stagnant because the ratio of fracture permeability to matrix permeability is higher than 10^5 (Matthai et al., 2004). Figure 6.9b shows the horizontal effective permeability at the base of the felsic lava flow, perpendicular to the outcrop surface, as a function of the matrix permeability. The effective permeability is approximately 2.5×10^{-08} m^2 and the fraction of fracture volume to total model volume is 1.1×10^{-04}. Also in this case the flow is dominated by the fractures and fluid flow in the matrix is negligible even for elevated matrix permeabilities of 1.0×10^{-12} m^2.

6.5 Numerical computation of the syn-eruptive groundwater flow dynamics in the Askja caldera

The geometry of the syn-eruptive Askja caldera groundwater flow model is based on studies of Carey et al. (2009a,b) that gives the location of the vents C and D and the approximative depth at which the interaction between water and magma took place. The numerically computed permeabilities $\hat{k_i}$ have been used to populate the model. The duration of the eruptive phases provided by eyewitness records (e.g. Carey (2008)) allowed to constrain the timing of the numerical simulations.

6.5.1 Model constraints from existing data

Carey et al. (2009b) show that in the 28–29 March 1875 Askja volcano eruption the vents migrated within the caldera. The change in activity of the eruption demarcated by the transition from C to D phase also involved a 1 km southwest shift in the position of the erupting vents (Figure 6.3). Using the erupted mass of magma during phase C given by Carey et al. (2009a) and summarised in Table 6.1, it has been back-calculated the volume of water involved in the eruption by assuming an optimum ratio between the mass of water, m_w, and the mass of magma, m_m, involved for both the phreatoplinian C1 and C2 phases, $\mathcal{M} = 0.3$, where $\mathcal{M} = m_w/m_m$. This yields a total water volume of 1.44×10^8 m^3. The eruptive products also showed that the widening of the vent and the availability of external water influenced the rapid changes in eruptive styles. The depth at which the water-magma interaction occurred can be estimated from the

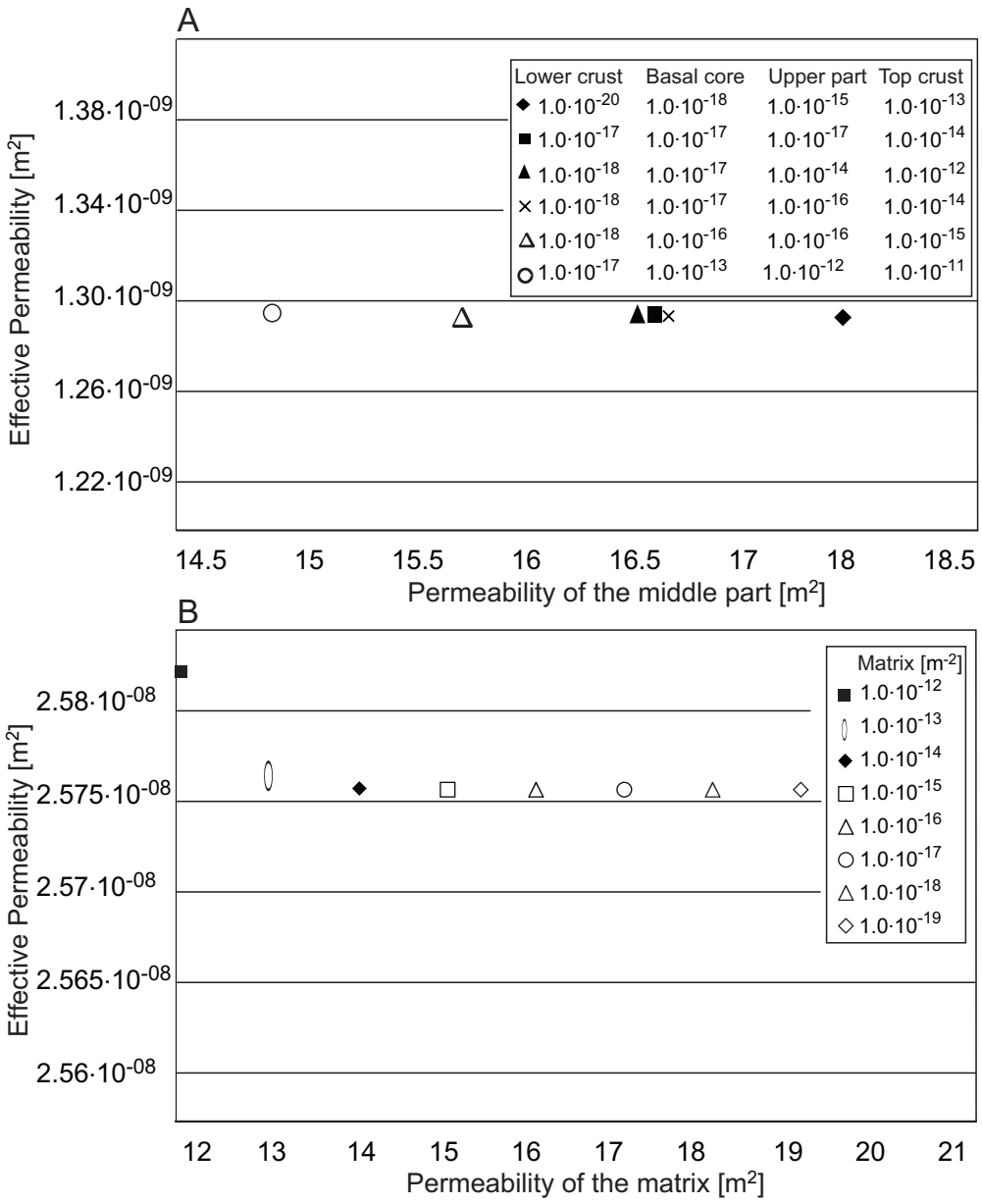

Figure 6.9: Numerically computed effective permeability of the a) representative basaltic and b) felsic lava flows for varying matrix permeabilities. - See Figure 6.10 for the location of the top crust, upper part, basal core, and lower crust. The felsic lava flow has an uniform matrix permeability.

phreatoplinian poumices clast textures which indicate that at fragmentation the rising magma was already a foam (Carey et al., 2009b). The decrease in the vesicle number density, together with the maturation of vesicle shapes throughout the C2 phase, suggest that the eruption intensity was decreasing. This, coupled with the fact that the deposits suggest a "drying out" with time throughout the C2 phases, indicates that there was a decrease in the availability of water (Carey et al., 2009b). Historical records of the 28 – 29 March 1875 Askja caldera prior the eruption have shown that no standing water was present at the time of the eruption on the caldera floor. Even though a small depression filled with a pond was present at the eruption site prior to the 28^{th} of March 1875, the amount of water available was at least one to two orders of magnitude too small for providing the amount of external water required for this explosive magma-water interaction. The historical records also state that a narrow stream of water was flowing out of the lava pile forming towards the pond. It is hence assumed that the lava pile was saturated. The eyewitness records also report that the weather was clear at the time of the eruption and fine grained deposit of the phreatoplinian phase C cannot be explained as rain-influenced fall out. An expedition to the eruption site during the summer 1875 specifically stated that no large scale melting of snow occurred in the Askja caldera. The evidence that minimal melting of snow took place prior to the 28-29 March 1875 eruption is the widespread occurrence of snow beneath the deposits of the 28 – 29 March 1875 eruption. Hence, it is highly unlikely that the phreatomagmatic activity was induced by large-scale local snow melt.

6.5.2 Geometry of the Askja caldera model

The pre-eruptive geological environment of the Askja caldera has been reconstructed using historical drawings (Anonymous, 1875; Carey, 2008), topographic maps, and field data. The total dimensions of the model are depicted in Figure 6.10a where it is shown as an aerial view. Figure 6.10b represents a schematic cross section across the lava pile. The geometry of the model was reconstructed with the CAD software Rhinoceros 4.0^{TM}. The Öskjuvatn caldera is not included in the simulations because its formation is related to the 1875 explosive activity. The model accounts for the topography of the Askja caldera and its surrounding mountains. The geological units considered in the model are shown schematically in Figure 6.10b and include: a) the hyaloclastic mountains that bound the Askja caldera, b) the deep lava pile (400 m thick) which fills

the caldera, c) a shallow lava pile (100 m thick) consisting of fractured basaltic lava flows (characterised by the numerically computed permeabilities of 1.3×10^{-9} m^2) that contains d) an approximately 15 m deep and 10 m thick layer representing the felsic lava flow characterised by the numerically computed permeabilities of 2.5×10^{-8} m^2. The felsic lava flow does not span the entire caldera: its basal area is less than 1/6 of the total area of the caldera floor (Figure 6.3). e) The magmatic conduit is recreated as a rhomboidal-base prism (each side 8 m long) and has been divided into two parts: a deeper impermeable part that did not interact with groundwater and a shallower part (20 m high) that represents the segment of the conduit that interacted with the groundwater. Studies on vesicle size distribution in pumices form the 1875 eruptive products indicate that the interaction of magma and external water took place after the melt was fully expanded to a foam and was close to fragment (Carey et al., 2009b). This implies that the interaction took place in the very shallow part of the conduit. Therefore it is assumed that only the upper part of the conduit interacts with the groundwater. It behaves like a "well" and removes the 1.44×10^{8} m^3 of groundwater stored in the highly permeable lava pile during the C-phase to drive the 2 hour-long phreatoplinian eruption. The CAD model has been discretised into approximately 1.35×10^{6} adaptively refined and unstructured tetrahedral finite elements using the commercial software ANSYS ICEM^{TM}. Below it is discussed the mathematical model which that is solved by the finite element method using the above finite element mesh and CSMP++, a simulator for fluid flow in structurally complex geological environments (Matthai et al., 2007).

6.5.3 Conceptual and mathematical modelling

The syn-eruptive groundwater dynamics were simulated by assuming that the water-magma interaction occurring at the conduit, during phase C1, removes groundwater and hence leads to approximately radial flow of groundwater towards the conduit as consequence of the "pumping" action of the conduit. The mathematical formulation used in this study does not resolve properly the fuel-coolant interaction around the conduit where complex thermodynamic processes occur (Wohletz, 1986, 2003). Historical records and field observations today show that the loose sediment cover and rock formations at the Askja caldera is always fully saturated, hence it is assumed that the water table is laterally continuous and equal to the topography and the groundwater aquifer is unconfined. In this case the pre-eruptive groundwater flow is driven by elevation only.

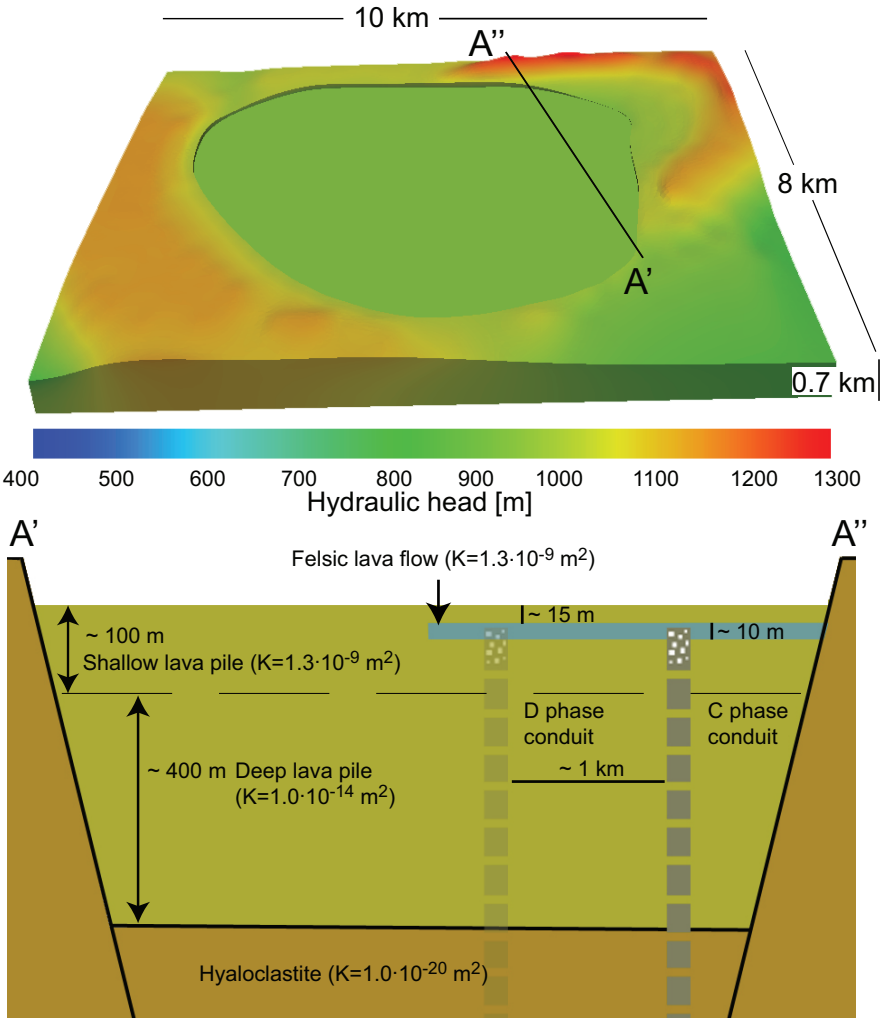

Figure 6.10: Top view of the hydraulic head distribution before the onset of the eruption in the Askja model. - The dimensions of the model are shown in the picture. The ring faults bound the caldera floor that is represented with a subsidence of approximately 20 m. The white ellipses show the position of the conduits of the phases C and D. The cross section shows a schematic representation of the model (not to scale) along the profile A'–A''. In the Askja groundwater flow model it only accounted for the conduit of the phase C1 which has a rhomboidal base and a maximum width of 5 m. The part of the conduit that is in contact with the groundwater is shown in grey with white dots. Ring faults (in black) separate the lava pile and the hyaloclastitic rocks. The shallow lava pile (100 m thick) consist of fractured basaltic and lava flows. Basaltic lava flows occur 15 m below the ground surface and between 25 and 100 m depth. The felsic lava flow occurs between 15 and 25 m depth. The shallow lava pile is characterised by the computationally calculated average (effective) permeabilities. The lava flows that comprise the deep lava pile are assumed to be characterised by lower permeabilities due to secondary mineralization. The rock properties used to configure the models are summarised in Table 6.2.

The subsequent dry-out of the C2 phase could then be caused by the decline of the groundwater table because the fast "pumping" of the conduit causes rapid flow towards it. As the water table drops, the flux of groundwater towards the conduit is reduced and ultimately the water supply can no longer maintain a phreatomagmatic style of activity. To model this scenario, the hydraulic head in the Askja caldera is computed by solving groundwater flow equation (Ingebritsen et al., 2006)

$$S\left(\frac{\partial h}{\partial t}\right) = \nabla(K\nabla h) + Q, \tag{6.4}$$

where S is the storativity for an unconfined aquifer [m^{-1}], h the hydraulic head [m], K the hydraulic conductivity [m s^{-1}], and Q [s^{-1}] the rate at which the fluid is removed. The hydraulic conductivity K is defined as

$$K = \frac{k\rho g}{\mu}, \tag{6.5}$$

while the hydraulic head is given by

$$h = z + \frac{P_f}{\rho \mathbf{g}} \tag{6.6}$$

where z is the elevation, ρ the fluid density, $\mathbf{g}$ the acceleration due to gravity, k the permeability [m^2], and μ the viscosity.

Since the fracture apertures are wide, i.e. larger than 0.5 mm, and the capillary pressure can be approximated as inversely proportional to the fracture aperture, this model neglects capillary forces which occur as the groundwater level declines. The capillary pressure, $P_c = \frac{2\sigma\cos\theta}{0.5a}$, where θ is the contact angle and σ the interfacial tension between water and air, for 1 mm wide fracture is negligibly small, i.e. $\sim$ 280 Pa, assuming a water-wet rock ($\cos\theta$=1) and an air-water interfacial tension of 0.07 N m^{-1}. All simulations are assumed to be isothermal because temperature variations due to the geothermal gradient away from the conduit are not significant.

6.5.4 Model setup

All the boundaries of the model are considered as no-flow boundaries. Only a fixed pressure of 1 bar is applied to the top boundary , i.e. the topography. Table 6.2 summarises the rock properties that characterise the lithologies of the Askja caldera groundwater flow model. Figure 6.10b shows the geological units of the model schematically which

are described by permeabilities ranging from 1.0×10^{-8} m^2 to 1.0×10^{-20} m^2 and by porosities ranging between 0.01 and 0.1 (see Table 6.2). The hyaloclastites are considered as impermeable rock characterised by very low porosities. The major uncertainty is the co-eruptive variation of the lava pile permeability which may be subject to changes throughout the eruption. The lava pile at depths greater than 100 m is characterised by low permeability of 5.0×10^{-16} m^2 and a porosity of 0.05 %. The permeability of the deep parts of the lava pile are considered to be reduced significantly due to secondary mineralization. An uniform storativity of 0.1 m, representative of an unconfined aquifer (Ingebritsen et al., 2006), was used for the entire mode.

The shallow parts of the caldera are characterised by the numerically computed permeabilities of the fractured lava flows described above. That is, the fractured felsic lava flow and fractured basaltic lavas have permeabilities of 2.6×10^{-8} m^2 and 1.3×10^{-9} m^2, respectively. The rate at which the conduit removes water is 2.0×10^{4} m^3 s^{-1}, assuming a density of 1000 kg m^{-3}. The viscosity of the groundwater is 1.0×10^{-3} Pa sec^{-1} The total simulation time is two hours to account for the duration of the phreatoplinian (C1) and part of the following phase (C2) when the dilute density currents occurred. Time steps of three minutes are used to solve equation 6.4. The numerical results have been compared to an analytical line source solution for radial fluid flow (Zeng et al., 2002) for an idealised geometry and observed less than 1% error.

Geological unit	k [m^2]	ϕ [–]	S [m^{-1}]
Felsic lava flow	2.5×10^{-08}	0.6	0.1
Shallow lava pile$\star$	1.3×10^{-09}	0.1	0.1
Deep lava pile	1.0×10^{-14}	0.05	0.1
Hyaloclastite	1.3×10^{-20}	0.01	0.1
Ring faults	1.0×10^{-12}	0.09	0.1

Table 6.2: The units comprise the hydrostatigraphy of the Askja caldera (see Figure 6.10b for their locations). The permeability values of the felsic lava flow and shallow lava pile are based on the fracture upscaling procedure illustrated in section 6.4.2. $\star$ The shallow lava pile is characterised by the numerically computed permeabilities of the representative basaltic lava flow. The deep lava pile is assumed to be characterised by fractures and vesicles filled by secondary mineralization. The porosity values for the deep lava pile are based on the values suggested by Saar and Manga (1999) and the storativity by Ingebritsen et al. (2006).

6.6 Results

Figure 6.11 shows the evolution of fluid pressure along the profile M'–M" of Figure 6.3 for a model using the parameters presented in Table 6.2. The initial state (time t = 0 minutes) is characterised by a laterally homogenous fluid pressure distribution. Pressures of less than 1.0×10^5 Pa (atmospheric pressures) below the caldera surface indicate a drop in water table and imply air-filled lithologies (i.e. the fractured basaltic lava flows that comprise the shallow lava pile). The onset of the eruption causes the removal of groundwater in the vicinity of the conduit (t = 6 minutes). This is accompanied by a sudden drop of the hydraulic head around the conduit which leads to a decline of fluid pressure marked by the blue areas of Figure 6.11. This drop is approximately 100 m in diameter at the surface and 50 m deep near the conduit. With time the drop in fluid pressure becomes continuously wider and deeper (t = 15 and t = 30 minutes). The fluid pressure drop reaches approximately 300 m in diameter in the shallow parts of the caldera after t = 60 minutes and 500 m after t = 120 minutes. At t = 120 minutes atmospheric pressures occur up to depths of 15 m approximately 750 m far from the conduit. This is depicted by the inset in Figure 6.11 at t = 120 minutes. Figure 6.12 shows the syn-eruptive groundwater pore velocities (i.e. $\vec{q}/\phi$, where $\vec{q}$ is the Darcy velocity and ϕ the porosity) measured in the shallow lava pile, 180 m far from the conduit along the z-direction. The black bar in Figure 6.11 at time t = 0 indicates the region shown in Figure 6.12. The maximum pore velocities (the peaks in Figure 6.12) indicate regions of fast horizontal flow towards the conduit. The increasing depth of the pore velocity peaks highlights how groundwater is transported towards the conduit from progressively deeper regions of the lava pile. At t = 6 and t = 15 minutes, the maximum pore velocities occur 15 m below the caldera floor. At t = 6 minutes they are approximately 7.5×10^{-5} m s^{-1} and at t = 60 minutes they have already decreased by approximately 2 orders of magnitude ($\sim 1.5\times10^{-7}$ m s^{-1}). From time t = 30 minutes to t = 60 minutes the peaks migrate from 15 m to 42 m depth. In the following 60 minutes (i.e. between 60 minutes and 120 minutes) the pore velocities decrease to $\sim 1.0\times10^{-8}$ m s^{-1} and the peaks are now approximately 50 m deep. In the early stages of the C phase, the groundwater stored in the shallow lavas is removed first. With time, the area around the C-phase conduit that is affected by groundwater flow increases. Figure 6.13 shows the direction of the groundwater flow after 60 minutes using 3D stream-tubes. At

this time the groundwater has already been drained from the highly permeable shallow lava pile. Flow now occurs from the deeper and less permeable lavas (i.e. deep lava pile) towards the conduit and no longer in the shallow, and more permeable lava pile. The coloured stream-tubes in Figure 6.13 show that the highest velocities are reached near the conduit. Although they reach maximum values of 2.0×10^{-3} m s^{-1}, the complex thermodynamic processes that occur around the conduit is not modelled accurately (Wohletz, 1986, 2003), therefore the maximum velocities in this region might be lower or higher.

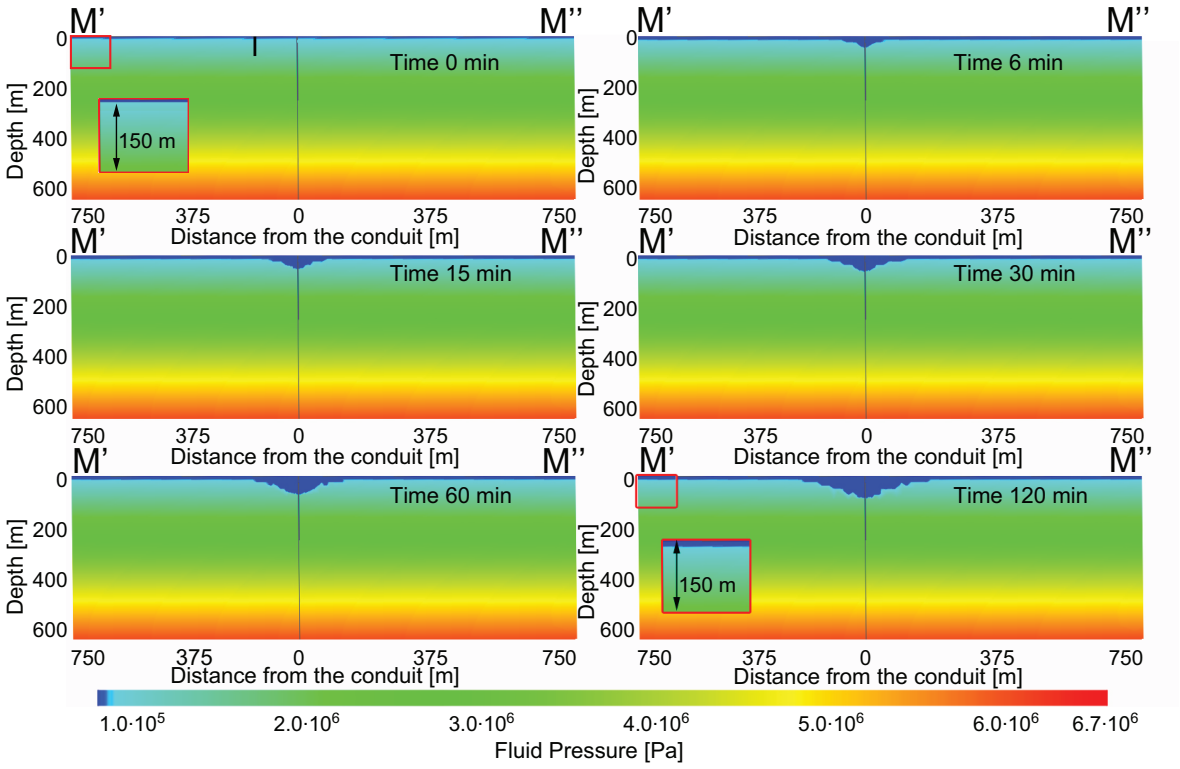

Figure 6.11: Syn-eruptive (phases C1 and C2) fluid pressure evolution in the profile M'–M" of Figure 6.3. - The sub-horizontal drop in fluid pressure around the conduit increases with time. Note that a pressure of 1 bar (1.0×10^5 Pa) corresponds to region where only air is present, i.e. where the groundwater table has fallen below the land surface, respectively. The jagged lines are due to interpolation effects when visualising surfaces on unstructured finite element grids. The insets at t = 0 and t = 120 minutes show the initial fluid pressure and the drop in fluid pressure below the caldera surface. The vertical thick black line at t = 0 minutes indicates the location of the vertical profile shown in Figure 6.12. The conduit is represented by the thin vertical line in the center of each image.

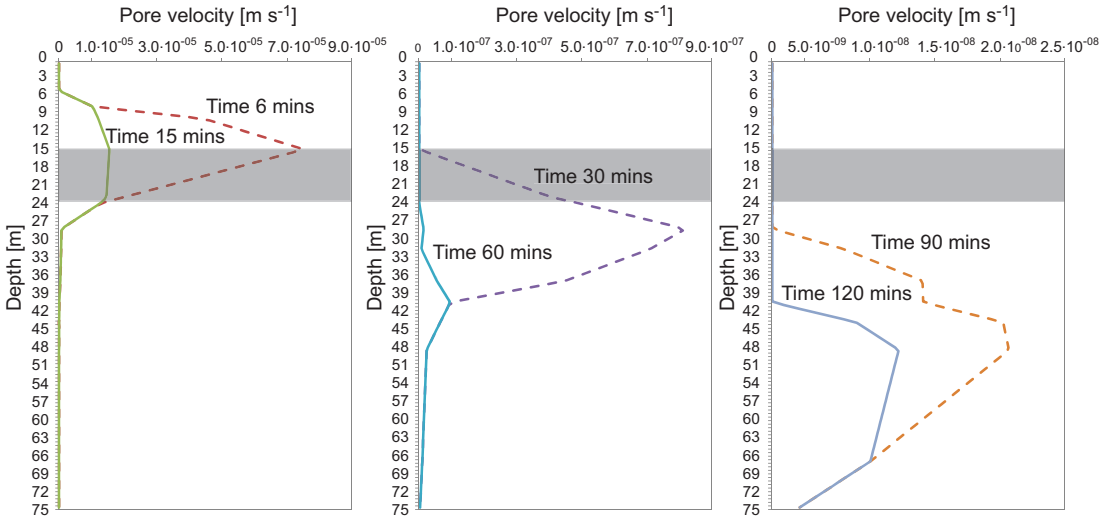

Figure 6.12: Syn-eruptive groundwater pore velocities along in x-direction for a vertical profile in the shallow lava pile at t = 6, 15, 30, 60, 90, and 120 minutes after the onset of the phase C1. - The location of the vertical profile is shown by the black thick line of Figure 6.11, t = 0. The grey horizontal band represents the 10 m thick fractured felsic lava flow (effective permeability: $2.5{\times}10^{-08}$ m^2). Above and below the felsic lava flow fractured basaltic lava flows occur (effective permeability: $1.3{\times}10^{-09}$ m^2). The peaks represent the maximum pore velocities of the groundwater flow towards the conduit.

6.7 Discussion

The groundwater dynamics emerging from the Askja caldera groundwater flow model, calibrated with existing field and laboratory data (Carey, 2008), provide a possible explanation for the eruptive dynamics that occurred on the 28^{th}–29^{th} of March 1875 at the Askja volcano. The model explains why the eruption was initially wet and then gradually dried out and culminated in the dry Plinian phase D.

The hydrodynamics that characterised the Askja 1875 eruption are summarised in Figure 6.14. Carey et al. (2009b) show that the vent of the subplinian activity (phase B) was located at the margin of the Askja caldera (Figure 6.1), intruding into an impermeable sequence dominated by hyaloclastic lithologies. Although the succession was fully saturated, the rising magma did not interact with groundwater at this time because of the low permeability of the hyaloclastic succession which restrained the

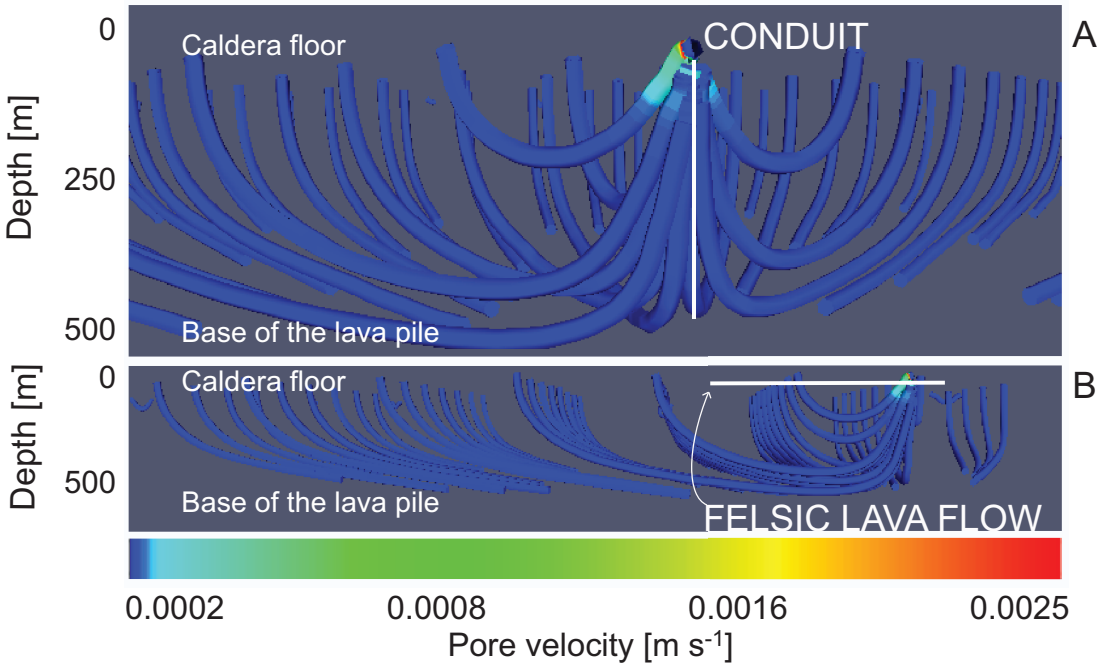

Figure 6.13: Frontal a) and lateral view b) of the stream tubes inside the entire lava pile at the end of phase C1, i.e. after 60 minutes - The stream tubes show the direction of the groundwater flow inside the Askja lava pile. The withe lines schematically indicate the conduit a) and the felsic lava flow b). The colouring of the stream tubes shows the magnitude of the pore velocities. Maximum velocities of 2.0×10^{-3} m s^{-1} are reached around the conduit. Note how groundwater flow bypass the high permeable felsic lava flow. Fluids are transported upwards from greater depths.

water supply to the conduit. After a pause of eruption, the location of the conduit of the phreatoplinian phase (C1) moved northwards cutting through the lava pile of the Askja caldera (Figure 6.1) (Carey et al., 2009b). Groundwater flow is most effective in the upper part of the lava pile (i.e. in the first 60 m below the ground surface) where the highly fractured lava flows occur (Figure 6.11). This lends support to the hypothesis that the groundwater stored in the top part of the lava pile surrounding the erupting C-conduit was sufficient to drive the phreatoplinian C1-phase. During the one hour long phreatoplinian activity, the groundwater stored within the lava pile was continuously drained. In this scenario, the felsic lava flow focussed the groundwater flow during the C phase as schematically shown in Figure 6.12 and 6.14b (at t = 6 and t = 15 minutes). The decline in the groundwater table (Figure 6.11 and 6.14c) is consistent with field observations (Carey et al., 2009a) that indicate decreasing involvement of external water with time, as well as a drop in the mass discharge rate. The progressive dry-out of the C2 phase feature a flow behaviour typical of a dual-porosity system (Warren and Root, 1963) in which increasingly less water was supplied by the pristine lavas and more water provided by the less permeable deep lavas. Furthermore the model indicates that the decrease of the hydraulic head induced by the drainage of groundwater may have extended to the region were the D-phase vent emerged. Given that the entire Askja caldera was fully saturated with groundwater, there is no reason to assume that the second vent intruded into a "dry" area. The draining of groundwater might have reduced the availability of water rendering the mass ratio $\mathcal{M}$ low and ineffective. This caused the D phase to be dry (Figure 6.14d).

We carried out sensitivity studies and tested several configurations for the Askja caldera groundwater flow model by characterising the geological units with different permeabilities and porosities. The thickness of the lava pile has also been varied. By using standard literature permeability values ranging from 1.0×10^{-10} m^2 to 1.0×10^{-14} m^2 for unfractured lavas (Saar and Manga, 1999) a wide depression of the hydraulic head was not obtained. Instead, the hydraulic head drops immediately to probably unrealistically low values ($\sim$ 100 m below the Askja caldera floor) directly adjacent to the conduit because water cannot be transported fast enough to the vent. Additional simulation tests have been run with reduced thicknesses of the lava pile (from 500 m to 100 m). This produced a fast drainage of groundwater around the conduit over

30 minutes. This is not in agreement with the historical records that reported the phreatoplinian activity to last for at least 1 hour.

We carefully considered the impact that the presence or absence of the felsic lava flow might have had on the syn-eruptive groundwater flow and therefore on the eruptive dynamics. A poor knowledge exists on the exact distribution of these lava flows inside the Askja caldera and their occurrence might be limited. Such restricted distribution is considered in the geological model (Figures 6.3 and 6.10) where it is only accounted for one felsic lava flow (Figure 6.10b). The distance from the two conduits of the phreatoplinian and Plinian phase has been estimated to approximately 1 km (Carey et al., 2009a). Based on field evidences, it is suggested that the felsic lava flow might have reached the Southern part of the Askja caldera close the location of the vent of the Plinian phase (D). This is supported by the fact that the felsic lava flow that crops out on the Northern rim of the Öskjuvatn caldera represents a proximal segment of the entire lava flow. This is not only based on the dimensions of the outcrop (more than 60 m wide and approximately 12 m high) but also on its vesicle distribution (sheared, numerous, and large centimeter-size vesicles in the middle and upper part of the flow). The highly sheared base suggests high velocities and therefore high extrusion rates that can only be reached close to the vent from which the lava is erupting. The lava pile of the Askja groundwater flow model is characterised by basaltic lava flows and the highly fractured felsic lava flow. Due to the structural complexity of the volcanic edifice, the occurrence of additional permeable units (i.e. lava tubes, loose volcanic deposits, and clinker layers) is likely. The occurrence of these units would enhanced the permeability of the shallow lava pile, facilitating the rapid drainage of groundwater. Note that the model does not consider the highly permeable 1 m to 2 m thick rubbly-clinckery horizons as separated layers. They are in fact considered as the "top crust-layer" of the representative basaltic lava flow during the numerical computation of the effective permeabilities. Accounting for meter-thick rubbly-clinckery layers in the model that separate the fractured lava flows would have enhanced the "pumping" effect of the conduit further. This would have facilitated the drying-out of the lava pile even more and caused a larger radial drop of the water table than shown in Figure 6.11.

The pore velocity peaks at t = 6 and t = 15 minutes shown in Figure 6.12 highlight that the groundwater flow towards the conduit is initially concentrated in the felsic lava flow. Additional simulations in which it was not accounted for the presence of the

felsic lava flow have been ran. A decline in fluid pressure similar to the one shown in Figure 6.11 has been obtained for models in which the lava pile was characterised by fractured basaltic lava flows only. Although not mandatory to support the model, the presence of the felsic lava flow helps to explain how enough groundwater reached the conduit, maintaining the phreatoplinian activity. The occurrence of the felsic lava flow also accelerates fluid pressure drop 750 m far from the conduit (Figure 6.11, t = 120 mins), i.e. approximately where the vent of the D phase intruded, yielding the D phase to be dry.

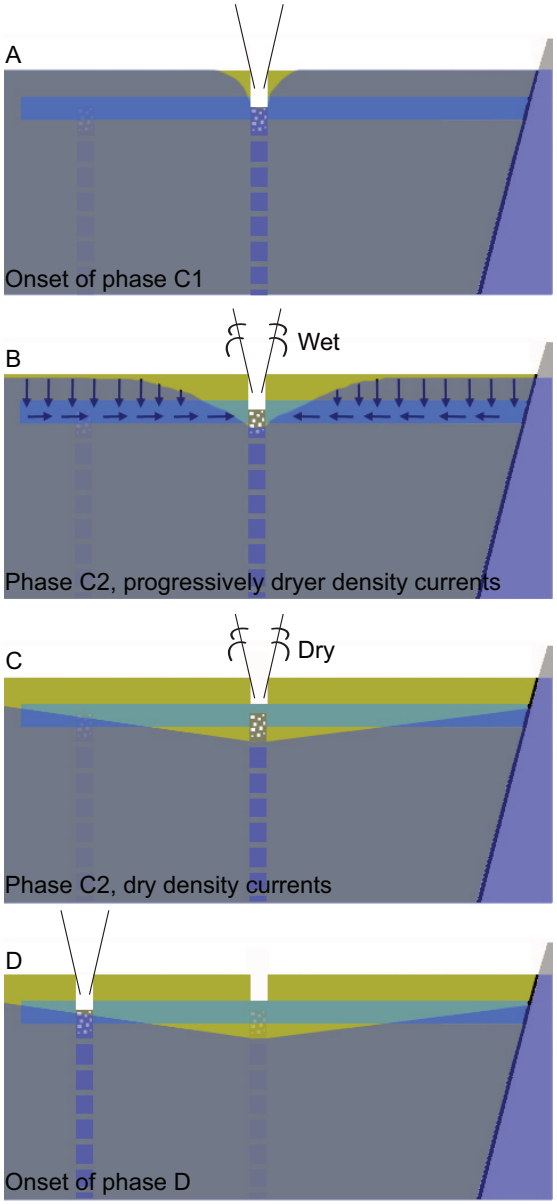

Figure 6.14: Simplified cartoon of the syn-eruptive groundwater dynamics during the March 1875 Askja eruption. - The dike which fed phase C1 intruded into the lava pile. b) The interaction between the shallow groundwater and the rising magma led to the occurrence of the phreatoplinian phase. The hydraulic head of the groundwater table decreased. Fluids were focused into the highly permeable felsic lava flow. c) The amount of water available in the shallow lava pile decreased as shown in the deposits of the phase C2 . d) After the C2 phase terminated, not enough groundwater was available in the lava pile and the ratio $\mathcal{M}$ was probably not large enough to maintain a phreatoplinian eruption.

7

Conclusions

This study presents one of the very first examples of high resolution simulations applied to high temperature hydrothermal systems. Two prime examples, the Tjörnes Fracture Zone and the Askja volcano have been selected for this work. The geological structures observed on seismic profiles and in the field, were explicitly accounted for in the numerical simulations, as well as the complex physics of high-temperature hydrothermal fluid flow. In the first case numerical simulations underpinned how fluid flow links to seismicity in the Tjörnes Fracture Zone. In the second case the syn-eruptive groundwater flow model of the Askja caldera highlighted how groundwater flow can affect the explosive behaviour of an eruptive event.

7.1 Large scale fluid flow and links to seismicity in the Tjörnes Fracture Zone

The regional fluid flow in the Tjörnes Fracture Zone has been simulated using a high resolution model based on geological and geophysical data and physically realistic thermodynamic properties for hydrothermal fluids. Such simulations are now computationally possible and allow for the study of the emergent behaviour of a particular hydrothermal system while also accounting for the geological structures observed in nature. From this it is possible to draw the following conclusions:

Most fluids in the sedimentary basins are comparatively cold because large areas of the shallow crust are dominated by fluids that percolate downwards from the seafloor. Only 10% of the sedimentary basins are characterised by hot plumes of hydrothermal

fluids which depart from the top of the crystalline basement and reach shallow depths. This explains the occurrence of isolated hydrothermal fields observed in the Tjörnes Fracture Zone.

Faults play a key role in controlling the large-scale and small-scale fluid flow dynamics of the the Tjörnes Fracture Zone and hence influence the temperature distribution. The location and the shape of the upflow areas is directly related to the permeability of the faults. Low permeability faults imply wide upflow areas at shallow depths while high permeability faults lead to narrower upflow areas. The occurrence of faults characterised by very low permeabilities is unlikely in the TFZ. On the other hand, the simulations showed that high permeability faults cause phase separation at shallow depths which has not been reported for the Tjörnes Fracture Zone. Based on this it is suggested that the deeper parts of the faults have a permeability that is slightly higher than the permeability of the surrounding basement rocks while the shallower parts have a permeability 10 to 50 times higher than the rocks comprising the sedimentary basin.

The key feature that emerges from the simulations and links the hydrodynamics and seismicity in the TFZ is the presence of two different fluid flow systems: one occurring in the sedimentary basins and one in the crystalline basement. The first is characterised by vigorous fluid convection and a heterogeneous geothermal gradient, the second by a more uniform geothermal gradient and conduction. The two flow domains form as a consequence of a moderate permeability contrast at the basement-basin interface. This reduces communication between the two systems. The large-scale flow pattern is thought to represent the "inter-seismic" state between main seismic events. The initially stable inter-seismic flow regime can be disturbed locally by co-seismic enhancements of permeability of faulted crustal portions. This causes rapid mixing between the shallow and the deep flow system because overpressured fluids rise at rates of possibly up to 1 m s^{-1}. As the fault permeability decays due to mineral precipitation and increase in effective fault normal stress, the communication between the two flow regimes decreases. This toggle switch mechanism was suggested based on hydrogeochemical variations observed before and after an 5.8 M_w earthquake in the Tjörnes Fracture Zone near the town of Húsavik. The simulations show that the hydrodynamic conditions in the Tjörnes Fracture Zone support this hypothesis. This implies that the toggle switch mechanism might be effective in the vicinity of the fault-hosted upflow zones.

To test the previous hypothesis pre-, co-, and post-seismic fluid flow as well as co- and post-seismic fault permeability behaviour were simulated in chapter 5 using the P-T-X distribution described in chapter 4. The simulations specifically accounted for a toggle switch mechanism that allows for fault permeability variations due to local changes in the effective fault normal stress that act on the faults during variations in pore pressure.

The distribution of pore pressures and their maximum values in the TFZ vary as function of the mantle degassing rates and crustal permeability during the pre-seismic state. The time required to reach a steady-state pore pressure distribution in the TFZ is most likely few hundred years, assuming a moderate mantle degassing rate of 3.0×10^{-9} m s^{-1} and reasonably permeability distributions. Afterwards, four clearly defined horizontal regions characterised by different pore pressures occur in the TFZ. The pore pressure conditions inside the crust are indicated by the pore fluid factor λ. The shallow crust has values of λ of approximately 0.15. λ increases in the sedimentary basins with depth from approximately 0.15 to 0.5. Values of λ of 0.15 occur in the area below the top of the basement, in agreement with an aseismic region observed in the TFZ, while λ values around 0.6 are reached at 7.5 km depth. The deep basement is characterised by elevated λ values ranging from 0.6 to 1. The faults always comprise more elevated pore pressures than the surrounding structures. At depth they are characterised by critical values of λ close to 1, which could explain the intense microseismicity observed in the Grimsey Lineament and in the Húsavik Flatey Fault.

Elevated pore pressures which are possibly close to lithostatic pressure are released by fault inflation. This is probably connected to seismic events. Elevated pore pressures migrate upwards along the fault plane, allowing for deep and shallow fluids to mix. During this co-seismic phase, pore velocities can exceed 0.01 m s^{-1} and transport chemically different fluids over long distances in short times, as observed in the TFZ. Pore pressure migration in the faults during fault inflation is accompanied by a large increase in permeability of up to 7 orders in magnitude as the effective fault normal stress decreases. While the pore pressure propagation and permeability increase occur within few minutes, time-scales for post-seismic fault sealing range from 2 to 3 years.

The simulations demonstrate that the Tjörnes Fracture Zone is a prime example of the toggle switch mechanism, which explains the observed link between seismicity and fluid movement in a tectonically and hydrothermally active oceanic setting. A complete

toggle switch cycle probably occurs within a few years and is accompanied by very short-lived and extreme fluid fluxes. Repeated cycles continually regenerate fault-controlled permeability and weaken the crust but a prerequisite is a moderate mantle degassing rate, which is needed to maintain elevated pore pressures. At least for the TFZ, the toggle switch mechanism appears to be clearly linked with distinct hydrogeochemical changes. This suggests that hydrogeochemical monitoring in the vicinity of faults could be used as an important tool to increase the confidence in earthquakes forecasting.

7.2 Groundwater flow during the 28–29 March 1875 Askja volcano eruption

The syn-eruptive Askja groundwater flow model simulates the groundwater dynamics during the March 1875 Askja eruption. It is proposed that the water involved in the phreatomagmatic activity was stored within the lava pile of the Askja caldera. Field data, eyewitness records and numerical discrete fracture techniques have been combined to characterise the groundwater flow model with representative data. For instance, the computation of the effective permeability of the fractured lava flows was needed to compute effective permeabilities which are representative of a fractured lava. These high permeabilities, 1.3×10^{-09} and 2.5×10^{-08} m^2 for the basaltic and felsic lava flows, respectively, proved to be key to quantify the large-scale approximately-radial drawdown. This supplied enough water to maintain a phreatoplinian eruption initially but caused a subsequent drying-out during phase C2 as increasingly more water was drained from the surrounding lavas (Figure 6.14).

The eruptive dry-wet-dry shift that characterised the transition between the eruptive phases B, C, and D, respectively, is an important aspect of this eruption. The key concept behind the model is that during the C phase of the 1875 Askja eruption, the conduit acted like a well removing water from the permeable lava pile. This lead to the dry out of the C1 phase as the water is drained from the aquifer, initially fast from the high-permeability layer(s) and then increasingly slower from the lower-permeability layers. The presence of the felsic lava flow is important but not mandatory to generate the dual-porosity behaviour and explain the groundwater dynamics which initially maintain but later cause the drying out of the phreatoplinian eruption and subsequent dry eruption. Fractured basalts, or possibly even lava tubes, klinkers, and other high-permeability

layers work equally well as long as they create a laterally extensive high-permeability layer.

Previous studies (Carey et al., 2008) have shown that the vent of phase B was intruded into the hyaloclastites that bound the Askja caldera. The low permeability of these lithologies restricted water supply to the conduit rendering the ratio of water mass to magma mass $\mathcal{M}$ too small to produce a phreatomagmatic activity. When the conduit of the phase C intruded into the lava pile, water could be transported rapidly enough to the conduit to maintain an optimal $\mathcal{M}$ ratio (Figure 6.14a), leading to the occurrence of phreatoplinian activity (phase C1). With time the water supply decreased causing the progressive dry-out of the density currents (Figure 6.14b, 6.14c). The groundwater table declined inside the Askja caldera after drainage during the phases C1 and C2. When the conduit of the phase D propagated into the lava pile, ~ 1 km away from the vent of the C phase, the ratio $\mathcal{M}$ was probably not large enough to produce a second phreatoplinian eruption (Figure 6.14d). The Askja caldera groundwater flow model shows for the first time how syn-eruptive groundwater flow can affect the eruptive style of a volcanic event.

7.3 Outlook

Several questions remain unanswered as result of this study and new hypothesis have been formed that can be tested in future research. The work highlighted the occurrence of two distinct fluid flow regimes, one in the basement and one in the sedimentary basins, and provides a consistent explanation for the mixing of these two separated systems due to seismic events. One critical aspect is that the models do not account for for the chemical reactions occurring at depth between high temperature hydrothermal fluids and hot basalts or colder sedimentary rocks. Hence future studies should include reactive transport simulations. The outcomes of this thesis now provide the relevant pressure, temperature, and salinity conditions in the TFZ at depth. To further test the hypothesis that two distinct flow regimes can mix during a seismic event, a new research project based at the University of Stockholm just started. It will use laboratory experiments to develop a more consistent reactive transport model for the TFZ to investigate how fast fluids can flow in the TFZ during pre-, co-, and post-seismic times and how pulses of deep fluids change the reaction dynamics in shallow aquifers.

Another important aspect is that the two-dimensional numerical simulations in this thesis do not allow to investigate processes acting in the third dimension. For example it is not possible to account for convection occurring in the fault planes and, perhaps more importantly, the complex 3D stress acting on the faults. This shortcoming can be now addressed. Computational power and algorithmic efficiency increased during the last years and CSMP++ can now be run in parallel. This significantly reduces the runtime required to simulate the large meshes that characterise three-dimensional models (Coumou et al., 2008c). Future work should focus on 3D simulations and ideally include further geophysical surveys to better constrain the heat flow in the TFZ in three dimensions and the connection between the fluid flow and seismicity. However, it should be noted that geometrical modelling and finite element meshing of complex three-dimensional structures still remains a major challenge.

The work on the groundwater flow dynamics during the eruption of the Askja volcano, however, has already demonstrated that realistic three-dimensional models are possible. In general the results for the Askja volcano suggest that 3D groundwater flow modelling could complement studies that asses the risk and hazard of active volcanoes to improve their reliability and predictability.

The outcome of such new research could not only be of importance to geologists, geochemists, and geophysicists working on high temperature hydrothermal systems. It also has the potential to improve the understanding how field data could be used to predict when volcanic eruptions and earthquakes will occur.

Bibliography

R. M. Allen. *The mantle plume beneath Iceland and its interaction with the North Atlantic Ridge: A seismological investigation.* PhD Thesis, Princeton University, 2001. 37, 38

R.M. Allen, G. Nolet, W.J. Morgan, K. Vogfjörd, M. Nettles, G. Ekstrom, B.H. Bergsson, P. Erlendsson, G.R. Foulger, S. Jakobsdottir, et al. Plume-driven plumbing and crustal formation in Iceland. *Journal of Geophysical Research*, 107(B8):2163, doi:10.1029/2001JB000584, 2002. 83, 116

Anonymous. *Most likely written by Jón Sigurðsson, Gautlönd, Mývatn* Domestic news (fréttir innlendar). *Norðanfari*, 14:25 – 36; 55 – 56, 1875. 37, 113, 132

H. Armannsson, A. Gudmundsson, and B.S. Steingrimsson. Exploration and development of the Krafla geothermal area. *Jökull*, (37):13–30, 1987. 40

S. Arnórsson and A. Andrésdóttir. Processes controlling the distribution of Boron and Chlorine in natural waters in Iceland. *Geochimica et Cosmochimica Acta*, 59(20): 4125–4146, 1995. 40

S. Arnórsson, G. Axelsson, and K. Saemundsson. Geothermal systems in Iceland. *Jökull*, 58:269–302, 2008. 38, 40

S. Arnórsson. Geothermal systems in Iceland: Structure and conceptual models I. High temperature areas. *Geothermics*, 24(5-6):561–602, 1995a. 49

S. Arnórsson. Geothermal systems in Iceland: Structure and conceptual models II. Low temperature areas. *Geothermics*, 24(5-6):603–629, 1995b. 49

D. Bächler, T. Kohl, and L. Rybach. Impact of graben-parallel faults on hydrothermal convection - Rhine graben case study. *Physics and Chemistry of the Earth*, 28(9-11): 431–441, 2003. 62, 72

A. Battistelli, C. Calore, and K. Pruess. The simulator TOUGH2/EWASG for modelling geothermal reservoirs with brines and non-condensible gas. *Geothermics*, 26(4):437–464, 1997. 19, 24

J. Bear. *Dynamics of fluids in porous media.* 1972. 21, 23

J. Bear. *Hydraulics of groundwater.* McGraw-Hill New York, 1979. 22

J. Bear. *Dynamics of fluids in porous media.* Dover Publications, 1988. 20

M. Belayneh, S. Geiger, and S.K. Matthai. Numerical simulation of water injection into layered fractured carbonate reservoir analogs. *AAPG bulletin*, 90(10):1473, 2006. 29

Y. Benderitter and G. Cormy. Possible approach to geothermal research and relative costs. *Small Geothermal Resources: A Guide to Development and Utilization, UNITAR, New York*, pages 59–69, 1990. 8

F. Bergerat and J. Angelier. Immature and mature transform zones near a hot spot: The South Iceland Seismic Zone and the Tjörnes Fracture Zone (Iceland). *Tectonophysics*, 447(1-4):35–46, 2007. 87

F. Bergerat, J. Angelier, and C. Homberg. Tectonic analysis of the Húsavik Flatey Fault (Northern Iceland) and mechanisms of an oceanic transform zone, the Tjörnes Fracture Zone. *Tectonics*, 19(6):1161–1177, 2000. 42, 87

C. Bergins, S. Crone, and K. Strauss. Multiphase flow in porous media with phase change. Part II: Analytical solutions and experimental verification for constant pressure steam injection. *Transport in Porous Media*, 60(3):275–300, 2005. 17

B. Berkowitz. Characterizing flow and transport in fractured geological media: A review. *Advances in water resources*, 25(8-12):861–884, 2002. 20

A. Bertagnini and P. Landi. The secche di lazzaro pyroclastics of Stromboli volcano: a phreatomagmatic eruption related to the Sciara del Fuoco sector collapse. *Bulletin of volcanology*, 58(2-3):239–245, 1996. 14, 114

G.G. Bianchi and I.N. McCave. Holocene periodicity in north atlantic climate and deep-ocean flow South of Iceland. *Nature*, 397(6719):515–517, 1999. 35

J.L. Bischoff and F.W. Dickson. Seawater-basalt interaction at 200 °C and 500 bars: implications for origin of sea-floor heavy-metal deposits and regulation of seawater chemistry. *Earth and Planetary Science Letters*, 25:385, 1975. 10

I.T. Bjarnason, W. Menke, O.G. Flovenz, and D. Caress. Tomographic image of the mid-atlantic plate boundary in southwestern Iceland. *Journal of Geophysical Research-Solid Earth*, 98(B4), 1993. 37, 38

I.T. Bjarnason, C.J. Wolfe, S.C. Solomon, and G. Gudmundson. Initial results from the icemelt experiment: Body-wave delay times and shear-wave splitting across Iceland. *Geophysical Research Letters*, 23(5):459–462, 1996. 37

I. Th. Bjarnason. An Iceland hotspot saga. *Jökull*, 58:–16, 2008. 83, 116

G. Björbsson and G. Bodvarsson. A survey of geothermal reservoir properties. *Geothermics*, 19(1):17–27, 1990. 26

G.S. Bodvarsson, S.M. Benson, O. Sigurdsson, V. Stefansson, and E.T. Eliasson. Krafla geothermal field, Iceland I: analysis of well test data. *Water Resour. Res*, 20(11), 1984a. 40, 49

G.S. Bodvarsson, K. Pruess, V. Stefansson, and E.T. Eliasson. The Krafla geothermal field, Iceland, II. The natural state of the system. *Water Resources Research*, 20(11): 153–1544, 1984b. 40, 49

G.S. Bodvarsson, K. Pruess, V. Stefansson, and E.T. Eliasson. Krafla geothermal field, iceland; III. The generating capacity of the field. *Water Resources Research*, 20(11), 1984c. 40, 49

R. Bodvarsson, S.T. Rögnvaldsson, S.S. Jakobsdóttir, R. Slunga, and R. Stefánsson. The SIL data acquisition and monitoring system. *Seismological Research Letters*, 67: 35–46, 1996. 83

A.M. Boullier, K. Fujimoto, T. Ohtani, G. Roman-Ross, E. Lewin, H. Ito, P. Pezard, and B. Ildefonse. Textural evidence for recent co-seismic circulation of fluids in the nojima fault zone, Awaji Island, Japan. *Tectonophysics*, 378(3-4):165–181, 2004. 13

D.R. Bower, K.C. Heaton, J.T. Andrews, R.M. Retherford, R.M. Stesky, D.W. Morrow, I.R. Mayers, J.P. Lefort, R.T. Haworth, P.D. Ward, et al. Response of an aquifer near ottawa to tidal forcing and the Alaskan earthquake of 1964. *Canadian Journal of Earth Sciences*, 15(3):331–340, 1978. 13

W.F. Brace. Permeability of crystalline and argillaceous rocks. 17(5):241–251, 1980. 26

W.F. Brace. Permeability of crystalline rocks: New in situ measurements. *J. Geophys. Res*, 89(B6):4327–4330, 1984. 26

A. Brack, G. Horneck, C.S. Cockell, A. Bérces, N.K. Belisheva, C. Eiroa, T. Henning, T. Herbst, L. Kaltenegger, A. Léger, et al. Origin and evolution of life on terrestrial planets. *Astrobiology*, 10(1):69, 2010. 11

B. Brandsdottir. Hitorical accounts of earthquakes associated with eruptive activity in the Askja volcanic system. *Jökull*, (42):1–12, 1992. 118

B. Brandisdottir, W. Menke, P. Einarsson, R. Wihite, and R. Staples. Faroe-Iceland ridge experiment – II. *Journal of Geophysical Research*, 102:7867 – 7886, 1997. 37, 38

K. Breddam. Kistufell: primitive melt from the Iceland mantle plume. *Journal of Petrology*, 43(2):345, 2002. 35

A.J.M.R. Breivik and J.I.M.Y. Faleide. Geomagnetism and paleomagnetism/marine geology and b07102-rates of continental breakup magmatism and seafloor spreading in the Norway basin-Iceland plume interaction. *Journal of Geophysical Research-Part B-Solid Earth, DOI 10.1029/2005JB004004*, 111(7), 2006. 35

W.S. Broecker, D.M. Peteet, and D. Rind. Does the ocean-atmosphere system have more than one stable mode of operation? *Nature*, 315(6014):21–26, 1985. 35

G.C. Brown, S.P. Everett, H. Rymer, D.W. McGarvie, and I. Foster. New light on caldera evolution – Askja, Iceland. *Geology*, 19(4):352, 1991. 116

R. J. Carey. *Conduit, eruption and plume dynamics throughout the 28 – 29 March 1875 eruption of Askja Volcano, Iceland.* PhD thesis, University of Hawai'i, 2008. xi, 14, 118, 119, 120, 130, 132, 139

R.J. Carey, B.F. Houghton, and T. Thordarson. Contrasting styles of welding observed in the proximal Askja 1875 eruption deposits II: Local welding. *Journal of Volcanology and Geothermal Research*, 171(1-2):20–44, 2008. 14, 113, 118, 119, 120, 125, 149

R.J. Carey, B.F. Houghton, and T. Thordarson. Tephra dispersal and eruption dynamics of wet and dry phases of the 1875 eruption of Askja volcano, Iceland. *Bulletin of Volcanology*, pages 1–20, 2009a. xi, xiii, 14, 113, 117, 118, 119, 120, 130, 141, 142

R.J. Carey, B.F. Houghton, and T. Thordarson. Abrupt shifts between wet and dry phases of the 1875 eruption of Askja volcano: Microscopic evidence for macroscopic dynamics. *Journal of Volcanology and Geothermal Research*, 184(3-4):256–270, 2009b. 14, 113, 130, 132, 133, 139, 141

S. Carey and R.S.J. Sparks. Quantitative models of the fallout and dispersal of tephra from volcanic eruption columns. *Bulletin of Volcanology*, 48(2):109–125, 1986. 119

R. Cataldi and P. Chellini. Geothermal energy in the mediterranean area before the middle ages. *Proceedings, World Geothermal Congress*, 1995. 8

L.M. Cathles. An analysis of the cooling of intrusives by ground-water convection which includes boiling. *Economic Geology*, 72(5):804, 1977. 7, 18, 19, 51

L.M. Cathles and J.J. Adams. Fluid flow and petroleum and mineral resources in the upper ($<$ 20 km) continental crust. *Economic Geology, 100th Anniversary Volume*, pages 77–110, 2005. 13

L.M. Cathles. Scales and effects of fluid flow in the upper crust. *Science*, 248(4953): 323, 1990. 1

L.M. Cathles and R. Shannon. How potassium silicate alteration suggests the formation of porphyry ore deposits begins with the nearly explosive but barren expulsion of large volumes of magmatic water. *Earth and Planetary Science Letters*, 262:92Ű-108, 2007. 112

D.S. Chapman and H.N. Pollack. Global heat flow - A new look. *Earth and Planetary Science Letters*, 28:23Ű-32, 1975. 1

L.B. Christiansen, S. Hurwitz, M.O. Saar, S.E. Ingebritsen, and P.A. Hsieh. Seasonal seismicity at western United States volcanic centers. *Earth and Planetary Science Letters*, 240(2):307–321, 2005. 85

L. Claesson, A. Skelton, C. Graham, C. Dietl, M. Morth, P. Torssander, and I. Kockum. Hydrogeochemical changes before and after a major earthquake. *Geology*, 32(8):641–644, 2004. 14, 15, 16, 36, 44, 45, 50, 51, 79, 81, 84, 92, 112

L. Claesson, A. Skelton, C. Graham, and C.M. Morth. The timescale and mechanisms of fault sealing and water-rock interaction after an earthquake. *Geofluids*, 7(4):427–440, 2007. 14, 15, 16, 36, 44, 45, 50, 51, 79, 80, 81, 84, 92, 99, 111

C. Clauser. Opacity–the concept of radiative thermal conductivity. *Handbook of Terrestrial Heat-Flow Density Determination, Kluwer, Dordrecht*, page 143, 1988. 23

C. Clauser. Permeability of crystalline rocks. *EOS EOSTAJ,*, 73(21), 1992. 26

J.S. Cline, R.J. Bodnar, and J.D. Rimstidt. Numerical simulation of fluid flow and silica transport and deposition in boiling hydrothermal solutions: application to epithermal gold deposits. *Journal of Geophysical Research-Solid Earth*, 97(B6), 1992. 19

A.T. Corey. Measurement of water and air permeability in unsaturated soil. *Soil Science Society of America Journal*, 21(1):7, 1957. 22

D. Coumou, T. Driesner, S. Geiger, C.A. Heinrich, and S. Matthai. The dynamics of mid-ocean ridge hydrothermal systems: Splitting plumes and fluctuating vent temperatures. *Earth and Planetary Science Letters*, 245(1-2):218–231, 2006. 19, 29

D. Coumou, T. Driesner, and C.A. Heinrich. The structure and dynamics of mid-ocean ridge hydrothermal systems. *Science*, 321(5897), 2008. 11, 19, 25, 29, 51, 74

D. Coumou, S. Matthäi, S. Geiger, and T. Driesner. A parallel fe-fv scheme to solve fluid flow in complex geologic media. *Computers & Geosciences*, 34(12):1697–1707, 2008. 30, 150

D. Coumou, T. Driesner, P. Weis, and C.A. Heinrich. Phase separation, brine formation, and salinity variation at black smoker hydrothermal systems. *Journal of geophysical research*, 114(B3), 2009. 19, 25, 29, 52, 62

S.F. Cox. Faulting processes at high fluid pressures: an example of fault valve behavior from the Wattle Gully Fault, Victoria, Australia. *Journal of Geophysical Research-Solid Earth*, 100(B7):12841–12859, 1995. 85

S.F. Cox. The application of failure mode diagrams for exploring the roles of fluid pressure and stress states in controlling styles of fracture-controlled permeability enhancement in faults and shear zones. *Geofluids*, doi:10.1111/j.1468-8123.2010.00281.x, 2010. 111

S.F. Cox and K. Ruming. The St Ives mesothermal gold system, western Australia–a case of golden aftershocks? *Journal of Structural Geology*, 26(6-7):1109–1125, 2004. 7, 85, 112

S. Crampin, A. Gudmundsson, and R. Stefansson. Indication of high pore-fluid pressures in a seismically-active fault zone. *Geophysical Journal International*, 151(2):1–5, 2002. 79, 108

A.E. Croucher and M.J. O' Sullivan. Application of the computer code TOUGH2 to the simulation of supercritical conditions in geothermal systems. *Geothermics*, 37(6): 622–634, 2008. 19

F.A. Darbyshire, I.T. Bjarnason, R.S. White, and O.G. Flovenz. Crustal structure above the Iceland mantle plume imaged by the ICEMELT refraction profile. *Geophysical Journal International*, 135(3):1131–1149, 1998. 37, 38, 83, 116

H. Darcy. Les fontaines publiques de la ville de Dijon. *Dalmont, Paris*, 647, 1856. 21

C. David, T.F. Wong, W. Zhu, and J. Zhang. Laboratory measurement of compaction-induced permeability change in porous rocks: Implications for the generation and maintenance of pore pressure excess in the crust. *Pure and Applied Geophysics*, 143 (1):425–456, 1994. 85, 95, 96

P.T. Delaney. Rapid intrusion of magma into wet rock: groundwater flow due to pore pressure increases. *Journal of Geophysical Research*, 87:7739–7756, 1982. 18

R. Di Napoli, A. Aiuppa, S. Bellomo, L. Brusca, W. D'Alessandro, E.G. Candela, M. Longo, G. Pecoraino, and M. Valenza. A model for Ischia hydrothermal system:

Evidences from the chemistry of thermal groundwaters. *Journal of Volcanology and Geothermal Research*, 186(3-4):133–159, 2009. 114

I.G. Donaldson. Temperature gradients in the upper layers of the earthŠs crust due to convective water flows. *J. Geophys. Res*, 67(9):3449–3459, 1962. 18

T. Driesner. The interplay of permeability and fluid properties as a first order control of heat transport, venting temperatures and venting salinities at mid-ocean ridge hydrothermal systems. *Geofluids*, 10:132–141, 2010. 18

T. Driesner and C.A. Heinrich. The system H_2O - NaCl. Part I: Correlation formulae for phase relations in temperature–pressure–composition space from 0 to 1000 °C, 1 to 5000 bar, and 0 to 1 XNaCl. *Geochimica et Cosmochimica Acta*, 71(20):4880–4901, 2007. 3, 5, 25, 51, 55, 62, 64, 93

T. Driesner. The system H_2O - NaCl. Part II: Correlations for molar volume, enthalpy, and isobaric heat capacity from 0 to 1000 °C, 1 to 5000 bar, and 0 to 1 XNaCl. *Geochimica et Cosmochimica Acta*, 71(20):4902–4919, 2007. 3, 25, 51, 55, 62, 64, 93

T. Driesner and S. Geiger. Numerical simulation of multiphase fluid flow in hydrothermal systems. *Reviews in Mineralogy and Geochemistry*, 65(1):187, 2007. 19, 25, 29, 49

B. Dutrow and D. Norton. Evolution of fluid pressure and fracture propagation during contact metamorphism. *Journal of Metamorphic Geology*, 13:677–677, 1995. 19

A.L. Edwards and A. Trump. *A computer program for transient and steady state temperature distribution in multidimensional systems.*, 1972. 29

J. Ehlers and P.L. Gibbard. Quaternary glaciations: extent and chronology. 2004. 35, 36

Th. Einarsson. Askja og Oskjugosidh 1961. *Nattrufraethingurinn*, 32:1–48, 1962. 116

P. Einarsson. Relative location of earthquakes in the Tjörnes fracture zone. *Soc. Sci. Iceland*, 5:45–60, 1976. 43

T. Einarsson and K.J. Albertsson. The glacial history of iceland during the past three million years. *Philosophical Transactions of the Royal Society of London. Series B, Biological Sciences*, pages 637–644, 1988. 35, 36

P. Einarsson. Earthquakes and present-day tectonism in Iceland. *Tectonophysics*, 189 (1-4):261–279, 1991. 41, 87

E. Ekstrom, R.S. Stein, J.P. Eaton, and Eberhart-Phillips D. Seismicity and geometry of a 110-km-long blind thrust fault: I. the 1985 Kettleman hills, California, earthquake. *Journal of Geophysical Research*, 97:4843–4864, 1992. 13

J.W. Elder. Steady free convection in a porous medium heated from below. *J. Fluid Mech*, 27(1):29–48, 1967. 17

W.A. Elders, G.O. Fridleifsson, D.K. Bird, M.H. Reed, P. Schiffman, and R. Zierenberg. The iceland deep drilling project (IDDP):(I) drilling for supercritical hydrothermal fluids is underway. page 2069, 2008. 40

J.E. Elkhoury, E.E. Brodsky, and D.C. Agnew. Seismic waves increase permeability. *Nature*, 441:1135–1138, 2006. 79

T.R. Elliott, C.J. Hawkesworth, and K. Grönvold. Dynamic melting of the Iceland plume. 1991. 35

S. Emmanuel and B. Berkowitz. An experimental analogue for convection and phase separation in hydrothermal systems. *Journal of Geophysical Research*, 111(B9), 2006. 17, 23

S. Emmanuel and B. Berkowitz. Phase separation and convection in heterogeneous porous media: Implications for seafloor hydrothermal systems. *Journal of Geophysical Research-Solid Earth*, 112(B5):B05210, 2007.

D.G. Evans and J.P. Raffensperger. On the stream function for variable-density groundwater flow. *Water Resources Research*, 28(8):141 – 145, 1992. 24

A.M. Evans. *Ore geology and industrial minerals: an introduction.* Wiley-Blackwell, 1993. 9

J.P. Evans, C.B. Forster, and J.V. Goddard. Permeability of fault-related rocks, and implications for hydraulic structure of fault zones. *Journal of Structural Geology*, 19 (11):1393–1404, 1997. 56, 85

A.T. Fisher. Permeability within basaltic oceanic crust. *Reviews of Geophysics*, 36(2): 143–182, 1998. 26

A.T. Fisher, E.E. Davis, M. Hutnak, L. Spiess, V. Zuhlsdorff, A. Cherkaoui, L. Christiansen, K. Edwards, R. Macdonald, H. Villinger, M.J. Motti, C.G. Wheat, and K. Becker. Hydrothermal recharge and discharge across 50 km guided by seamounts on a young ridge flank. *Nature*, 421:618–621, 2003. 51

G.M. Fleeger. Hydrologic effects of the pymatuning earthquake of September 25, 1998, in northwestern Pennsylvania. 1999. 13

Ó.G. Flóvenz. On geothermal energy in Iceland. *Presentation at the 11th International Symposium on District Heating and Cooling*, 2008. 49, 55, 72, 94

Ó.G. Flóvenz and K. Saemundsson. Heat flow and geothermal processes in Iceland. *Tectonophysics*, 225(1-2):123–138, 1993. 55, 56, 70, 72, 94

O.G. Flóvenz, L.S. Georgsson, and K. Árnason. Resistivity structure of the upper crust in Iceland. *Journal of Geophysical Research*, 90:10136–10150, 1985. 55, 72, 75

F.J. Fontaine, M. Rabinowicz, and J. Boulégue. Permeability changes due to mineral diagenesis in fractured crust: implications for hydrothermal circulation at mid-ocean ridges. *Earth and Planetary Science Letters*, 184(2):407–425, 2001. 19

F.J. Fontaine, W.S.D. Wilcock, and D.A. Butterfield. Physical controls on the salinity of mid-ocean ridge hydrothermal vent fluids. *Earth and Planetary Science Letters*, 257(1-2):132–145, 2007. 24, 51

G.R. Foulger. The Hengill geothermal area, Iceland: variation of temperature gradients deduced from the maximum depth of seismogenesis. *Journal of Volcanology and Geothermal Research*, 65(1-2):119–133, 1995. 40

G.R. Foulger, A.D. Miller, B.R. Julian, and J.R. Evans. Three-dimensional vp and vp/vs structure of the Hengill triple junction and geothermal area, Iceland, and the

repeatability of tomographic inversion. *Geophys. Res. Lett*, 22(10):1309–1312, 1995. 40

G.R. Foulger, M.J. Pritchard, B.R. Julian, J.R. Evans, R.M. Allen, G. Nolet, W.J. Morgan, B.H. Bergsson, P. Erlendsson, S. Jakobsdottir, and others. The seismic anomaly beneath Iceland extends down to the mantle transition zone and no deeper. *Geophysical Journal International*, 142(3):1–650, 2000. 37

I.B. Fridleifsson. Geothermal activity in Iceland. *Jokull*, 29:47–56, 1979. 40

G.O. Fridleifsson. Geothermal gradient and hydrothermal systems off North Iceland. *Orkustofnun, National Energy Authority. Report GÓF-94-05*, page 4, 1994. 72

I.B. Fridleifsson, R. Bertani, E. Huenges, J. Lund, A. Ragnarsson, and L. Rybach. The possible role and contribution of geothermal energy to the mitigation of climate change. pages 20–25, 2008. 8

T. Fridriksson, B.R. Kristjánsson, H. Ármannsson, E. Margrétardóttir, S. Ólafsdóttir, and G. Chiodini. CO_2 emissions and heat flow through soil, fumaroles, and steam heated mud pools at the Reykjanes geothermal area, SW Iceland. *Applied Geochemistry*, 21(9):1551–1569, 2006. 79, 80, 94, 111

Y. Fujimitsu, S. Ehara, R. Oki, and R. Kanou. Numerical model of the hydrothermal system beneath Unzen volcano, Japan. *Journal of Volcanology and Geothermal Research*, 175(1-2):35–44, 2008. 19

K.P. Furlong, R.B. Hanson, and J.R. Bowers. Modeling thermal regimes. *Reviews in Mineralogy and Geochemistry*, 26(1):437, 1991. 24

S. Garcia, J. Angelier, F. Bergerat, and C. Homberg. Tectonic analysis of an oceanic transform fault zone based on fault-slip data and earthquake focal mechanisms: the Húsavik Flatey Fault zone, Iceland. *Tectonophysics*, 344(3-4):157–174, 2002. 41, 42, 83, 89, 96, 99, 110

Z. Garfunkel. Internal structure of the Dead Sea leaky transform (rift) in relation to plate kinematics. *Tectonophysics*, 32(80):81–108, 1981. 42

G. Garven, S.W. Bull, and R.R. Large. Hydrothermal fluid flow models of stratiform ore genesis in the mcarthur basin, Northern territory, Australia. *Geofluids*, 1(4):289–311, 2001. 51

S. Geiger, R. Haggerty, J.H. Dilles, M.H. Reed, and S.K. Matthai. New insights from reactive transport modelling: the formation of the sericitic vein envelopes during early hydrothermal alteration at Butte, Montana. *Geofluids*, 2(3):185–201, 2002. 19, 29

S. Geiger. *Numerical Simulation of the Hydrodynamics and Thermodynamics of NaCl–H_2O Fluids.* PhD thesis, PhD thesis, ETH Zurich, Switzerland, 2004, 2004. 11

S. Geiger, S. Roberts, S.K. Matthai, C. Zoppou, and A. Burri. Combining finite element and finite volume methods for efficient multiphase flow simulations in highly heterogeneous and structurally complex geologic media. *Geofluids*, 4(4):284–299, 2004. 19, 30, 32, 63, 67

S. Geiger, T. Driesner, C.A. Heinrich, and S.K. Matthäi. On the dynamics of NaCl – H_2O fluid convection in the earth's crust. *J. Geophys. Res*, 110, 2005. 3, 13, 25, 52, 62, 99

S. Geiger, T. Driesner, C.A. Heinrich, and S.K. Matthäi. Multiphase thermohaline convection in the EarthŠs crust: I. A new finite element–finite volume solution technique combined with a new equation of state for NaCl - H_2O. *Transport in Porous Media*, 63(3):399–434, 2006. 19, 28, 29, 62, 63, 86, 93

S. Geiger, T. Driesner, C.A. Heinrich, and S.K. Matthäi. Multiphase thermohaline convection in the EarthŠs crust: II. Benchmarking and application of a finite element–finite volume solution technique with a NaCl - H_2O equation of state. *Transport in Porous Media*, 63(3):435–461, 2006b. 19, 28, 29, 63

S. Geiger, S.K. Matthäi, Niessner J., and R. Helmig. Black-oil simulations for three-component - three-phase flow in fractured porous media. *SPE Journal.*, 14(5114): 338–354, 2009. 29

S. Geiger and S. Emmanuel. Non-fourier thermal transport in fractured geological media. *Water Resources Research*, (B5), 2010, doi: 10.1029/2009WR008488 23, 29

A. Geirsdottir. Extent and chronology of glaciations in iceland; a brief overview of the glacial history. *Quaternary glaciations: extent and chronology. Part I: Europe, 175 – 182. Elsevier, Amsterdam*, 2004. 35, 36

L. Geoffroy and C. Dorbath. Deep downward fluid percolation driven by localized crust dilatation in Iceland. *Geophysical Research Letters*, 35(17), 2008. 77

A.R. Geptner, B. Richter, Y.I. Pikovskii, S.S. Chernyansky, and T.A. Alekseeva. Hydrothermal polycyclic aromatic hydrocarbons in marine and lagoon sediments at the intersection between Tjörnes fracture zone and recent rift zone (Skjálfandi and Öxarfjörður bays), Iceland. *Marine Chemistry*, 101(3-4):153–165, 2006. 72

M.L. Gerdes, L.P. Baumgartner, and M. Person. Stochastic permeability models of fluid flow during contact metamorphism. *Geology*, 23(10):945, 1995. 19

E.R. Giambalvo, C.I. Steefel, A.T. Fisher, N.D. Rosenberg, and C.G. Wheat. Effect of fluid-sediment reaction on hydrothermal fluxes of major elements, eastern flank of the Juan de Fuca Ridge. *Geochimica et Cosmochimica Acta*, 66(10):1739–1758, 2002. 19

G. Giordano, M. Porreca, P. Musacchio, and M. Mattei. The holocene Secche di Lazzaro phreatomagmatic succession (Stromboli, Italy): evidence of pyroclastic density current origin deduced by facies analysis and ams flow directions. *Bulletin of Volcanology*, 70(10):1221–1236, 2008. 114

Glitnir bank. Geothermal energy, market report, september 2007. 2007. 9

J. Gottsmann, R. Carniel, N. Coppo, L. Wooller, S. Hautman, and H. Rymer. Oscillations in hydrothermal systems as a source of periodic unrest at caldera volcanoes: Multiparameter insights from Nisyros, Greece. *Geophysical Research Letters*, 34(L07307), 2007. 114

R.W. Griffiths. The dynamics of lava flows. *Annual Review of Fluid Mechanics*, 32(1): 477–518, 2000. 126

A. Gudmundsson. Formation and growth of normal faults at the divergent plate boundary in Iceland. *Terra Nova*, 5(4):464–471, 1992. 43

A. Gudmundsson. On the structure and formation of fracture zones. *Terra Nova*, 5(3): 215–224, 1993. 96

A. Gudmundsson. Infrastructure and mechanics of volcanic systems in Iceland. *Journal of Volcanology and Geothermal Research*, 64(1-2):1–22, 1995. 46

A. Gudmundsson. Fluid overpressure and stress drop in fault zones. *Geophys. Res. Lett*, 26(1):115–118, 1999. 12, 70, 72, 111

A. Gudmundsson. Dynamics of volcanic systems in Iceland: example of tectonism and volcanism at juxtaposed hot spot and mid-ocean ridge systems. *Annual Review of Earth and Planetary Sciences*, 28(1):107–140, 2000. 39, 46

A. Gudmundsson. Fluid overpressure and flow in fault zones: field measurements and models. *Tectonophysics*, 336(1-4):183–197, 2001. 12, 13, 56

A. Gudmundsson. Infrastructure and evolution of ocean-ridge discontinuities in Iceland. *Journal of Geodynamics*, 43(1):6–29, 2007. 43, 50, 53, 56, 83

K. Gunnarsson. Sedimentary basins of the N-Iceland shelf. Draft version for discussion (April – May 1998). *Orkustofnun Report: OS-98014*, 1998. x, 42, 50, 53, 54, 56, 86, 91, 92

A. Gudmundsson, S. Brynjolfsson, and M.T. Jonsson. Structural analysis of a transform fault-rift zone function in North Iceland. *Tectonophysics*, 220(1-4):205–221, 1993. 43, 50

A. Gunnarsson, B.S. Steingrimsson, E. Gunnlaugsson, J. Magnusson, and R. Maack. Nesjavellir geothermal co-generation power plant. *Geothermics*, 21(4):559–583, 1992. 40

B. Hanson. The hydrodynamics of contact metamorphism. *Bulletin of the Geological Society of America*, 107(5):595, 1995. 19, 51

R.B. Hanson. Effects of fluid production on fluid flow during regional and contact metamorphism. *Journal of Metamorphic Geology*, 10(1):87–97, 1992. 19, 24

R.B. Hanson. Hydrodynamics of magmatic and meteoric fluids in the vicinity of granitic intrusions. *Geological Society of America Special Papers*, 315:251, 1996. 19

D.O. Hayba and S.E. Ingebritsen. The computer model hydrotherm, a three-dimensional finite-difference model to simulate ground-water flow and heat transport in the temperature range of 0 to 1200 °c. *US Geological Survey Water-Resources Investigations Report*, 94:4045, 1994. 27, 28

D.O. Hayba and S.E. Ingebritsen. Multiphase groundwater flow near cooling plutons. *J. Geophys. Res*, 102(6):12235–12252, 1997. 18, 19, 51

K.L. Heft, K.M. Gillis, M.A. Pollock, J.A. Karson, and E.M. Klein. Role of upwelling hydrothermal fluids in the development of alteration patterns at fast spreading ridges: Evidence from the sheeted dike complex at Pito deep. *Geochemistry Geophysics Geosystems*, 9(5):Q05O07, 2008. 74

M. Hellweg. Physical models for the source of lascar's harmonic tremor. *Journal of Volcanology and Geothermal Research*, 101(1-2):183–198, 2000. 12

P. Henry. Fluid flow at the toe of the Barbados accretionary wedge constrained by thermal, chemical, and hydrogeologic observations and models. *Journal of Geophysical Research*, 105(B11): 25855–25872, 2000. 96

M. Hensch, C. Riedel, J. Reinhardt, and T. Dahm. Hypocenter migration of fluid-induced earthquake swarms in the Tjörnes fracture zone (North Iceland). *Tectonophysics*, 2007. 41, 43, 50, 51, 53, 84, 87, 89, 94, 99, 108, 109, 111, 112

C. Herzberg and E. Gazel. Petrological evidence for secular cooling in mantle plumes. *Nature*, 458(7238):619–622, 2009. 35

S. Hickman, R. Sibson, and R. Bruhn. Introduction to special section: Mechanical involvement of fluids in faulting. *Journal of Geophysical Research*, 100:12831–12840, 1995. 12

W. Hildreth. Gradients in silicic magma chambers: implications for lithospheric magmatism. *Journal of Geophysical Research*, 86(B11):10153, 1981. 7

D.P. Hill, P.A. Reasenberg, A. Michael, W.J. Arabaz, G. Beroza, D. Brumbaugh, J.N. Brune, R. Castro, S. Davis, D. dePolo, et al. Seismicity remotely triggered by the magnitude 7.3 Landers, California, earthquake. *Science*, 260(5114):1617–1623, 1993. 13, 50

D.P. Hill, F. Pollitz, and C. Newhall. Earthquake-volcano interactions. *Physics Today*, 55(11):41–47, 2002. 85

M.P. Hochstein. Classification and assessment of geothermal resources. *Small Geothermal Resources: A Guide to Development and Utilization, UNITAR, New York*, pages 31–57, 1990. 8

N. Hogeweg, T.E.C. Keith, E.M. Colvard, and S.E. Ingebritsen. Ongoing hydrothermal heat loss from the 1912 ash-flow sheet, valley of ten thousand smokes, alaska. *Journal of Volcanology and Geothermal Research*, 143(4):279–291, 2005. 19

B.F. Houghton, C.J.N. Wilson, R.T. Smith, and J.S. Gilbert. Phreatoplinian eruptions. *Encyclopedia of volcanoes. Academic Press, San Diego*, pages 513–516, 2000. 14, 114

M.K. Hubbert. The theory of ground-water motion. *The Journal of Geology*, 48:785–944, 1940. 22

M.K. Hubbert. Entrapment of petroleum under hydrodynamic conditions. *AAPG Bulletin*, 37(8):1954–2026, 1953.

M.K. Hubbert and W. Rubey. Role of fluid pressure in mechanics of overthrust faulting, pts. I and II. *Geological Society of America Bulletin*, 70:115–205, 1959. 6, 12

S. Hurwitz, S.E. Ingebritsen, and M.L. Sorey. Episodic thermal perturbations associated with groundwater flow: An example from Kilauea volcano, Hawaii. *J. Geophys. Res*, 107:2297, 2002. 114

S. Hurwitz, K.L. Kipp, S.E. Ingebritsen, and M.E. Reid. Groundwater flow, heat transport, and water table position within volcanic edifices: Implications for volcanic processes in the cascade range. *J. Geophys. Res*, 108:2557, 2003. 8, 19, 51, 114

S. Hurwitz, L.B. Christiansen, and P.A. Hsieh. Hydrothermal fluid flow and deformation in large calderas: Inferences from numerical simulations. *J. Geophys. Res*, 112, 2007. 19

S. Husen, R. Taylor, RB Smith, and H. Healser. Changes in geyser eruption behavior and remotely triggered seismicity in yellowstone national park produced by the 2002 m 7.9 denali fault earthquake, Alaska. *Geology*, 32(6):537–540, 2004. 14, 50, 84

M. Hutnak, S. Hurwitz, SE Ingebritsen, and PA Hsieh. Numerical models of caldera deformation: Effects of multiphase and multicomponent hydrothermal fluid flow. *J. Geophys. Res*, 114(B4):441,2009. 19

S.E. Ingebritsen, D.R. Sherrod, and R.H. Mariner. Heat flow and hydrothermal circulation in the Cascade Range, North-central Oregon. *Science*, 243(4897):1458–1462, 1989.

S.E. Ingebritsen and M.A. Scholl. The hydrogeology of kilauea volcano. *Geothermics*, 22(4):255–270, 1993. 25, 114, 115, 128

S.E. Ingebritsen, W.E. Sanford, and C.E. Neuzil. *Groundwater in geologic processes.* Cambridge Univ Pr, 2006. 3, 4, 7, 21, 22, 23, 25, 96, 135, 136

S.E. Ingebritsen and C.E. Manning. Permeability of the continental crust: dynamic variations inferred from seismicity and metamorphism. *Geofluids*, 9999(9999), 2010. 26

SE Ingebritsen, S. Geiger, S. Hurwitz, and T. Driesner. Numerical simulation of magmatic hydrothermal systems. *Reviews of Geophysics*, 48(1), 2010. 7, 14, 19, 23, 24, 33, 49, 51, 85

J.C. Jaeger, N.G.W. Cook, and R.W. Zimmerman. Fundamentals of rock mechanics. *Blackwell Publishing*, 2007. 96

S. S. Jakobsdóttir. Seismicity in Iceland: 1997 – 2004. *Jökull*, 58:75–100, 2008. 41, 83

S.P. Jakobsson. Petrology of recent basalts of the eastern volcanic zone, Iceland. *J. Petrology*, 19:669 – 705, 1978. 46

S.P. Jakobsson. Petrology of recent basalts of the eastern volcanic zone, Iceland. *Acta Natur. Isl.*, 26:1 – 103, 1979. 46

S.S. Jakobsdóttir, G.B. Gudmundsson, and R. Stefansson. Seismicity in Iceland 1991–2000 monitored by the SIL seismic system. *Jokülll*, 51:87–94, 2002.

S. Jakobsdóttir, S. Seismicity in Iceland: 1994-2007. *Jökull*, 58(2005):75–100, 2008. 41, 83

X.W. Jiang, X.S. Wan, and L. Wan. Semi-empirical equations for the systematic decrease in permeability with depth in porous and fractured media. *Hydrogeology Journal*, doi:10.1007/s10040-010-0575-3, 2010. 85

H. Jóhannesson and K. Sæmundsson. Geological map of Iceland. 1: 500 000. *Tectonics* Icelandic Institute of Natatural History, Reykjavík, 1998. 49

H.P. Johnson, M. Hutnak, R.P. Dziak, C.G. Fox, I. Urcuyo, J.P. Cowen, J. Nabelek, and C. Fisher. Earthquake-induced changes in a hydrothermal system on the Juan de Fuca mid-ocean ridge. *Nature*, 407(6801):174–177, 2000. 14, 50, 84

F. Jöhnstrup. Indberetning om den af professor johnstrup foretagne undersogelsesreise paa island i sommerem 1876 (hermed 2 kort og 2 tegninger), saerskilt. *Aftryk af Rigsdagstidenden for den*, (29):1876–77, 1877. 116

J.L. Join, J.L. Folio, and B. Robineau. Aquifers and groundwater within active shield volcanoes. Evolution of conceptual models in the Piton de la Fournaise volcano. *Journal of Volcanology and Geothermal Research*, 147(1-2):187–201, 2005. 51, 114

O. Jonsson. Trölladyngjur. *Nattrufraethingurinn*, (11):76 – 88, 1941. 116

T. Jupp and A. Schultz. A thermodynamic explanation for black smoker temperatures. *Nature*, 403(6772):880–883, 2000. 24

G.N. Keating. The role of water in cooling ignimbrites. *Journal of Volcanology and Geothermal Research*, 142(1-2):145–171, 2005. 19

G.N. Keating, J.W. Geissman, and G.A. Zyvoloski. Multiphase modeling of contact metamorphic systems and application to transitional geomagnetic fields. *Earth and Planetary Science Letters*, 198(3-4):429–448, 2002. 27

G. Keller. Results of an experimental drill hole c, Hawaii. *Journal of Volcanology and Geothermal Research*, 5:345–385, 1979. 114

K.L. Kipp, P.A. Hsieh, and S.R. Charlton. Guide to the revised ground-water flow and heat transport simulator: HydrothermŮversion 3. *US Geological Survey Techniques and Methods 6– A*, 2008. 27, 28

W.M. Kissling. Transport of three-phase hyper-saline brines in porous media: theory and code implementation. *Transport in Porous Media*, 61(1):25–44, 2005a. 19

W.M. Kissling. Transport of three-phase hyper-saline brines in porous media: Examples. *Transport in Porous Media*, 60(2):141–157, 2005b. 19

H. Kitagawa, K. Kobayashi, A. Makishima, and E. Nakamura. Multiple pulses of the mantle plume: Evidence from tertiary Icelandic lavas. *Journal of Petrology*, 2008. 35

A.H. Knoll. Life on a young planet: the first three billion years of evolution on earth. 2004. 11

N. Koe, E. Jansen, and H. Haflidason. Paleoceanographic reconstructions of surface ocean conditions in the Greenland, Iceland and Norwegian seas through the last 14 ka based on diatoms. *Quaternary Science Reviews*, 12(2):115–140, 1993. 35

E.M. Kwicklis, A.V. Wolfsberg, P.H. Stauffer, M.A. Walvoord, and M.J. Sully. Multiphase, multicomponent parameter estimation for liquid and vapor fluxes in deep arid systems using hydrologic data and natural environmental tracers. *Vadose Zone Journal*, 5(3):934, 2006. 28

M.G. Langseth, M.J. Mottl, M.A. Hobart, and A. Fisher. The distribution of geothermal and geochemical gradients near site 501/504: Implications for hydrothermal circulation in the oceanic crust. *Proceedings of ODP initial reports*, 111:23–32, 1988. 11

L.M. Larsen, A.K. Pedersen, G.K. Pedersen, and S. Piasecki. Timing and duration of early tertiary volcanism in the North atlantic: new evidence from west Greenland. *Geological Society London Special Publications*, 68(1):321, 1992. 37

G. Larsen and J. Eiriksson. Late quaternary terrestrial tephrochronology of iceland-frequency of explosive eruptions, type and volume of tephra deposits. *Journal of Quaternary Science*, 23(2):109–120, 2007. 46

G. Larsen and J. Eiríksson. Holocene tephra archives and tephrocronology in Iceland – a brief overview. *Jökull*, 58(2005):229–250, 2008. 118

K.C. Lewis and R.P. Lowell. Mathematical modeling of phase separation of seawater near an igneous dike. *Geofluids*, 4(3):197–209, 2004. 19

K.C. Lewis and R.P. Lowell. Numerical modeling of two-phase flow in the NaCl-H_2O system: Introduction of a numerical method and benchmarking. *Journal of Geophysical Research*, 114(B5):B05202, 2009. 19

K. Li and R.N. Horne. Systematic study of steam-water capillary pressure. *Geothermics*, 36(6):558–574, 2007. 24

R.P. Lowell. Modeling continental and submarine hydrothermal systems. *Rev. Geophys*, 29:457–476, 1991. 49

R.P. Lowell, S.R. Gosnell, and Y. Yang. Numerical simulations of single-pass hydrothermal convection at mid-ocean ridges: Effects of the extrusive layer and temperature-dependent permeability. *Geochem. Geophys. Geosystems*, 8:Q10011, 2007. 51

M. Lupi, S. Geiger, and C. Graham. Hydrothermal fluid flow within a tectonically active rift–ridge transform junction: the Tjörnes Fracture Zone, Iceland. *Journal of Geophysical Research*, 31(115), 2010. 84, 88, 92, 94, 95, 99

R.A. Lutz and M.J. Kennish. Ecology of deep-sea hydrothermal vent communities: a review. *Reviews of Geophysics*, 31(3), 1993. 10

R. MacDonald, R.S.J. Sparks, H. Sigurdsson, D.P. Mattey, D.W. McGarvie, and R.L. Smith. The 1875 eruption of Askja volcano. *Iceland: Combined fractional crystallization and selective contamination in the generation of rhyolite magma: Mineralogical Magazine*, 51:183–202, 1987. 118

F.T. Mackenzie and R.M. Garrels. Chemical mass balance between rivers and oceans. *American Journal of Science*, 264(7):507, 1966. 11

M. Manga. Origin of postseismic streamflow changes inferred from baseflow recession and magnitude-distance relations. *Geophysical Research Letters*, 28(10):2133–2136, 2001. 13

M. Manga and E. Brodsky. Seismic triggering of eruptions in the far field: Volcanoes and geysers. *Annual review of earth and planetary sciences*, 34:263, 2006. 13, 49, 84

C.E. Manning and S.E. Ingebritsen. Permeability of the continental crust: Implications of geothermal data and metamorphic systems. *Reviews of Geophysics*, 37(1):127–150, 1999. 6, 26, 60, 70, 85, 91, 95, 103

W. Martin, J. Baross, D. Kelley, and M.J. Russell. Hydrothermal vents and the origin of life. *Nature Reviews Microbiology*, 6(11):805–814, 2008. 11

S.K. Matthai, C.A. Heinrich, and T. Driesner. Is the mount isa copper deposit the product of forced brine convection in the footwall of a major reverse fault? *Geology*, 32(4):357–360, 2004. 51, 115, 129, 130

S.K. Matthai and M. Belayneh. Fluid flow partitioning between fractures and a permeable rock matrix. *Geophysical Research Letters*, 31(7):7602–6, 2004. 29

S.K. Matthäi, S. Geiger, and S. G. Roberts. Complex systems platform, CSP5.0, userŠs guide. *http://csmp.ese.imperial.ac.uk/wiki*, (1), 2004. 29

S.K. Matthäi, M. Belayneh, A. Mezentsev, and R. Tomlinson. CSP Model building & interface guide. *http://csmp.ese.imperial.ac.uk/wiki*, (1), 2005. 29

S.K. Matthäi, A. Mezentsev, and M. Belayneh. Control-volume finite-element two-phase flow experiments with fractured rock represented by unstructured 3D hybrid meshes. *SPE Reservoir Simulation Symposium*, 2005.

S.K. Matthäi, S. Geiger, S.G. Roberts, A. Paluszny, M. Belayneh, A. Burri, A. Mezentsev, H. Lu, D. Coumou, T. Driesner, et al. Numerical simulation of multi-phase fluid flow in structurally complex reservoirs. *Geological Society London Special Publications*, 292(1):405, 2007. 29, 30, 51, 63, 114, 133

J.S. McClain, M.L. Begnaud, M.A. Wright, J. Fondrk, and G.K. Von Damm. Seismicity and tremor in a submarine hydrothermal field: The northern juan de fuca ridge. *Geophysical Research Letters*, 20(17):1883–1886, 1993. 12

I. McDougall, N.D. Watkins, G.P.L. Walker, and L. Kristjansson. Potassium-argon and paleomagnetic analysis of Icelandic lava flows: Limits on the age of anomaly 5. *Journal of Geophysical Research*, 81(8):1505–1512, 1976. 35

I. McDougall, K. Saemundsson, H. Johannesson, N.D. WATKINS, and L. Kristjansson. Extension of the geomagnetic polarity time scale to 6.5 my: K-ar dating, geological and paleomagnetic study of a 3,500-m lava succession in western Iceland. *Geological Society of America Bulletin*, 88(1):1, 1977. 35

W. Menke, B. Brandsdottir, P. Einarsson, and I.T. Bjarnason. Reinterpretation of the rrisp-77 Iceland shear-wave profiles. *Geophysical Journal International*, 126(1): 166–172, 1996. 37, 38

W. Menke, M. West, B. Brandsdottir, and D. Sparks. Compressional and shear velocity structure of the lithosphere in northern Iceland. *Bulletin of the Seismological Society of America*, 88(6):1561, 1998. 37, 38

S.A. Miller and A. Nur. Permeability as a toggle switch in fluid-controlled crustal processes. *Earth and Planetary Science Letters*, 183(1-2):133–146, 2000. x, 13, 50, 80, 85, 87, 88, 92

S.A. Miller, C. Collettini, L. Chiaraluce, M. Cocco, M. Barchi, and B.J.P. Kaus. Aftershocks driven by a high-pressure CO_2 source at depth. *Nature*, 427(6976):724–727, 2004. 12, 79, 85, 87, 92, 95, 96, 112

P. Muffler and R. Cataldi. Methods for regional assessment of geothermal resources. *Geothermics*, 7(2-4):53–89, 1978. 8

T.N. Narasimhan and P.A. Witherspoon. An integrated finite difference method for analyzing fluid flow in porous media. *Water Resources Research*, 12:57–64, 1976. 29

C.E. Neuzil. Abnormal pressures as hydrodynamic phenomena. *American Journal of Science*, 295(6):742, 1995. 4, 6

D. Norton and J. Knight. Transport phenomena in hydrothermal systems: cooling plutons. *American Journal of Science*, 277(8):937–981, 1977. 7, 18, 19

D. Norton and H.P. Taylor Jr. Quantitative simulation of the hydrothermal systems of crystallizing magmas on the basis of transport theory and oxygen isotope data: an analysis of the skaergaard intrusion. *Journal of Petrology*, 20(3):421, 1979. 7

A. Okamoto and N. Tsuchiya. Velocity of vertical fluid ascent within vein-forming fractures. *Geology*, 37(6):563–566, 2009. 85, 112

C.M. Oldenburg and K. Pruess. Simulation of propagating fronts in geothermal reservoirs with the implicit leonard total variation diminishing scheme. *Geothermics*, 29 (1):1–25, 2000. 19

M.J. Osborne and R.E. Swarbrick. Mechanisms for generating overpressure in sedimentary basins: a reevaluation. *American Association of Petroleum Geologist*, 29(81): 10–23, 1997. 4

N. Oskarsson, G.E. Sigvaldason, and S. Steinthorsson. A dynamic model of rift zone petrogenesis and the regional petrology of Iceland. *Journal of Petrology*, 23(1):28, 1982. 35

G. Palmason. Heat flow and hydrothermal activity in Iceland. *Geodynamics of Iceland and the North Atlantic area*, 297–306, 1974. 72

G. Palmason and K. Saemundsson. Iceland in relation to the mid-atlantic ridge. *Annual Review of Earth and Planetary Sciences*, 2(1):25–50, 1974. 49

A. Paluszny, SK Matthai, and M. Hohmeyer. Hybrid finite element-finite volume discretization of complex geologic structures and a new simulation workflow demonstrated on fractured rocks. *Geofluids*, 7(2):186–208, 2007. 19, 30, 56, 92

H. Pape, C. Clauser, and J. Iffland. Permeability prediction for reservoir sandstones and basement rocks based on fractal pore space geometry. *Geophysics*, 64(5):1447–1460, 1999.

E.M. Parmentier. Numerical experiments on 18o depletion in igneous intrusions cooling by groundwater convection. *Journal of Geophysical Research*, 86:7131–7144, 1981. 19

R. Pawar, N. Warpinski, R. Benson, R. Grigg, J. Krumhansl, and B. Stubbs. Geologic sequestration of co2 in a depleted oil reservoir: An overview of a field demonstration project. *SPE Annual Technical Conference and Exhibition*, 2004. 28

R.J. Pawar. Numerical simulations of large-scale co_2 injection incorporating effect of potential wellbore leakage. *Proceedings of the 2007 DOE Conference on Carbon Capture and Storage, May 7–10, 2007, Pittsburgh, PA.*, 2007. 28

E.D. Pittman. Relationship of porosity and permeability to various parameters derived from mercury injection-capillary pressure curves for sandstone. *AAPG Bulletin*, 76 (2):191–198, 1992.

S. Prejean, A. Stork, W. Ellsworth, D. Hill, and B. Julian. High precision earthquake locations reveal seismogenic structure beneath mammoth mountain, california. *Geophysical Research Letters*, 30(24):2247, 2003. 13

K. Pruess. Shaft, mulkom, tough: A set of numerical simulators for multiphase fluid and heat flow. *Geotermia, Rev. Mex. Geoenergia*, 4(1):185–202, 1988. 27

K. Pruess. Tough2: A general-purpose numerical simulator for multiphase fluid and heat flow. 1991. 27

K. Pruess. The tough codes–a family of simulation tools for multiphase flow and transport processes in permeable media. *Vadose Zone Journal*, 3(3):738, 2004. 27

K. Pruess. Enhanced geothermal systems (egs) using co2 as working fluid–a novel approach for generating renewable energy with simultaneous sequestration of carbon. *Geothermics*, 35(4):351–367, 2006. 8

K. Pruess, G.S. Bodvarsson, V. Stefansson, and E.T. Eliasson. The krafla geothermal field, iceland, 4, history match and prediction of individual well performance. *Water Resources Research*, 20(11):1561–1584, 1984. 40

K. Pruess, C. Calore, R. Celati, and YS Wu. An analytical solution for heat transfer at a boiling front moving through a porous medium. *International journal of heat and mass transfer*, 30(12):2595–2602, 1987. 17

K. Pruess, C. Oldenburg, and G. Moridis. Tough2 userŠs guide, version 2.0., 1999. 27, 29

K. Pruess, T. Xu, J. Apps, and J. Garcia. Numerical modeling of aquifer disposal of CO_2. *SPE Journal*, 8(1):49–60, 2003. 8

D.M. Pyle. The thickness, volume and grainsize of tephra fall deposits. *Bulletin of Volcanology*, 51(1):1–15, 1989. 119

J.P. Raffensperger and G. Garven. The formation of unconformity-type uranium ore deposits; 1, coupled groundwater flow and heat transport modeling. *American Journal of Science*, 295(5):581, 1995a. 1, 2

J.P. Raffensperger and G. Garven. The formation of unconformity-type uranium ore deposits; 2, coupled hydrochemical modeling. *American Journal of Science*, 295(6): 639, 1995b. 2

J.P. Raffensperger. Evidence and modeling of large-scale groundwater convection in precambrian sedimentary basins. *Basin-Wide Diagenetic Patterns: Integrated Petrologic, Geochemical, and Hydrologic Considerations*, 57:15–26, 1997. 23

S. Rahmstorf. Bifurcatii of the atlantic thermohaline circulation in response to changes in the hydrological cycle. *Nature*, 378:9, 1995. 35

H.J. Ramey. Proceedings of special panel on geothermal model intercomparison study; supplement to sixth workshop on geothermal reservoir engineering. 1980. 27

P. Renard and G. De Marsily. Calculating equivalent permeability: a review. *Advances in Water Resources*, 20(5):253–278, 1997. 20

J.R. Rice. Fault stress states, pore pressure distributions, and the weakness of the San Andreas Fault. *International geophysics series*, 51:475–475, 1992. x, 13, 85, 86, 95, 96, 98

B. Richter. Structure of the törnes basin, north iceland; possible forming of oil and gas within a young, shallow sedimentary basin with high geothermal gradient. *Orkustofnun (National Energy Authority) and University of Iceland*, Internal report, 2006. 42, 89

B. Richter. Basin modelling with emphasis on the effects of an active volcanic environment on petroleum source rock, maturation and basin formation. In *Oral presentation*, 2006. 36, 42

C. Riedel, M. Schmidt, R. Botz, and F. Theilen. The grimsey hydrothermal field offshore North Iceland: crustal structure, faulting and related gas venting. *Earth and Planetary Science Letters*, 193(3-4):409–421, 2001. 72, 111

C. Riedel, A. Tryggvason, T. Dahm, R. Stefanson, R. Bödvarson, and G.B. Gudmundsson. The seismic velocity structure North of Iceland from joint inversion of local earthquake data. *Journal of Seismology*, 9(4):383–404, 2005. 53, 54, 56, 57, 70, 77, 83, 89

B.A. Robinson, H.S. Viswanathan, and A.J. Valocchi. Efficient numerical techniques for modeling multicomponent ground-water transport based upon simultaneous solution of strongly coupled subsets of chemical components. *Advances in Water Resources*, 23(4):307–324, 2000. 28

E.A. Roeloffs. Hydrologic precursors to earthquakes: A review. *Pure and Applied Geophysics*, 126(2):177–209, 1988. 13

E.A. Roeloffs. Persistent water level changes in a well near parkfield, california, due to local and distant earthquakes. *Journal of Geophysical Research*, 103:869–889, 1998. 13

E. Roeloffs, M. Sneed, D.L. Galloway, M.L. Sorey, C.D. Farrar, J.F. Howle, and J. Hughes. Water-level changes induced by local and distant earthquakes at long valley caldera, california. *Journal of Volcanology and Geothermal Research*, 127(3-4): 269–303, 2003. 14, 50, 84

S.T. Rögnvaldasson, A. Gudmundsson, and R. Slunga. Seismotectonic analysis of the Tjörnes fracture zone, an active transform fault in North Iceland. *Journal of geophysical research*, 103(B 12):30117–30129, 1998. 41, 50, 89, 91

S. Rojstaczer, S. Wolf, and R. Michel. Permeability enhancement in the shallow crust as a cause of earthquake-induced hydrological changes. 1995. 13

S.A. Rojstaczer, S.E. Ingebritsen, and D.O. Hayba. Permeability of continental crust influenced by internal and external forcing. *Geofluids*, 8(2):128–139, 2008 4, 26, 85, 98, 101, 103

S.A. Rojstaczer. Ground water and fault strength. *Hydrogeology*, page 447, 1988. 12

S. Rojstaczer and S. Wolf. Permeability changes associated with large earthquakes: An example from Loma Prieta, California. *Geology*, 20(3):211, 1992. 13

M.J. Rossi. Morphology and mechanism of eruption of postglacial shield volcanoes in iceland. *Bulletin of volcanology*, 57(7):530–540, 1996. 46

W.W. Rubey and M.K. Hubbert. Role of fluid pressure in mechanics of overthrust. *Geological Society of America Bulletin*, 76:469–474, 1965. 85

M.J. Russell and I. Kanik. Why does life start, what does it do, where will it be, and how might we find it? *Journal of Cosmology*, 5, 2010. 11

H. Rymer and E. Tryggvason. Gravity and elevation changes at Askja, Iceland. *Bulletin of Volcanology*, 55(5):362–371, 1993. 116

M.O. Saar and M. Manga. Permeability-porosity relationship in vesicular basalts. *Geophys. Res. Lett*, 26(1):111–114, 1999. 115, 128, 136, 141

MO Saar and M. Manga. Depth dependence of permeability in the Oregon Cascades inferred from hydrogeologic, thermal, seismic, and magmatic modeling constraints. 2004. 26, 85

S. Self and R.S.J. Sparks. Characteristics of widespread pyroclastic deposits formed by the interaction of silicic magma and water. *Bulletin of Volcanology*, 41(3):196–212, 1978.

K. Saemundsson. Evolution of the axial rifting zone in northern Iceland and the Tjörnes fracture Zone. *Bulletin of the Geological Society of America*, 85(4):495–504, 1974. 35, 41, 42, 43, 50, 87, 96, 99, 110

K. Saemundsson. Fissure swarms and central volcanoes of the neovolcanic zones of iceland. *Geol. J. Special Issue*, 10:415 – 432, 1978. 46

K. Saemundsson. Outline of the geology of iceland. *Jökull*, 29:7–28, 1979. 46, 49

K. Saemundsson. The geology of the krafla volcanic system. *Nattura M vatns. Hislenska natturufraedhifelag, Reykjavik*:25–95, 1991. 46

E.A. Sammel, S.E. Ingebritsen, and R.H. Mariner. The hydrothermal system at newberry volcano, oregon. *Journal of Geophysical Research-Solid Earth*, 93(B9):149 – 162, 1988. 19

J.H. Sass, A. Lachenbruch, T.H. Moses, and P. Morgan. Heat flow from a scientific research well at cajon pass, california. *Journal of Geophysical Research*, 97:5017–5030, 1992. 23

A.D. Saunders, J.G. Fitton, A.C. Kerr, M.J. Norry, and R.W. Kent. The north atlantic igneous province. *Geophysical monograph*, 100:45–93, 1997. 37, 39

C. Schardt, R. Large, and J. Yang. Controls on heat flow, fluid migration, and massive sulfide formation of an off-axis hydrothermal system–the Lau basin perspective. *American Journal of Science*, 306(2):103, 2006. 74

P. Schiffman and GO Fridleifsson. The smectite–chlorite transition in drillhole nj-15, nesjavellir geothermal field, iceland: Xrd, bse and electron microprobe investigations. *Journal of Metamorphic Geology*, 9(6):679–696, 2007. 40

J.G. Sclater, C. Jaupart, and D. Galson. The heat flow through oceanic and continental crust and the heat loss of the earth. *Reviews of Geophysics*, 18(1):269–311, 1980. 3

M. Sekioka. Geothermal energy in history. the case of japan: our common heritage. 1995. 8

M.C. Serreze, F. Carse, R.G. Barry, and J.C. Rogers. Icelandic low cyclone activity: Climatological features, linkages with the nao, and relationships with recent changes in the northern hemisphere circulation. *Journal of Climate*, 10(3):453–464, 1997. 35

R.H. Sibson. Frictional constraints on thrust, wrench and normal faults. *Nature*, 249: 542 – 544, 1974. 6, 7, 12, 96

R.H. Sibson. Controls on low-stress hydro-fracture dilatancy in thrust, wrench and normal fault terrains. *Nature*, 289:665 – 667, 1981. 6, 7, 12, 96, 112

R.H. Sibson. Stopping of earthquake ruptures at dilational fault jogs. *Nature*, 316:248 – 251, 1985. 84

R.H. Sibson. Conditions for fault-valve behaviour. *Geological Society London Special Publications*, 54(1):15, 1990. 13, 85

R.H. Sibson. Implications of fault-valve behaviour for rupture nucleation and recurrence. *Tectonophysics*, 211(1-4):283–293, 1992. 85

R.H. Sibson. An episode of fault-valve behaviour during compressional inversion?–the 2004 M 6.8 mid-Niigata prefecture, Japan, earthquake sequence. *Earth and Planetary Science Letters*, 257(1-2):188–199, 2007. 79, 85

R.H. Sibson and J.V. Rowland. Stress, fluid pressure and structural permeability in seismogenic crust, North Island, New Zealand. *Geophysical Journal International*, 154(2):584–594, 2003. 6

F. Sigmundsson. Iceland geodynamics: crustal deformation and divergent plate tectonics. *Springer Verlag*, 2006. 87

H. Sigurdsson and S.R.J. Sparks. Lateral magma flow within rifted Icelandic crust. *Nature*, 274:126 – 130, 1978. 118

H. Sigurdsson and R.S.J. Sparks. Rifting episode in North Iceland in 1874–1875 and the eruptions of Askja and Sveinagja. *Bulletin of Volcanology*, 41(3):149–167, 1978a. 118

G.E. Sigvaldason. Basalts from the centre of the assumed Icelandic mantle plume. *Journal of Petrology*, 15(3):497, 1974. 35

G.E. Sigvaldason. Rifting, magmatic activity and interaction between acid and basic liquids. *Nordic Volcanological Institute*, 79:03, 1979. 116, 118, 119

G.E. Sigvaldason. Samspil vatns og kviku: Oskugosith 1875. *Eldur eri northri. Sogufelagith. Reykjavik*, 37–49, 1982. 118

G.E. Sigvaldason. Volcanic and tectonic processes coinciding with glaciation and crustal rebound: an early Holocene rhyolitic eruption in the Dyngjufjoll volcanic centre and the formation of the Askja caldera, North Iceland. *Bulletin of Volcanology*, 64(3): 192–205, 2002. 116, 118

R.L. Smith and H.R. Shaw. Igneous-related geothermal systems. *Assessment of geothermal resources of the United StatesŮ1975: US Geological Survey Circular*, 726:58–83, 1975. 7

R.T. Smith and B.F. Houghton. Vent migration and changing eruptive style during the 1800a Taupo eruption: new evidence from the Hatepe and Rotongaio phreatoplinian ashes. *Bulletin of Volcanology*, 57(6):432–439, 1995. 113, 114

D.T. Snow. Rock fracture spacings, openings, and porosities. *Proceedings American Society of Civil Engineers*, 94: 73–19, 1968. 98, 129

C.H. Sondergeld and D.L. Turcotte. An experimental study of two-phase convection in a porous medium with applications to geological problems. *Journal of Geophysical Research*, 82:2045–2053, 1977. 17

L. Sonnette, J. Angelier, T. Villemin, and F. Bergerat. Faulting and fissuring in active oceanic rift: Surface expression, distribution and tectonic-volcanic interaction in the Thingvellir fissure swarm, Iceland. *Journal of Structural Geology*, 2010. 35

M.L. Sorey, M.A. Grant, and E. Bradford. Nonlinear effects in two phase flow to wells in geothermal reservoirs. *Water Resources Research*, 16(4):767–777, 1980. 22

R.S.J. Sparks, L. Wilson, and H. Sigurdsson. The pyroclastic deposits of the 1875 eruption of Askja, Iceland. *Philosophical Transactions of the Royal Society of London. Series A, Mathematical and Physical Sciences*, 299(1447):241–273, 1981. 46, 116, 118, 119

R.S.J. Sparks. Forecasting volcanic eruptions. *Earth and Planetary Science Letters*, 210 (1-2):1–15, 2003. 114

R. S. J. Sparks and H. Sigurdsson. The 1875 eruption of Askja volcano, Iceland: combined fractional crystallization and selective contamination in the generation of rhyolitic magma. *Mineralogical Magazine*, 51(360):183–202, 1987. 113, 116

H. Spethmann. Islands grosster vulkan: die Dyngjufjoll mit der Askja. 1913. 116

P. Sruoga, N. Rubinstein, and G. Hinterwimmer. Porosity and permeability in volcanic rocks: a case study on the serie tobifera, South Patagonia, Argentina. *Journal of Volcanology and Geothermal Research*, 132(1):31–43, 2004. 115, 128

R.K. Staples, R.S. White, B. Brandsdottir, W. Menke, and P. Maguire. Faroe-iceland ridge experiment 1. Crustal structure of northeastern Iceland. *J. Geophys. Res*, 102: 7849–7866, 1997. 37, 38

E. Stanislavsky and G. Garven. A theoretical model for reverse water-level fluctuations induced by transient permeability in thrust fault zones. *Earth and Planetary Science Letters*, 210(3-4):579–586, 2003. 85

H.T. Stearns. *Hydrogeology of Volcanic terranes. Chapter XV.* Physics of the Earth, 1942. 115, 128

C.I. Steefel and A.C. Lasaga. A coupled model for transport of multiple chemical species and kinetic precipitation/dissolution reactions with applications to reactive flow in single phase hydrothermal systems. *American Journal of Science*, 294(5):529–592, 1994. 19

R. Stefánsson and P. Halldórsson. Strain release and strain build-up in the south iceland seismic zone. *Tectonophysics*, 152(3-4):267–276, 1988. 41

R. Stefánsson, G.B. Gudmundsson, and P. Halldorsson. Tjörnes fracture zone. new and old seismic evidences for the link between the North Iceland rift zone and the Mid-Atlantic ridge. *Tectonophysics*, 447(1-4):117–126, 2008. 41, 43, 51, 53, 56, 79, 83, 84, 87, 89, 92, 94, 108, 111

R. Stefánsson, G.B. Gudmundsson, and P. Halldórsson. The South Iceland earthquakes 2000: a challenge for earthquake prediction research. *Vedur Report*, 2003. 83

C.A. Stein and S. Stein. Constraints on hydrothermal heat flux through the oceanic lithosphere from global heat flow. *J. Geophys. Res*, 99(B2):3081–3095, 1994. 3

J. Stigall and B. Dugan. Overpressure and earthquake initiated slope failure in the Ursa region, northern Gulf of Mexico. *Journal of Geophysical Research*, 115:B04101, doi:10.1029/2009JB006848, 2010. 84

K. Stüben. A review of algebraic multigrid. *Journal of Computational and Applied Mathematics*, 128:281–309, 2001. 30, 63

I. Sumita and M. Manga. Suspension rheology under oscillatory shear and its geophysical implications. *Earth and Planetary Science Letters*, 269(3-4):468–477, 2008.

L.R. Sykes. Mechanism of earthquakes and nature of faulting on the mid-oceanic ridges. *Journal of Geophysical Research*, 72(8):2131–2153, 1967. 43

P. Talwani, L. Chen, and K. Gahalaut. Seismogenic permeability, k_s. *Geophys. Res*, 112, 2007. 26

H.P. Taylor Oxygen isotope evidence for large-scale interaction between meteoric ground waters and tertiary granodiorite intrusions, western cascade range, oregon. *Journal of Geophysical Research*, 76:7855–7874, 1971. 7

K. Terzaghi. Erdbaumechanik. *Franz Deuticke, Wien*, 1925. 85

K. Terzaghi. Die Berechnung der Durchlässigkeitsziffer des Tones aus dem Verlauf der Hydrodynamischen Spannungserscheinungen. *Akademie der Wissenschaften in Wien, Sitzungsberichte, Mathematisch-Natuerwissenschaftliche Klasse*, 132:125-138, 1923. 85

S. Thorarinsson and G.E. Sigvaldason. The eruption in Askja, 1961; a preliminary report. *American Journal of Science*, 260(9):641, 1962. 116, 118

T. Thordarson and S. Self. The roza member, columbia river basalt group- a gigantic pahoehoe lava flow field formed by endogenous processes? *Journal of Geophysical Research*, 103(B11):27411–27446, 1998. 125

T. Thordarson. Postglacial volcanism in Iceland. *Jökull*, 58:197–228, 2008. 39, 45, 46

T. Thordarson and G. Larsen. Volcanism in Iceland in historical time: Volcano types, eruption styles and eruptive history. *Journal of Geodynamics*, 43(1):118–152, 2007. 46

T. Thoroddsen. Explorations in Iceland. *Nature*, 30:563–565, 1884. 116

T. Thoroddsen. Die geschichte der islandischen vulkane: D. kgl. danske vidensk. *Selsk. Skr. Afdl*, 8, 1925. 116

A. Timur. An investigation of permeability, porosity, and residual water saturation relationships. *SPWLA 9th Annual Logging Symposium*, 1968.

M. Todesco. Hydrothermal fluid circulation and its effect on caldera unrest. *Developments in Volcanology*, pages 393–416, 2008. 114

M. Todesco, J. Rutqvist, G. Chiodini, K. Pruess, and C.M. Oldenburg. Modeling of recent volcanic episodes at Phlegrean fields (Italy): geochemical variations and ground deformation. *Geothermics*, 33(4):531–547, 2004. 19

J. Tomasson, G. Palmason, J. Jonsson, and S. Bjornsson. Jardhiti vid Húsavik. Litholog-ical report from the Icelandic energy association. Orkustofnun, Jardhitadeild. 1969. 37, 53, 70, 71, 72

J. Toth. A theoretical analysis of groundwater flow in small drainage basins. *Journal of Geophysical Research*, 68(16):4795–4812, 1963. 1

J. Townend and M.D. Zoback. How faulting keeps the crust strong . *Geology*, 28(5): 595–598, 2000. 85

E. Tryggvason. Seismicity, earthquake swarms, and plate boundaries in the Iceland region. *Bulletin of the Seismological Society of America*, 63(4):1327–1348, 1973. 43

R.W. Van Bemmelen and M.G. Rutten. Tablemountains of northern Iceland: Leiden. *EJ Brill Co*, 217, 1955. 116

J.K. Vennard. Elementary fluid mechanics. 1961. 22

E.V. Verzhbitsky, M.V. Kononov, A.F. Byakov, and O.V. Grinberg. Tectonic evolution of the Iceland region, North Atlantic. *Geotectonics*, 43(6):501–521, 2009. 35

S. Violette, E. Ledoux, P. Goblet, and J.P. Carbonnel. Hydrologic and thermal modeling of an active volcano: The piton de la Fournaise, Reunion. *Journal of Hydrology*, 191 (1-4):37–63, 1997. 114

K.L. Von Damm. Seafloor hydrothermal activity: black smoker chemistry and chimneys. *Annual Review of Earth and Planetary Sciences*, 18(1):173–204, 1990.

K.L. Von Damm. Controls on the chemistry and temporal variability of seafloor hydrothermal fluids. *Seafloor Hydrothermal Systems: Physical, Chemical, Biological, and Geological Interactions*, pages 222–247, 1995. 3

H.D. Vosteen and R. Schellschmidt. Influence of temperature on thermal conductivity, thermal capacity and thermal diffusivity for different types of rock. *Physics and Chemistry of the Earth, Parts A/B/C*, 28(9-11):499–509, 2003. 23

G. Wald. The origins of life. *Proceedings of the National Academy of Sciences of the United States of America*, 52(2):595, 1964. 11

G.P.L. Walker. Characteristics of two phreatoplinian ashes, and their water-flushed origin. *Journal of Volcanology and Geothermal Research*, 9(4):395–407, 1981. 114

R.M. Waller, H.E. Thomas, and R.C. Vorhis. Effects of the good friday earthquake on water supplies. *American Water Works Association Journal*, 57:123–131, 1965. 13

J. Wang. Historical aspects of geothermal energy in china. *Proceedings, World Geothermal Congress*,1:75–80, 1995. 8

J.C. Ward. Turbulent flow in porous media. *J. Hydaul. Div. Am. Soc. Civ. Eng*, 90: 1–12, 1964. 22

J.E. Warren and P.J. Root. The behavior of naturally fractured reservoirs. *Old SPE Journal*, 3(3):245–255, 1963. 141

W.S.D. Wilcock. Cellular convection models of mid-ocean ridge hydrothermal circulation and the temperatures of black smoker fluids. *Journal of Geophysical Research*, 103(B2), 1998. 51

D.L. Williams and R.P. Von Herzen. Heat loss from the earth: New estimate. *Geology*, 2(7):327, 1974. 3

J.T. Wilson. Continental drift. *Scientific American*, 208(4):86–100, 1963. 37

D. Wiprut and M.D. Zoback. Fault reactivation and fluid flow along a previously dormant normal fault in the Northern North Sea. *Geology*, 28(7):595–598, 2000. 85

K.H. Wohletz. Explosive magma-water interactions: thermodynamics, explosion mechanisms, and field studies. *Bulletin of Volcanology*, 48(5):245–264, 1986. 14, 133, 138

K.H. Wohletz. Water/magma interaction: physical considerations for the deep submarine environment. *Geophysical Monograph American Geophysical Union*, 140:25–50, 2003. 14, 133, 138

R.A. Wooding. Steady state free thermal convection of liquid in a saturated permeable medium. *Journal of Fluid Mechanics*, 2:273–285, 1957. 18

A.W. Woods. Liquid and vapor flow in superheated rock. *Annual Review of Fluid Mechanics*, 31(1):171–199, 1999. 17

C.C. Wu and G.J. Hwang. Flow and heat transfer characteristics inside packed and fluidized beds. *Journal of Heat Transfer*, 120:667, 1998. 23

T. Xu and K. Pruess. Modeling multiphase non-isothermal fluid flow and reactive geochemical transport in variably saturated fractured rocks: 1. Methodology. *American Journal of Science*, 301(1):16–33, 2001. 19

T. Xu, Y. Ontoy, P. Molling, N. Spycher, M. Parini, and K. Pruess. Reactive transport modeling of injection well scaling and acidizing at Tiwi field, Philippines. *Geothermics*, 33(4):477–491, 2004. 19

H.Y. Zeng, N.R. Diao, and Z.H. Fang. A finite line-source model for boreholes in geothermal heat exchangers. *Heat Transfer-Asian Research*, 31(7):558–567, 2002. 136

M.L. Zoback and M. Zoback. Crustal stress and intraplate deformation. *Geowissenschaften – Weinheim*, 15:116–123, 1997. 4

M.D. Zoback and J.C. Zinke. Production-induced normal faulting. *Pure and Applied Geophysics*, 159(1-3):403–420, 2002. 85

M.D. Zoback, C.A. Barton, M. Brudy, D.A. Castillo, T. Finkbeiner, B.R. Grollimund, D.B. Moos, P. Peska, C.D. Ward, and D.J. Wiprut. Determination of stress orientation and magnitude in deep wells. *International Journal of Rock Mechanics and Mining Sciences*, 40(7-8):1049–1076, 2003. 96

G. Zyvoloski, Z. Dash, and S. Kelkar. FEHM: finite element heat and mass transfer code. 1988. 27

G.A. Zyvoloski, B.A. Robinson, Z.V. Dash, and L.L. Trease. *Summary of the models and methods for the FEHM application-a finite-element heat-and mass-transfer code.*, 1997.
19, 27, 28